30 January 2009 | $10

Science

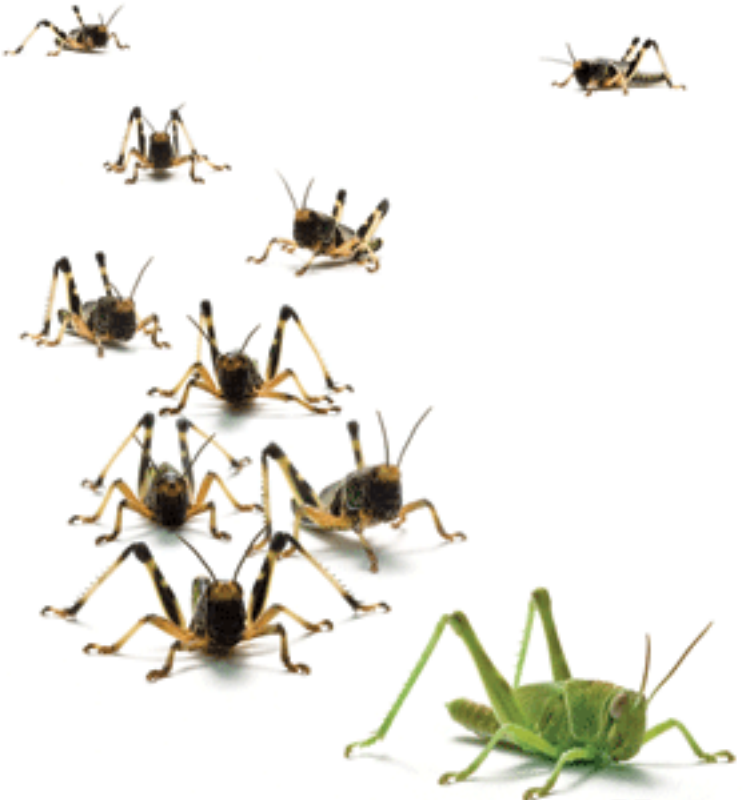

AAAS

EDITORIAL

561 U.S.-China S&T at 30
Norman P. Neureiter and Tom C. Wang

NEWS OF THE WEEK

568 Celebration and Concern Over U.S. Trial of Embryonic Stem Cells

569 Early Start for Human Art? Ochre May Revise Timeline

570 European Science Not As Intense As Hoped

570 Iraq Museum May Reopen Amid Controversy

571 A Stimulus for Science

572 Report Calls for Fresh Look at What Happens Outside School

572 Fingerprints Enhance the Sense of Touch
>> Science *Express Report by J. Scheibert* et al.

573 How Sorghum Withstands Heat and Drought

NEWS FOCUS

574 Seeds of Discontent
>> Science *Podcast*

576 DOD Funds New Views on Conflict With Its First Minerva Grants

578 Beset by Delays, U.S. Astronomers Ponder a Better To Do List
Priorities Nearer to Home in Need of Better Cost Estimates

580 HPV Casts a Wider Shadow

LETTERS

582 Systems Politics and Political Systems
H. Ashrafian
Scientists Not Immune to Partisanship
D. H. Guston et al.
Law and Science Not Mutually Exclusive
D. D. deRosier
Credit for Coauthors
N. T. Hagen
Response
C. H. Sekercioglu

583 CORRECTIONS AND CLARIFICATIONS

583 TECHNICAL COMMENT ABSTRACTS

BOOKS *ET AL.*

584 Science on the Air
M. C. LaFollette, reviewed by A. J. Wolfe

585 Human
M. S. Gazzaniga, reviewed by R. Adolphs

EDUCATION FORUM

586 Learning and Scientific Reasoning
L. Bao et al.

PERSPECTIVES

588 The Force Is with Us
M. A. Schwartz
>> Reports pp. 638 and 642

589 Transforming Graphene
A. Savchenko
>> Report p. 610

590 An Abnormal Normal State
G. S. Boebinger
>> Research Article p. 603

592 Pores in Place
F. D. Sack and J.-G. Chen
>> Report p. 649

593 Unfolding the Secrets of Calmodulin
R. B. Best and G. Hummer
>> Report p. 633

594 The Key to Pandora s Box
P. A. Stevenson
>> Report p. 627

REVIEW

602 Sudden Death of Entanglement
T. Yu and J. H. Eberly

BREVIA

602 Facile Synthesis of AsP_3
B. M. Cossairt et al.
The question of the stability of solid AsP_3, a simple inorganic molecule, has been settled by its synthesis.

CONTENTS continued >>

page 574

page 584

COVER

Desert locusts, *Schistocerca gregaria*, are normally solitary and avoid each other (green individual, lower right). Forced proximity between them leads to the release of the neurotransmitter serotonin, which changes their behavior to mutual attraction and initiates a cascade of events leading to swarm formation, including a change in appearance (black and yellow group). See page 627.

Image: Tom Fayle, Swidbert Ott, and Stephen Rogers/University of Cambridge

DEPARTMENTS

559 This Week in *Science*
562 Editors Choice
564 *Science* Staff
565 Random Samples
567 Newsmakers
596 AAAS News & Notes
655 New Products
656 *Science* Careers

Published by AAAS

RESEARCH ARTICLE

603 Anomalous Criticality in the Electrical Resistivity of $La_{2-x}Sr_xCuO_4$
R. A. Cooper et al.
High magnetic fields can strip away the superconducting regime of a cuprate superconductor, revealing the presence of an enigmatic quantum critical point.
>> Perspective p. 590

REPORTS

607 Revealing the Maximum Strength in Nanotwinned Copper
L. Lu et al.
Studies of nanocrystalline copper reveal changes in deformation mechanisms with grain size and the role played by twin boundaries.

610 Control of Graphene s Properties by Reversible Hydrogenation: Evidence for Graphane
D. C. Elias et al.
Graphene can be transformed from a conductor to an insulator by exposure to hydrogen atoms and reversed by a thermal treatment.
>> Perspective p. 589

614 Dynamical Quorum Sensing and Synchronization in Large Populations of Chemical Oscillators
A. F. Taylor et al.
Communication between chemical oscillators in solution can mimic that of large populations of single-celled organisms.

617 Single Nanocrystals of Platinum Prepared by Partial Dissolution of Au-Pt Nanoalloys
M. Schrinner et al.
Gold-platinum nanoparticles, held in polymer networks on latex beads, are converted into platinum nanocrystals.

620 Cascadia Tremor Located Near Plate Interface Constrained by *S* Minus *P* Wave Times
M. La Rocca et al.
A series of microearthquakes near Puget Sound originate near or on the subduction zone fault from a recurrent source.

623 Divergent Evolution of Duplicate Genes Leads to Genetic Incompatibilities Within *A. thaliana*
D. Bikard et al.
The divergent evolution of a duplicated gene results in genetic incompatibilities between strains of the plant *Arabidopsis*.

627 Serotonin Mediates Behavioral Gregarization Underlying Swarm Formation in Desert Locusts
M. L. Anstey et al.
Serotonin induces the phenotypic switch from solitary to gregarious behavior in desert locusts.
>> Perspective p. 594; Science *Podcast*

630 Survival from Hypoxia in *C. elegans* by Inactivation of Aminoacyl-tRNA Synthetases
L. L. Anderson et al.
Reduced activity of aminoacyl transfer RNA synthetases allows for survival from hypoxic insult in the nematode *C. elegans*.

633 Ligand-Dependent Equilibrium Fluctuations of Single Calmodulin Molecules
J. P. Junker et al.
Single-molecule force spectroscopy reveals the equilibrium dynamics of calmodulin folding and how it is modulated by peptide ligands.
>> Perspective p. 593

638 Stretching Single Talin Rod Molecules Activates Vinculin Binding
A. del Rio et al.
Force-induced stretching of proteins can expose previous cryptic binding sites and promote binding to their ligands.
>> Perspective p. 588

642 Mechanically Activated Integrin Switch Controls $\alpha_5\beta_1$ Function
J. C. Friedland et al.
Myosin contraction and extracellular matrix stiffness drive a tension-induced cell-surface integrin switch that regulates cell signaling.
>> Perspective p. 588

644 A Human Telomerase Holoenzyme Protein Required for Cajal Body Localization and Telomere Synthesis
A. S. Venteicher et al.
Telomerase Cajal body protein 1 (TCAB1) is the fourth discovered subunit of the chromosome end-capping enzyme telomerase.

649 PAN1: A Receptor-Like Protein That Promotes Polarization of an Asymmetric Cell Division in Maize
H. N. Cartwright et al.
Asymmetric cell division in plants is regulated by a receptor-like kinase, implicating a signaling cascade in cell polarization.
>> Perspective p. 592

651 Calcineurin/NFAT Signaling Is Required for Neuregulin-Regulated Schwann Cell Differentiation
S.-C. Kao et al.
The cell signaling components calcineurin/NFATc and Sox10 control Schwann cell myelination.

CONTENTS continued **>>**

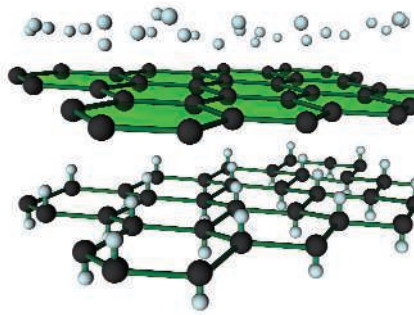

page 589 & 610

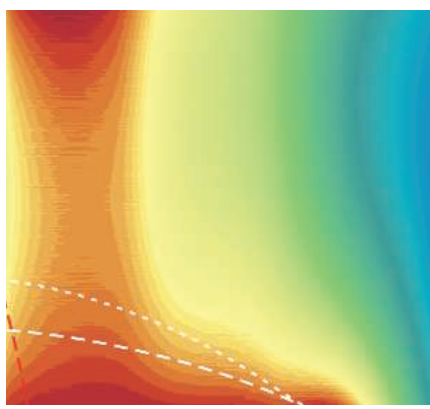

page 590 & 603

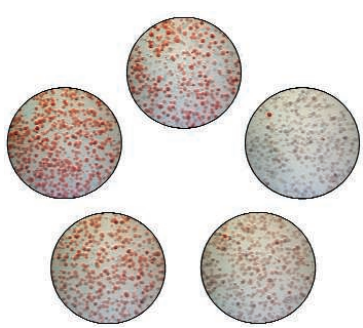

page 614

Published by AAAS

SCIENCEONLINE

SCIENCEXPRESS
www.sciencexpress.org

A Role for RNAi in the Selective Correction of DNA Methylation Defects
F. K. Teixeira et al.

An RNA interference dependent DNA methylation rescue system helps to preserve a subset of DNA methylation marks in *Arabidopsis.*
10.1126/science.1165313

The Role of Fingerprints in the Coding of Tactile Information Probed with a Biomimetic Sensor
J. Scheibert et al.

Fingertip ridges improve the tactile perception of fine features.
>> *News story p. 572*
10.1126/science.1166467

Zircon Dating of Oceanic Crustal Accretion
C. J. Lissenberg et al.

Zircon dates from the slow-spreading mid-Atlantic Ridge show that magmatic intrusions formed new oceanic crust regularly and evenly, thereby providing cooling times.
10.1126/science.1167330

Inducing a Magnetic Monopole with Topological Surface States
X.-L. Qi et al.

A magnetic monopole is theoretically predicted to be induced at the surface of a topological insulator.
10.1126/science.1167747

TECHNICALCOMMENTS

Comment on Arsenic (III) Fuels Anoxygenic Photosynthesis in Hot Spring Biofilms from Mono Lake, California
B. Schoepp-Cothenet et al.

full text at www.sciencemag.org/cgi/content/full/323/5914/583c

Response to Comment on Arsenic(III) Fuels Anoxygenic Photosynthesis in Hot Spring Biofilms from Mono Lake, California
R. S. Oremland et al.

full text at www.sciencemag.org/cgi/content/full/323/5914/583d

SCIENCENOW
www.sciencenow.org
Highlights From Our Daily News Coverage

A Millennia-Long Greenhouse Disaster
The physics of global warming would make for essentially irreversible global damage.

No Feces for This Species
Dung beetle gives up excrement for the life of a hunter.

Death March of the Penguins?
Shrinking sea ice may decimate penguin population that starred in 2005 movie.

SCIENCESIGNALING
www.sciencesignaling.org
The Signal Transduction Knowledge Environment

EDITORIAL GUIDE: Freedom of Materials
M. B. Yaffe

Intellectual property concerns bring into conflict data sharing and accessibility of materials.

RESEARCH ARTICLE: Direct Response to Notch Activation Signaling Crosstalk and Incoherent Logic
A. Krejčí et al.

Identification of the direct target genes of Notch reveals complex input into multiple signaling pathways that goes beyond coordination of transcriptional networks.

RESEARCH ARTICLE: Differential Requirement of mTOR in Postmitotic Tissues and Tumorigenesis
C. Nardella et al.

Conditional inactivation of *mTor* has little effect in the adult mouse prostate, but it suppresses tumor initiation and progression.

RESEARCH ARTICLE: Characterization of the Intrinsic and TSC2-GAP Regulated GTPase Activity of Rheb by Real-Time NMR
C. B. Marshall et al.

An NMR-based assay enables real-time analysis of the GTPase activity of Rheb and of the effect of its GTPase-activating protein TSC2.

RESEARCH ARTICLE: EGFR Signals to mTOR Through PKC and Independently of Akt in Glioma
Q.-W. Fan et al.

Akt is dispensable for signaling between EGFR and mTOR in glioma cells, whereas PKC is critical.

PERSPECTIVE: Grab Your Partner with Both Hands Cytoskeletal Remodeling by Arp2/3 Signaling
S. H. Soderling

Dimerization provides an additional layer of regulation to the activity of a family of actin-nucleating factors.

PODCAST
J. F. Foley and A. M. VanHook

Leptin secreted by adipose tissue decreases insulin production through both direct and indirect mechanisms.

NETWATCH: iBioSeminars

View seminars from leading cell biology researchers; in Web Broadcasts.

NETWATCH: Foldit

A computer game teaches students about the energetics and dynamics of protein folding; in Educator Sites.

SCIENCECAREERS
www.sciencecareers.org/career_magazine
Free Career Resources for Scientists

Women M.D.-Ph.D. s: Life in the Trenches
K. Hede

Physician-scientists urge a focus on solutions, not problems, to advance women in academic medicine.

Perspective: Ensuring Retention of Women in Physician-Scientist Training
J. M. Pauff and M. C. Richards

Why do more women than men drop out of M.D.-Ph.D. programs?

Feet on the Ground, Head in the Sky
E. Pain

Spain s Juan A. Añel has quickly established himself in the field of atmospheric physics.

SCIENCEPODCAST
www.sciencemag.org/multimedia/podcast
Free Weekly Show

Download the 30 January *Science* Podcast to hear about the influence of serotonin on swarming behavior, predicting protests in China, your letters to *Science*, and more.

ORIGINSBLOG
blogs.sciencemag.org/origins
A History of Beginnings

SCIENCEINSIDER
blogs.sciencemag.org/scienceinsider
Science Policy News and Analysis

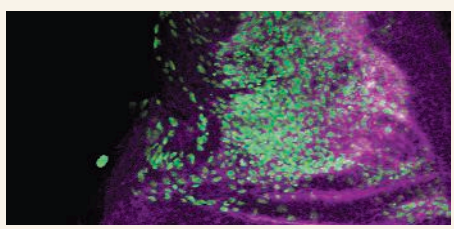

SCIENCESIGNALING
Specifying muscle.

CREDIT: (*SCIENCE SIGNALING*) SARAH J. BRAY/UNIVERSITY OF CAMBRIDGE

SCIENCE (ISSN 0036-8075) is published weekly on Friday, except the last week in December, by the American Association for the Advancement of Science, 1200 New York Avenue, NW, Washington, DC 20005. Periodicals Mail postage (publication No. 484460) paid at Washington, DC, and additional mailing offices. Copyright © 2009 by the American Association for the Advancement of Science. The title SCIENCE is a registered trademark of the AAAS. Domestic individual membership and subscription (51 issues): $146 ($74 allocated to subscription). Domestic institutional subscription (51 issues): $835; Foreign postage extra: Mexico, Caribbean (surface mail) $55; other countries (air assist delivery) $85. First class, airmail, student, and emeritus rates on request. Canadian rates with GST available upon request, GST #1254 88122. Publications Mail Agreement Number 1069624. **Printed in the U.S.A.**

Change of address: Allow 4 weeks, giving old and new addresses and 8-digit account number. **Postmaster:** Send change of address to AAAS, P.O. Box 96178, Washington, DC 20090 6178. **Single-copy sales:** $10.00 current issue, $15.00 back issue prepaid includes surface postage; bulk rates on request. **Authorization to photocopy** material for internal or personal use under circumstances not falling within the fair use provisions of the Copyright Act is granted by AAAS to libraries and other users registered with the Copyright Clearance Center (CCC) Transactional Reporting Service, provided that $20.00 per article is paid directly to CCC, 222 Rosewood Drive, Danvers, MA 01923. The identification code for *Science* is 0036-8075. *Science* is indexed in the *Reader s Guide to Periodical Literature* and in several specialized indexes.

AAAS
ADVANCING SCIENCE, SERVING SOCIETY

Norman P. Neureiter is director of the Center for Science, Technology, and Security Policy at the American Association for the Advancement of Science (AAAS), Washington, DC.

Tom C. Wang is director for international cooperation at the AAAS, Washington, DC.

U.S.-China S&T at 30

IN 1972, THE SHANGHAI COMMUNIQUE OF PRESIDENT NIXON AND CHINESE PREMIER ZHOU ENLAI ended 23 years of isolation between the United States and China. Tucked into a single sentence was a brief reference to cooperation in science and technology (S&T). Visits by scientists and scholars then gradually increased, guided on the U.S. side by the nongovernmental National Academy of Sciences. Six years later, and presaging formal diplomatic relations in 1979, came the breakthrough science diplomacy mission of the President's Science Advisor Frank Press, accompanied by representatives of nearly every technical federal agency. That trip laid the groundwork for the formal Agreement on Cooperation in S&T, signed exactly 30 years ago this week by President Carter and the Chinese leader Deng Xiaoping.

The new U.S. president firmly believes in the power of science to address domestic and global challenges, making this 30th anniversary year an excellent time to assess the U.S.-China S&T relationship and ensure that it is on the right track for the future.

These ties have come a long way. Over a million Chinese students have studied at U.S. universities, some two-thirds of them in S&T. Many have stayed, and today about 8% of science and engineering Ph.D.s in the United States were born in China.* In recent years, almost 40% of Chinese science and engineering articles in international journals have had U.S. coauthors, and almost 8% of U.S. international papers have had Chinese coauthors. In 2004, $622 million of China's total R&D was performed by U.S.-owned companies and affiliates in China. With the exception of one areaÐ space explorationÐ research cooperation between universities as well as government labs is broad and diverse. Furthermore, China has declared that its path to the future will be driven largely by S&T, and it is making the needed commitments to education, facilities, and research.[2]

However, the overall relationship with China is not without tensions. The massive U.S. trade deficit is equated with the loss of U.S. jobs, the alleged manipulation of currency exchange rates, and concerns over U.S. competitiveness. China's economic boom and soaring demand for resources (now easing) could be a source of future conflict. Taiwan remains an area of potential confrontation. And China's increasing investment in its military has raised concerns, being used in the United States to justify more investment in new weapons and defense systems. China is also in a special category for U.S. visas and export controls, due to a controversial 1999 U.S. congressional report charging China with espionage in nuclear and missile technologies. Despite being America's principal creditor, the Chinese have concerns about U.S. long-term intentions toward Asia and their country. There is a level of mistrust on both sides.

Science provides a common language that can help bridge cultures and serve to lessen mistrust and increase transparency. The Obama administration should work to raise S&T cooperation with China to a new level of partnership. The existing Joint S&T Commission, chaired by the President's Science Advisor and China's S&T minister, should meet annually (instead of every 2 years), and the 2009 meeting should lay out a 10-year plan of cooperative research focused on global challenges faced by both countries, including climate change, energy, food, health, and security. On the U.S. side, new funds will be needed to complement the agencies' domestic programs in these areas. The United States must also ensure that all qualified Chinese (and other foreign) scientists can obtain visas on a timely basis, and that our export controls protect national security but do not prevent U.S. corporations from fully participating in the global civil economy.[3] The United States and China must be true partners in seeking technical solutions that will support a global population of some nine billion people by 2050. Such cooperation can also mitigate inevitable tensions in the overall relationshipÐ both splendid goals for the next 30 years.

Norman P. Neureiter and Tom C. Wang

10.1126/science.1170938

*National Science Board Science and Enginering Indicators 2008, www.nsf.gov/statistics/seind08/.

[2] Wen Jiabao, *Science* **322**, 649 (2008).

[3] See *Beyond Fortress America* (National Academies Press, Washington, DC, 2009); available at www.nap.edu/catalog.php?record_id=12567.

CREDITS: (LEFT TOP AND BOTTOM) AAAS; (RIGHT) ASSOCIATED PRESS

Published by AAAS

www.sciencemag.org

Science

1200 New York Avenue, NW
Washington, DC 20005
Editorial: 202-326-6550, FAX 202-289-7562
News: 202-326-6581, FAX 202-371-9227
Bateman House, 82-88 Hills Road
Cambridge, UK CB2 1LQ
+44 (0) 1223 326500, FAX +44 (0) 1223 326501

Subscription Services For change of address, missing issues, new orders and renewals, and payment questions: 866-434-AAAS (2227) or 202-326-6417, FAX 202-842-1065. Mailing addresses: AAAS, P.O. Box 96178, Washington, DC 20090-6178 or AAAS Member Services, 1200 New York Avenue, NW, Washington, DC 20005

Institutional Site Licenses please call 202-326-6755 for any questions or information

Reprints: Author Inquiries 800-635-7181
Commercial Inquiries 803-359-4578

Permissions 202-326-7074, FAX 202-682-0816

Member Benefits AAAS/Barnes&Noble.com bookstore www.aaas.org/bn; AAAS Online Store www.apisource.com/aaas/ code MKB6; AAAS Travels: Betchart Expeditions 800-252-4910; Apple Store www.apple/eppstore/aaas; Bank of America MasterCard 1-800-833-6262 priority code FAA3YU; Cold Spring Harbor Laboratory Press Publications www.cshlpress.com/affiliates/aaas.htm; GEICO Auto Insurance www.geico.com/landingpage/go51.htm?logo=17624; Hertz 800-654-2200 CDP#343457; Office Depot https://bsd.officedepot.com/portalLogin.do; Seabury & Smith Life Insurance 800-424-9883; Subaru VIP Program 202-326-6417; VIP Moving Services www.vipmayflower.com/domestic/index.html; Other Benefits: AAAS Member Services 202-326-6417 or www.aaasmember.org.

science_editors@aaas.org	(for general editorial queries)
science_letters@aaas.org	(for queries about letters)
science_reviews@aaas.org	(for returning manuscript reviews)
science_bookrevs@aaas.org	(for book review queries)

Published by the American Association for the Advancement of Science (AAAS), *Science* serves its readers as a forum for the presentation and discussion of important issues related to the advancement of science, including the presentation of minority or conflicting points of view, rather than by publishing only material on which a consensus has been reached. Accordingly, all articles published in *Science* including editorials, news and comment, and book reviews are signed and reflect the individual views of the authors and not official points of view adopted by AAAS or the institutions with which the authors are affiliated.

AAAS was founded in 1848 and incorporated in 1874. Its mission is to advance science, engineering, and innovation throughout the world for the benefit of all people. The goals of the association are to: enhance communication among scientists, engineers, and the public; promote and defend the integrity of science and its use; strengthen support for the science and technology enterprise; provide a voice for science on societal issues; promote the responsible use of science in public policy; strengthen and diversify the science and technology workforce; foster education in science and technology for everyone; increase public engagement with science and technology; and advance international cooperation in science.

Information for Authors
See pages 634 and 635 of the 1 February 2008 issue or access www.sciencemag.org/about/authors

EDITOR-IN-CHIEF **Bruce Alberts**
EXECUTIVE EDITOR **Monica M. Bradford**
DEPUTY EDITORS **R. Brooks Hanson, Barbara R. Jasny, Katrina L. Kelner**
NEWS EDITOR **Colin Norman**

Editorial supervisory senior editor Phillip D. Szuromi; **senior editor/perspectives** Lisa D. Chong; **senior editors** Gilbert J. Chin, Pamela J. Hines, Paula A. Kiberstis (Boston), Marc S. Lavine (Toronto), Beverly A. Purnell, L. Bryan Ray, Guy Riddihough, H. Jesse Smith, Valda Vinson; **associate editors** Kristen L. Mueller, Jake S. Yeston, Laura M. Zahn; **online editor** Stewart Wills; **associate online editors** Robert Frederick, Tara S. Marathe; **web content developer** Martyn Green; **book review editor** Sherman J. Suter; **associate letters editor** Jennifer Sills; **editorial manager** Cara Tate; **senior copy editors** Jeffrey E. Cook, Cynthia Howe, Harry Jach, Barbara P. Ordway, Trista Wagoner; **copy editors** Chris Filiatreau, Lauren Kmec; **editorial coordinators** Carolyn Kyle, Beverly Shields; **publications assistants** Ramatoulaye Diop, Joi S. Granger, Jeffrey Hearn, Lisa Johnson, Scott Miller, Jerry Richardson, Jennifer A. Seibert, Brian White, Anita Wynn; **editorial assistants** Carlos L. Durham, Emily Guise, Patricia M. Moore; **executive assistant** Sylvia S. Kihara; **administrative support** Maryrose Madrid

News deputy news editors Robert Coontz, Eliot Marshall, Jeffrey Mervis, Leslie Roberts; **contributing editors** Elizabeth Culotta, Polly Shulman; **news writers** Yudhijit Bhattacharjee, Adrian Cho, Jennifer Couzin, David Grimm, Constance Holden, Jocelyn Kaiser, Richard A. Kerr, Eli Kintisch, Andrew Lawler (New England), Greg Miller, Elizabeth Pennisi, Robert F. Service (Pacific NW), Erik Stokstad; **intern** Jackie D. Grom; **contributing correspondents** Jon Cohen (San Diego, CA), Daniel Ferber, Ann Gibbons, Robert Koenig, Mitch Leslie, Charles C. Mann, Virginia Morell, Evelyn Strauss, Gary Taubes; **copy editors** Linda B. Felaco, Melvin Gatling, Melissa Raimondi; **administrative support** Scherraine Mack, Fannie Groom; **bureaus** New England: 207-549-7755, San Diego, CA: 760-942-3252, FAX 760-942-4979, Pacific Northwest: 503-963-1940

Production director James Landry; **senior manager** Wendy K. Shank; **assistant manager** Rebecca Doshi; **senior specialists** Steve Forrester, Chris Redwood; **specialist** Anthony Rosen; **Preflight director** David M. Tompkins; **manager** Marcus Spiegler

Art director Yael Kats; **associate art director** Laura Creveling; **illustrators** Chris Bickel, Katharine Sutliff; **senior art associates** Holly Bishop, Preston Huey, Nayomi Kevitiyagala; **art associate** Jessica Newfield; **photo editor** Leslie Blizard

***Science* International**

Europe (science@science-int.co.uk) **editorial: international managing editor** Andrew M. Sugden; **senior editor/perspectives** Julia Fahrenkamp-Uppenbrink; **senior editors** Caroline Ash, Stella M. Hurtley, Ian S. Osborne, Peter Stern; **associate editor** Maria Cruz; **editorial support** Deborah Dennison, Rachel Roberts, Alice Whaley; **administrative support** John Cannell, Janet Clements; **news: europe news editor** John Travis; **deputy news editor** Daniel Clery; **contributing correspondents** Michael Balter (Paris), John Bohannon (Vienna), Martin Enserink (Amsterdam and Paris), Gretchen Vogel (Berlin); **intern** Sara Coelho

Asia Japan Office: Asca Corporation, Eiko Ishioka, Fusako Tamura, 1-8-13, Hirano-cho, Chuo-ku, Osaka-shi, Osaka, 541-0046 Japan; +81 (0) 6 6202 6272, FAX +81 (0) 6 6202 6271; asca@os.gulf.or.jp; **asia news editor** Richard Stone (Beijing: rstone@aaas.org); **contributing correspondents** Dennis Normile (Japan: +81 (0) 3 3391 0630, FAX +81 (0) 3 5936 3531; dnormile@gol.com); Hao Xin (China: +86 (0) 10 6307 4439 or 6307 3676, FAX +86 (0) 10 6307 4358; cindyhao@gmail.com); Pallava Bagla (South Asia: +91 (0) 11 2271 2896; pbagla@vsnl.com)

EXECUTIVE PUBLISHER **Alan I. Leshner**
PUBLISHER **Beth Rosner**

Fulfillment Systems and Operations (membership@aaas.org); **director** Waylon Butler; **senior systems analyst** Jonny Blaker; **customer service supervisor** Pat Butler; **specialists** Latoya Casteel, LaVonda Crawford, Vicki Linton, April Marshall; **data entry supervisor** Cynthia Johnson; **specialists** Eintou Bowden, Tarrika Hill, William Jones

Business Operations and Administration director Deborah Rivera-Wienhold; **assistant director, business operations** Randy Yi; **manager, business analysis** Michael LoBue; **manager, business operations** Jessica Tierney; **financial analysts** Priti Pamnani, Celeste Troxler; **rights and permissions: administrator** Emilie David; **associate** Elizabeth Sandler; **marketing director** Ian King; **marketing manager** Allison Pritchard; **marketing associates** Aimee Aponte, Alison Chandler, Mary Ellen Crowley, Julianne Wielga, Wendy Wise; **international marketing manager** Wendy Sturley; **marketing executive** Jennifer Reeves; **marketing/member services executive** Linda Rusk; **director, site licensing** Tom Ryan; **director, corporate relations** Eileen Bernadette Moran; **publisher relations, eresources specialist** Kiki Forsythe; **senior publisher relations specialist** Catherine Holland; **publisher relations, east coast** Phillip Smith; **publisher relations, west coast** Philip Tsolakidis; **fulfillment supervisor** Iquo Edim; **fulfillment coordinator** Laura Clemens; **electronic media: manager** Lizabeth Harman; **project manager** Trista Snyder; **assistant manager** Lisa Stanford; **senior production specialists** Christopher Coleman, Walter Jones; **production specialists** Nichele Johnston, Kimberly Oster

Advertising director, worldwide ad sales Bill Moran

Product (science_advertising@aaas.org); **midwest/west coast/w. canada** Rick Bongiovanni: 330-405-7080, FAX 330-405-7081; **east coast/e. canada** Laurie Faraday: 508-747-9395, FAX 617-507-8189; **uk/europe/asia** Roger Goncalves: TEL/FAX +41 43 243 1358; **japan** Mashy Yoshikawa: +81 (0) 3 3235 5961, FAX +81 (0) 3 3235 5852; **senior traffic associate** Deiandra Simms

Commercial Editor Sean Sanders: 202-326-6430

Project Director, Outreach Brianna Blaser

Classified (advertise@sciencecareers.org); **inside sales manager: midwest/canada** Daryl Anderson: 202-326-6543; **inside sales representative** Karen Foote: 202-326-6740; **key account manager** Joribah Able; **northeast** Alexis Fleming: 202-326-6578; **southeast** Tina Burks: 202-326-6577; **west** Nicholas Hintibidze: 202-326-6533; **sales coordinators** Rohan Edmonson, Shirley Young; **international: sales manager** Tracy Holmes: +44 (0) 1223 326525, FAX +44 (0) 1223 326532; **sales** Susanne Kharraz, Dan Pennington, Alex Palmer; **sales assistant** Louise Moore; **japan** Mashy Yoshikawa: +81 (0) 3 3235 5961, FAX +81 (0) 3 3235 5852; **advertising production operations manager** Deborah Tompkins; **senior production specialist/graphic designer** Amy Hardcastle; **senior production specialist** Robert Buck; **senior traffic associate** Christine Hall; **publications assistant** Mary Lagnaoui

AAAS Board of Directors retiring president, chair David Baltimore; **president** James J. McCarthy; **president-elect** Peter C. Agre; **treasurer** David E. Shaw; **chief executive officer** Alan I. Leshner; **board** Lynn W. Enquist, Susan M. Fitzpatrick, Alice Gast, Linda P. B. Katehi, Nancy Knowlton, Cherry A. Murray, Thomas D. Pollard, Thomas A. Woolsey

AAAS
ADVANCING SCIENCE, SERVING SOCIETY

SENIOR EDITORIAL BOARD

John I. Brauman, *Chair, Stanford Univ.*
Richard Losick, *Harvard Univ.*
Robert May, *Univ. of Oxford*
Marcia McNutt, *Monterey Bay Aquarium Research Inst.*
Linda Partridge, *Univ. College London*
Vera C. Rubin, *Carnegie Institution*
Christopher R. Somerville, *Univ. of California, Berkeley*

BOARD OF REVIEWING EDITORS

Joanna Aizenberg, *Harvard Univ.*
David Altshuler, *Broad Institute*
Arturo Alvarez-Buylla, *Univ. of California, San Francisco*
Richard Amasino, *Univ. of Wisconsin, Madison*
Angelika Amon, *MIT*
Meinrat O. Andreae, *Max Planck Inst., Mainz*
Kristi S. Anseth, *Univ. of Colorado*
John A. Bargh, *Yale Univ.*
Cornelia I. Bargmann, *Rockefeller Univ.*
Ben Barres, *Stanford Medical School*
Marisa Bartolomei, *Univ. of Penn. School of Med.*
Facundo Batista, *London Research Inst.*
Ray H. Baughman, *Univ. of Texas, Dallas*
Stephen J. Benkovic, *Penn State Univ.*
Ton Bisseling, *Wageningen Univ.*
Mina Bissell, *Lawrence Berkeley National Lab*
Peer Bork, *EMBL*
Robert W. Boyd, *Univ. of Rochester*
Paul M. Brakefield, *Leiden Univ.*
Dennis Bray, *Univ. of Cambridge*
Stephen Buratowski, *Harvard Medical School*
Joseph A. Burns, *Cornell Univ.*
William P. Butz, *Population Reference Bureau*
Mats Carlsson, *Univ. of Oslo*
Peter Carmeliet, *Univ. of Leuven, VIB*
Mildred Cho, *Stanford Univ.*
David Clapham, *Children s Hospital, Boston*
David Clary, *Oxford University*
J. M. Claverie, *CNRS, Marseille*
Jonathan D. Cohen, *Princeton Univ.*
Andrew Cossins, *Univ. of Liverpool*
Robert H. Crabtree, *Yale Univ.*
Wolfgang Cramer, *Potsdam Inst. for Climate Impact Research*
F. Fleming Crim, *Univ. of Wisconsin*
William Cumberland, *Univ. of California, Los Angeles*
Jeff L. Dangl, *Univ. of North Carolina*
Stanislas Dehaene, *Collège de France*
Edward DeLong, *MIT*
Emmanouil T. Dermitzakis, *Wellcome Trust Sanger Inst.*
Robert Desimone, *MIT*
Dennis Discher, *Univ. of Pennsylvania*
Scott C. Doney, *Woods Hole Oceanographic Inst.*
W. Ford Doolittle, *Dalhousie Univ.*
Jennifer A. Doudna, *Univ. of California, Berkeley*
Julian Downward, *Cancer Research UK*
Denis Duboule, *Univ. of Geneva/EPFL Lausanne*
Christopher Dye, *WHO*
Gerhard Ertl, *Fritz-Haber-Institut, Berlin*
Mark Estelle, *Indiana Univ.*
Barry Everitt, *Univ. of Cambridge*
Paul G. Falkowski, *Rutgers Univ.*
Ernst Fehr, *Univ. of Zurich*
Tom Fenchel, *Univ. of Copenhagen*
Alain Fischer, *INSERM*
Scott E. Fraser, *Cal Tech*
Chris D. Frith, *Univ. College London*
Wulfram Gerstner, *EPFL Lausanne*
Charles Godfray, *Univ. of Oxford*
Diane Griffin, *Johns Hopkins Bloomberg School of Public Health*
Christian Haass, *Ludwig Maximilians Univ.*
Niels Hansen, *Technical Univ. of Denmark*
Dennis L. Hartmann, *Univ. of Washington*
Chris Hawkesworth, *Univ. of Bristol*
Martin Heimann, *Max Planck Inst., Jena*
James A. Hendler, *Rensselaer Polytechnic Inst.*
Ray Hilborn, *Univ. of Washington*
Ove Hoegh-Guldberg, *Univ. of Queensland*
Brigid L. M. Hogan, *Duke Univ. Medical Center*
Ronald R. Hoy, *Cornell Univ.*
Olli Ikkala, *Helsinki Univ. of Technology*
Meyer B. Jackson, *Univ. of Wisconsin Med. School*
Stephen Jackson, *Univ. of Cambridge*
Steven Jacobsen, *Univ. of California, Los Angeles*
Peter Jonas, *Universität Freiburg*
Barbara B. Kahn, *Harvard Medical School*
Daniel Kahne, *Harvard Univ.*
Gerard Karsenty, *Columbia Univ. College of P&S*
Bernhard Keimer, *Max Planck Inst., Stuttgart*
Elizabeth A. Kellog, *Univ. of Missouri, St. Louis*
Alan B. Krueger, *Princeton Univ.*
Lee Kump, *Penn State Univ.*
Mitchell A. Lazar, *Univ. of Pennsylvania*
Virginia Lee, *Univ. of Pennsylvania*
Olle Lindvall, *Univ. Hospital, Lund*
Marcia C. Linn, *Univ. of California, Berkeley*
John Lis, *Cornell Univ.*
Richard Losick, *Harvard Univ.*
Ke Lu, *Chinese Acad. of Sciences*
Andrew P. MacKenzie, *Univ. of St Andrews*
Raul Madariaga, *École Normale Supérieure, Paris*
Anne Magurran, *Univ. of St Andrews*
Charles Marshall, *Harvard Univ.*
Virginia Miller, *Washington Univ.*
Yasushi Miyashita, *Univ. of Tokyo*
Richard Morris, *Univ. of Edinburgh*
Edvard Moser, *Norwegian Univ. of Science and Technology*
Naoto Nagaosa, *Univ. of Tokyo*
James Nelson, *Stanford Univ. School of Med.*
Timothy W. Nilsen, *Case Western Reserve Univ.*
Roeland Nolte, *Univ. of Nijmegen*
Helga Nowotny, *European Research Advisory Board*
Eric N. Olson, *Univ. of Texas, SW*
Stuart H. Orkin, *Dana-Farber Cancer Inst.*
Erin O Shea, *Harvard Univ.*
Elinor Ostrom, *Indiana Univ.*
Jonathan T. Overpeck, *Univ. of Arizona*
John Pendry, *Imperial College*
Simon Phillpot, *Univ. of Florida*
Philippe Poulin, *CNRS*
Mary Power, *Univ. of California, Berkeley*
Molly Przeworski, *Univ. of Chicago*
Colin Renfrew, *Univ. of Cambridge*
Trevor Robbins, *Univ. of Cambridge*
Barbara A. Romanowicz, *Univ. of California, Berkeley*
Edward M. Rubin, *Lawrence Berkeley National Lab*
Shimon Sakaguchi, *Kyoto Univ.*
Jürgen Sandkühler, *Medical Univ. of Vienna*
David W. Schindler, *Univ. of Alberta*
Georg Schulz, *Albert-Ludwigs-Universität*
Paul Schulze-Lefert, *Max Planck Inst., Cologne*
Christine Seidman, *Harvard Medical School*
Terrence J. Sejnowski, *The Salk Institute*
David Sibley, *Washington Univ.*
Joseph Silk, *Univ. of Oxford*
Montgomery Slatkin, *Univ. of California, Berkeley*
Davor Solter, *Inst. of Medical Biology, Singapore*
Joan Steitz, *Yale Univ.*
Elsbeth Stern, *ETH Zürich*
Jerome Strauss, *Virginia Commonwealth Univ.*
Jurg Tschopp, *Univ. of Lausanne*
Derek van der Kooy, *Univ. of Toronto*
Bert Vogelstein, *Johns Hopkins Univ.*
Ulrich H. von Andrian, *Harvard Medical School*
Bruce D. Walker, *Harvard Medical School*
Christopher A. Walsh, *Harvard Medical School*
Graham Warren, *Yale Univ. School of Med.*
Colin Watts, *Univ. of Dundee*
Detlef Weigel, *Max Planck Inst., Tübingen*
Jonathan Weissman, *Univ. of California, San Francisco*
Ellen D. Williams, *Univ. of Maryland*
Ian A. Wilson, *The Scripps Res. Inst.*
Jerry Workman, *Stowers Inst. for Medical Research*
Xiaoling Sunney Xie, *Harvard Univ.*
John R. Yates III, *The Scripps Res. Inst.*
Jan Zaanen, *Leiden Univ.*
Huda Zoghbi, *Baylor College of Medicine*
Maria Zuber, *MIT*

BOOK REVIEW BOARD

John Aldrich, *Duke Univ.*
David Bloom, *Harvard Univ.*
Angela Creager, *Princeton Univ.*
Richard Shweder, *Univ. of Chicago*
Ed Wasserman, *DuPont*
Lewis Wolpert, *Univ. College London*

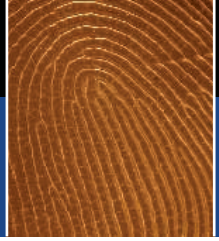

Why we have fingerprints
572

Sorghum decoded
573

BIOTECHNOLOGY

Celebration and Concern Over U.S. Trial of Embryonic Stem Cells

Almost exactly 10 years after two groups isolated human embryonic stem cells, igniting tremendous hope for new cures, the cells are about to be injected into humans for the first time. Last week, the U.S. Food and Drug Administration (FDA) gave Geron in Menlo Park, California, permission to conduct a safety test in a handful of patients with a recent spinal cord injury.

For Geron and the scientists who work with it, FDA's decision was the culmination of a huge effortÐ including studies of nearly 2000 rodents with spinal-cord injuries and a 22,500-page application. ª I actually have a glass of champagne in my hand right now,º says a key player, Hans Keirstead, a neuroscientist at the University of California, Irvine. Several years ago, he approached Geron with the idea to commercialize his finding that stem cells could be used to mitigate spinal cord injury in rodents. He has been working with the company ever since. ª I don't expect this treatment to allow patients to jump out of wheelchairs and play soccer,º but ª a meaningful and incremental advanceº in mobility is a real possibility, he says.

But many stem cell researchers, particularly those in academia, who have struggled since 2001 with the Bush Administration's strict limits on the development and use of new stem cell lines, are concerned that this trial may not be the best first candidate. Safety is one worry: For example, a big fear is that the cells could form a type of tumor called a teratoma. Some also question the trial's scientific rationale.

Evan Snyder, a neuroscientist who directs the stem cell research center at the nonprofit Burnham Institute for Medical Research in San Diego, California, warns that a shaky start could set the field back enormously. ª There's a lot of debate among spinal cord researchers that the preclinical data itself doesn't justify the clinical trial,º says Snyder, who is working on using neural stem cells for drug delivery. Among the concerns he cited: The rodents Geron studied had more moderate injuries than patients expected in the trial, suggesting that the results might not translate, and the therapy has not been tried in larger animals. John Gearhart of the University of Pennsylvania, who led one of the teams that isolated the cells in 1998, adds that ª we're still ¼ a long way from really understanding a good deal about these cells and how to use them safely.º

Geron will be testing oligodendrocyte progenitor cells, precursors to some nervous system cells the company developed from one of the original human embryonic stem cell linesÐ created with Geron funding in James Thomson's lab at the University of Wisconsin, Madison. Eight to 10 patients will receive the cells a week or two after a serious spinal cord injury. The goal is not to create new nerve fibers but to support those still intact by making the nerve insulator myelin. To prevent rejection, patients will take immune-suppressing drugs for about 60 days. Although the primary goal is to assess safety, Geron will be looking for hints that the cells had an effectÐ for example, improving bladder and bowel function, sensation, or mobility.

All smiles. Neuroscientist Hans Keirstead initiated the work that led to Geron s new therapy for spinal cord injury, using cells derived from an embryonic stem cell line (*inset*).

Geron CEO Thomas Okarma says he isn't concerned about one of the risks that people mention: ending up with the wrong type of cell. In rodents, he says the injected cells only formed glial cells, as expectedÐ exactly the result he and FDA wanted. Geron has also performed extensive rodent studies that assured the company and FDA that the experimental cells did not cause tumors in the animals. Keirstead and Okarma assert that, despite the criticisms, they've done everything they can before taking the next step. ª There's nothing we can do but go to humans now,º says Keirstead. Animal testing has its limitations, he addsÐ including the fact that there are no large animal models of spinal cord injury. (FDA declined to comment in detail on its decision to let the trial begin.)

Okarma suggests that academic researchers may be concerned because they're not fully aware of what the company has accomplished. Geron has published or presented little of its oligodendrocyte work; so far only FDA officials have been privy to most of it. ª There is so little expertise in the academic world about cell therapy that these people are rightly nervous,º Okarma says. ª We are so far ahead of them.º Geron is also examining whether its oligodendrocytes might help Alzheimer's disease, stroke, or multiple sclerosis sufferers.

Other companies, meanwhile, are developing products derived from embryonic stem cells, and it's expected that upcoming trials will advance more easily. Keirstead, for example, is working with a second California company that is coaxing the cells to form motor neurons and plans to test them in infants with spinal muscular atrophy.

Gearhart says that for years ª we were always told, `Cure a patient and then all of this [controversy] will go away,' º and embryonic stem cells will quickly gain acceptance. Now, he says: ª Here comes the first test out of the box.º **JENNIFER COUZIN**

CREDITS: DANIEL A. ANDERSON, UC IRVINE COMMUNICATIONS; (INSET) GERON

Published by AAAS

Forecasting protests in China
574

A military foray into social science
576

HUMAN EVOLUTION

Early Start for Human Art? Ochre May Revise Timeline

In 2002, a discovery at Blombos Cave in South Africa began to change how researchers view the evolution of modern human behavior. Archaeologists reported finding two pieces of red ochre engraved with crosshatched patterns, dated to 77,000 years ago. Many experts interpreted the etchings as evidence of symbolic expression and possibly even art, 40,000 years earlier than many researchers had thought (*Science*, 11 January 2002, p. 247). Now the Blombos team reports on an additional 13 engraved ochre pieces, many dated to 100,000 years ago. The researchers suggest that some of the engravings may represent an artistic or symbolic tradition. If so, the timeline for the earliest known symbolic behavior must once again be redrawn.

[a] [I] almost fell off my chair[o] on seeing the latest ochre etchings, says archaeologist Paul Mellars of the University of Cambridge in the United Kingdom. At least some [a] are unquestionably deliberate designs; ¼ they have to be some kind of symbols,[o] he says. Archaeologist Paul Pettitt of the University of Sheffield, U.K., a skeptic about the original discovery, says, [a] The new material removes any doubt whatsoever.[o]

Others remain cautious, however, suggesting that the etched lines may have been produced incidentally when working ochre for utilitarian reasons.

Pettitt, Mellars, and other experts attended a meeting earlier this month in Cape Town, South Africa, where the Blombos paper was presented; it is also in press at the *Journal of Human Evolution* (*JHE*). After the meeting, researchers toured the site, which has become crucial for understanding early human behavior. Archaeologist Christopher Henshilwood of the University of the Witwatersrand in Johannesburg, South Africa, lead author and the cave's discoverer, has reported numerous signs of apparent symbolic behavior from Blombos, including incised ochre, shell beads, and sophisticated tools, all presumably crafted by *Homo sapiens* (*Science*, 16 April 2004, p. 369). Blombos is one of several sites in Africa and the Near East that have challenged the notion that full-fledged symbolism, such as cave paintings, did not appear before about 40,000 years ago in Europe. [a] There is now no question that explicitly symbolic behavior was taking place by 100,000 years ago or earlier,[o] says Mellars.

He and others say that the Blombos dates seem accurate. Henshilwood's team has used at least four dating methods, including optically stimulated luminescence (OSL) dating of quartz grains from the cave's sediments and thermoluminescence dating of stone tools. The most recent round of OSL dating put the earliest archaeological levels at BlombosÐ where eight of the 13 new ochre pieces were foundÐ at about 99,000 years ago. [a] The stratigraphy is impeccable, with remarkably well-layered and discrete lenses of material,[o] says Pettitt, a dating expert.

Traces of an artist s hand? Engravings on this ancient ochre may have had symbolic meanings.

To analyze the latest finds, Henshilwood teamed up with Francesco d' Errico of the University of Bordeaux in France and independent ochre expert Ian Watts, who is based in Athens. The trick with ancient ochre is to figure out what early humans were using it for. Many previous studies have concluded that ochre was often ground to make a powder, which could have been used to paint bodiesÐ a form of social identification usually considered symbolicÐ or for more utilitarian purposes. For example, Lynnette Wadley of Witwatersrand has argued from modern-day experiments that ground ochre could have been used as a kind of glue to haft stone tools into wooden or bone handles.

So Henshilwood and colleagues focused their attention on 13 pieces engraved in ways that seemed inconsistent with grinding alone. Some pieces have lines arranged in apparent fan-shaped or crosshatched designs; others are etched in wavy patterns. Microscopic examination showed that these engravings had been made with a pointed stone tool and a finely controlled hand.

Wadley agrees that [a] some of the pieces seem engraved for reasons other than ochre powder removal,[o] although she is not yet convinced that those reasons were symbolic. Archaeologist Richard Klein of Stanford University in Palo Alto, California, says that ultimately the question of whether the engravings were symbolic [a] is not something that science can resolve.[o] The team points out, however, that some of the oldest pieces have a crosshatched pattern similar to that of the two original ochre pieces dated to 77,000 years ago. And other researchers have very recently discovered similar crosshatched patterns on a few African stone and bone objects thought to be as old as the new finds, or nearly so. This refutes suggestions that the marks are merely doodles, Henshilwood says, and suggests a 25,000-year tradition of symbolic representation.

If so, modern humans were probably engaging in symbolic behavior even before the 100,000-year mark at Blombos and possibly since the origin of our species, sometime between 160,000 and 200,000 years ago, says Mellars.

Still, even if the engravings are symbolic, Klein says, the question remains: [a] What did they symbolize?[o] Researchers agree that we may never know.

MICHAEL BALTER

CREDIT: CHRISTOPHER HENSHILWOOD AND FRANCESCO D ERRICO

Published by AAAS

RESEARCH FUNDING

European Science Not As Intense As Hoped

European research got a mixed report card in an analysis released last week by the European Union. The report says that the 27 E.U. nations have done well at increasing their research work force: Numbers grew twice as fast as in the United States between 2000 and 2006, reaching 640,000 researchers, while also attracting more foreign researchers to come and work there. Europe also attracted record amounts of private R&D funding from U.S. companies during that period. But at the same time its R&D intensity (research spending as a percentage of gross domestic product) pretty much stuck at about 1.84% a long way from the E.U. s self-imposed goal of reaching an R&D intensity of 3% by 2010.

Across the E.U., there is much variation in R&D intensity, with 17 countries, particularly new members in eastern Europe, making marked improvements. But 10 countries, including science powers such as France and the United Kingdom, declined. Meanwhile, Japan increased its intensity from 3.04% to 3.39%, Korea from 2.39% to 3.23%, and China from 0.90% to 1.42%. (U.S. research intensity fell, from 2.74% to 2.61%.) **DANIEL CLERY**

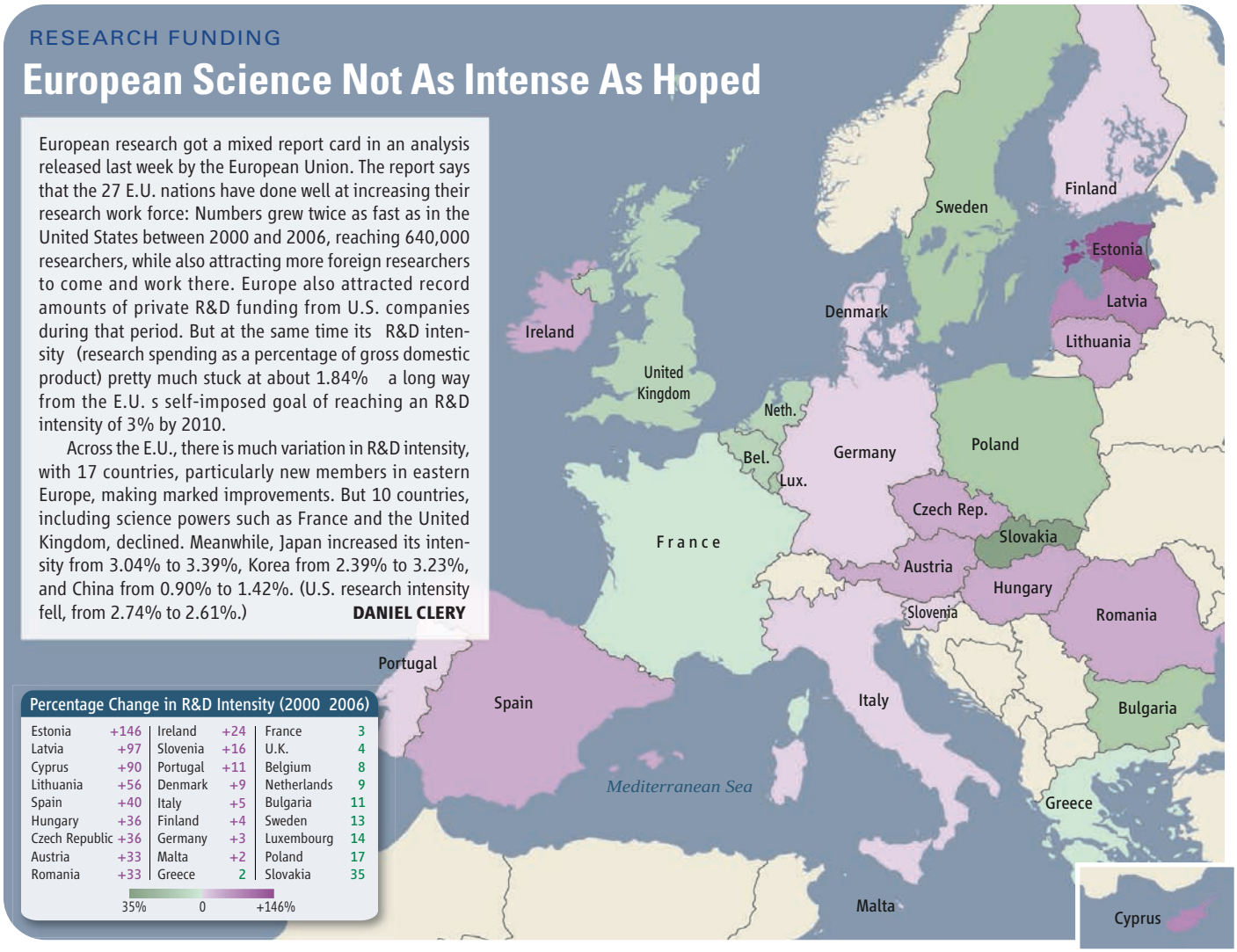

Percentage Change in R&D Intensity (2000 2006)

Estonia	+146	Ireland	+24	France	3
Latvia	+97	Slovenia	+16	U.K.	4
Cyprus	+90	Portugal	+11	Belgium	8
Lithuania	+56	Denmark	+9	Netherlands	9
Spain	+40	Italy	+5	Bulgaria	11
Hungary	+36	Finland	+4	Sweden	13
Czech Republic	+36	Germany	+3	Luxembourg	14
Austria	+33	Malta	+2	Poland	17
Romania	+33	Greece	2	Slovakia	35

35% 0 +146%

SOURCE: SCIENCE, TECHNOLOGY AND COMPETITIVENESS KEY FIGURES REPORT 2008/2009

ARCHAEOLOGY

Iraq Museum May Reopen Amid Controversy

A dispute over whether it is safe to reopen Iraq's renowned archaeology museum in Baghdad has cost the head of the country's archaeology board her job. The battle over the Baghdad museum, closed since before the U.S. invasion in 2003, is one of several sticking points in the ongoing debate over how to manage the country's cultural heritage.

Iraq's new minister for tourism and antiquities, Qahtan al-Juburi, visited the Iraq Museum on 3 January and demanded that the museum be opened to the public by mid-February, according to several Iraqi and American sources. The acting head of the State Board of Antiquities and Heritage, Amira Edan, argued against the minister's proposal for security reasons, says Donny George, former head of SBAH now teaching in the United States, who spoke with Edan about the incident. Edan had previously offered to resign because she lacked the confidence of the ministry, says another source who requested anonymity, but that offer was ignored. Following Iraqi media reports of her opposition to reopening the museum, however, al-Juburi accepted her resignation on 11 January. Neither the ministry nor Edan responded to requests for interviews.

The ministry is controlled by a Shiite party eager to see U.S. troops depart Iraq, and several U.S. and Iraqi archaeologists say that reopening the museum would be a potent political symbol. [a] That would be a message to the world that everything is fine and that the Americans can leave,[o] says George, who believes that unlocking the museum doors [a] is a terrible thing to do.[o] Another researcher familiar with the situation, however, says that opening some of the galleries poses no major threat because [a] there is a good security system installed.[o] But the source adds that the SBAH chief should have a say in the decision and that her dismissal [a] is disturbing.[o]

Al-Juburi also refused to allow a team of Iraqi archaeologists, including Edan and her replacement, Qais Hussein Rashid, to visit Washington, D.C., this month to discuss how to spend a $700,000 grant from the U.S. State Department to help develop a master plan for the ancient Mesopotamian capital of Babylon, once the world's largest and richest city. Babylon has suffered from years of neglect, shoddy reconstruction, and damage during recent occupation by U.S. and Polish troops. Provincial authorities are eager to open the fragile site to tourism, but archaeologists want to preserve it.

Provincial authorities have also asserted their claims to ancient objects discovered by farmers and construction workers, although by law such objects must be sent to the national

Published by AAAS

U.S. BUDGET

A Stimulus for Science

As the U.S. economy slides deeper into a recession, universities are following other sectors in freezing salaries, canceling job searches, and trimming expenses. At the same time, however, academic researchers are on the verge of receiving a major influx of federal funding as part of a 2-year, $825 billion economic stimulus package moving rapidly through Congress.

The bills, drawn up in consultation with the new Obama Administration, include some $360 billion in new spending, along with $275 billion in tax breaks and a large expansion of mandatory programs. The research and science infrastructure components tucked into the first category amount to roughly $15 billion spread across several federal research agencies. As *Science* went to press, the House of Representatives was preparing to vote on legislation introduced on 15 January by Democratic leaders, while the Senate was just beginning deliberations on its version. Democratic leaders have promised to have the bill ready for the president's signature by mid-February.

The table below shows the major science components, by agency, of each bill. **JEFFREY MERVIS**

AGENCY	HOUSE OF REPRESENTATIVES	SENATE
NIH	**Total: $3.5 billion** $1.5 billion for extramural research, $1.5 billion for extramural facilities, and $500 million for on-campus buildings.	**Total: $3.5 billion** $2.7 billion split between director's office and the institutes, $500 million for on-campus buildings, and $300 million for extramural instrumentation.
NSF	**Total: $3 billion** $2 billion for research, $100 million for education, $400 million for new facilities, $300 million for instrumentation, and $200 million for academic renovation.	**Total: $1.4 billion** $1 billion for research, $50 million for education, $150 million for new facilities, and $200 million for instrumentation.
DOE	**Total: $41 billion** $2 billion for Office of Science and $400 million for ARPA-E.	**Total: $40 billion** $430 million for Office of Science, $2.6 billion for energy efficiency and renewable-energy research.
NASA	**Total: $600 million** $400 million for science, $150 million for aeronautics, and $50 million for hurricane repairs.	**Total: $1.5 billion** $500 million for science, $250 million for aeronautics, $500 million for human exploration, and $250 million for hurricane repairs.
NOAA	**Total: $1 billion** $600 million for climate sensors and modeling, $400 million for habitat restoration.	**Total: $1.2 billion** $795 million for facilities/equipment, $427 million for restoration/maintenance.
NIST	**Total: $520 million** $300 million for extramural buildings, $100 million for intramural research, and $70 million for Technology Innovation Program.	**Total: $575 million** $357 million for intramural facilities, $218 million for competitive grants.
Biodefense	**Total: $900 million** $430 million for BARDA and $420 million for pandemic flu vaccine.	**$870 million** for pandemic flu vaccine.
USGS	**Total: $200 million** Upgrade laboratories; enhance National Map project and various monitoring networks.	**Total: $135 million**

museum for cataloging and analysis. [a] But each [province] hopes to become independent, so they won't send in the antiquities,[o] says an archaeologist close to Edan, who has pleaded with the provinces to cooperate.

Another source of tension is the fate of ancient Jewish manuscripts captured during the invasion. Widah Na'srat, a member of the Iraq Interior Ministry's Criminal Investigations Department, told the London-based publication *Al-Hayyat* on 18 January that he suspects U.S. contractors of smuggling some of the manuscripts to Israel. He did not elaborate but said he would visit Washington soon to investigate the matter. Jeffrey Spurr, a Harvard University researcher, says the manuscripts were housed in Saddam Hussein's secret service headquarters and damaged by water during the fighting, then frozen and flown to Texas for conservation in the summer of 2003 with the permission of SBAH. They are now in a Maryland facility, he says, but have not been cataloged. **ANDREW LAWLER**

Safety first. Amira Edan led visiting dignitaries and Iraqi officials, shown here in the Assyrian gallery, on a November tour of the closed and heavily guarded Baghdad museum.

SOURCE: (TOP) U.S. HOUSE OF REPRESENTATIVES, U.S. SENATE; (BOTTOM) ALI YUSSEF/AFP/GETTY IMAGES

Published by AAAS

INFORMAL EDUCATION

Report Calls for Fresh Look at What Happens Outside School

A 5-year-old who devours everything she can find on dinosaurs is not only learning about the natural world, she's also experiencing the joy of becoming an expert. That feeling, says Dennis Bartels, executive director of the famed Exploratorium in San Francisco, California, is no less important to becoming scientifically literate than is her ability, as she moves through school, to define photosynthesis or explain Newton's laws of motion. Standardized tests may be good at assessing the latter type of knowledge, Bartels says, but they don't capture what gets students excited about science.

Bare-bones education? Museums are only one of many informal settings in which people learn about science.

A new report from the U.S. National Academies comes to grips with a knotty problem for science educators, namely, tracking the science that people learn when they're not in school. Part of the solution, according to *Learning Science in Informal Settings: People, Places, and Pursuits*, is to stop taking snapshots of a person's understanding of a topic. Instead of quizzing them on a museum exhibit they've attended or a television program they've just watched, researchers need metrics that recognize that learning occurs in countless locations and spans a lifetime.

"People don't realize that they are learning science through everyday experiences," says David Ucko, head of informal science education at the U.S. National Science Foundation in Arlington, Virginia, which spends $65 million a year on such activities and requested the academies' report. That's true not just for children, Ucko adds, but also for the adults who teach them.

The idea that people learn about science in many ways may seem obvious, admits panel chair Bruce Lewenstein, a professor of science communications at Cornell University. But too few researchers take that into account when studying the impact of informal science activities. The result, says Lewenstein, is an "uneven body of research" on the subject.

"Although there is strong evidence for the impact of educational television on science learning," the report concludes, "there is substantially less evidence regarding the impact of other mediaÐ newspapers, magazines, gaming, radioÐ on science learning." Lewenstein says that "what's been missing

NEUROSCIENCE

Fingerprints Enhance the Sense of Touch

Fingerprints can help nab a criminal, but that's not why they evolved. In fact, scientists aren't entirely sure of the purpose of the tiny ridges on our fingertips. Some have argued that they improve our grip on slippery objects, much as the treads on tires help grip the road. Others have suggested that they improve our sense of touch. The two hypotheses aren't mutually exclusive, but online in *Science* this week (www.sciencemag.org/cgi/content/abstract/1166467), a team of physicists presents circumstantial evidence for the latter theory.

After a series of experiments with a sensor designed to mimic a small patch of skin on a human fingertip, Alexis Prevost, Georges Debrégeas, and their colleagues at the École Normale Supérieure in Paris conclude that fingerprints likely enhance the perception of texture by increasing vibrations in the skin as fingers rub across a textured surface. In particular, fingerprints amplify vibrations in the frequency range that best stimulates Pacinian corpuscles, mechanoreceptors in the skin important for texture perception.

"Texture information plays a huge role in our ability to identify objects by touch," says Sliman Bensmaïa, a neuroscientist at Johns Hopkins University in Baltimore, Maryland. The new paper demonstrates how fingerprints could enhance this ability, Bensmaïa says. "Their evidence is pretty compelling."

The artificial fingertip used in the experiments consists of a half-millimeter-wide sensor covered with a dome of an artificial, rubberlike material with mechanical properties similar to those of human skin. The researchers created two versions of this "skin": a smooth version and one with parallel ridges whose size and spacing approximated those of human fingerprints. Then they compared the vibrations picked up by the sensor when they slid a glass slide etched with fine lines across the two types of skin. (To the human touch, the glass has a slight roughness, Debrégeas says.)

Key evidence. Investigations with a biomimetic sensor suggest that fingerprints aid texture perception.

The ridges made the vibrations picked up by the underlying sensor up to 100 times stronger, the researchers found. Moreover, when the glass slid over the skin at a speed comparable to the typical motion of a person scanning his fingers over a surface, the resulting vibrations tended to be in the sensitivity sweet spot for Pacinian corpuscles. "It's a really interesting finding because it demonstrates the extent to which the physical and mechanical properties of a sensor can perform a computation," says Mitra Hartmann, a biomedical engineer at Northwestern University in Evanston, Illinois.

CREDITS (TOP TO BOTTOM): SERGIO DIONISIO/GETTY IMAGES; CLOUDS HILL IMAGING LTD./CORBIS

Published by AAAS

are studies that measure the acquisition of knowledge across time and outside of the traditional educational media. Such studies aren't easy, but they can be done.º

In addition to conducting new types of research, the report says scientists should add ª excitementº and ª self-identification with scienceº to the definition of what it means to learn about science. A 2007 academies' report, titled *Taking Science to School*, used traditional metrics such as whether students understand and apply the scientific method to explore the natural world, think about science as a way of knowing, and engage in hands-on activities. But that's too narrow a definition, agrees developmental psychologist Kevin Crowley of the University of Pittsburgh in Pennsylvania, who worked on the 2007 report.

ª Schools have so many requirements on how to do STEM [science, technology, engineering, and math] education that aren't compatible with informal science education,º he notes. ª Not only are kids compelled to be in school, but the adults in their lives who are most excited about science are often not their teachers. We need to do a better job of taking into account those out-of-school experiences.º

Amen, says Bartels. ª As my colleagues like to say, `Nobody ever flunked a nature walk.' º

JEFFREY MERVIS

Selecting and amplifying the signals important for texture perception could in principle be accomplished within the nervous system, Hartmann says. But in this case, it seems to be the design of the hardware rather than the programming of the neural software that does the trick.

The new results leave open why human fingerprints are arranged in elliptical swirls. Bensmaïa notes that the amplification effect was strongest when the textured glass slid perpendicular to the ridges, so it's possible that the loops ensure that no matter how the fingers move, some ridges are always optimally oriented. It's puzzling, however, that macaque monkeys have ridges parallel to the long axis of their fingers, Bensmaïa says. The loops could represent an evolutionary upgrade in humans, he suggests. Or perhaps the monkeys use their fingers differently when exploring a surface, says Hartmann.

The work may one day lead to improved prosthetic hands, Bensmaïa adds. ª It would be pretty straightforward to take their device and put it in a prosthetic hand, and I think that could enhance tactile feedback quite a bit.º

GREG MILLER

CREDIT: COURTESY OF ANDREW PATERSON

PLANT GENETICS

How Sorghum Withstands Heat and Drought

Sorghum is no fair-weather cereal. Able to thrive in hot, semidry places, it feeds more than 500 million people in 98 countries, primarily in the developing world. Sorghum is also an important U.S. biofuel. Now, the analysis of its genome sequence has revealed clues about how this crop toughs out subpar growing conditions. Drought tolerance may arise from extra copies of key genes, and sorghum's efficient photosynthetic pathway was gradually cobbled together from existing photosynthetic genes and duplicated genes that shifted their function over millions of years, says Andrew Paterson, a plant geneticist at the University of Georgia in Athens.

ª Having the genome sequence of sorghum is a significant landmark,º says William Dar, director-general of the International Crops Research Institute for the Semi-Arid Tropics in Andhra Pradesh, India. ª We anticipate using a variety of approaches for harnessing this genome sequence in our applied crop-improvement programs.º

At 730 million bases, the *Sorghum bicolor* genome is 75% larger than that of rice, the first sequenced cereal, but only a quarter that of maize, whose genome has been sequenced but not yet analyzed. Many plants, including rice and wheat, depend on C3 photosynthesis, so named because carbon dioxide is initially converted to a three-carbon compound. But sorghum, which originated in Africa, uses the C4 pathway, initially making four-carbon compounds. This pathway involves a special enzyme that takes up carbon dioxide faster than does C3 photosynthesis, enabling the plant to curtail water loss through carbon dioxide± absorbing pores. As a result, C4 plants do better than C3 plants in hot climates.

When Paterson and his 44 colleagues studied the 34,496 putative genes unearthed in the sorghum genome, they discovered that the C4 pathway includes genes derived from several belonging to the C3 pathway, as well as recently duplicated genes and genes that date back 70 million years to a whole-genome duplication. ª This all suggests that it took quite a long time to evolve,º says Paterson.

With respect to withstanding drought, sorghum has four more copies than rice of a regulatory gene that activates a key gene family in a wide variety of plants during droughts, Paterson and his colleagues report in the 29 January issue of *Nature*. Sorghum also has a surplus of genes for proteins called expansins, which may help sorghum bounce back from water shortages. In addition, it has 328 cytochrome P450 genes, which help plants respond to stress, whereas rice has 228 such genes. These specializations ª bear explorationº and may be useful for improving other crops, says Neal Gutterson, CEO of Mendel Biotechnology Inc. in Hayward, California.

Given the toll global warming is taking on agriculture, ª understanding how major cereal crops can be made to adapt to conditions of high temperature, high light intensity, and limited water supply, which can be elucidated from the sorghum genome sequence, will make a great impact in agriculture,º says Takuji Sasaki, a rice geneticist at the National Institute of Agrobiological Sciences in Tsukuba, Japan.

New cereal sequence. Like rice (foreground), sorghum now has a deciphered genome that s revealing its genetic history.

With respect to biofuels, sorghum's sequence may help researchers improve more complex biofuel crops such as *Miscanthus* and sugarcane. ª The small genome should help [in] identifying candidate flowering time genes that may directly lead to manipulating biomass production,º says Thomas Brutnell, a plant geneticist at Cornell University.

ELIZABETH PENNISI

Published by AAAS

Seeds of Discontent

Social scientists blame poor local governance for China s rising unrest; the global financial crisis, they warn, could make things far worse

BEIJING On 22 June 2008, the body of a young woman was fished out of a river in Weng' an County in southwestern China. The deceased was quickly identified as 17-year-old Li Shufen. Rumors began to swirl about how the student died. Relatives went to Weng' an's police station to inquire about the investigation but were rebuffed; an uncle was beaten. On 28 June, the police released their findings: Li had committed suicide. A few hundred angry people, convinced that the police were wrong, descended on the station. Word spread and the crowd swelled to 30,000Ð nearly half the population of Weng' an's biggest town, Yongyang. That evening, a mob torched three government buildings and burned cars before police arrived with tear gas.

The seeds of unrest were sown long before Li's death. In 2003, Weng' an County, in Guizhou Province, approved construction of a dam but failed to adequately compensate thousands of people who were ordered to relocate, says Wang Erping of the Institute of Psychology of the Chinese Academy of Sciences (CAS). Later, Weng' an officials mandated setting aside nearly 20% of the county's arable land for peppers, overriding farmers' objections. And in 2006, another young woman died mysteriously; that case remains open. [a] People were already unhappy with the local government,[o] says Wang, who says Li's death was the [a] spark[o] that ignited pent-up anger.

Until a year or so ago, China's central government routinely censored reports of mass disturbances. But the Guizhou incident, like other recent protests, received extensive coverage in the Chinese press. The change is due largely to the rising influence of China's social scientists. [a] We want to tell the public what really happened,[o] says Shan Guangnai, a senior fellow at the Institute of Sociology of the Chinese Academy of Social Sciences (CASS) here, which in 2007 advised the government to publicize mass incidents. [a] It's critical to stop rumors from spreading.[o]

That glasnost will likely be put to the test in the coming months. Social scientists predict that the global financial crisis will sharply escalate unrest in China. [a] The first half of 2009 will be a hard time,[o] says Shan. Already, sagging demand for Chinese goods has forced some 670,000 companies to close, resulting in millions of job losses. In an annual rite, tens of millions of ChineseÐ including now-jobless migrant workersÐ returned to their home villages for the Lunar New Year holiday that started on 26 January. Many are unlikely to be satisfied with jobs in the countryside after having tasted city life, says Shan.

Online
sciencemag.org
Podcast interview with author Richard Stone.

Train station scrum. Tens of millions of Chinese migrated home this month for Lunar New Year celebrations. After the glow fades, unrest may surge.

Despite President Hu Jintao's intention to create a [a] harmonious society,[o] protests have grown more frequent with China's rapid development. Top officials lay the blame for social unrest primarily on labor disputes and environmental woes. Although numbers are hard to come by, in 2005, for instance, there were 51,000 conflicts over ecological degradation, such as contaminated water, dust, and landslides (*Science*, 1 August 2008, p. 611).

Hindsight may be 20/20. But can science predict mass incidents before they happen? Wang thinks so. After compiling statistics and conducting interviews across China, he and his team have developed a methodology that, they say, enables them to forecast the likelihood that a county will experience a disturbance in the coming months. CAS briefed the central government on the findings last October, and the State Council's Emergency Management office has since asked Wang to advise it on how to monitor social attitudes in areas traumatized by last May's devastating earthquake in Sichuan Province. The project [a] has potential to generate findings of considerable policy value,[o] says Li Lianjiang, an expert on public administration at the Chinese University of Hong Kong.

Others are skeptical that such forecasts are worthwhile. [a] Who can observe or measure `the potential' to riot?[o] asks Ching Kwan Lee, a sociologist at the University of California, Los Angeles. [a] But there is no point in arguing one way or the other. If they think they can predict, let them and see if they get it right.[o]

If forecasting pans out, it could be a boon to leaders here. [a] It can help the government deal with mass disturbances before they occur,[o] says Wan Chuan of the Beijing Academy of Social Sciences. Knowing which tinderboxes are hottest might enable the central govern-

CREDITS (TOP TO BOTTOM): ANDY WONG/AP; ALVIN CHAN/REUTERS

Case study. Paramilitary police restore order after last June s violent incident in Weng an County.

ment to focus resources and ameliorate conditions in the most dysfunctional districts. Such forecasts might also be used to suppress dissent, some experts warn. But Wang and Shan don't see a dark side: They say that the central government consistently strives to rectify the poor local governance and policy failures lying at the heart of unrest. Toward that end, Wang says, "we need a national social monitoring system for social stability."

A wake-up call

For decades in China, research on social problems was taboo. The central government, as architect of wrenching societal transformations such as the Cultural Revolution, was responsible for many societal illsÐ and didn't want unauthorized opinions being aired. Reform policies, initiated 30 years ago by the late top leader Deng Xiaoping, opened the door to social research. In 1998, Wang's team at the Institute of Psychology focused on public administration. "It was not as easy as we imagined it would be," Wang says. They scraped for funding for several years. Then the Wanzhou incident occurred.

On 18 October 2004, an explosive riot ensued when police tried to break up a street fight in the Wanzhou district of Chongqing, a major city on the Yangtze River in central China. Unlike most mass incidents in China, which take place in towns or rural areas, this one roiled Chongqing, a city province, threatening to destabilize a region inhabited by more than 30 million people. "Wanzhou was a wake-up call," says Shan.

But CASS and CAS social monitoring research met strong resistance. When Wang's 18-strong team fanned out across China to collect statistics on crimes, protests, and citizens' complaints, local officials often claimed the data were too sensitive to share. "Many local governments try to hide their administrative faults," Wang says.

The farther from Beijing the scientists roam, the less cooperation they tend to receive. Last September, for example, Wang and a doctoral student made a fact-finding trip to Menglian County in Yunnan Province, just across the border from Myanmar. As soon as they arrived, officials advised them to high-tail it back to Beijing. Local authorities, they explained, were preoccupied with combating drug traffickers, and their research would not be convenient." Shan adds that gathering data often requires subterfuge. When he and his two dozen CASS colleagues who study social unrest anticipate local antipathy, he says, "we pretend to be tourists or relatives of local residents."

Despite such obstacles, Chinese social scientists have amassed a wealth of data. Wang's team, for instance, has compiled dossiers on 132 counties in the past 4 years. Common threads have emerged. The root causes of the vast majority of incidents, Wang says, are poor local governance and miscarriages of justice. "Grievances accumulate over time," he says. Whatever the source of resentment, Chinese communities follow similar arcs. "The first reaction is to endure, to avoid fights," Wang says. When confronted with unfair treatment, Chinese usually attempt to privately negotiate a solution, he says. When that fails, they may seek redress from the government, the courts, or through the media. If grievances remain, resentment buildsÐ and can prime a community for an outburst.

Beyond the pale. Research on incidents in Tibet, like last March s violent protest against Chinese rule, is off limits.

A new wildcard

Shan insists that the protests and mass incidents now plaguing China are fundamentally different from those other countries experience. According to CASS research, he says, incidents in China are directed strictly at the government. Crowds may turn violent, but violence is focused. "People don't rob banks, they don't loot, they don't burn private cars," Shan says. "Our disturbances are not an abstract phenomenon" but usually arise from local grievances. For that reason, he argues, incidents like the one in Weng' an are exceedingly unlikely to spread to other regions.

Trickier to anticipate are incidents steeped in religious conflict or separatism. Last March, for example, rioters rampaged through Lhasa, the capital of Tibet, killing at least a dozen people. Wang's CAS group plans to launch surveys of ethnic and religious conflicts later this year. But Tibet and Xinjiang Province in western ChinaÐ the site of deadly terrorist attacks last summer attributed to Uighur separatistsÐ are too sensitive for such research now, Wang says. His group will cut its teeth on ethnic enclaves in Guangxi, Ningxia, or Qinghai.

The global financial crisis is also terra nova. "The crisis may stimulate a more widespread disaffection," Shan says. Even before the crisis, peasants and laborersÐ the majority of China's 1.3 billion peopleÐ were struggling to pay for education and medical care. "The financial crisis is pounding these people," says Shan. The result, he says, is simmering resentment: not because blue-collar workers are edging into poverty, but because they feel a sense of injusticeÐ real or imaginedÐ that the financial crisis is hitting them harder than it is China's well-heeled white-collar workers. The gap between societal benefits and people's expectations is widening, warns Shan. That's a recipe for mass discontent. "We're very afraid of this phenomenon," he says.

The financial crisis offers a prime window for Wang's CAS team to hone its forecasting. Team members search for correlations between how people feel and how they act. Based on data gathered in 2007, they forecast the likelihood of mass incidents in 35 counties last year; they were correct for 33. CASS researchers say they are reluctant to forecast unrestÐ but like their CAS colleagues, they have a good idea where blood is boiling. "We can't say exactly where and when mass disturbances will occur, but we can tell you that they may happen because there are conflicts of interest or arguments over land," says Yu Jianrong of CASS's Rural Development Institute. The problem, Shan says, is that it's impossible to predict when a sparkÐ like Li Shufen's death in Weng' anÐ will set off a mass incident.

Last July, several days after the incident, Shan's team visited Weng' an. The province had already replaced the county's top four officials. The CASS researchers didn't have to disguise their objectiveÐ the new leaders readily met with them. "They learned their lesson," Shan says. One of their first acts was to open a grievance bureau that by August had logged more than 2000 complaints. They fired the police officer who had assaulted Li's uncle, and they reopened the investigation into her death.

It was ruled a suicide.

RICHARD STONE

CREDIT: ANDREAS STEINBICHLER/AP

Published by AAAS

SOCIAL SCIENCES

DOD Funds New Views on Conflict With Its First Minerva Grants

The Pentagon makes a $45 million bet that social scientists can help it understand the world and protect the United States

Mark Woodward is an unlikely soldier in the global war on terrorism. A professor of religious studies at Arizona State University (ASU), Tempe, and a lifelong academic, he says [a] a lot of my research involves sitting in coffee shops and talking to people.[o] Woodward has spent much of the past 30 years trying to understand how local communities throughout Southeast Asia preserve their own religious and cultural identities as radical and violent Islamic movements gain strength around the world.

Currently a visiting professor at Gadjah Mada University in Yogyakarta, Indonesia, Woodward recalls a recent visit to a mosque nearly destroyed by an earthquake. A Saudi Arabian foundation that was financing its reconstruction also wanted to provide a teacher who would disseminate Wahabi-style Islam. Village elders politely but firmly declined the instructional assistance, Woodward says. [a] This is Wahabi colonialism,[o] said one local leader. [a] We don't need Arabs to teach us Islam.[o] That reaction is why Woodward believes that [a] the forces of locality[o] will prevail in a clash of ideologies. [a] I think that attempts to establish hegemonic Islam are going to fail, through very creative uses of traditional rituals and language,[o] he says.

U.S. military leaders want to find out if he's right. Last month, the U.S. Department of Defense (DOD), which is waging wars in Iraq and Afghanistan and spending billions at home to counter the threat from Islamic extremists, chose Woodward to lead a team that proposed a study of [a] the diffusion and influence of counter-radical Muslim discourse[o] in Southeast Asia, West Africa, and Europe. The project is one of seven led by social scientists that were selected earlier this month to receive a total of $45 million from a controversial DOD program called the Minerva Research Initiative. The Pentagon plans to issue a second solicitation this spring of roughly the same size, and officials have hinted strongly that there will be subsequent rounds.

Minerva is a banquet for a field accustomed to living on scraps. But some social scientists see it as a threat to academic freedom. They cite the military's history of questionable research practices and worse going back to the Vietnam War, running through the interrogation of prisoners at Guantánamo Bay, Cuba, and continuing with the much-maligned Human Terrain Teams now in Afghanistan. They say DOD's choice of topics reflects a narrow, military perspective on the world. In addition to [a] the strategic impact of religious and cultural changes in the Islamic world[o] that Woodward's project addresses, DOD solicited proposals relating to [a] terrorist organizations and ideologies,[o] the relationship between Chinese technological and military growth, and Ba'athist Party materials seized at the start of the Iraq war. Critics also worry that the lure of so much money will cause researchers to shift their attention from more important issues.

> ***In the cyberworld, anybody can play. We need ... the conceptual tools to couple the virtual and the real worlds.***
>
> **NAZLI CHOUCRI**

[a] The problem is the process,[o] says Brown University professor Catherine Lutz, one of many anthropologists who have been scornful of the program. [a] DOD shouldn't be involved because it's not likely to fund the best work. My fear is also that DOD will choose researchers who agree with them about the problems that the world is facing.[o]

DOD officials say they've bent over backward to address those concerns. When Secretary of Defense Robert Gates unveiled Minerva last spring in a talk to the Association of American Universities, he acknowledged the often [a] hostile[o] relationship between the military and social scientists and pledged that Minerva would abide by a policy of [a] complete openness and rigid adherence to academic freedom and integrity.[o]

Toward that end, DOD held a well-attended community workshop in August. And there's a Web site run by the Social Science Research Council (SSRC), a venerable New York City±based nonprofit research organization, that has published 18 essays on the controversy (www.ssrc.org/essays/minerva/). Webmaster Thomas Asher, an anthropologist by training, says he hopes the dialogue will improve future solicitations; ironically, SSRC's own bylaws preclude it from accepting military funding.

William Rees, deputy undersecretary of defense for labs and basic research, who oversees the Minerva initiative, emphasizes that the research is unclassified and that results will be posted on the project's Web site (Minerva.dtic.mil). He says his goal is to attract the best researchers, to expand the pool of scientists addressing these questions, and to foster collaborations among researchers from many fields. An examination of the first cohort of winners suggests that he's come close to hitting all three targets.

DOD received 211 initial queries from researchers seeking funding in one of five categories, four times the number community leaders had told him to expect, says Rees. [a] Rees was worried about getting the top researchers to participate,[o] says Howard Silver, executive director of the Washington, D.C.±based Consortium of Social Science Associations. [a] My sense is that he got the A team.[o]

Many of the Minerva grantees already have ties to the defense establishment. One such grantee is David Matsumoto, a professor of psychology at San Francisco State University in California. His team will study the role of emotion in stok-

Imagemakers. A 2007 video of Osama bin Laden, released by a group that monitors terror messages, is part of the cyberworld of diplomacy that Nazli Choucri (*inset*) is studying.

CREDITS: SITE INSTITUTE/VIDEO GRAB/HANDOFF/EPA/CORBIS; PHOTOS.COM; (INSET) MIT

Published by AAAS

ing or quelling ideologically driven movements. A longtime collaborator with psychologist Paul Ekman in his work on microexpressions, Masumoto has helped train airport screeners for the Transportation Security Administration and has worked with several DOD agencies over the years on what he calls [a] behavior-detection techniques.[o]

On the other end of the career continuum is Jacob Shapiro, an assistant professor of public affairs at Princeton University. A former U.S. naval officer who was on active duty from 1998 to 2002, he completed his postdoc only 1 year ago and is lead researcher on a project to understand the economics of counterinsurgency movements around the world. [a] I entered the academic community because I felt there were not enough veterans in the academy, and that is not a good thing,[o] he says. [a] The military represents all of society and so should the academy.[o]

Rees hopes the Minerva program will bring together scientists who haven't had a chance to work on a problem of mutual interest and allow small interdisciplinary groups to expand their activities. That's what Nazli Choucri, a political scientist at the Massachusetts Institute of Technology (MIT) in Cambridge, is hoping to accomplish with her project to examine cyber international relationships. The team includes foreign policy and national intelligence heavyweights such as Harvard University's Ashton Carter and Joseph Nye, as well as Internet and artificial intelligence gurus such as MIT's David Clark.

[a] Our current theories are inadequate, and what we know now is anecdotal,[o] says Choucri. [a] In the cyberworld, anybody can play. We need a fuller vocabulary to understand cyberspace as an environment, as well as the conceptual tools to couple the virtual and the real worlds.[o] Choucri is in line to receive the largest single Minerva grant, which Pentagon officials expect to be approximately $10.4 million over 5 years. (Grantees are still negotiating with DOD on funding levels.)

That type of funding is on a scale most social scientists have only dreamed about. [a] We're talking about a huge order of magnitude bigger[o] than a typical grant, says Woodward, who requested $5.8 million. Woodward is working with Muhammad Sani Umar of Northwestern University in Evanston, Illinois, an expert on Islam in western Africa, and David Jacobson, a professor of global studies at ASU, who'll examine Islamic communities in France and Germany. The project will combine ethnographic fieldwork at each location with global survey data on public attitudes toward Muslims. It will also feature a Web component to track the flow of ideas across the various Islamic communities and analyze their influence on daily life.

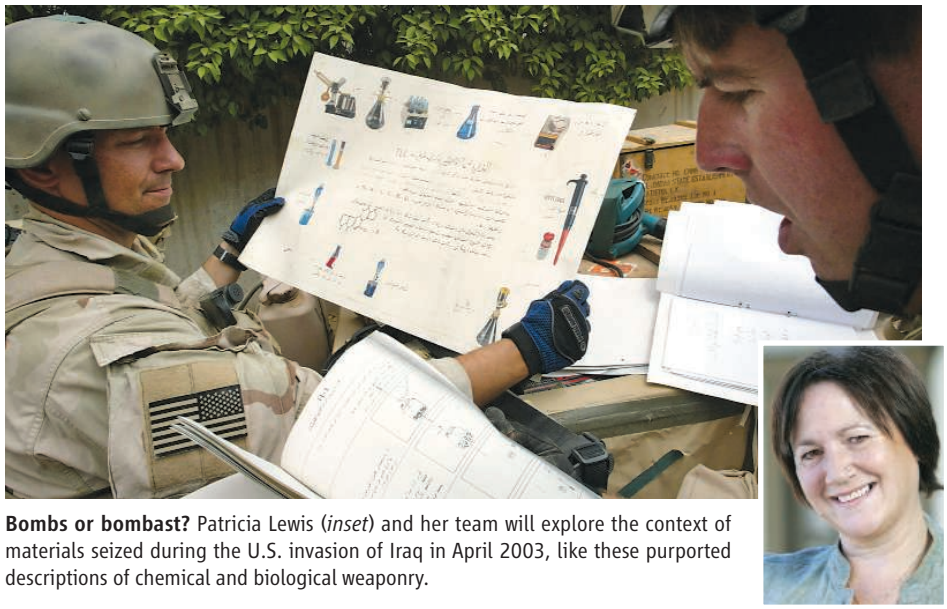

Bombs or bombast? Patricia Lewis (*inset*) and her team will explore the context of materials seized during the U.S. invasion of Iraq in April 2003, like these purported descriptions of chemical and biological weaponry.

For labor economist Eli Berman of the University of California, San Diego (UCSD), the Minerva grant is a game changer. He is working with Shapiro to understand what it takes for communities to counteract grass-roots movements such as Hamas or the Tamil Tigers. [a] Instead of just a summer salary and a graduate student, I'll be able to do surveys and experiments around the world, partner with additional organizations, and bring on postdocs as well as several graduate students,[o] he says. [a] We'll be able to accomplish things in a matter of years rather than decades.[o]

> ***I m interested in how we interpret information and how we too often see things in the light of what we already believe.***
>
> **PATRICIA LEWIS**

Berman is also a research director for the UC-wide Institute on Global Conflict and Cooperation, based at UCSD, that received a grant to explore how China's growing technological prowess is fueling the modernization of its military forces. The driving force behind the project is the institute's Tai Ming Cheung, a former journalist who has seen the literature on the topic explode over the past 2 decades in step with China's booming economy.

[a] Tai Ming has been working on this for years as the lonely monk scholar, and this grant will allow us to engage many other researchers,[o] says Susan Shirk, who directs the institute and is the named principal investigator on the grant. [a] Most of the social scientists working in China are looking at rural development, or urbanization, issues that are a lot easier to study and less sensitive. It's hard to find academic jobs from which you can look at [Chinese] national security issues.[o]

None of the grantees who spoke to *Science* expressed concern about limitations on their research or on how it could be presented. [a] We're not in the business of providing DOD with information that is tactical or operational,[o] says Woodward. [a] This is basic social science research. It's not telling the government what it wants to hear.[o]

In fact, one grantee who has written about [a] why we got it so wrong[o] on the status of Iraqi biological weapons before the U.S. invasion hopes her project will help policymakers understand that uncertainty is inevitable and that perfect knowledge is impossible. Patricia Lewis, a nuclear physicist who directs nonproliferation research at the Monterey Institute of International Studies in California, will lead a team analyzing materials captured in 2003 that many social scientists say do not even belong in U.S. hands. [a] I'm interested in how we interpret information and how we too often see things in the light of what we already believe,[o] says Lewis. [a] Biases are everywhere, and the worst sorts are those that aren't disclosed.[o]

That culture of openness apparently means something different to political scientist James Lindsay of the University of Texas, Austin, who refused to discuss his Minerva project, which is titled [a] Climate Change, State Stability, and Political Risk in Africa.[o] He told *Science*, [a] I don't owe you an explanation, and I have nothing to say about the program.[o]

JEFFREY MERVIS

CREDITS: ANJA NIEDRINGHAUS/AP PHOTO; (INSET) JAMES MARTIN CENTER FOR NONPROLIFERATION STUDIES

Published by AAAS

ASTRONOMY

Beset by Delays, U.S. Astronomers Ponder a Better To Do List

With only five of 20 projects from the last decadal survey completed and only five more started, scientists search for ways to make their list of priorities more effective

Wendy Freedman yearns to take the sharpest look ever at the wonders of the cosmos. An astronomer at the Carnegie Observatories in Pasadena, California, Freedman is one of 50 researchers developing the Giant Magellan Telescope, a $700 million behemoth that would combine seven 8.4-meter-wide mirrors into one enormous [a] segmented mirror[o] effectively 24.5 meters across. It would bring celestial marvels into the sharpest focus yet achieved.

In fact, Freedman had expected to be well on the way to completing such a telescope by now. In 2001, astronomers in the United States ranked a giant segmented-mirror telescope as their first choice for ground-based facilities to be built in the following 10 years. Usually, that endorsement suffices to push a project along. [a] Certainly it was the expectation that the number-one ranked project would move forward,[o] Freedman says. But plans for a giant telescopeÐ and half the proposals in the 2001 surveyÐ have yet to come to fruition.

That presents astronomers with an unusual problem. Early each decade since the 1960s, they have developed a list of priority projectsÐ an exercise known as a [a] decadal survey[o] Ð to tell funding agencies and the U.S. Congress which projects their community wants most. Conducted by the National Research Council, those surveys have earned astronomers a reputation for self-discipline. [a] Congress listens to them and says, `Okay, these people have got their act together,' [o] says John Mather, an astrophysicist at NASA's Goddard Space Flight Center in Greenbelt, Maryland.

But now, as a new committee begins the 18-month process of mulling over proposals for inclusion in the next decadal survey, 15 of the 20 projects listed in the especially ambitious 2001 survey remain unfinished. Only two of the major initiatives (ground-based projects with capital costs greater than $50 million and space missions with capital costs above $500 million) have received approval for construction (see table), and the committee will have to reconsider the unapproved proposals even as it evaluates myriad new ideas. In weighing more than 170 proposals, the committee will surely have to make some unpopular decisions.

[a] The pressure is on as never before to make tough choices,[o] says Roger Blandford, a theoretical astrophysicist at Stanford University in Palo Alto, California, who chairs the new survey committee. [a] There are going to be a lot of proposals for very expensive projects, and the very good is going to be trumped by the excellent.[o]

Astronomers will have to come up with more than a wish list, however. Many of the cost estimates in the 2001 survey turned out to be far too low, so this time officials at the U.S. National Science Foundation (NSF), NASA, and the Department of Energy want numbers that will stick. They also want guidance on keeping projects on trackÐ or reshuffling the list should some fall behind, says Craig Foltz, acting director of NSF's astronomical sciences division. [a] There's a logjam,[o] Foltz says, [a] and we need help breaking it.[o]

Bigger, pricier, slower

Not every large project in past surveys has been completed within 10 years. The top priority from the 1991 survey, an infrared satellite observatory now called the Spitzer Space Telescope, rocketed into orbit in August 2003. The 1991 survey also called for an array of millimeter-wavelength radio dishes that is only now being built in Chile. However, astronomers and government officials worry that uncompleted projects are becoming the rule rather than the exception.

Part of the problem is that projects have grown far bigger and more expensive, says Martha Haynes, an astronomer at Cornell University and a member of the survey committee. The 1991 survey listed one ground-

	PROJECT	COST ESTIMATE 2001	Current
✓	James Webb Space Telescope	$1 billion	$4.5 billion
	Giant segmented-mirror telescope	$700 million	$700 million
	Orbiting x-ray observatory	$800 million	New int l project
✓	Upgrade of Very Large Array of radio dishes	$140 million	$82 million*
	Large Synoptic Survey Telescope	$170 million	$400 million
	Spacecraft to find Earth-like planets	$1.7 billion	Project in limbo
	Far-infrared space telescope	$600 million	>$1.5 billion

*Phase one only

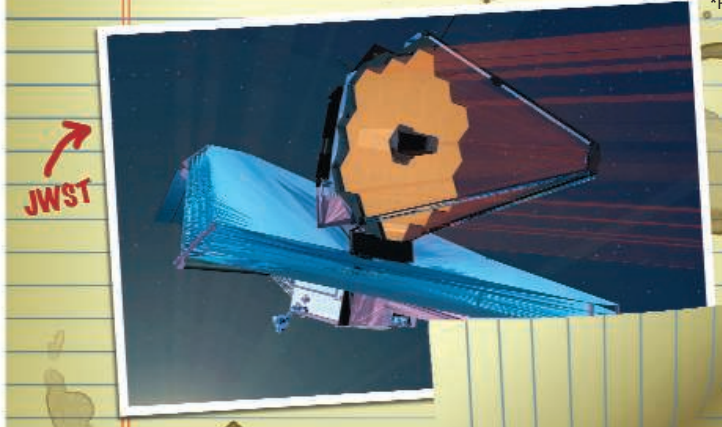

Unfinished business. Only two of the seven major initiatives listed in the 2001 survey have been approved for construction (checks). For the last two projects, only research and development money was recommended in 2001.

CREDITS: JUPITER IMAGES; NASA

Published by AAAS

based project with a price above $100 million. NSF is currently developing three that cost $250 million or moreÐ more than the agency's annual astronomy budget. ª These megaprojects just take a very long time,º Haynes says.

ª Woefully lowº cost estimates in the 2001 survey compounded the problem, says Lennard Fisk, a space scientist at the University of Michigan, Ann Arbor. In that survey, the construction cost of a successor to the Hubble Space Telescope was estimated at $1 billion. Now that satellite, NASA's James Webb Space Telescope, is approved for construction and expected to launch in 2013 or later with a total mission cost of $4.5 billion. The Advanced Technology Solar Telescope, to be built on Haleakala in Hawaii, was estimated to cost $60 million; the current price tag is $250 million.

Reasons for the underestimates vary. For example, Mather, who leads development of the Webb telescope, says the $1 billion figure for it in the 2001 report was not a rigorous estimate but a goal set by NASA officials as part of then±NASA Administrator Daniel Goldin's push to do things ª faster, better, cheaper.º ª I told [the 2001 committee] that this is what Dan Goldin wanted us to try to achieve,º he says. ª I didn't promise them that we could do it.º

The poor cost estimates played havoc with agency plans. At NASA, which funds space-based astronomy, the Webb telescope gobbled up money intended for other missions. At NSF, spiraling costs left the agency struggling to develop several big projects at the same time. Such problems might have been avoided if the 2001 survey had provided guidance on adjusting priorities as projects developed, Fisk says. ª What happens if the cost [of a project] increases by a factor of 2 or 3?º he says. ª The survey didn't address that issue.º

This decade s theme: Credibility

Given the problems getting through the 2001 ª to doº list, both scientists and funding agency officials are looking for something different this time. Above all, the committee will try to nail down a realistic cost estimate for each proposal. ª If your budget and schedule and scope are not believable, you will lose,º Haynes warns.

In fact, the committee will hire cost contractors who will independently estimate the costs of the various proposals, says Marcia Rieke, an astronomer at the University of Arizona, Tucson, who is a member of the committee. ª I don't want to advertise that our numbers will be good to 10%, but I'm hoping we can do better than a factor of 3 or 4,º she says. The numbers should be ª free of any spin from an agency or proponent group,º she says.

Officials would also like a protocol for reordering projects should one or another burst its budget or should funding to agencies fail to rise as expected. Rieke says the committee will try to identify technological milestones that each project must reach to stay on track and will suggest ways of shuffling priorities should a project fall behind.

Some scientists say there is a limit to how much guidance the ad hoc committee can provide on reprioritizing. ª I think that searching for a mechanism that will work like clockwork when the committee is gone is a mistake,º Mather says. Rather, he says, agency officials ª need to be empowered to make the decisions they need to make.º

Foreign observers have some reservations about the current survey. Committee members ª are in a terrible position because if they don't recommend the things that were put forward last time, they'll most likely get canceled,º says Simon White, a theorist at the Max Planck Institute for Astrophysics in Garching, Germany.

Martin Rees, an astronomer at the University of Cambridge in the U.K., wonders whether the decadal survey is losing its punch. Head-to-head comparisons aren't much use, he notes, for big projects funded by different agenciesÐ such as the Webb telescope and the giant segmented-mirror telescope. And nowadays, when most big projects are international efforts, a national ranking has less impact than it used to.

Still, U.S. astronomers and officials say the decadal survey serves a crucial purpose by identifying the proposals with the greatest scientific potential. ª It's the science questions that will drive the field in the next decade,º says Jon Morse, director of NASA's astrophysics division. It's less clear that a mention in the decadal survey will still propel a project to completion.

ADRIAN CHO

Priorities Nearer to Home in Need of Better Cost Estimates

Planetary scientists are generally pleased with the results so far of their first-ever prioritization of new solar system missions, covering the years 2003 to 2013. But like their colleagues in astronomy (see main text), they have seen early cost estimates for two missions blow up, sending shock waves into their next decadal survey due in 2011. The survey process was the way to go, says Wesley Huntress, director of the Carnegie Institution for Science s Geophysical Laboratory in Washington, D.C., but those tackling the next planetary decadal survey need a less naïve idea of what missions will cost.

MSL rover. Bigger, costlier.

Some cost estimates served well enough. Small missions (costing less than $325 million) should launch every 18 months, the study conducted by the National Research Council (NRC) concluded. Launches occurred in 2004, 2005, and 2007, and more are scheduled for 2009 and 2011. A medium-cost mission (less than $650 million) is on its way to Pluto, and another is in the works for Jupiter. Among small Mars missions (a separate prioritization), the Phoenix lander has finished its mission in the martian arctic, while a mission to study the martian upper atmosphere has been selected.

But priorities for large missions (costing more than $650 million) did not fare as well. A mission to Jupiter s moon Europa turned out to be wildly more costly than $650 million, so it dropped out of the decade. And returning samples from Mars always seen as a huge-ticket item is not even getting a serious look. Most surprising, though, was the ballooning of costs for the Mars Science Laboratory (MSL). Pegged in the survey at less than $650 million, its cost has swelled to more than $2 billion as technical problems triggered a delay of 2 years. MSL sucked big money out of [the planetary program], but it is what we want to do, says John Mustard of Brown University, chair of NASA s Mars Exploration Program Analysis Group.

Getting what scientists want without jeopardizing future missions will require better cost estimates early on, says Huntress, who chaired an NRC midterm review of the decadal survey. NASA should spend enough money before the decadal survey so you have a better idea what class a mission will be, he says. The situation is improving, he adds, and Congress is pitching in. It has mandated that decadal surveys include independent estimates of the life cycle costs and technical readiness of missions whenever possible. Scientists will no doubt find out whether their eyes are still bigger than NASA s stomach.

RICHARD A. KERR

CREDIT: NASA/JPL-CALTECH

Published by AAAS

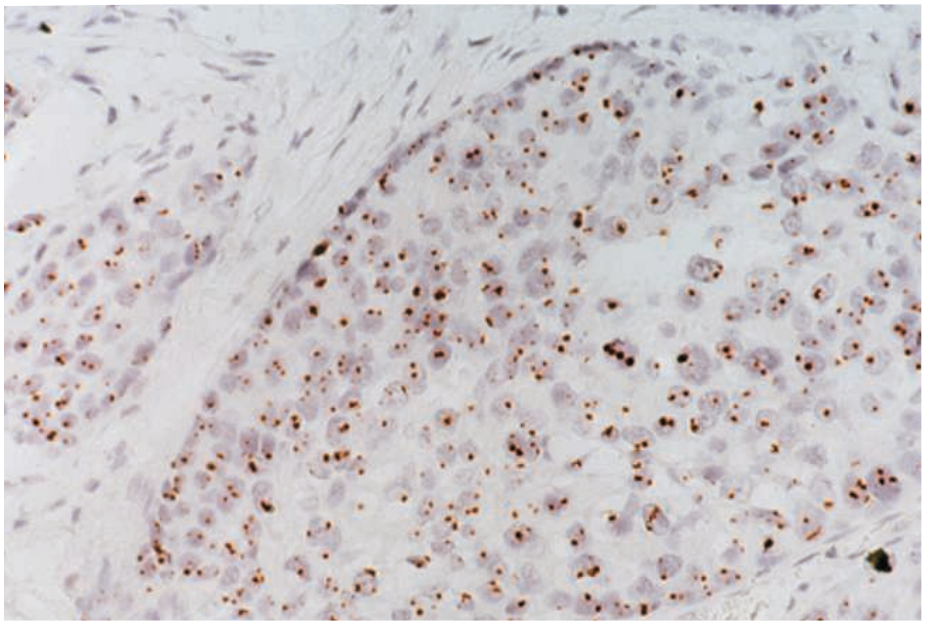

Telltale linkage. Molecular studies have identified strain 16 of the human papilloma virus in oral cancers, such as this tonsillar tumor.

CANCER

HPV Casts a Wider Shadow

Recent studies link certain oral cancers to the virus that causes cervical cancer; some researchers want to vaccinate both men and women against it

When he began practicing in 1994, head and neck cancer specialist Wendell Yarbrough knew just what type of patients would walk through his clinic doors. They were typically in their 50s or 60s, and in most cases he attributed their throat and tonsil cancer to years of lighting up tobacco and chugging down alcohol. Yarbrough's patient roster at the Vanderbilt-Ingram Cancer Center in Nashville, Tennessee, now tells a different story: It's not unusual to see patients in their late 20s or 30s, he says, and few of the younger patients smoke.

Nationally, while the total number of oropharyngeal cancersÐ affecting the area from the base of the tongue through the tonsilsÐ is in decline, the rate among Americans younger than age 50 is creeping upward. According to surveillance data from the National Cancer Institute (NCI), rates of oropharyngeal cancer in the 20 to 49 age group more than doubled from 1975 to 2005.

A search for the cause has led to a familiar suspect: the human papilloma virusesÐ specifically HPV 16 and to a lesser extent HPV 18, the same strains that cause 70% of cervical cancers in the United States. Several papers in recent years have documented active HPV DNA in tumor samples from oral cancer patients. In November, an epidemiological analysis from the Centers for Disease Control and Prevention (CDC) in Atlanta, Georgia, linked up to 60% of oropharyngeal cancer cases from 1998 and 2003 to HPV. The link is [a] as solid as it is for cervical cancer,º says pathologist Lubomir Turek of the University of Iowa in Iowa City.

How significant HPV infection is as a risk factorÐ and what behaviors put someone at risk for cancerÐ remain unclear. But the realization that HPV is behind a subset of head and neck cancers is prompting researchers and clinicians to reevaluate how they diagnose and treat oral cancer, which strikes about 34,000 Americans each year. And it's adding another facet to the picture of the health threat of HPV as public health officials weigh expanding vaccination programs. This year, Merck is seeking to get its anti-HPV vaccine Gardasil, which was approved for women in 2006, approved for use in men.

High-risk group? The U.S. rate of oropharyngeal cancer among people aged 20 to 49 rose sharply between 1975 and 2005.

Viral connection

One of the first to publish suspicions that HPV might cause oral cancer is dentist-turned-researcher Stina Syrjänen of the University of Turku in Finland. She and her colleagues started to examine oral cancer tumors for HPV after virologist Harald zur Hausen began isolating HPV DNA in cervical cancer lesions in the early 1980s. The Syrjänen group's initial surveys and immunochemistry staining of 40 lesions published in 1983 turned up nearly a quarter that were shaped like HPV lesions in cervical cancer. But there wasn't much interest in this at the time, Syrjänen says.

Papers from other European labs trickled in documenting the presence of HPV antibodies in some oral cancer tumors. One published in 1995 by R. D. Steenbergen and colleagues at the Free University Hospital in Amsterdam showed that HPV 16 was integrated and its onco proteins were expressed in an oral cancer tumor cell line.

Those findings had a big impact on Maura Gillison, then a postdoc at Johns Hopkins University in Baltimore, Maryland. [a] I was pretty convinced from this one caseº that the link between the virus and this oral cancer was real, she says. Gillison, now a chair of cancer research at Ohio State University, Columbus, began looking for more evidence that the virus actually was triggering oral cancers. Using PCR, sequencing, Southern blot assays, and in situ hybridization, Gillison and colleagues at Johns Hopkins examined 253 head and neck tumors and identified HPV in 62 of them, as they reported in the 3 May 2000 *Journal of the National Cancer Institute*.

Recent research on HPV and cervical cancer suggests how the process works. Two specific HPV genes, E6 and E7, turn off proteins in cervical cells that suppress tumor growth. In their 2000 study, Gillison and colleagues examined these tumor suppressor proteins in head and neck cancer samples. Previous work revealed that the tumor suppressor proteins of HPV-negative oral cancers often show mutations, likely caused by long-term exposure to carcinogens and alcohol. But the researchers found few such mutations in the HPV-positive samples, so they argued that the onco-

CREDITS (TOP TO BOTTOM): COURTESY OF MAURA GILLISON/OSU AND WILLIAM WESTRA/JOHNS HOPKINS UNIVERSITY; SOL SILVERMAN/UCSF

Published by AAAS

proteins were disarming the cell's tumor suppressors, just as they do in cervical cancer. Over the next several years, labs in the United States and in Europe confirmed the findings. At the 2007 American Society for Clinical Oncology (ASCO) meeting in Chicago, Illinois, Yale University researcher Amanda Psyrri reported that suppressing E6 and E7 RNA in HPV-positive oral cancer cells reactivated the cells' natural tumor suppression genes.

The molecular and pathological evidence that HPV, particularly HPV 16, can cause oral cancer is convincing, researchers say. [a] HPV-related head and neck cancer represents a new entity that is now well-defined,[o] Dana-Farber Cancer Institute oncologist Robert I. Haddad wrote to the Oral Cancer Foundation after the 2007 ASCO meeting.

Gillison and colleagues at Johns Hopkins and NCI have been building up an epidemiological picture of HPV-positive oral cancer. A May 2007 paper in *The New England Journal of Medicine* (*NEJM*) examined 100 cases of oropharyngeal cancer and found that HPV infection could be a risk factor independent of smoking or drinking history. In February 2008, the researchers reported in the *Journal of Clinical Oncology* that U.S. National Institutes of Health records show that rates of HPV-related oral cancers significantly increased between 1973 and 2004 while rates of non-HPV oral cancers declined.

When the researchers interviewed patients about their health behaviors, they reported in the 19 March 2008 *Journal of the National Cancer Institute*, two different profiles emerged. Risk factors for HPV-negative tumors included several decades of pack-a-day smoking, years of heavy drinking, and losing teethÐ but not having more sex partners. In contrast, having more oral sex partners significantly increased the risk of developing HPV-positive cancer. Unexpectedly, a history of heavy marijuana usage also seemed to increase risk for HPV-negative tumors in these patients.

Gillison says she has concluded that HPV-positive oral cancer isn't just a subset of oral cancer but a completely independent disease: [a] If the risk factors are that different, what other evidence do you need?[o]

What you need, Turek and Syrjänen say, are more confirmatory studies. They agree that Gillison's team is on the right track in doing the larger, case-control studies of the past 2 years. But questions remain. As Turek and Syrjänen have noted, Gillison's group used the anatomic site of some tumors (around the tonsils, where HPV-positive tumors overwhelmingly occur) as a proxy for evidence of HPV's presence. Gillison says her team is now doing a molecular analysis of these tumor samples and expects results this year.

Large epidemiological studies could help clinch the risk-factor profile. Stephen Schwartz, an epidemiologist at the University of Washington, Seattle, who studies HPV-related cancers, says he's skeptical of a proposed link between HPV-positive oral cancer and marijuana usage, because only one study has demonstrated it so far. But the evidence that disease risk increases with more sexual partners seems stronger, having been suggested in several studies by independent researchers, he says.

CREDIT: COURTESY OF OHIO STATE UNIVERSITY MEDICAL CENTER

"I was pretty convinced from a 1995 study that the link between the virus and this oral cancer was real."

MAURA GILLISON, OHIO STATE UNIVERSITY

One question all the researchers agree remains unresolved is the natural history of HPV-positive oral cancer. Researchers know it can take 20 to 30 years after HPV infection for cervical cancer to develop in an otherwise healthy woman. They don't know how long it takes oral cancer to develop or how much of the virus must be present in oral cells to trigger cancer, Turek says. A single study of 292 HPV-positive oral cancer patients published in 2001 in *NEJM* suggests it might take only a decade, but researchers agree that studies are needed to confirm that finding and explain why oral cancer might develop so much faster than cervical cancer.

Gillison argues that researchers don't need to wait for all questions to be resolved before reassessing how they diagnose and treat HPV-positive oral cancer patients. In November, Gillison pressed her case to more than 80 head and neck cancer experts at a closed meeting at NCI in Bethesda, Maryland. She and other researchers, including Turek, believe the standard treatment protocol for oral cancerÐ chemotherapy and radiation, followed by possible surgeryÐ may be too aggressive for patients with HPV-positive tumors. Researchers and clinicians say they have noticed that these patients tend to respond much better to treatment, specifically radiation: About 85% of patients with HPV-positive tumors are still alive within 5 years of their cancer diagnosis, compared with about 45% of those with non-HPV tumors. So radiation alone might be enough to treat some of these patients, Gillison argues.

Public health officials, meanwhile, are asking what can be done to prevent the disease. CDC has approved four vaccines against HPV for use in young women to prevent cervical cancer; now the question is whether to expand the recommendations to include young men. Preliminary results from a Merck-funded study found that Gardasil effectively prevented HPV infection in the genitals of men, says study leader Joel Palefsky of the University of California, San Francisco. Full results are expected some time this spring, he says. NCI epidemiologists are also conducting clinical trials to assess whether the vaccine can prevent oral HPV infection. It may be years before those results come in, says study leader Aimee Kreimer.

Well before that, CDC's Advisory Committee on Immunization Practices (ACIP) hopes to give its own recommendations on whether men should get vaccinated for HPV and if so, at what age, says CDC medical epidemiologist Lauri Markowitz. She says ACIP is currently reviewing data from the Merck trials, along with studies on HPV and oral cancer. Schwartz says he thinks the vaccine will be approved for use in men soon, before researchers fill in the lingering gaps in knowledge about HPV and oral cancer or how effectively vaccination programs might prevent disease. That means taking a bit on faith, he says: [a] I don't have any real reason to think it won't work, but we have to acknowledge we're just taking more of a leap here.[o]

RACHEL ZELKOWITZ

Rachel Zelkowitz is a writer in Washington, D.C.

Published by AAAS

Broadcasting science 584

Cellular force mechanics 588

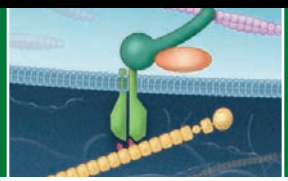

LETTERS

edited by Jennifer Sills

Systems Politics and Political Systems

IN HIS EDITORIAL A SCIENTIFIC APPROACH TO POLICY (5 DECEMBER 2008, P. 1435), B. ALBERTS wrote that when dealing with complex political issues, policy-makers would benefit from applying the experiment-based, problem-solving approach of scientists and engineers.

The suggestion that the complexity of intercellular and subcellular interactions is equivalent in a sense to political interchange holds true at many levels. Indeed, many parallels have been made between politics and systemic biology. For example, autoimmunity results from a misguided national defense (immune) force attacking its own subjects (cells), and regulatory steps of a governmental construction policy mirror the communication, trafficking, and machinery control involved in cell polarization.

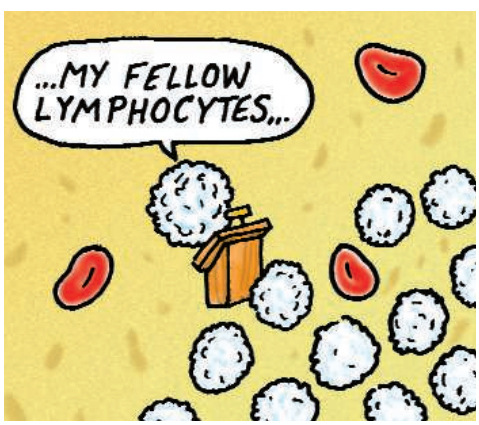

These comparisons can work both ways, and therefore it is incumbent on scientists to learn from policy-makers as well. Leadership, management, public engagement, and economic awareness are all characteristics that can enhance the phenotype of the next generation of scientists.

HUTAN ASHRAFIAN

Department of Biosurgery and Surgical Technology, Imperial College London, London W2 1NY, UK. E-mail: h.ashrafian@imperial.ac.uk

Scientists Not Immune to Partisanship

THE EDITORIAL BY B. ALBERTS (A SCIENTIFIC approach to policy,º 5 December 2008, p. 1435) persists in promoting a long-refuted notion that scientists constitute an apolitical elite that will, by bypassing partisanship and ideology, improve policy-making. Although the three ª scientific habits of mindº that he describesÐ optimism, long-term thinking, and pragmatismÐ are admirable virtues, they are not exclusive to members of the scientific community, nor universal among scientists, nor guarantees of wise action. Who is to decide the ends to which such virtues are applied? A can-do attitude and a pragmatic approach to realizing a long-term goal of dubious value gets society nowhere (or worse). Indeed, some scientists (in their optimism about getting rich) applied these very qualities to the development of financial models that have contributed to the current economic meltdown that Alberts blames entirely on the unrealistic assumptions of financial managers (*1*). David Halberstam (*2*) documented the disastrous application of similar faith among such ª nonideological policy-makersº in the conduct of the Vietnam War. The obvious point is that the application of our scientific knowledge is inseparable from the subjective contexts in which it is applied. Science and technology bring not only wonderful benefits, but also challenges and risks, from threats to personal and national security, to skewed distribution of wealth and social capital, to environmental and cultural degradation. While we may be pleased that the prospects of a new administration in Washington will correct the recent era of hyperpartisanship, we note that in the 1990s it was conservatives who were calling for more ª sound scienceº in policy matters. Science will continue to be used by players at all positions within the political spectrum as a cover for political agendas until we abandon the doctrine that Alberts insists on perpetuating. The claim that science and values can be kept apart in the policy world confuses the means of science with the ends of democracyÐ a confusion that is dangerous for the health of both.

DAVID H. GUSTON,* DANIEL SAREWITZ, CLARK MILLER

Consortium for Science, Policy, and Outcomes, Arizona State University, Tempe, AZ 85287, USA.

*To whom correspondence should be addressed. E-mail: david.guston@asu.edu

References

1. J. Nocera, Risk Management, *The New York Times Magazine* (4 January 2008), pp. 4 33.
2. D. Halberstam, *The Best and the Brightest* (Random House, New York, 1969).

Law and Science Not Mutually Exclusive

AS SOMEONE WITH DEGREES IN BOTH PHYSICS and law, I agreed with the Editorial ª A call to serveº by W. A. Wulf and A. K. Jones (14 November 2008, p. 1025) until I reached the fifth paragraph, in which the authors seemed to suggest that lawyers think differently from scientists and engineers. Do the authors think that those lawyers who also have science and engineering degrees were rendered incapable of thinking as scientists and engineers once they received their law degrees?

The authors also suggest that lawyers ª disproportionately populate government positions.º What do the authors believe the correct proportion to be? Many people get law degrees with the intent of public service. I suspect that an understanding of law makes one a more effective public servant, just as knowledge of science helps somebody who serves on the National Science Foundation or on the National Science Board. Are the authors

CREDIT: JOE SUTLIFF

Published by AAAS

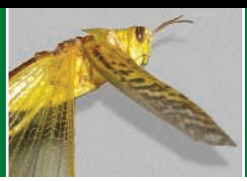

willing to suggest that those positions are disproportionately taken up by people with backgrounds in science and engineering?

The authors suggest that scientists and engineers are [a]trained[o] to follow wherever the evidence leads. I disagree that majoring in science or engineering is the only way to learn how to consider a problem from all angles. The authors have set up a false dichotomyÐ being trained to form an argument that best supports a given conclusion does not preclude the ability to examine a situation dispassionately and reach the correct conclusion. Certainly, there are lawyers who are unqualified to make policy decisions on scientific issues, both because they lack basic scientific understanding and because they have other interests besides promoting the best available policies, but the authors have made unwarranted (and insulting) generalizations about lawyers.

DONALD D. DEROSIER

Carmichael, CA 95608, USA. E-mail: derosied@earthlink.net

(*2*). They detailed the advantages of their scheme and proposed the formula: Points = [(1/*i*)/(1 + (1/2) + ¼ + (1/*N*)] 100 for the *i*th author out of *N*. The denominator in the formula is the well-known harmonic series; and the points are standardized to 100 per paper. Apart from the standardization, this is exactly what Sekercioglu proposes.

Sekercioglu's Letter opens by citing a never-cited 40-year-old contribution to *Science* that argued that more than three authors on one paper is not justifiable. It is interesting to note that both Price and Hodge and Greenberg proposed division of authorship credit [a]¼ to discourage putting many authors on a single paper[o] (*1*).

Authorship trends have not progressed as Price and Hodge and Greenberg had hoped. Sekercioglu's letter highlights the need for a critical reappraisal of the way modern bibliometry allocates publication credit (*3*).

NILS T. HAGEN

Department of Biosciences and Aquaculture, Bod University College, N-8049 Bod , Norway. E-mail: Nils.Hagen@hibo.no

References

1. S. E. Hodge, D. A. Greenberg, *Science* **213**, 950 (1981).
2. D. D. S. Price, *Science* **212**, 986 (1981).
3. N. T. Hagen, *PLos ONE* **3**, e4021 (2008).

Response

I THANK HAGEN FOR POINTING OUT A CRITIcal reference (*1*) that I inadvertently omitted. A key difference in my formulation is that author rank can be independent from author order. This is essential in many cases where the last author is the senior author or where some authors may have contributed equally to the publication. Hodge and Greenberg's proposal does not allow for this. They state that [a]the first author always receives twice as many points as the second[o] and they have deliberately not allowed for the last author being the senior author, as they [a]do not wish to encourage this pernicious habit.[o]

We need to encourage the conversation on quantifying coauthor credit so that proposals are rigorously debated, improved, and decided upon by the scientific community. Otherwise, we may still be having this discussion three decades from now.

CAGAN H. SEKERCIOGLU

Center for Conservation Biology, Department of Biology, Stanford University, Stanford, CA 94305, USA. E-mail: cagan@stanford.edu

Reference

1. S. E. Hodge, D. A. Greenberg, *Science* **213**, 950 (1981).

Credit for Coauthors

IN THE LETTER QUANTIFYING COAUTHOR contributions[o] (17 October 2008, p. 371), C. H. Sekercioglu's proposal that the *k*th ranked coauthor be considered to contribute 1/*k* as much as the first author is not novel. It was originally made in 1981 in a letter to *Science* by Susan E. Hodge and David A. Greenberg titled [a]Publication credit[o] (*1*).

Hodge and Greenberg were responding to a plea from Derek De Solla Price for dividing authorship credit equally among all coauthors

Letters to the Editor

Letters (~300 words) discuss material published in *Science* in the previous 3 months or issues of general interest. They can be submitted through the Web (www.submit2science.org) or by regular mail (1200 New York Ave., NW, Washington, DC 20005, USA). Letters are not acknowledged upon receipt, nor are authors generally consulted before publication. Whether published in full or in part, letters are subject to editing for clarity and space.

CORRECTIONS AND CLARIFICATIONS

Reports: A null mutation in human *APOC3* confers a favorable plasma lipid profile and apparent cardioprotection by T. I. Pollin *et al*. (12 December 2008, p. 1702). On page 1703, the exon was mischaracterized. The second sentence in the second full paragraph of the first column should read as follows: Sequencing of the coding region of *APOC3* revealed a C → T substitution at the terminal nucleotide of exon 2, the 55th nucleotide from the ATG start codon; this substitution resulted in a premature stop codon for an arginine residue at amino acid position 19 (R19X).

TECHNICAL COMMENT ABSTRACTS

COMMENT ON Arsenic (III) Fuels Anoxygenic Photosynthesis in Hot Spring Biofilms from Mono Lake, California

B. Schoepp-Cothenet, S. Duval, J. M. Santini, W. Nitschke

Kulp *et al*. (Reports, 15 August 2008, p. 967) described a bacterium able to photosynthetically oxidize arsenite [As(III)] via arsenate [As(V)] reductase functioning in reverse. Based on their phylogenetic analysis of As(V) reductase, they proposed that this enzyme was responsible for the anaerobic oxidation of As(III) in the Archean. We challenge this proposition based on paleogeochemical, bioenergetic, and phylogenetic arguments.

Full text at www.sciencemag.org/cgi/content/full/323/5914/583c

RESPONSE TO COMMENT ON Arsenic (III) Fuels Anoxygenic Photosynthesis in Hot Spring Biofilms from Mono Lake, California

R. S. Oremland, J. F. Stolz, M. Madigan, J. T. Hollibaugh, T. R. Kulp, S. E. Hoeft, J. Fisher, L. G. Miller, C. W. Culbertson, M. Asao

Schoepp-Cothenet *et al*. bring a welcome conceptual debate to the question of which came first in the course of planetary biological evolution, arsenite [As(III)] oxidation or dissimilatory arsenate [As(V)] reduction. However, we disagree with their reasoning and stand by our original conclusion.

Full text at www.sciencemag.org/cgi/content/full/323/5914/583d

Published by AAAS

Comment on "Arsenic (III) Fuels Anoxygenic Photosynthesis in Hot Spring Biofilms from Mono Lake, California"

B. Schoepp-Cothenet,[1]* S. Duval,[1] J. M. Santini,[2] W. Nitschke[1]

Kulp *et al*. (Reports, 15 August 2008, p. 967) described a bacterium able to photosynthetically oxidize arsenite [As(III)] via arsenate [As(V)] reductase functioning in reverse. Based on their phylogenetic analysis of As(V) reductase, they proposed that this enzyme was responsible for the anaerobic oxidation of As(III) in the Archean. We challenge this proposition based on paleogeochemical, bioenergetic, and phylogenetic arguments.

The report by Kulp *et al*. (*1*) demonstrates the ability of anoxygenic photosynthetic bacteria to use reduced arsenic compounds as electron-donating substrates. As pointed out by the authors, this result provides a possible solution to a paleogeochemical/phylogenetic conundrum. Phylogenetic analyses of relevant proteins have been interpreted to indicate ancient (i.e., pre-Archaea/Bacteria divergence) roots for the bioenergetic mechanism of AsIII oxidation (*2*). By contrast, the ultimate electron-accepting substrate observed so far in most extant arsenite oxidizers, that is, O_2, is unlikely to have been present on the early Earth. We have recently suggested nitrogen oxides as possible alternatives to O_2 playing the role of strong oxidants in the early Archean (*3*). The existence of organisms feeding electrons from the oxidation of As(III) into an anoxygenic photosynthetic chain constitutes another solution to this nagging contradiction.

The observation of photosynthetic As(III) oxidation per se substantially advances our understanding of a possible bioenergetic role for As(III) in the Archean era. Kulp *et al*. (*1*), however, further conclude that the existence of a biological pathway generating the oxidized element, arsenate (AsV), "requires that the antiquity of prokaryotic arsenate respiration be reevaluated…." It was indeed assumed previously that dissimilatory arsenate reduction could only have evolved after the increase in oxidation level of the environment brought about by oxygenic photosynthesis (*4*).

We challenge this conclusion by Kulp *et al*. based on the following paleogeochemical, bioenergetic, and phylogenetic arguments. The abundance of reduced compounds, and especially of high concentrations of Fe(II), in the Archean biosphere provides a powerful chemical reductant for the photosynthetically produced As(V), keeping the total bioavailable amount of As(V) at very low levels. This also implies that the As(III)/As(V) ratio has remained high despite the photosynthetic production of As(V). The resulting operating potential of the As(III)/As(V) couple is therefore not likely to substantially exceed 0 mV (versus standard hydrogen electrode), rendering it bioenergetically useful only as an acceptor for rather low potential substrates. Finally, our phylogenetic analysis of arsenate reductase (*5*) suggests a late origin for this enzyme followed by subsequent dissemination by horizontal gene transfer. In this context, we note that the outgroup position of the branch in figure 3D in (*1*) labeled *Pyrobaculum aerophilum* and considered to represent the ArrA protein of this Archaeon, would indeed support the authors' conclusion on an early origin of dissimilatory arsenate reductase. However, several arguments indicate this enzyme to be a polysulphide/thiosulphate reductase rather than an arsenate reductase (*5*). In summary, we conclude that the presently available evidence argues against a role of dissimilatory arsenate reductase in arsenic cycling on the early Earth.

[1]Bioénergétique et Ingénierie des Protéines, IFR88, CNRS, 13402 Marseille, France. [2]Department of Structural and Molecular Biology, University College London, London WC1E 6BT, UK.

*To whom correspondence should be addressed. E-mail: schoepp@ifr88.cnrs-mrs.fr

References

1. T. R. Kulp *et al*., *Science* **321**, 967 (2008).
2. E. Lebrun *et al*., *Mol. Biol. Evol.* **20**, 686 (2003).
3. A.-L. Ducluzeau *et al*., *Trends Biochem. Sci*. **34**, 9 (2009).
4. R. S. Oremland, J. F. Stolz, *Science* **300**, 939 (2003).
5. S. Duval *et al*., *BMC Evol. Biol.* **8**, 206 (2008).

21 August 2008; accepted 31 December 2008
10.1126/science.1164967

Response to Comment on "Arsenic(III) Fuels Anoxygenic Photosynthesis in Hot Spring Biofilms from Mono Lake, California"

R. S. Oremland,[1]* J. F. Stolz,[2] M. Madigan,[3] J. T. Hollibaugh,[4] T. R. Kulp,[1] S. E. Hoeft,[1] J. Fisher,[4]† L. G. Miller,[1] C. W. Culbertson,[5] M. Asao[3]

Schoepp-Cothenet *et al*. bring a welcome conceptual debate to the question of which came first in the course of planetary biological evolution, arsenite [As(III)] oxidation or dissimilatory arsenate [As(V)] reduction. However, we disagree with their reasoning and stand by our original conclusion.

Schoepp-Cothenet *et al*. (*1*) challenge our conclusions regarding dissimilatory arsenic reduction on primordial Earth (*2*). The authors argue their points based on suppositions concerning the redox state of the Archean, and their entrained bioenergetic/phylogenetic reasoning. With regard to their point about redox state, although Fe(II) is believed to have been abundant in the anoxic Archean, this chemical species does not reduce As(V) to As(III). Free sulfide can reduce As(V), but this requires a very low pH for any reasonable kinetic resolution (*3*). In addition, the production of As(V) by As(III)-linked anoxygenic phototrophy would have opened localized niches for As(V) respiration without affecting the overall redox balance of the Archean Earth. This is similar to what has been proposed for photosynthetically linked Fe(II) oxidation and banded iron formations (*4*). Indeed, the tight coupling of As(V) reduction/As(III) oxidation has been seen in periphyton samples (*5*) and salt-saturated anoxic sediments from Searles Lake (*6*). We have also observed this phenomenon in "red" hot spring biofilms from Mono Lake as part of an ongoing study. Finally, although in silico phylogenetic analyses of genomes can provide grist for evolutionary schemes, their validity is dependent on correct annotation. Unless proof of function is known for a given homolog, biochemical or genetic confirmation is necessary (*7*). For example, the dimethyl sulfoxide reductase family of molybdenum enzymes is composed of oxidases, reductases, and dehydrogenases, and enzymes sharing high sequence identity can have very different functions (*8*). Moreover, arsenate respiration has been demonstrated in two *Pyrobaculum* species; however, the respiratory arsenate reductase in these organisms has yet to be identified. Investigations of the *arrA* amplicons obtained from the extreme environment of Searles Lake, California, suggest unexpectedly high sequence diversity, with most lying well outside the boundaries established with cultured anaerobes from the domain Bacteria (*9*). Such observations indicate that there are many more "novel" prokaryotes out there (including Archaea) with the capacity to respire As(V), awaiting isolation and characterization and, ultimately, genomic analysis.

[1]U.S. Geological Survey (USGS), Menlo Park, CA 94025, USA. [2]Department of Biological Sciences, Duquesne University, Pittsburgh, PA 15282, USA. [3]Department of Microbiology, Southern Illinois University, Carbondale, IL 62901–6508, USA. [4]Department of Marine Sciences, University of Georgia, Athens, GA 30602–3636, USA. [5]USGS Water Sciences Center, Augusta, ME 04330, USA.

*To whom correspondence should be addressed. E-mail: roremlan@usgs.gov

†Present address: Division of Earth and Ecosystem Science, Desert Research Institute, Las Vegas, NV 89119, USA.

References

1. B. Schoepp-Cothenet, S. Duval, J. M. Santini, W. Nitschke, *Science* **323**, 583 (2009); www.sciencemag.org/cgi/content/full/323/5914/583d.
2. T. R. Kulp *et al*., *Science* **321**, 967 (2008).
3. J. A. Cherry *et al*., *J. Hydrol. (Amst.)* **43**, 373 (1979).
4. A. Ehrenreich, F. Widdell, *Appl. Environ. Microbiol.* **60**, 4517 (1994).
5. T. R. Kulp *et al*., *Appl. Environ. Microbiol.* **70**, 6428 (2004).
6. R. S. Oremland *et al*., *Science* **308**, 1305 (2005).
7. R. S. Oremland *et al*., *Nat. Rev. Microbiol.* **3**, 572 (2005).
8. J. F. Stolz *et al*., *Annu. Rev. Microbiol.* **60**, 107 (2006).
9. T. R. Kulp *et al*., *Appl. Environ. Microbiol.* **72**, 6514 (2006).

25 September 2008; accepted 31 December 2008
10.1126/science.1166435

SCIENCE COMMUNICATION

Faulty Transmission

Audra J. Wolfe

Science on the Air
Popularizers and Personalities on Radio and Early Television

by Marcel Chotkowski LaFollette

University of Chicago Press, Chicago, 2008. 324 pp. $$27.50, £14.50. ISBN 9780226467597.

Writing a history of print journalism is a fairly straightforward process: microform and now digital collections have made even obscure, short-lived publications widely available. But radio? That's a different story. There is no such thing as a comprehensive *Reader's Guide to Periodic Literature* for radio, and what listings are available tell little about what exactly happened on the shows. For science journalism, the problem is compounded by the fact that science programming rarely made it onto the networks, appearing instead as filler on regional stations. And yet, in the fascinating *Science on the Air*, Marcel LaFollette manages to suss out most of the major players in science popularization in the first three decades of broadcast journalism. It is a remarkable achievement.

Ironically, LaFollette's task was made somewhat easier by the rarity of scientific programming in the golden age of radio. The book focuses on the story of how American scientific institutions failed to grasp the power of broadcast media to shape public attitudes about and understanding of science. Their few forays into the medium were marked by a profound unwillingness to take the concerns of audiences, advertisers, and network executives seriously. The few examples of commercially successful science programming that LaFollette, an independent historian, unearths were mostly developed by corporate interests.

It didn't have to be this way. The story opens in 1923 with a phone call from a station manager at WRC, a Washington, DC±based affiliate of RCA, to the secretary of the Smithsonian Institution, Charles D. Walcott. Like many of his peers, this station manager was open to suggestions on how to distinguish his station's offerings from the typical fare of sermons, jazz bands, and sports. The call was passed along to Austin Clark, an ambitious curator and invertebrate biologist, who was soon scheduling lectures by Smithsonian scientists on such topics as ª Creatures That Fly and How They Do Itº and ª Animal Terrors of Past Ages.º

For Clark and his colleagues, radio was an extension of the Smithsonian's public lecture programming. Many of the scientists who appeared on the show did not own radio sets, had never listened to radio programming, and did not understand that the airwaves were mostly dominated by musical performances. Clark further insisted that his guests don tuxedos at the recording booth in keeping with the dignity of science. This level of stodginess was acceptable in 1923, when much of the radio dial was occupied by earnest, amateurish programming, but fell out of favor during the wave of consolidation that soon affected the industry. Whereas station managers defined a successful program by the number of listeners (and potential advertising rate), officials at the Smithsonian judged the show by the caliber of the guests and Clark's ability to get the lectures published as pamphlets or magazine articles. WRC canceled *Radio Talks* in 1927.

LaFollette tells a nearly identical story for programs developed by the Franklin Institute, the American Museum of Natural History, and a few entrepreneurial scientists, including naturalist Thornton Burgess and Harvard astronomer Harlow Shapley. The American Psychological Association and the American Medical Association were slightly more successful in developing programs that could sustain listener interest in the 1930s, largely because they were forced to respond to the charismatic hucksters who peddled quack remedies over the airwaves. All of these organizations emphasized education over entertainment. The lone voice advocating a more popular approach belonged to Watson Davis, first as managing editor and later as director of Science Service, Incorporated, a news syndication service that produced a long-running audio news digest called *Science Service Talks*. That Davis's contributionsÐ theme music, introductions by nonscientists, interviews instead of straight lecturesÐ were seen as radical gives some indication of how tedious early science radio programming must have been.

Innovation in science radio was instead left to the corporate giants who had the necessary resources both to produce quality programming and to purchase air time. General Electric, Westinghouse, and, especially, DuPont created lavish radio productions that incorporated dramatization, fictionalization, and quiz shows into scientific programming. DuPont produced nearly 800 episodes of its *Cavalcade of America* for radio, followed by an additional 200 for television before finally taking it off the air in 1957. The critical acclaim and popular success of this program finally convinced the staid American scientific establishment to

CREDIT: SMITHSONIAN INSTITUTION ARCHIVES, SCIENCE SERVICE RECORDS, NEGATIVE SIA2008-1817

Advocate for popularization. Beginning in the 1920s, Science Service journalist Watson Davis (right) used a series of radio programs to deliver news about science and scientists.

The reviewer is at the Chemical Heritage Foundation, 315 Chestnut Street, Philadelphia, PA 19106, USA. E-mail: awolfe@chemheritage.org

Published by AAAS

experiment with broadcasting from planetariums and scientific expeditions, but it was too little, too late. By then, the airwaves were being controlled by the national networks, and the networks' gatekeepers had decided that science couldn't pay its own way.

The pattern would be repeated in the early years of television, where complex production requirements, expensive sets, and demanding visuals left little room for amateurish productions. As on the radio, the most creative uses of the medium for science popularization came from media behemoths like ABC and Disney rather than scientific institutions.

LaFollette minces no words in referring to the [a] imaginative failures[o] of the American scientific establishment in making use of mass media technologies. Commenting on an effort to increase the amount of educational programming on 1930s-era radio, for example, she argues that the scientific organizations' [a] inability ¼ to cooperate with each other, their intellectual snobbery and undisguised disdain for the very medium they were supposedly trying to utilize, and their unwillingness to invest significant resources in production of quality programs all hobbled their effectiveness.[o] LaFollette's extensive use of archival collections, including meeting minutes and personal correspondence, offers ample support for her damning conclusions. Her criticism is bracing but fair. Now, she argues, podcasts, online video-sharing sites, and blogs are giving scientists another opportunity to communicate directly with the public. The question is: Will they take it?

10.1126/science.1168311

NEUROSCIENCE

Who Are We?

Ralph Adolphs

It is blatantly apparent that humans are quite different from all other animals, in ways both good and bad. But articulating what that difference consists of and uncovering the biology behind it have formed a large and difficult project tackled by biologists, anthropologists, psychologists, and philosophers. Michael Gazzaniga's *Human: The Science Behind What Makes Us Unique* provides a masterful overview of what we know, who the key players are, and what the future might hold. The book is at once dense with facts (there are 748 endnotes) and an easy read; it is both entertaining and informative.

Gazzaniga, a professor of psychology at the University of California, Santa Barbara, is the director of the SAGE Center for the Study of the Mind at UCSB. There he has been absorbing the views of scholars in residence who visit for weeks to months, a rich source of information reflected in the book's contents. *Human* is organized into four parts: The first describes some of the genetic, cellular, and behavioral ways in which humans may be unique and sets the stage for the subsequent sections, which emphasize cognition and the brain. The second and third parts treat topics ranging from morality to empathy to art and conclude with two chapters discussing consciousness. The fourth part provides a view to the future, exploring such possibilities as brain-machine interfaces and artificial intelligence. Roughly speaking, the book becomes more speculative, and tackles tougher topics, the further on one reads.

Although the majority of topics that Gazzaniga discusses in the book are contentious, many of them highly so, his treatment of them is scholarly and balanced. No grand conclusions are drawn, and he does not offer specific theories of his own so much as survey those of others. The book is also highly accessible, quite a feat given its scope and density. Brief interludes provide the science background for those who need it. For instance, the last chapter includes, sandwiched between discussions of fyborgs (functional cyborgs) and cyborgs, a wonderful 5-page introduction to cellular neurophysiology to help readers understand what follows. Each chapter also ends with a brief conclusion, which summarizes the main points. The author is clearly someone who has written textbooks and knows how to teach.

Human
The Science Behind What Makes Us Unique
by Michael S. Gazzaniga
Ecco (HarperCollins), New York, 2008. 461 pp. $27.50, C$29.50, £14.99. ISBN 9780060892883.

Perhaps not surprisingly, Gazzaniga favors a modular view of the mind informed by evolutionary psychology, a view he previously advocated in *The Social Brain* (*1*) and one in line with people he frequently cites (Steven Pinker, Leda Cosmides, John Tooby; the latter two colleagues of his at UCSB). Modules make fun reading and serve to quantize the exposition. But how do they work together? The penultimate chapter tackles the issue of how various modules coordinate their activity and selectively contribute to the contents of our integrated conscious experience. It begins with a brief reminiscence of how the author once lost consciousness as an intoxicated college student (he was at the time a member of the original Animal House at Dartmouth) and quickly moves on to survey some of the most popular theories and review his own. In one of his early books [(*2*), co-authored with his student Joseph LeDoux], he introduced readers to [a] the Interpreter[o]: a left-hemisphere mechanism that analyzes our actions, integrates the outputs from many modules, and generates a narrative that constitutes our stream of conscious experience. Yet Gazzaniga clearly notes that our ability to consciously experience the world is shared with many other animals, even though the nature of human consciousness may be unique.

So what are the aspects of cognition that make humans unique? Gazzaniga considers a long list: control over our thoughts, emotions, and actions; planning into the future; self-reflection and self-consciousness; language; aspects of imitation and social learning; episodic memory; imagination; creativity; cooperation and altruism; theory of mind; and many more. Trying to find a single theme that ties all these together or subsumes them is daunting. Nor is it clear whether these are differences in degree or in kind. Gazzaniga does not attempt an answer here, although he hints at one in the book's short Afterword: [a] Just like other animals, we are constrained by our biology. ¼ But the ability to wish or imagine that we can be better is notable. No other species aspires to be more than it is. Perhaps we can be.[o] This ability to step outside of ourselvesÐ to view the world and us in it from arbitrarily abstract perspectivesÐ does indeed seem uniquely human, and it cuts across many of the specific abilities in the above list. It makes us responsible for our actions and inactions in a way that other animals are not. It is our burden and yet offers hope for our species and our planet.

Human delivers what the best popular science writing should. Gazzaniga tackles the most difficult questions, provides an expert survey of the field, and, most important, instills a sense of wonder and enjoyment about the subject matter. Lay readers and young scientists alike should benefit, and perhaps our species will too.

References
1. M. S. Gazzaniga, *The Social Brain: Discovering the Networks of the Mind* (Basic, New York, 1985).
2. M. S. Gazzaniga, J. E. LeDoux, *The Integrated Mind* (Plenum, New York, 1978).

10.1126/science.1169620

The reviewer is in the Division of Humanities and Social Sciences 228-77, California Institute of Technology, 1200 East California Avenue, Pasadena, CA 91125, USA. E-mail: radolphs@hss.caltech.edu

Published by AAAS

PHYSICS

Learning and Scientific Reasoning

Comparisons of Chinese and U.S. students show that content knowledge and reasoning skills diverge.

Lei Bao,[1]* Tianfan Cai,[2] Kathy Koenig,[3] Kai Fang,[4] Jing Han,[1] Jing Wang,[1] Qing Liu,[1] Lin Ding,[1] Lili Cui,[5] Ying Luo,[6] Yufeng Wang,[2] Lieming Li,[7] Nianle Wu[7]

The development of general scientific abilities is critical to enable students of science, technology, engineering, and mathematics (STEM) to successfully handle open-ended real-world tasks in future careers (*1*±*6*). Teaching goals in STEM education include fostering content knowledge and developing general scientific abilities. One such ability, scientific reasoning (*7*±*9*), is related to cognitive abilities such as critical thinking and reasoning (*10*±*14*). Scientific-reasoning skills can be developed through training and can be transferred (*7*, *13*). Training in scientific reasoning may also have a long-term impact on student academic achievement (*7*). The STEM education community considers that transferable general abilities are at least as important for students to learn as is the STEM content knowledge (*1*±*4*). Parents consider science and mathematics to be important in developing reasoning skills (*15*).

We therefore asked whether learning STEM content knowledge does in fact have an impact on the development of scientific-reasoning ability. The scientific-reasoning ability studied in this paper focuses on domain-general reasoning skills such as the abilities to systematically explore a problem, to formulate and test hypotheses, to manipulate and isolate variables, and to observe and evaluate the consequences.

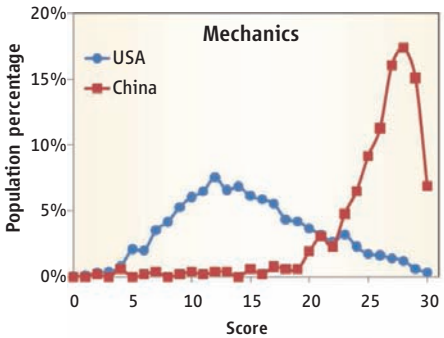

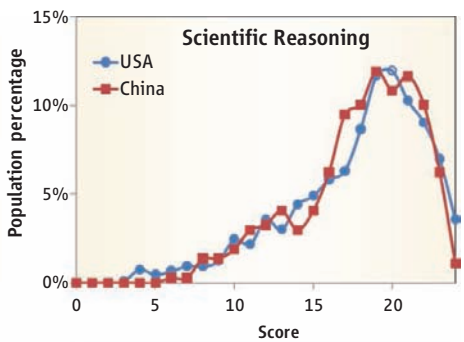

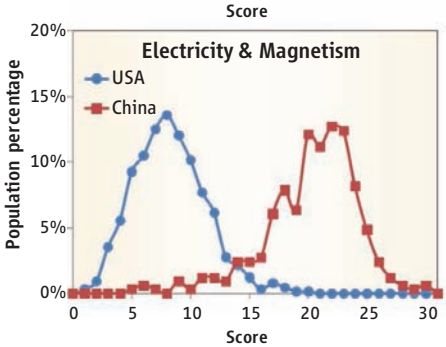

TEST SCORES (%)			
Test	*China (n)*	*USA (n)*	*Effect size*
FCI	85.9 ± 13.9 (523)	49.3 ± 19.3 (2681)	1.98
BEMA	65.6 ± 12.8 (331)	26.6 ± 10.0 (650)	3.53
LCTSR	74.7 ± 15.8 (370)	74.2 ± 18.0 (1061)	0.03

Content knowledge and reasoning skills diverge. Comparisons of U.S. and Chinese freshmen college students show differences on tests of physics content knowledge but not on tests of scientific reasoning.

Research Design

Students in China and the United States go through very different curricula in science and mathematics during their kindergarten through 12th grade (K±12) school years. This provides systemically controlled long-term variation on STEM content learning, which we used to study whether or not such learning has any impact on the development of scientific-reasoning ability. Scientific reasoning is not explicitly taught in schools in either country.

In China, K±12 education is dominated by the nationwide college admission exam given at the end of grade 12. To comply with the requirements of this exam, all Chinese schools adhere to a national standard within all courses. In physics, for example, every student goes through the same physics courses, which start in grade 8 and continue every semester through grade 12, providing 5 years of continuous training on introductory physics topics (*16*). The courses are algebra-based with emphasis on development of conceptual understanding and skills needed to solve problems.

In contrast, K±12 physics education in the United States is more varied. Although students study physics-related topics within other general science courses, only one of three high school students enrolls in a two-semester physics course (*17*). As a result, the amount of instructional time and the amount of emphasis on conceptual physics understanding and problem-solving skills are very different in the two countries. Similar curriculum differences between the United States and China are reflected in other STEM areas such as chemistry, biology, and mathematics (*16*).

Chinese students go through rigorous problem-solving instruction in all STEM subject areas throughout most of their K±12 school years and become skillful at solving content-based problems. It remains unclear, however, whether this training is transferable beyond the specific content areas and problem types taught.

We used quantitative assessment instruments (described below) to compare U.S. and Chinese students' conceptual understanding in physics and general scientific-reasoning ability. Physics content was chosen because the subject is conceptually and logically sophisticated and is commonly emphasized in science education (*15*). Assessment data were collected from both Chinese and U.S. freshmen college students before college-level physics instruction. In this way the data reflect students' knowledge

[1]Department of Physics, The Ohio State University, Columbus, OH 43210, USA. [2]Department of Physics, Beijing Jiaotong University, Beijing 100044, China. [3]Department of Physics, Wright State University, Dayton, OH 45435, USA. [4]Department of Physics, Tongji University, Shanghai 200092, China. [5]Department of Physics, University of Maryland, Baltimore County, Baltimore, MD 21250, USA. [6]Department of Physics, Beijing Normal University, Beijing 100875, China. [7]Department of Physics, Tsinghua University, Beijing 100084, China.

*Author for correspondence. E-mail: bao.15@osu.edu

Published by AAAS

and skill development from their formal and informal K±12 education experiences.

Data Collection and Analysis

From the early 1980s, researchers and educators in psychology and cognitive science (*11*±*14*) have developed many quantitative instruments that assess reasoning ability. Some are included as components in standard assessments such as the Graduate Record Examination, whereas others are stand-alone tests such as Lawson's *Classroom Test of Scientific Reasoning* (LCTSR) (*8*, *9*). We used the LCTSR because of its popularity among STEM educators and researchers. Common categories of reasoning ability assessments include proportional reasoning, deductive and inductive reasoning, control of variables, probability reasoning, correlation reasoning, and hypothesis evaluation, all of which are crucial skills needed for a successful career in STEM.

Research-based standardized tests that assess student STEM content knowledge are also widespread. For example, in physics, education research has produced many instruments. We used the *Force Concept Inventory* (FCI) (*18*, *19*) and the *Brief Electricity and Magnetism Assessment* (BEMA) (*20*). These tools are regularly administered by physics education researchers and educators to evaluate student learning of specific physics concepts.

Using FCI (mechanics), BEMA (electricity and magnetism), and LCTSR (scientific reasoning), we collected data (see figure, page 586) from students (N = 5760) in four U.S. and three Chinese universities. All the universities were chosen to be of medium ranking (*15*). The students tested were freshmen science and engineering majors enrolled in calculus-based introductory physics courses. The tests were administered before any college-level instruction was provided on the related content topics. The students in China used Chinese versions of the tests, which were first piloted with a small group of undergraduate and graduate students (n = 22) to remove language issues.

The FCI results show that the U.S. students have a broad distribution in the medium score range (from 25 to 75%). This appears to be consistent with the educational system in the United States, which produces students with a blend of diverse experiences in physics learning. In contrast, the Chinese students had all completed an almost identical extensive physics curriculum spanning five complete years from grade 8 through grade 12. This type of education background produced a narrow distribution that peaks near the 90% score.

For the BEMA test, the U.S. students have a narrow distribution centered a bit above the chance level (chance 20%). The Chinese students also scored lower than their performance on the FCI, with the score distribution centered around 70%. The lower BEMA score of students in both countries is likely due to the fact that some of the topics on the BEMA test (for example, Gauss's law) are not included in standard high school curricula.

The FCI and BEMA results suggest that numerous and rigorous physics courses in the middle and high school years directly affect student learning of physics content knowledge and raise students to a fairly high performance level on these physics tests.

The results of the LCTSR test show a completely different pattern. The distributions of the Chinese and U.S. students are nearly identical. Analyses (*15*) suggest that the similarities are real and not an artifact of a possible ceiling effect. The results suggest that the large differences in K±12 STEM education between the United States and China do not cause much variation in students' scientific-reasoning abilities. The results from this study are consistent with existing research, which suggests that current education and assessment in the STEM disciplines often emphasize factual recall over deep understanding of science reasoning (*2*, *21*±*23*).

What can researchers and educators do to help students develop scientific-reasoning ability? Relations between instructional methods and the development of scientific reasoning have been widely studied and have shown that inquiry-based science instruction promotes scientific-reasoning abilities (*24*±*29*). The current style of content-rich STEM education, even when carried out at a rigorous level, has little impact on the development of students' scientific-reasoning abilities. It seems that it is not what we teach, but rather how we teach, that makes a difference in student learning of higher- order abilities in science reasoning. Because students ideally need to develop both content knowledge and transferable reasoning skills, researchers and educators must invest more in the development of a balanced method of education, such as incorporating more inquiry-based learning that targets both goals.

Our results also suggest a different interpretation of assessment results. As much as we are concerned about the weak performance of American students in TIMSS and PISA (*30*, *31*), it is valuable to inspect the assessment outcome from multiple perspectives. With measurements on not only content knowledge but also other factors, one can obtain a more holistic evaluation of students, who are indeed complex individuals.

References and Notes

1. R. Iyengar *et al*., *Science* **319**, 1189 (2008).
2. A. Y. Zheng *et al*., *Science* **319**, 414 (2008).
3. B. S. Bloom, Ed., *Taxonomy of Educational Objectives: The Classification of Educational Goals, Handbook I: Cognitive Domain* (David McKay, New York 1956).
4. National Research Council (NRC), *National Science Education Standards* (National Academies Press, Washington, DC, 1996).
5. NRC, *Learning and Understanding: Improving Advanced Study of Mathematics and Science in U.S. High Schools* (National Academies Press, Washington, DC, 2002).
6. H. Singer, M. L. Hilton, H. A. Schweingruber, Eds., *America s Lab Report* (National Academies Press, Washington, DC, 2005).
7. P. Adey, M Shayer, *Really Raising Standards: Cognitive Intervention and Academic Achievement* (Routledge, London, 1994).
8. A. E. Lawson, *J. Res. Sci. Teach*. **15**, 11 (1978).
9. Test used in this study was *Classroom Test of Scientific Reasoning*, rev. ed. (2000).
10. P. A. Facione, *Using the California Critical Thinking Skills Test in Research, Evaluation, and Assessment* (California Academic Press. Millbrae, CA, 1991).
11. H. A. Simon, C. A. Kaplan in *Foundations of Cognitive Science*s, M. I. Posner, Ed. (MIT Press, Cambridge, MA, 1989), pp. 1 47.
12 R. E. Nisbett, G. T. Fong, D. R. Lehman, P. W. Cheng, *Science* **238**, 625 (1987).
13. Z. Chen, D. Klahr, *Child Dev.* **70**, 1098 (1999).
14. D. Kuhn, D. Dean, *J. Cognit. Dev.* **5**, 261 (2004).
15. See Supporting Online Material for more details.
16. This is based on the Chinese national standards on K 12 education (www.pep.com.cn/cbfx/cpml/).
17. J. Hehn, M. Neuschatz, *Phys. Today* **59**, 37 (2006).
18. D. Hestenes, M. Wells, G. Swackhamer, *Phys. Teach.* **30**, 141 (1992).
19. The test used in this study is the 1995 version.
20. L. Ding, R.Chabay, B. Sherwood, R. Beichner, *Phys. Rev. ST Phys. Educ. Res.* **2**, 010105 (2006).
21. M. C. Linn *et al*., *Science* **313**, 1049 (2006).
22. A. Schoenfeld, *Educ. Psychol.* **23**, 145 (1988).
23. A. Elby, *Am. J. Phys*. **67**, S52 (1999).
24. C. Zimmerman, *Dev. Rev.* **27**, 172 (2007).
25. P. Adey, M. Shayer, *J. Res. Sci. Teach.* **27**, 267 (1990).
26. A. E. Lawson, *Science Teaching and the Development of Thinking* (Wadsworth, Belmont, CA, 1995).
27. R. Benford, A. E. Lawson, *Relationships Between Effective Inquiry Use and the Development of Scientific Reasoning Skills in College Biology Labs* (Arizona State University, Tempe, AZ, 2001); Educational Resources Information Center (ERIC) accession no. ED456157.
28. E. A. Marek, A. M. L. Cavallo, *The Learning Cycle and Elementary School Science* (Heinemann, Portsmouth, NH, 1997).
29. B. L. Gerber, A. M. Cavallo, E. A. Marek, *Int. J. Sci. Educ.* **23**, 5359 (2001).
30. Trends in International Mathematics and Science Study (TIMSS), http://nces.ed.gov/timss/.
31. Programme for International Student Assessment (PISA), www.pisa.oecd.org/.

32. We wish to thank all the teachers who helped with this research.

Supporting Online Material

www.sciencemag.org/cgi/content/full/323/5914/586/DC1

10.1126/science.1167740

Published by AAAS

CELL BIOLOGY

The Force Is with Us

Through changes in protein conformation and interactions, cells sense and respond to forces at their point of attachment to extracellular matrix.

Martin A. Schwartz

The ability of cells and tissues to respond to mechanical force is central to many aspects of biology. Areas relevant to human physiology and disease include development and maintenance of bone, blood vessels, and muscles; regulation of blood pressure; motility of cells; and regulation of cell proliferation (*1*). Mechanosensitive adhesions mediated by membrane proteins called integrins are believed to underlie a number of these behaviors (*2*). Forces applied either by the cells' own cytoskeleton or from external sources induce strengthening of these adhesions and trigger a variety of intracellular signals through these effects. Two papers in this issue, one by Friedland *et al*. on page 642 (*3*) and the other by del Rio *et al*. on page 638 (*4*), increase our understanding of the molecular basis for these phenomena.

Current models for mechanotransduction generally involve alterations in protein conformation by forces (*1*, *5*). Stretch-activated membrane channels, present in cells from all organisms that have been examined, undergo conformational transitions in response to changes in membrane tension. For cytoskeletal and extracellular matrix proteins that form linear polymers, tension is thought to cause partial or complete unfolding of domains, exposing new binding sites or other motifs. The extracellular matrix protein fibronectin is the best-studied example. Fibronectin requires tension to assemble into fibrils (*6*, *7*), and fluorescence resonance energy transfer measurements showed that fibronectin in fibrils is in an extended state (*8*). Stretching fibronectin exposes a cryptic binding site in the first type III domain, leading to associations between fibronectin proteins that promote fibril formation (*6*).

Integrins are one link in a connection that runs from extracellular matrix proteins such as fibronectin across the plasma membrane to the actin cytoskeleton. Integrins form this connection in part by binding the cytoskeletal protein talin, which binds actin directly, as well as by recruiting the cytoskeletal protein vinculin, which also binds actin (*9*). Because every component in this chain experiences tension, each one is in principle a potential mechanotransducer.

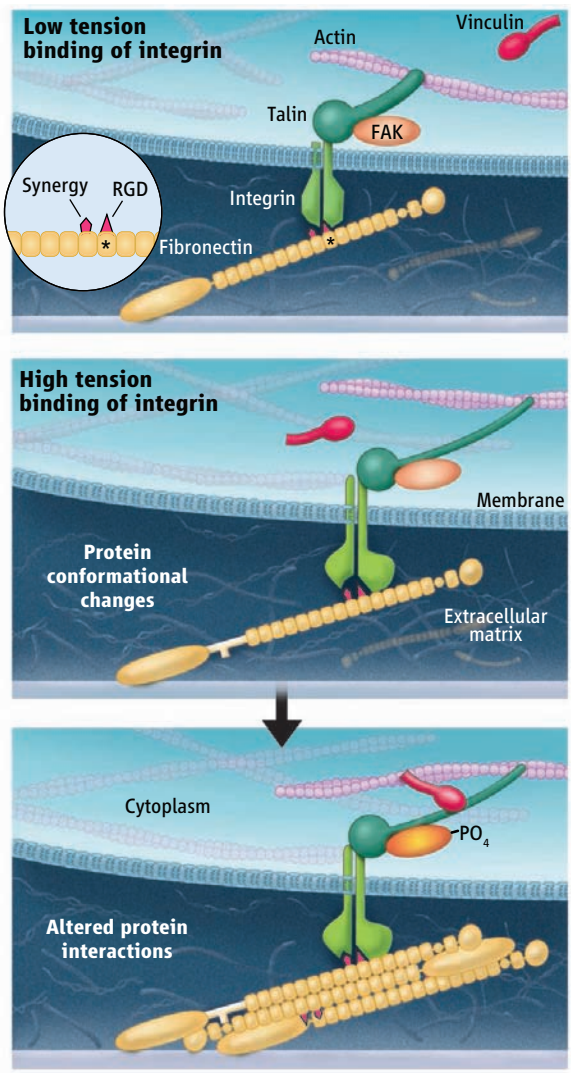

Force mechanics. At points of cell attachment to extracellular matrix, when tension is low, integrin $\alpha_5\beta_1$ binds to the RGD sequence in fibronectin. The cytoplasmic domain of integrin $\alpha_5\beta_1$ is associated with talin, but most vinculin binding sites on talin are inaccessible. Increased tension triggers conformational changes in the integrin, talin, and fibronectin. These alterations reveal new vinculin binding sites in talin, enhance the affinity of $\alpha_5\beta_1$ for the synergy site in fibronectin, and reveal new self-association sites in fibronectin. These changes lead to increased vinculin binding to talin, tighter binding of the integrin to fibronectin, increased fibronectin matrix assembly, and activation of FAK. These events may also promote increased clustering of integrins.

CREDIT: K. SUTLIFF/*SCIENCE*

The best-defined response of integrin-dependent cell adhesions to tension is reinforcement of the adhesions to resist the applied force (*2*). These responses occur over several time scales. Over tens of seconds, vinculin is recruited to small adhesions, most likely without recruitment of additional integrins (*10*). Over a few minutes, adhesions grow larger and lengthen in the direction of the applied force (*11*), which appears to involve recruitment of additional integrins. Indeed, application of force by stretching elastic substrata triggers conversion of unoccupied, low-affinity integrins to a high-affinity state, which induces new binding to the extracellular matrix (*12*). These reinforcement mechanisms may also mediate changes in downstream signaling. Indeed, the activity of focal adhesion kinase (FAK), a tyrosine kinase that transduces multiple signals from integrins, requires actin- and myosin-dependent tension (*13*).

Friedland *et al*. provide evidence that the major fibronectin-binding integrin, $\alpha_5\beta_1$, undergoes a force-dependent conformational transition. This conclusion is based on the ability of integrin $\alpha_5\beta_1$ to be chemically cross-linked to fibronectin. Force is required for conversion of the bond from a non±cross-linkable to a cross-linkable state, suggesting a change in proximity of key residues. Integrin $\alpha_5\beta_1$ binds to two sites in fibronectin: an Arg-Gly-Asp (RGD) sequence in the 10th type III repeat and a secondary (so-called) synergy site in the 9th repeat (*7*) (see the figure). Friedland *et al*. also show that conversion to the cross-linkable state requires the synergy site and that these events correlate with phosphorylation (thus, activation) of FAK. The picture that emerges from these results is that initial low-tension binding of integrin $\alpha_5\beta_1$ to fibronectin involves association of the integrin with the RGD sequence, which under force converts to a higher-strength, more readily cross-linked bond that involves the synergy site. Only this second conformation can activate FAK and transmit downstream signals.

Talin is the focus of the study by del Rio *et al*. It binds directly to the β_1 inte-

Departments of Microbiology, Cell Biology, and Biomedical Engineering, Cardiovascular Research Center and Mellon Urological Cancer Research Institute, University of Virginia, Charlottesville, VA 22908, USA. E-mail: maschwartz@virginia.edu

Published by AAAS

grin cytoplasmic domain and forms one of the links to actin. Talin binding is also crucial in the conversion of low-affinity to high-affinity integrins (*14*) and in the recruitment of vinculin to sites of adhesion (*2*). Interestingly, the talin rod domain contains multiple vinculin binding sites, but in the intact molecule, most of these sites are buried among bundles of α helices. Indeed, these structural data led to the prediction that unfolding of the talin rod domain under force might expose these cryptic sites to recruit vinculin (*15*). Because vinculin can also connect to actin, it would reinforce the link between the integrin and the cytoskeleton. Using single-molecule techniques, del Rio *et al*. show that application of force at the piconewton level results in unfolding of the talin rod domain and binding of vinculin, thus confirming this key prediction.

The advances made by Friedland *et al*. and del Rio *et al*. will facilitate answering a number of long-standing questions about integrin-mediated mechanotransduction. What is the precise nature of the force-activated conformation of the integrin and how does this conformation promote FAK activation? It's also not yet clear how recruitment of vinculin to talin mediates downstream signaling, or whether there are other intracellular components recruited to newly exposed binding sites in talin that mediate these functions. Finally, does altered integrin binding to fibronectin directly affect fibronectin matrix assembly, or does this occur through the previously described unfolding of fibronectin domains under force and subsequent self-association (*6*)? Growing evidence suggests that the entire adhesion apparatus functions as a force-transducing and -sensing machine. These two studies bring us several steps closer to understanding its detailed dynamics.

References

1. A. W. Orr, B. P. Helmke, B. R. Blackman, M. A. Schwartz, *Dev. Cell* **10**, 11 (2006).
2. A. D. Bershadsky, N. Q. Balaban, B. Geiger, *Annu. Rev. Cell Dev. Biol.* **19**, 677 (2003).
3. J. C. Friedland, M. H. Lee, D. Boettiger, *Science* **323**, 642 (2009).
4. A. del Rio *et al.*, *Science* **323**, 638 (2009).
5. V. Vogel, *Annu. Rev. Biophys. Biomol. Struct.* **35**, 459 (2006).
6. C. Zhong *et al.*, *J. Cell Biol.* **141**, 539 (1998).
7. I. Weirzbicka-Patynowski, J. E. Schwarzbauer, *J. Cell Sci.* **116**, 3269 (2003).
8. G. Baneyx, L. Baugh, V. Vogel, *Proc. Natl. Acad. Sci. U.S.A.* **99**, 5139 (2002).
9. K. Burridge, M. Chrzanowska-Wodnicka, *Annu. Rev. Cell Dev. Biol.* **12**, 463 (1996).
10. C. G. Galbraith, K. M. Yamada, M. P. Sheetz, *J. Cell Biol.* **159**, 695 (2002).
11. D. Riveline *et al.*, *J. Cell Biol.* **153**, 1175 (2001).
12. A. Katsumi, T. Naoe, T. Matsushita, K. Kaibuchi, M. A. Schwartz, *J. Biol. Chem.* **280**, 16546 (2005).
13. R. W. Tilghman, J. T. Parsons, *Semin. Cancer Biol.* **18**, 45 (2008).
14. S. Tadokoro *et al.*, *Science* **302**, 103 (2003).
15. D. R. Critchley, *Biochem. Soc. Trans.* **33**, 1308 (2005).

10.1126/science.1169414

MATERIALS SCIENCE

Transforming Graphene

Synthesis of a new material by the hydrogenation of graphene offers the opportunity for wider device applications.

Alex Savchenko

Hydrogenation is a process in which an added hydrogen atom bonds to another atom by sharing its only electron with this atom. Organic chemists use hydrogenation to convert unsaturated into saturated fats and to transfer alkenes into alkanes (*1*). On page 610 of this issue, Elias *et al.* (*2*) show that a similar process can also be realized in condensed matter physics. Incorporating hydrogen into grapheneÐ a single layer of carbon atoms arranged in a hexagonal crystal lattice and the thinnest material conducting electricityÐ transforms it into graphane, a new material whose physical properties are very different from those of graphene.

A graphene layer can be separated from a crystal of graphite by a peeling process while preserving its crystal structure and excellent electrical conduction (*3*). Furthermore, its electrical conduction can be tunedÐ similar to that of a field-effect transistorÐ by putting it on a substrate and varying the density of mobile particles (electrons and holes) by applying a voltage between the layer and substrate. The unique physical and electrical properties of graphene allow not only the experimental testing of fundamental principles of quantum physics but also the fabrication of new devices for future carbon-based nanoelectronics (*4*).

Unlike in conventional semiconductors, the conducting electrons and holes in graphene are massless and behave like photons. In addition, there is no gap between the two energy bands in which the electrons and holes are located. Therefore, the electrical conductance of graphene is nonzero, even when the voltage between the layer and substrate is tuned so that there are no free charged particles in the graphene layer (*4*). Some device applications, however, require a gap between the two bands. One way to create such a gap is to cut a narrow ribbon from the graphene sheet with a width of less than 100 nanometers, thereby confining the electrons and holes to a ª quantum boxº and splitting the energies of the two bands (*5*, *6*). Such cutting

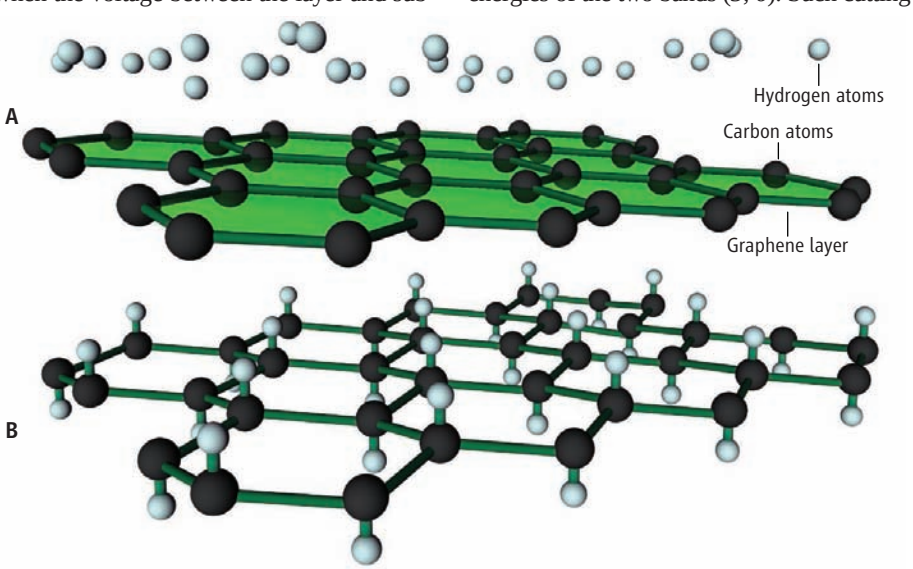

Graphene hydrogenation. (**A**) A graphene layer, where delocalized electrons are free to move between carbon atoms, is exposed to a beam of hydrogen atoms. (**B**) In nonconductive graphane, the hydrogen atoms bond their electrons with electrons of carbon atoms and pull the atoms out of the plane.

CREDIT: P. HUEY/*SCIENCE*

School of Physics, University of Exeter, Exeter EX4 4QL, UK. E-mail: a.k.savchenko@exeter.ac.uk

Published by AAAS

can modify further the properties of graphene, because the dangling electron bonds at the ribbon edges are chemically active and can capture elements from the environment (*7*).

The surface of graphene is thought to be relatively inert. The electrons that are not part of the bonds between carbon atoms in the plane are shared between all atoms. It is these mobile electrons that are responsible for electrical conduction. In a recent theoretical study, Sofo *et al.* predicted that hydrogenation of the graphene surface should create a stable material, graphane, with a large energy band (*8*). In hydrogenated graphene, alternating carbon atoms are pulled out of the plane in opposite directions by the attached hydrogen atoms (see the figure, panel B). This atomic arrangement resembles that in diamond, a nonconductive form of carbon with a large energy gap. In hydrogenated graphene, though, the size of the gap can be controlled by varying the amount of hydrogen on its surface (*9*).

Elias *et al.* present the first experimental demonstration that graphane can be synthesized, showing that the surface of graphene is chemically active and that the energy gap can be produced without cutting graphene into a ribbon. The authors also show that the chemical modification of graphene is reversible; the original properties of graphene can be largely restored by annealing the hydrogenated samples at high temperatures.

Adding atomic hydrogen to graphene is not a simple task: Hydrogenation first requires breaking apart the diatomic molecules of hydrogen gas; this is why hydrogenation in chemistry is usually performed with a hot catalyst. Instead, Elias *et al.* exposed the graphene samples to a hydrogen plasma discharge, in which the hydrogen gas is dissociated into hydrogen ions (see the figure, panel A). The sample has to be placed some distance from the plasma discharge to avoid mechanical damage of graphene by energetic ions.

The emergence of the energy gap manifests itself in the electrical conductance, which becomes strongly temperature dependent. It shows an exponential dependence corresponding to so-called electron "hopping." Such dependence has been seen in thin electron layers confined within semiconductors with an energy gap, such as silicon (*10*) and gallium arsenide (*11*). Although in pristine graphene, electrons are free to move across the crystal, the presence of the gap after hydrogenation forces them to "hop" from one site to another, and this conduction mechanism is much more efficient at higher temperatures.

Another direct confirmation of the modification due to hydrogenation is provided by the diffraction image of the new crystal lattice in transmission electron microscopy, where a noticeable decrease of the separation between the carbon atoms caused by the pulling effect of hydrogen atoms is seen. Raman spectroscopy, which is sensitive to the vibrations of the atoms in the crystal lattice (phonons), also shows the evolution of the lattice during hydrogenation.

The demonstration of reversible hydrogenation of graphene is an important step in expanding the device applications for this exciting material. There will be a search for optimal ways of graphene hydrogenation, including chemical methods: Recently there has been a study of graphene hydrogenation using dissociation of a hydrogen-rich material deposited on graphene (*12*). Future research should aim at using graphene for hydrogen storage in hydrogen-fuel technologies, because graphane has a very high hydrogen density (*8*). This extremely thin material with an energy gap is also likely to find use in nanoelectronics. But research will probably not be limited to adding only hydrogen to graphene. Elias *et al.* show that the graphene surface can be used as a base for creating new materials, and it will be interesting to study the effects of incorporating other elements into its structure.

References

1. R. O. C. Norman, D. J. Waddington, *Modern Organic Chemistry* (Collins Educational, London, 1995).
2. D. C. Elias *et al*. *Science* **323**, 610 (2009).
3. K. S. Novoselov *et al.*, *Science* **306**, 666 (2004).
4. K. S. Novoselov, A. K. Geim, *Nat. Mater.* **6**, 183 (2007).
5. M. Y. Han, B. Özyilmaz, Y. Zhang, P. Kim, *Phys. Rev. Lett.* **98**, 206805 (2007).
6. X. Li, X. Wang, L. Zhang, S. Lee, H. Dai, *Science* **319,** 1229 (2008).
7. T. Wassmann, A. P. Seitsonen, A. M. Saitta, M. Lazzeri, F. Mauri, *Phys. Rev. Lett.* **101**, 096402 (2008).
8. J. O. Sofo, A. S. Chaudhari, G. D. Barber, *Phys. Rev. B* **75**, 153401 (2007).
9. D. W. Boukhvalov *et al.*, *Phys. Rev. B* **77**, 035427 (2008).
10. M. Pepper, S. Pollitt, C. J. Adkins, R. E. Oakeley, *Phys. Lett. A* **47**, 71 (1974).
11. E. I. Laiko *et al.*, *Sov. Phys. JETP* **66**, 1258 (1987).
12. S. Ryu *et al.*, *Nano Lett*. **8**, 4597 (2008).

10.1126/science.1169246

PHYSICS

An Abnormal Normal State

Gregory S. Boebinger

A metallic phase of a high-temperature superconductor reveals unexpected properties in the zero-temperature limit.

High-temperature cuprate superconductors were discovered in 1986, yet many properties of these materials remain unexplained. When confronted with a new material with complicated behavior, physicists often map out its "phase diagram"; they plot the different phases assumed by the material (solid, liquid, gas, magnet, metal, insulator, and many more complicated versions of these) as a function of thermodynamic parameters (including temperature, pressure, magnetic field, and number of charge carriers). In the phase diagram of the cuprates, the superconducting phase is not the only one that is lacking a clear theoretical basis. Several "normal" insulating and metallic phases form at higher temperatures or in high magnetic fields that are also puzzling. The unusual way in which the electrical resistivity changes with temperature in these "normal" phases could provide clues to the mechanism of electron pairing in the superconducting phase.

National High Magnetic Field Laboratory, Florida State University, Tallahassee, FL 87545, USA. E-mail: gsb@magnet.fsu.edu

On page 603 of this issue, Cooper *et al.* (*1*) use high magnetic fields to suppress the superconducting state in a cuprate, $La_{2-x}Sr_xCuO_4$, which extends the study of the resistivity of its metallic phase to lower temperatures. The Cooper *et al.* data fail to support the standard working model phase diagram for the cuprates: that a quantum phase transition between the insulating and metallic phases occurs at a single point (*2*, *3*). Instead, the results add to the list of strange cuprate behaviors.

The only well-understood phase of the cuprates, an antiferromagnet, has no transition to the superconducting phase (see the figure, panel A). As strontium doping adds holes to the system, the static magnetism of the antiferromagnet gives way to magnetic fluctuations. There is a broad consensus that these magnetic fluctuations provide the pairing mechanism required for superconductivity in the cuprates. The development of a detailed theory of high-temperature superconductivity might benefit from understanding how magnetic fluctuations manifest themselves in the nearby normal phases. In particular, electrical resistivity provides insights into how electrons scatter in the material, and different scattering mecha-

Published by AAAS

nisms give rise to characteristic temperature dependences of the resistivity.

In the underdoped region (fewer holes than optimal for superconductivity), a "messy insulating phase" forms that is not yet understood. Unlike a normal insulator, this phase does not have a true energy gap that prevents electrons from reaching the conduction band. In this phase, a dramatic suppression of the density of states at low energies robs electrons of the states they use to move through the material, making them prone to localization and correlated behavior that arise from the Coulomb and magnetic interactions between electrons.

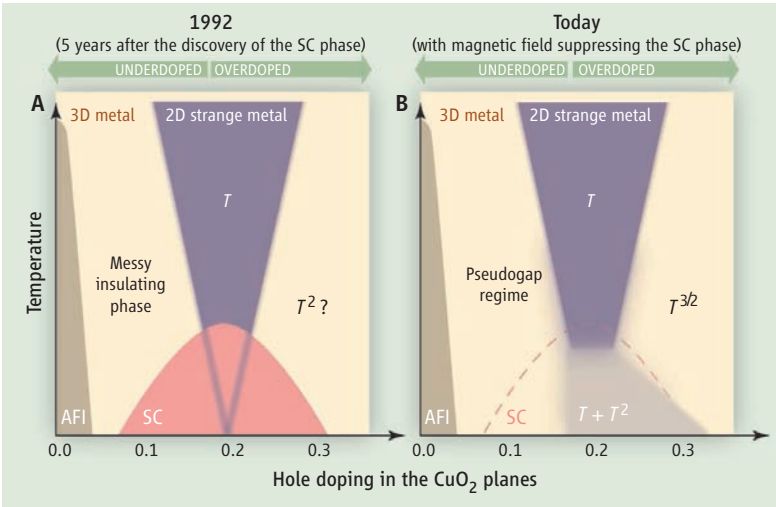

The evolving cuprate phase diagram. (**A**) Schematic phase diagram of the high-temperature superconductors from 1992. The solid lines delineating the antiferromagnetic insulator (AFI) and superconducting (SC) phases are the only true phase transitions, the extent of the other regimes remaining ill-defined. The doping level for optimum superconductivity is the same as for the strange metal. The temperature dependence depicted refers to resistivity, as described in the text. (**B**) The phase diagram presented by Cooper *et al.* when sufficiently intense magnetic fields suppress the superconducting phase. The boundary of the suppressed superconducting phase is shown with a dashed line. A much broader strange metal regime forms at low temperatures than had been expected (the region labeled $T + T^2$)

The electron transport is two-dimensional (2D); the electron momentum is not isotropic but is largely restricted to the copper-oxygen planes. When magnetic fields suppress superconductivity, the resistivity, ρ, of the pseudogap state at low temperatures increases logarithmically with decreasing temperature (T). This characteristic feature of the pseudogap state has been observed in several of the cuprates, but it is not yet understood in terms of an electron-scattering mechanism. (*4*).

In the overdoped region, the three-dimensional (3D) metallic phase also shows an unexpected temperature dependence. Instead of ρ changing as T^2, as expected for electrons scattering off other electrons, it follows a curious T^{32} behavior (*5*).

Between the messy insulator and 3D metal, in the region of optimum hole doping for superconductivity, lies the "2D strange metal" (see the figure, panel A). In early studies, samples exhibiting the highest superconducting transition temperature displayed a normal-state resistivity that varied linearly in T (*6*). This observation has been borne out by more recent systematic studies (*7*). The linear ρ±T relation extends over such a large temperature range with such striking precision (*8*, *9*) that understanding its origin might lead to an understanding of the mechanism of high-temperature superconductivity.

The temperature dependence of the resistivity of the normal states is unusual but not totally unprecedented. Similarities have long been noted between the high-temperature superconductors and the heavy fermion systems, in which magnetic fluctuations are also believed to cause superconductivity and in which the role of electron conduction is better understood. The phase diagrams are similar (*10*), and the 3D resistivity in heavy fermion systems arising from magnetic fluctuations varies as $T^{3/2}$ (*11*), just as in the 3D metal regime of the high-temperature superconductors.

The heavy fermions exhibit a zero-temperature quantum phase transition that is normally obscured by the superconducting phase but that can be revealed by applying a strong magnetic field to suppress the superconductivity. Much of the interest in examining the low-temperature limiting behavior of the normal state in the high-temperature superconductors is to see whether they exhibit a similar zero-temperature quantum phase transition near optimum doping.

In this model, there should be a single point in the low-temperature normal stateÐ a particular degree of hole dopingÐ that marks the location of a quantum phase transition. This point would be found by extrapolating the 2D strange metal regime to zero temperature (see the figure, panel A). The linear dependence of ρ with T might then be caused by critical fluctuations that extend to high temperatures. Many physical quantities, such as specific heat and the Knight shift, suggest that there might be such a phase transition (*3*). Anomalies in the Hall coefficient observed near optimum doping might be direct evidence of such a transition (*12*, *13*) because the Hall coefficient is sensitive to changes in the electronic density of states that would be expected to change at the quantum phase transition between the 2D pseudogap state and the 3D metallic state.

Through a systematic study of resistivity in overdoped samples, Cooper *et al.* now shed a different light on the abnormal normal state of the high-temperature superconductors. Instead of a single point at which the resistivity shows linear-T behavior, Cooper *et al.* argue that the resistivity should not be interpreted as a single power-law dependence on T, but rather as a mixture of linear-T behavior and T^2 behavior throughout the right-hand side of the superconducting dome, once superconductivity is suppressed by high magnetic fields (see the figure, panel B). Resistivity consistent with a sum of T and T^2 terms down to low temperatures had been noted previously at a single point in the 3D metal regime (*14*). However, Cooper *et al.* report the first systematic study of many samples throughout this entire regime.

A linear-T component existing over a broad range of doping is a challenge to the prevailing thinking that the converging boundaries of the 2D strange metal would extrapolate in the zero-temperature limit to a quantum phase transition at a single specific doping. To paraphrase *Alice in Wonderland*, the abnormal normal state gets curiouser and curiouser.

References

1. R. A. Cooper *et al.*, *Science* **323**, 603 (2009); published online 11 December 2008 (10.1126/science.1165015).
2. G. S. Boebinger *et al.*, *Phys. Rev. Lett.* **77**, 5417 (1996).
3. J. L. Tallon, J. W. Loram, *Physica* C **349**, 53 (2001).
4. Y. Ando, G. S. Boebinger, A. Passner, T. Kimura, K. Kishio, *Phys. Rev. Lett.* **75**, 4662 (1995).
5. H. Takagi *et al.*, *Phys. Rev. Lett.* **69**, 2975 (1992).
6. H. L. Stormer *et al.*, *Phys. Rev. B* **38**, 2472 (1988).
7. Y. Ando *et al.*, *Phys. Rev. Lett.* **93**, 267001 (2004).
8. S. Martin, A. T. Fiory, R. M. Fleming, L. F. Schneemeyer, J. V. Waszczak, *Phys. Rev. Lett.* **60**, 2194 (1988).
9. S. Martin, A. T. Fiory, R. M. Fleming, L. F. Schneemeyer, J. V. Waszczak, *Phys. Rev. B* **41**, 846 (1990).
10. N. D. Mathur *et al.*, *Nature* **394**, 39 (1998).
11. P. Gegenwart *et al.*, *Physica* C 408-410, 157 (2004).
12. F. F. Balakirev *et al.*, *Nature* **424**, 912 (2003).
13. F. F. Balakirev *et al.*, *Phys. Rev. Lett.* **102**, 017004 (2009).
14. A. P. Mackenzie, S. R. Julian, D. C. Sinclair, C. T. Lin, *Phys. Rev. B* **53**, 5848 (1996).

10.1126/science.1168952

Published by AAAS

PLANT SCIENCE

Pores in Place

Signals that control plant cell division and fate also control epidermal pore development and gas exchange.

Fred D. Sack and Jin-Gui Chen

The plant shoot epidermis is studded with stomata, pores (each surrounded by a pair of guard cells) that regulate gas and water vapor exchange between plants and the atmosphere. Stomata develop through unequal cell divisions, but the mechanisms that establish this polarity and regulate cell fate are mostly unknown (*1*). On page 649 of this issue, Cartwright *et al.* identify a receptor that positions cell divisions with respect to adjacent cells (*2*). And a recent study by Lampard *et al.* shows that stomatal number is regulated by the phosphorylation of a specific transcription factor (*3*).

Because a plant cell is surrounded by a wall of carbohydrates, the position of the two daughter cells that arise from cell division depends on the position of the new cell wall that forms to separate the cytoplasm, two new nuclei, and other cellular constituents. This wall placement can involve communication between adjacent cells. In maize, for example, subsidiary mother cells produce cells that flank stomata at maturity. This relationship is established when young flanking cells are positioned next to the stomatal precursor cell (guard mother cell) (*4*). This suggests that the guard mother cell broadcasts signals to the subsidiary mother cells to orient unequal division (see the figure). Other polarities develop within neighbor cells as well, including nuclear migration and the formation of cytoskeletal (actin) patches close to the guard mother cell. But the specific regulators that establish polarity across plant cells are still poorly understood.

The *PANGLOSS1* (*PAN1*) gene was identified by screening for mutant maize plants that disrupt stomatal development (*4*). *PAN1* is required to orient nuclear migration, actin distribution, and asymmetric cell division (*2*, *4*). It encodes a transmembrane, receptor-like kinase that is preferentially localized in the subsidiary mother cells next to the guard mother cell. The polar distribution of PAN1 develops before nuclear and actin polarization and cell division. Thus, PAN1 likely perceives cues from the guard mother cell that orient subsidiary mother cell polarity and division. Other receptors, such as ERECTA (ER) and TOO MANY MOUTHS (TMM) in the plant *Arabidopsis thaliana*, also orient asymmetric cell division in stomatal development (*5*, *6*). Like PAN1, TMM likely orients the division axis in response to intercellular cues (*6*). But unlike PAN1, TMM is dispensable for asymmetric division and is distributed throughout the cell. Thus, PAN1 seems to be a novel plant example of a cell-intrinsic receptor protein polarized by extrinsic cues (*7*). How PAN1 acts is unclear, given that it lacks apparent kinase activity as well as critical amino acids present in functional kinases. But it might function in a network, as it is required for the phosphorylation of another membrane protein.

In *Arabidopsis*, protein phosphorylation is essential for stomatal development via a mitogen-activated protein kinase (MAPK) cascade, a phosphorylation signal amplification pathway that here includes YODA and MPK3/6 kinases (*8*, *9*). This signaling pathway restricts stomatal initiation, because loss-of-function mutations in components of the pathway induce excess stomata. However, neither the target of the stomatal pathway MAPK nor that of any developmentally related MAPK cascade in plants was known before the work of Lampard *et al.* (*3*). Two sets of transcription factorsÐ proteins that regulate the expression of target genesÐ have been shown to control cell fate in the stomatal pathway (*10*±*13*). One such factor is SPEECHLESS (SPCH), because *spch* mutations block stomatal initiation (*10*, *11*).

Lampard *et al.* (*3*) recently showed that SPCH is a substrate of MPK3/6 and that its phosphorylation limits the number of divisions initiated by SPCH. SPCH is therefore required for stomatal formation, whereas the MAPK cascade limits stomatal output. Together they constitute a core module that integrates positive and negative signals to regulate stomatal frequency (see the figure). It is possible, but not shown, that an ER receptor kinase complex restricts divisions by triggering the MAPK cascade. Thus, the first developmental MAPK substrate to be identified in plants is one that

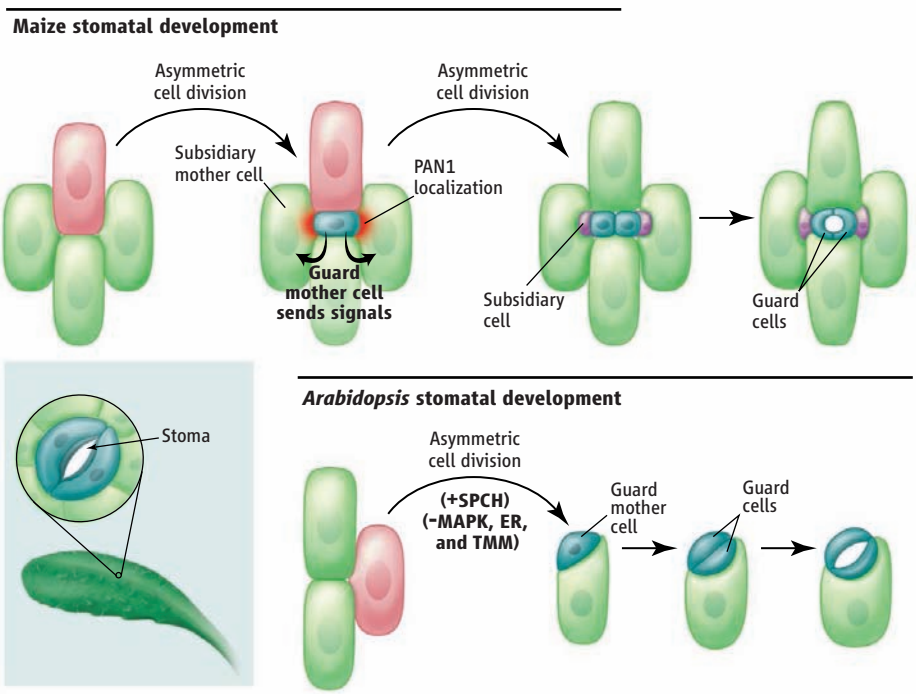

Division control. In maize, unequal division of an epidermal cell (pink) produces a guard mother cell (blue), which sends signals to adjacent subsidiary mother cells that polarize the distribution of the protein PAN1 (red). PAN1 is required for orienting division of the subsidiary mother cells so that the smaller daughter cells (purple) flank the stomata. In *Arabidopsis*, stomatal initiation starts when an epidermal cell (pink) divides unequally. Initiation is promoted by SPCH and restricted by a MAPK signaling pathway. Final stomatal number depends on the extent of phosphorylation of SPCH by MAPK.

CREDIT: K. SUTLIFF/*SCIENCE*

Department of Botany, University of British Columbia, Vancouver, BC V6T 1Z4, Canada. E-mail: fsack@interchange.ubc.ca; jingui@interchange.ubc.ca

Published by AAAS

produces an adaptive number of stomata and helps put them in their place. This stomatal module might be widespread, given that *SPCH*-like genes are present in grasses and other plants.

Collectively, the studies by Cartwright *et al*. and Lampard *et al*. (*3*) reveal mechanisms that control plant cell fate specification and division polarization. Questions outstanding include the nature of intercellular cues that polarize PAN1, how PAN1 coordinates polar cell division and cell fate allocation, and how a MAPK cascade that controls many different plant processes specifically regulates stomatal development.

Life on Earth depends in no small part on stomata that control plant evaporative cooling and CO_2 uptake for photosynthesis, thereby influencing global water and carbon cycling. Pangloss pontificated in Voltaire's *Candide* that [a]this is the best of all possible worlds.[o] It is fitting that his eponymous protein and the loquacious SPEECHLESS make this planet lush and green.

References

1. D. C. Bergmann, F. D. Sack, *Annu. Rev. Plant Biol.* **58**, 163 (2007).
2. H. N. Cartwright, J. A. Humphries, L. G. Smith, *Science* **323**, 649 (2009).
3. G. R. Lampard, C. A. MacAlister, D. C. Bergmann, *Science* **322**, 1113 (2008).
4. K. Gallagher, L. G. Smith, *Curr. Biol.* **10**, 1229 (2000).
5. E. D. Shpak, J. M. McAbee, L. J. Pillitteri, K. U. Torii, *Science* **309**, 290 (2005).
6. J. A. Nadeau, F. D. Sack, *Science* **296**, 1697 (2002).
7. C. A. ten Hove, R. Heidstra, *Curr. Opin. Plant Biol.* **11**, 34 (2008).
8. D. C. Bergmann, W. Lukowitz, C. R. Somerville, *Science* **304**, 1494 (2004).
9. H. Wang, N. Ngwenyama, Y. Liu, J. C. Walker, S. Zhang, *Plant Cell* **19**, 63 (2007).
10. C. A. MacAlister, K. Ohashi-Ito, D. C. Bergmann, *Nature* **445**, 537 (2007).
11. K. Ohashi-Ito, D. C. Bergmann, *Plant Cell* **18**, 2493 (2006).
12. L. J. Pillitteri, D. B. Sloan, N. L. Bogenschutz, K. U. Torii, *Nature* **445**, 501 (2007).
13. M. M. Kanaoka *et al*., *Plant Cell* **20**, 1775 (2008).

10.1126/science.1169553

BIOCHEMISTRY

Unfolding the Secrets of Calmodulin

Researchers have now observed in real time how a single molecule of calmodulin refolds and how it binds to a ligand.

Robert B. Best,[1] Gerhard Hummer[2]

Single-molecule experiments are providing an increasingly detailed picture of the function of biomolecules and their assemblies. By watching one molecule at a time, one can observe phenomena that would be lost in macroscopic measurements averaged over large numbers of molecules. Force spectroscopy is particularly well suited to probe changes in biomolecular conformation (*1*±*4*). Like other single-molecule methods (*5*), it monitors the distance between two sites in a macromolecule, but in addition, a variable pulling force is coupled to this distance. Because stability is roughly exponentially sensitive to applied force, conformational equilibria can be probed over a wide free-energy range.

On page 633 of this issue, Junker *et al*. (*1*) report the use of atomic force microscopy (AFM) to explore the force-dependent kinetics of calmodulin folding and ligand binding. Calmodulin, a calcium ion (Ca^{2+})±sensing protein ubiquitous in eukaryotes, contains two Ca^{2+}-binding domains connected by a flexible linker. Upon Ca^{2+} binding, the domains open and partially expose their hydrophobic interior. This conformational change enables binding to various targets involved in biological processes ranging from apoptosis to muscle contraction (*6*).

Junker *et al*. elucidate calmodulin's conformational dynamics at unprecedented resolution. In addition to the now familiar [a]saw-tooth[o] patterns in the force-extension curves, in which a sharp drop of the force indicates unfolding, the authors directly observe refolding of the protein: They record a remarkable succession of unfolding and folding events near the rupture point, where previously only a single unfolding event would have been recorded. The observation of refolding was made possible by operating closer to equilibrium, taking advantage of improved instrument stability. Together with optical tweezers (*2*, *3*) and force-clamp AFM (*4*), this technique is part of a new generation of force-spectroscopy experiments for observing continuous dynamical trajectories close to equilibrium.

The ability to watch folding or binding dynamics in real time opens the way for direct observations of molecular reaction mechanisms as a sequence of structural events along the microscopic pathways (*5*). In a classical analysis of bulk experiments that probe changes in population of metastable species, a reaction mechanism would be inferred from the combined effects of perturbations (such as mutations) on the kinetics and thermodynamics (*7*). For example, macroscopic kinetic measurements have shown that ribonuclease H folds via a stable intermediate (*8*). However, these experiments did not reveal whether the intermediate was on the pathway between the unfolded and folded states or was an off-pathway trap. A single-molecule optical-tweezer experiment demonstrated an on-pathway intermediate by directly observing transitions between the three states near equilibrium (*2*).

Junker *et al*. now provide new insights into the mechanisms of

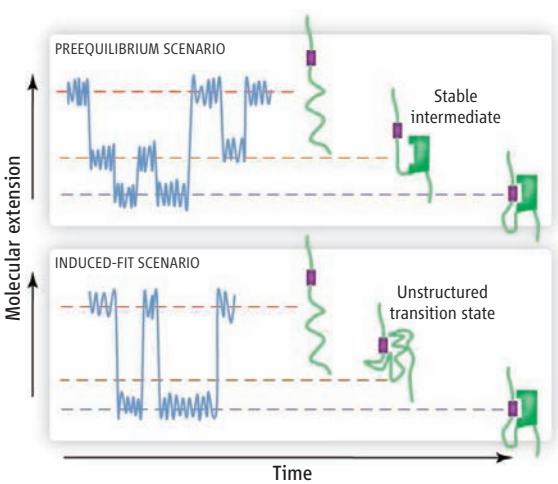

Mechanisms of coupled folding and binding. These schematic trajectories portray the extension of a protein (green) with a covalently attached ligand (purple) as a function of time. In a preequilibrium scenario, folding precedes binding, resulting in an intermediate; Junker *et al.* observed this scenario for binding of the MLCK peptide to calmodulin. In contrast, in an induced-fit scenario, binding and folding would occur together via an unstructured transition state; Junker *et al*. deduced this scenario for the binding of Ca^{2+} at high concentrations.

[1]Department of Chemistry, University of Cambridge, Lensfield Road, Cambridge CB2 1EW, UK. [2]Laboratory of Chemical Physics, National Institute of Diabetes and Digestive and Kidney Diseases (NIDDK), National Institutes of Health, Bethesda, MD 20892, USA. E-mail: gerhard.hummer@nih.gov

Published by AAAS

coupled folding and binding, a central issue in the function of natively unstructured proteins (*9*±*11*). Calmodulin has long served as a textbook example of the preequilibrium scenario in ligand binding (see the figure). In this scenario, unbound proteins are predominantly in the ligand-free ([a] apo[o]) structure. However, ligands bind not to these apo structures, but to a preexisting small population of [a] holo-like[o] proteins that are structurally similar to the ligand-bound ([a] holo[o]) state. In the case of calmodulin, the folded apo and holo-like states are in rapid exchange in the absence of Ca^{2+} (*12*, *13*), and peptide ligands and Ca^{2+} are thought to bind to the already folded holo-like structure. By using force to counteract the stabilizing effects of bound Ca^{2+}, Junker *et al*. could resolve folding of the calmodulin carboxyl-terminal domain. Their results imply that the preequilibrium scenario does not hold under all conditions.

The authors find that Ca^{2+} stabilizes the protein by increasing the folding rate without affecting the unfolding rate. Thus, under the conditions of high Ca^{2+} concentration in this study, calmodulin folds by a different pathway, in which folding and Ca^{2+} binding occur together, bypassing the folded Ca^{2+}-free apo and holo-like intermediates. This binding-induced folding (*11*) follows an induced-fit scenario, in which the ligand itself triggers the conformational change (see the figure). At low Ca^{2+} concentration, the preequilibrium mechanism is expected to prevail. These two alternative folding mechanisms have also been seen in molecular simulations (*14*).

By contrast to Ca^{2+} binding, Junker *et al*. find that peptide binding to calmodulin has a different effect on the folding energy landscape. The two peptide ligands that they consider bind only to the folded protein and stabilize it by decreasing the unfolding rate, conforming to a preequilibrium mechanism. To demonstrate this mechanism directly, the authors linked one of the peptides, the calmodulin-binding domain of myosin light-chain kinase, to calmodulin in such a way that binding of the peptide induces a change in length of the protein-ligand construct. They observed an obligatory intermediate corresponding to the folded protein in the absence of the ligand, thus confirming the mechanism inferred from their kinetic measurements: Only in the preequilibrium case would it be possible to observe a distinct binding-competent intermediate before ligand binding (see the figure).

Future single-molecule studies may be able to probe the effect of force on the folding mechanism itself. If the pulling direction is not correlated with the motions along the intrinsic unfolding (or unbinding) route, the mechanism should switch from the intrinsic mechanism at low force to a different mechanism at high force (*15*). This switch may have a role in the mechanical strength of proteins and could make a protein more resistant to unfolding by tensile force. Previous work inferred such a switch by comparing the extrapolation of unfolding kinetics at high force with ensemble measurements at zero force (*16*). The ability to study folding over a wider range of forces opens the possibility of observing this switch directly.

References and Notes

1. J. P. Junker, F. Ziegler, M. Rief, *Science* **323**, 633 (2009).
2. C. Cecconi, E. A. Shank, C. Bustamante, S. Marqusee, *Science* **309**, 2057 (2005).
3. W. J. Greenleaf, K. L. Frieda, D. A. N. Foster, M. T. Woodside, S. M. Block, *Science* **319**, 630 (2008).
4. J. M. Fernandez, H. Li, *Science* **303**, 1674 (2004).
5. B. Schuler, W. A. Eaton, *Curr. Opin. Struct. Biol.* **18**, 16 (2008).
6. M. Ikura, G. M. Clore, A. M. Gronenborn, G. Zhu, C. B. Klee, A. Bax, *Science* **256**, 632 (1992)
7. A. R. Fersht, A. Matouschek, L. Serrano, *J. Mol. Biol.* **224**, 771 (1992).
8. T. M. Raschke, J. Kho, S. Marqusee, *Nat. Struct. Biol*. **6**, 825 (1999).
9. Y. Levy, S. S. Cho, J. N. Onuchic, P. G. Wolynes, *J. Mol. Biol.* **346**, 1121 (2005).
10. K. Sugase, H. J. Dyson, P. E. Wright, *Nature* **447**, 1021 (2007).
11. A. G. Turjanski, J. S. Gutkind, R. B. Best, G. Hummer, *PLoS Comp. Biol.* **4**, e1000060 (2008).
12. N. Tjandra, H. Kuboniwa, H. Ren, A. Bax, *Eur. J. Biochem.* **230**, 1014 (1995).
13. A. Malmendal, J. Evenäs, S. Forsén, M. Akke, *J. Mol. Biol.* **293**, 883 (1999).
14. Y.-G. Chen, G. Hummer, *J. Am. Chem. Soc.* **129**, 2414 (2007).
15. R. B. Best, E. Paci, G. Hummer, O. K. Dudko, *J. Phys. Chem. B* **112**, 5968 (2008).
16. P. M. Williams *et al.*, *Nature* **422**, 446 (2003).

17. R.B.B. is supported by a Royal Society University Research Fellowship. G.H. acknowledges support by the intramural research program of the NIDDK, NIH. We thank A. Bax, W. A. Eaton, and A. Szabo for their comments on the manuscript.

10.1126/science.1169555

ECOLOGY

The Key to Pandora s Box

When desert locusts meet up, their nervous systems release serotonin, which causes them to become mutually attracted, a prerequisite for swarming.

P. A. Stevenson

On page 627 of this issue, Anstey *et al*. (*1*) describe how social encounters between desert locusts promote release of the neurochemical serotonin, which turns out to be both sufficient and necessary for switching their behavior from mutual avoidance to aggregationÐ a prerequisite for building swarms of migrating plague locusts. This finding advances our understanding of how social interactions implement behavioral adaptations. Further research on amine-containing neurons and their interactions with other messenger system±orchestrating behavior in insects could lead to new pest control strategies.

The notorious desert locust *Schistocerca gregaria* lives mostly an inconspicuous solitary existence, cryptic in color (green) and behavior, avoiding others and flying alone at nighttime. This changes dramatically when, under favorable climatic conditions and flourishing vegetation, their numbers explode, triggering a striking transformation to the crowded, gregarious phase (*2*, *3*). Bright yellow in color, the locusts now attract each other, forming bands of marching hoppers and eventually swarms comprising billions of voracious plague locusts that are tuned for long-distance migration and mass devastation of crops. This change is highly complex and encompasses many morphological, physiological, and behavioral features controlled by numerous chemical messengers (*2*, *3*) and involving more than 500 genes (*4*). Until now, however, no single agent has been identified as primarily responsible for transforming the meek solitary phase into the swarming gregarious phase.

The breakthrough by Anstey *et al*. caps a series of investigations coordinated mostly by Stephen Simpson in collaboration with Malcolm Burrows (*5*±*8*). From observational data of hundreds of locusts, the authors constructed a mathematical model for assessing an individual's degree of gregariousness based on walking speed and time spent near other locusts, motionless or grooming. The results

Institute for Biology II, Faculty for Biosciences, Psychology and Pharmacology, Leipzig University, Talstrasse 33, 04103 Leipzig, Germany. E-mail: stevenson@rz.uni-leipzig.de

Published by AAAS

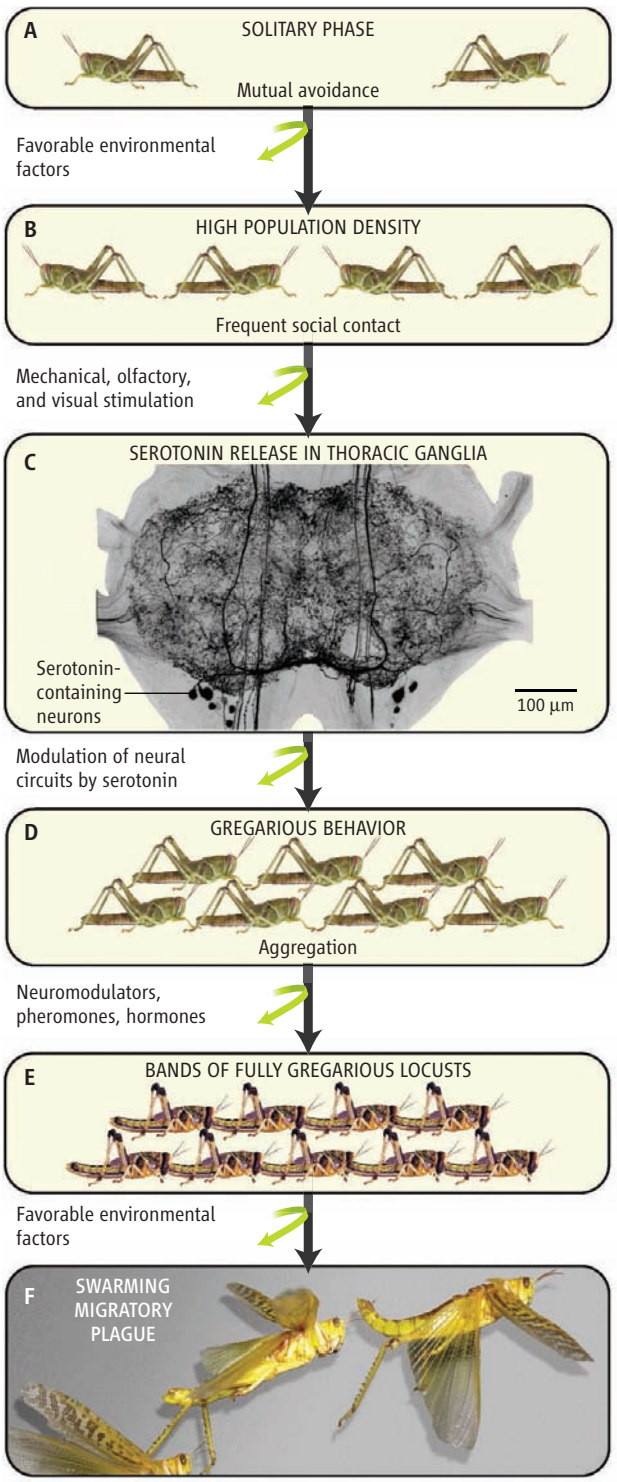

CREDITS: LOCUST CARTOONS IN PANELS A, D, AND E, FROM (*1*); PHOTOMICROGRAPH IN PANEL C, P. A. STEVENSON/UNIVERSITY OF LEIPZIG; PHOTOGRAPH IN PANEL F, E. BUHL/UNIVERSITY OF LEIPZIG

Serotonin s role in locust swarming. (**A**) Solitary locusts are scarce and avoid each other. (**B**) Under favorable climatic conditions, population density and hence social contact increases. (**C**) As shown by Anstey *et al*., the resulting mechanical, olfactory, and visual stimuli induce serotonin release, possibly from neurons in the thoracic nervous system (arrow). (**D**) Serotonin promotes gregarious behavior and aggregation (*1*), presumably by selectively modulating specific neuronal circuits (*7*, *8*). (**E**) Crowding recruits additional chemical messengers, leading to acquisition of all gregarious traits, including color change from green to yellow (*2*, *3*). (**F**) Environmental factors (such as drought or food shortage) promote swarming and migration of adult gregarious locusts (*2*, *3*).

revealed that solitary locusts exhibit full gregarious behavior within only 2 hours of enforced crowding. Gregarious behavior was also induced by the mere sight and smell of other locusts, and most effectively by simply stroking touch-sensitive hairs on a leg or stimulating the leg nerve electrically. Regardless of how it was induced, the degree of gregariousness was greater in locusts with more serotonin in their nervous system. Furthermore, treatment with this amine, its precursor, or receptor agonists induced gregarious behavior in solitary locusts, whereas serotonin receptor antagonists and synthesis inhibition prohibited it.

Serotonin is thus sufficient and necessary for inducing gregarious behavior (see the figure). Hence, serotonin is the key that turns the behavior of solitary locusts from mutual repulsion to attraction, a prerequisite for swarming of gregarious locusts and opening Pandora's Box.

Will this insight lead to more effective pest control measures? In the short term, probably not. To be effective, antiserotonin-like chemicals would need to be applied when the animals are solitary locusts and scarce targets in vast expanses of desert (about three locusts per 100 m^2). Current serotonergic drugs are not designed for passing through the insect cuticle and sheath encasing the nervous system, nor are they insect-selective, hence their use is ecologically unjustifiable.

Nonetheless, the new insights into the mechanism underlying locust phase change harbors considerable potential. But first we need to know more. The first insect serotonin receptor was cloned in fruit flies 17 years ago (*9*), but still little is known about the function and pharmacology of the different receptor subtypes in other insects. Serotonin-containing neurons were identified in locusts 25 years ago (*10*), and although they comprise only five cell pairs in each thoracic compartment of the nervous system (see the figure, panel C), their function and connectivity are unknown. Can these neurons drive the complete process of gregarization? How does serotonin interact with other messengers controlling phase polymorphism? Can gregarious locusts be chemically reconverted to the solitary phase, as can occur naturally after prolonged isolation?

Clues will also probably emerge from investigating other behavioral roles of amines in insects. Serotonin-induced aggregation of locusts is analogous to suppressing escape behavior by serotonin in other insects (*11*) and arthropods, where its effect depends on social status (*12*). This and many other actions of serotonin are opposed by octopamine, the invertebrate's adrenaline, which regulates the decisions to fight, retreat, or court in crickets and fruit flies (*11*, *13*, *14*) and to rest or forage in cockroaches and honey bees (*15*, *16*) by biasing the operation of neural circuits (*17*). Complete understanding of locust phase change, and with it viable solutions for pest control, will thus depend on continued basic research on all aspects of insect biology, where the aim is to discover how animals adapt to ensure survival in the face of changing environmental conditions.

References

1. M. L. Anstey, S. M. Rogers, S. R. Ott, M. Burrows, S. J. Simpson, *Science* **323**, 627 (2009).
2. M. P. Pener, Y. Yerushalmi, *J. Insect Physiol.* **44**, 365 (1998).
3. S. W. Applebaum, Y. Heifetz, *Annu. Rev. Entomol*. **44**, 317 (1999).
4. L. Kang *et al*., *Proc. Natl. Acad. Sci. U.S.A.* **101**, 17611 (2004).
5. P. Roessingh, S. J. Simpson, S. James, *Proc. R. Soc. London Ser. B* **252**, 43 (1993).
6. S. J. Simpson, E. Despland, B. F. Hagele, T. Dodgson, *Proc. Natl. Acad. Sci. U.S.A.* **98**, 3895 (2001).
7. S. M. Rogers *et al*., *J. Exp. Biol.* **206**, 3991 (2003).
8. S. M. Rogers *et al*., *J. Exp. Biol.* **207**, 3603 (2004).
9. R. Hen, *Trends Pharmacol. Sci*. **13**, 160 (1992).
10. N. M. Tyrer, J. D. Turner, J. S. Altman, *J. Comp. Neurol.* **227**, 313 (1984).
11. P. A. Stevenson, V. Dyakonova, J. Rillich, K. Schildberger, *J. Neurosci.* **25**, 1431 (2005).
12. D. H. Edwards, S.-R. Yeh, B. E. Musolf, B. L. Antonsen, F. B. Krasne, *Brain Behav. Evol.* **60**, 360 (2002).
13. S. C. Hoyer *et al*., *Curr. Biol.* **18**, 159 (2008).
14. S. J. Certel, M. G. Savella, D. C. F. Schlegel, E. A. Kravitz, *Proc. Natl. Acad. Sci. U.S.A.* **104**, 4706 (2007).
15. D. Wicher, *Endocr. Metab. Immune Disord. Drug Targets* **7**, 304 (2007).
16. D. J. Schulz, A. B. Barron, G. E. Robinson, *Brain Behav. Evol*. **60**, 350 (2002).
17. F. Libersat, H.-J. Pflüger, *Bioscience* **54**, 17 (2004).

10.1126/science.1169280

Published by AAAS

PROFILE

Agre: A New Era of Science Outreach at Home and Abroad

In the middle years of his career, long before he had won the Nobel Prize for solving a central mystery of cell biology, Peter Agre figured that it would be natural to make a career shift at about the time he turned 50. He would spend more time outside the lab, and he would devote more energy to public service.

Since following through on that plan, Agre has helped found Scientists and Engineers for America, which promotes researchers' involvement in politics and public policy. He brieflyÐ and very publiclyÐ considered running for the U.S. Senate. He served as an adviser to a presidential candidate. He even did a late-night TV turn on *The Colbert Report.*

Agre is planning to expand his role as an ambassador for science when he becomes president of AAAS in February. Because climate change and the financial crisis open the door to an era of innovation and transformation, he sees an opportune moment for researchers to reach out to schoolchildren and their teachers, local and national policymakers, and S&T colleagues overseas.

[a] Scientists have been so worried about getting funded that they probably have not invested as much as they should in terms of public awareness,[o] Agre said in a recent interview. [a] But it seems to me that every tenured faculty in America owes something, and my idea would be tithing 10% of your time for the public good¼ .I think being part of the public debate is very importantÐ and that's where we're overdue.[o]

It's impossible to understand Agre's work without understanding his youth in Minnesota. His father, a chemist, brought his children to the lab on weekends and set up simple experiments for them. Agre, with his brother Jim, became an Eagle Scout. He did get a D in chemistry during his senior year of high schoolÐ an anomaly he attributes to the distractions and rebellion of late adolescence.

Now 60, his medical experience and research give him enormous credibility in the policy world, and that's enhanced by his easy-going, self-effacing manner. In 1970, he graduated from Augsburg College in Minneapolis with a degree in chemistry. Four years later, he received his M.D. from Johns Hopkins; it was there, he says, that he became committed to biomedical research. After clinical training at Case Western University Hospitals in Cleveland and postgraduate medical training at the University of North Carolina at Chapel Hill, he returned to Hopkins.

Peter Agre

In 2003, Agre won the Nobel Prize in Chemistry for his team's 1991 discovery of aquaporinsÐ channels that allow water molecules to pass through cell membranes, a process essential to life. (He shared the prize with Roderick MacKinnon of Rockefeller University.)

Heartland values still echo in his outlook. Public service is crucial, he says. Science must respect people's religious beliefs, even when they question scientific findings. He has deep admiration for teachersÐ and he insists they deserve better salaries.

Science teachers [a] are the ones who make science interesting,[o] he said. [a] I remember in my Nobel banquet speech reciting a line that I realized really resonated with the audience: `Early in the life of every scientist, a child's first interest in science was sparked by a teacher.' [o]

Agre was a science adviser to the campaign of Barack Obama, and the new president's respect for science [a] gives me great confidence,[o] he said. [a] Until this economic recession or fear of depression is remedied, there may not be increased budgets¼ But if the government is listening, great things can happen.[o]

Agre will become AAAS president on 17 February, at the end of the AAAS Annual Meeting in Chicago. He succeeds Harvard climate and ocean researcher James J. McCarthy, who will become chair of the AAAS Board of Directors. Already, Agre has had an extensive interview with the *New York Times.*

Though he is a strong public advocate for science, he's not ready to quit the lab. After a stint as vice chancellor for science and technology at Duke University Medical Center, he returned to Hopkins last year to head its Malaria Research Institute.

[a] Science is about new adventures,[o] Agre said. [a] I still have a few years ahead of me, and I don't want to just rest on the past.[o]

SCIENCE POLICY

Obama Taps Past AAAS Leaders for Key S&T Posts

U.S. President Barack Obama has chosen 2006 AAAS President John P. Holdren to serve as his top science adviser and has selected three other distinguished researchers with ties to AAAS for key positions in his administration.

Holdren, a climate and energy scholar at Harvard and director of the Woods Hole Research Center, has been appointed assistant to the president for science and technology and director of the White House Office of Science and Technology Policy.

Oregon State University marine ecologist Jane Lubchenco has been appointed administrator of the National Oceanic and Atmospheric Administration. Lubchenco served as AAAS president in 1997 and received the 2005 AAAS Award for Public Understanding of Science and Technology.

Eric Lander and Harold Varmus, both AAAS Fellows, will join Holdren on the President's Council of Advisors on Science and Technology. Lander, who received the 2004 AAAS Public Understanding award, is a principal leader of the Human Genome Project and founding director of the Broad Institute. Varmus is president and CEO of Memorial Sloan-Kettering Cancer Center and a former director of the National Institutes of Health.

Becky Ham

Published by AAAS

AAAS

Call for Nomination of 2009 AAAS Fellows

AAAS Fellows who are current members of the association are invited to nominate members for election as Fellows. A Fellow is defined as a member [a] whose efforts on behalf of the advancement of science or its applications are scientifically or socially distinguished.[o] A nomination must be sponsored by three AAAS Fellows, two of whom must have no affiliation with the nominee's institution.

Nominations undergo review by the steering groups of the association©sections (the chair, chair-elect, retiring chair, secretary, and four members-at-large of each section). Each steering group reviews only those nominations designated for its section. Names of Fellow nominees who are approved by the steering groups are presented to the AAAS Council for election.

Nominations with complete documentation must be received by 11 May 2009. Nominations received after that date will be held for the following year. The nomination form and a list of current AAAS Fellows can be found at www.aaas.org/aboutaaas/fellows. To request a hard copy of the nomination form, please contact the AAAS Executive Office, 1200 New York Avenue N.W., Washington, DC 20005, USA; at 202-326-6635; or at jarias@aaas.org.

Results of the 2008 Election of AAAS Officers

Following are the results of the 2008 election. Terms begin on 17 February 2009.

General Offices
President-Elect: Alice S. Huang
Board of Directors: Julia M. Phillips, David S. Sabatini
Committee on Nominations: Steven Chu, Susan Hackwood, Sallie Keller-McNulty, Jack Dixon

Section on Agriculture, Food, and Renewable Resources
Chair-Elect: Brian A. Larkins
Member-at-Large: Barbara Valent
Electorate Nominating Committee: Ann M. Hirsch, Mark E. Sorrells
Council Delegate: Daniel J. Cosgrove

Section on Anthropology
Chair-Elect: Clark Spencer-Larsen
Member-at-Large: Carol V. Ward
Electorate Nominating Committee: Anne C. Stone, Dolores R. Piperno

Section on Astronomy
Chair-Elect: Alan P. Boss
Member-at-Large: Donald Campbell
Electorate Nominating Committee: Michael Werner, Giovanni G. Fazio

Section on Atmospheric and Hydrospheric Sciences
Chair-Elect: Alan Robock
Member-at-Large: Kevin E. Trenberth
Electorate Nominating Committee: Margaret (Peggy) LeMone, Jim Coakley

Section on Biological Sciences
Chair-Elect: Trudy Mackay
Member-at-Large: Margaret Werner-Washburne
Electorate Nominating Committee: Joan W. Bennett, Eric Ursell Selker

Section on Chemistry
Chair-Elect: Charles P. Casey
Member-at-Large: Ronald W. Woodard
Electorate Nominating Committee: Brian M. Stoltz, Jonathan A. Ellman

Section on Dentistry and Oral Health Sciences
Chair-Elect: Margarita Zeichner-David
Member-at-Large: Ira B. Lamster
Electorate Nominating Committee: Laurie K. McCauley, Frank A. Scannapieco

Section on Education
Chair-Elect: Joseph Krajcik
Member-at-Large: Jay B. Labov
Electorate Nominating Committee: Suzanne O Connell, Mary Monroe Atwater

Section on Engineering
Chair-Elect: Duncan T. Moore
Member-at-Large: Christine M. Maziar
Electorate Nominating Committee: Kristen Fichthorn, Pradeep K. Khosla
Council Delegate: Gail H. Marcus, James L. Merz

Section on General Interest in Science and Engineering
Chair-Elect: Kathryn D. Sullivan
Member-at-Large: Sharon M. Friedman
Electorate Nominating Committee: Gloria J. Takahashi, Robert J. Griffin

Section on Geology and Geography
Chair-Elect: Malcolm Hughes
Member-at-Large: Jean Lynch-Stieglitz
Electorate Nominating Committee: Timothy Gordon Fisher, Elizabeth A. Canuel

Section on History and Philosophy of Science
Chair-Elect: Richard Creath
Member-at-Large: Heather E. Douglas
Electorate Nominating Committee: Nancy J. Nersessian, Alain Touwaide
Council Delegate: Virginia Trimble

Section on Industrial Science and Technology
Chair-Elect: Jennie C. Hunter-Cevera
Member-at-Large: Harry S. Hertz
Electorate Nominating Committee: Qinghuang Lin, Robert Boily
Council Delegate: Steven W. Popper

Section on Information, Computing, and Communication
Chair-Elect: Bart Selman
Member-at-Large: Julia Gelfand
Electorate Nominating Committee: Christine L. Borgman, Bonnie C. Carol

Section on Linguistics and Language Science
Chair-Elect: David W. Lightfoot
Member-at-Large: Suzanne Flynn
Electorate Nominating Committee: Elizabeth C. Traugott, Douglas H. Whalen

Section on Mathematics
Chair-Elect: Kenneth C. Millett
Member-at-Large: Tony F. Chan
Electorate Nominating Committee: Douglas N. Arnold, Robert M. Fossum

Section on Medical Sciences
Chair-Elect: Judy Lieberman
Member-at-Large: Robert Doms
Electorate Nominating Committee: Beverly Davidson, Wendy C. Brown
Council Delegate: Jennifer M. Puck, James H. Hughes, Etty (Tika) Benveniste, Reed E. Pyeritz, Terence S. Dermody

Section on Neuroscience
Chair-Elect: Michael T. Shipley
Member-at-Large: Gail Mandel
Electorate Nominating Committee: Michael S. Wolfe, Erik D. Herzog

Section on Pharmaceutical Sciences
Chair-Elect: Gary M. Pollack
Member-at-Large: William T. Beck
Electorate Nominating Committee: Craig K. Svensson, Per Artursson

Section on Physics
Chair-Elect: Charles W. Clark
Member-at-Large: Alexander L. Fetter
Electorate Nominating Committee: Elizabeth H. Simmons, Ali Yazdani

Section on Psychology
Chair-Elect: Stephen J. Suomi
Member-at-Large: Jenny Saffran
Electorate Nominating Committee: Denise Park, David Shapiro
Council Delegate: John Gabrieli

Section on Social, Economic, and Political Sciences
Chair-Elect: Eugene A. Rosa
Member-at-Large: Wendy Baldwin
Electorate Nominating Committee: Robert F. Rich, Anil B. Deolalikar
Council Delegate: Nicholas Christakis

Section on Societal Impacts of Science and Engineering
Chair-Elect: Bruce V. Lewenstein
Member-at-Large: Melanie Leitner
Electorate Nominating Committee: Robert M. Simon, Michael L. Telson

Section on Statistics
Chair-Elect: Joel B. Greenhouse
Member-at-Large: Kenneth W. Wachter
Electorate Nominating Committee: Nancy Reid, Mary A. Foulkes

Published by AAAS

Sudden Death of Entanglement

Ting Yu[1]* and J. H. Eberly[2]*

A new development in the dynamical behavior of elementary quantum systems is the surprising discovery that correlation between two quantum units of information called qubits can be degraded by environmental noise in a way not seen previously in studies of dissipation. This new route for dissipation attacks quantum entanglement, the essential resource for quantum information as well as the central feature in the Einstein-Podolsky-Rosen so-called paradox and in discussions of the fate of Schrödinger's cat. The effect has been labeled ESD, which stands for early-stage disentanglement or, more frequently, entanglement sudden death. We review recent progress in studies focused on this phenomenon.

Quantum entanglement is a special type of correlation that can be shared only among quantum systems. It has been the focus of foundational discussions of quantum mechanics since the time of Schrödinger (who gave it its name) and the famous EPR paper of Einstein, Podolsky, and Rosen (*1*, *2*). The degree of correlation available with entanglement is predicted to be stronger as well as qualitatively different compared with that of any other known type of correlation. Entanglement may also be highly nonlocal—e.g., shared among pairs of atoms, photons, electrons, etc., even though they may be remotely located and not interacting with each other. These features have recently promoted the study of entanglement as a resource that we believe will eventually find use in new approaches to both computation and communication, for example, by improving previous limits on speed and security, in some cases dramatically (*3*, *4*).

Quantum and classical correlations alike always decay as a result of noisy backgrounds and decorrelating agents that reside in ambient environments (*5*), so the degradation of entanglement shared by two or more parties is unavoidable (*6*–*9*). The background agents with which we are concerned have extremely short (effectively zero) internal correlation times themselves, and their action leads to the familiar law mandating that after each successive half-life of decay, there is still half of the prior quantity remaining, so that a diminishing fraction always remains.

However, a theoretical treatment of two-atom spontaneous emission (*10*) shows that quantum entanglement does not always obey the half-life law. Earlier studies of two-party entanglement in different model forms also pointed to this fact (*11*–*15*). The term now used, entanglement sudden death (ESD, also called early-stage disentanglement), refers to the fact that even a very weakly dissipative environment can degrade the specifically quantum portion of the correlation to zero in a finite time (Fig. 1), rather than by successive halves. We will use the term "decoherence" to refer to the loss of quantum correlation, i.e., loss of entanglement.

This finite-time dissipation is a new form of decay (*16*), predicted to attack only quantum entanglement, and not previously encountered in the dissipation of other physical correlations. It has been found in numerous theoretical examinations to occur in a wide variety of entanglements involving pairs of atomic, photonic, and spin qubits, continuous Gaussian states, and subsets of multiple qubits and spin chains (*17*). ESD has already been detected in the laboratory in two different contexts (*18*, *19*), confirming its experimental reality and supporting its universal relevance (*20*). However, there is still no deep understanding of sudden death dynamics, and so far there is no generic preventive measure.

How Does Entanglement Decay?

An example of an ESD event is provided by the weakly dissipative process of spontaneous emission, if the dissipation is "shared" by two atoms (Fig. 1). To describe this we need a suitable notation.

The pair of states for each atom, sometimes labeled (+) and (−) or (1) and (0), are quantum analogs of "bits" of classical information, and hence such atoms (or any quantum systems with just two states) are called quantum bits or "qubits." Unlike classical bits, the states of the atoms have the quantum ability to exist in both states at the same time. This is the kind of superposition used by Schrödinger when he introduced his famous cat, neither dead nor alive but both, in which case the state of his cat is conveniently coded by the bracket (+ ⇔ −), to indicate equal simultaneous presence of the opposite + and − conditions.

This bracket notation can be extended to show entanglement. Suppose we have two opposing conditions for two cats, one large and one small, and either waking (W) or sleeping (S). Entanglement of idealized cats could be denoted with a bracket such as [(*Ws*) ⇔ (*Sw*)], where we have chosen large and small letters to distinguish a big cat from a little cat. The bracket would signal via the term (*Ws*) that the big cat is awake and the little cat is sleeping, but the other term (*Sw*) signals that the opposite is also true, that the big cat is sleeping and the little cat is awake.

One can see the essence of entanglement here: If we learn that the big cat is awake, the (*Sw*) term must be discarded as incompatible with what we learned previously, and so the two-cat state reduces to (*Ws*). We immediately conclude that the little cat is sleeping. Thus, knowledge of the state of one of the cats conveys information about the other (*21*). The brackets are symbols of information about the cats' states, and do not belong to one cat or the other. The brackets belong to the reader, who can make predictions based on the information the brackets convey. The same is true of all quantum mechanical wave functions.

Entanglement can be more complicated, even for idealized cats. In such cases, a two-party joint state must be represented not by a bracket as above, but by a matrix, called a density matrix and denoted ρ in quantum mechanics [see (*22*) and Eq. S3]. When exposed to environmental noise, the density matrix ρ will change in time, becoming degraded, and the accompanying change in entanglement can be tracked with a quantum mechanical variable called concurrence (*23*), which is written for qubits such as the atoms *A* and *B* in Fig. 1 as

$$C(\rho) = \max[0, Q(t)] \qquad (1)$$

where $Q(t)$ is an auxilliary variable defined in terms of entanglement of formation, as given explicitly in Eq. S4. $C = 0$ means no entanglement and is achieved whenever $Q(t) \leq 0$, while for

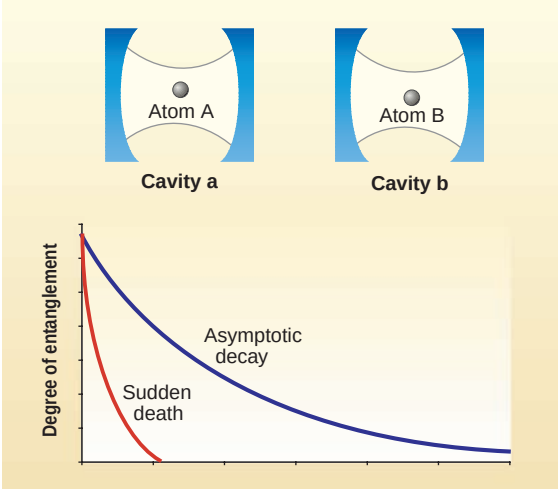

Fig. 1. Curves show ESD as one of two routes for relaxation of the entanglement, via concurrence $C(\rho)$, of qubits *A* and *B* that are located in separate overdamped cavities.

[1]Department of Physics and Engineering Physics, Stevens Institute of Technology, Hoboken, NJ 07030–5991, USA. [2]Rochester Theory Center and Department of Physics and Astronomy, University of Rochester, Rochester, NY 14627–0171, USA.

*E-mail: ting.yu@stevens.edu (T.Y.), eberly@pas.rochester.edu (J.H.E.)

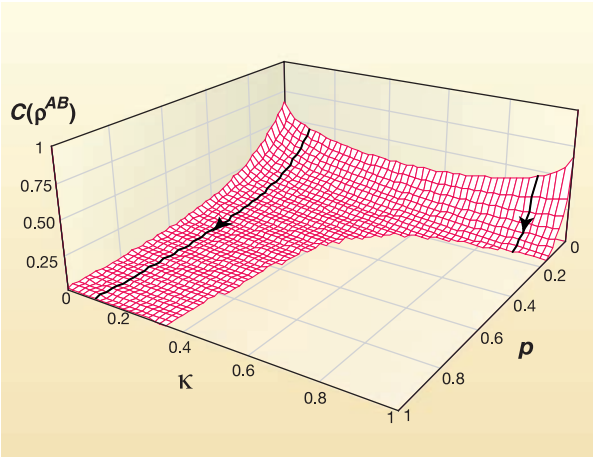

Fig. 2. Atom-atom entanglement is plotted as a function of time for κ values in the range 0 to 1. [Adapted from (*20*)] For all values of κ less than 1/3, the half-life rule is obeyed, but for κ between 1/3 and 1, it is not. For those values, the curves show ESD, i.e., becoming zero in a finite time and remaining zero thereafter. The two curves marked with arrows are similar to the curves in Fig. 1. Time is represented by $p = 1 - \exp(-\Gamma_t)$.

maximally entangled states $C = 1$, and C is limited to the range $1 \geq C \geq 0$.

In the case of spontaneous emission there is no environment at all, except for the vacuum. The vacuum can still have a noisy degrading effect through its quantum fluctuations, which cannot be avoided, so both atoms in Fig. 1 must eventually lose their excitation and come to their ground states with the rate Γ. Then their state is simply (−−), a completely disentangled situation because learning that the state of one atom is (−) does not change our information about the other, also (−). Thus, disentanglement is the eventual fate of the pair.

The question is, how quickly do they meet their fate? For the initial density matrix shown in Eq. S5, the answer is supplied by the surface graphed in Fig. 2, which shows possible pathways for entanglement dissipation as a function of time. The κ axis shows that the time evolution of entanglement depends on the value of the parameter that encodes the initial probability for the two atoms to be in the doubly excited state (++). The two extreme concurrence curves for $\kappa = 1$ and $\kappa = 0$ are the ones already shown in Fig. 1.

The sudden death behavior shown in the right highlighted curve of Fig. 2 is a new feature for physical dissipation (*16*, *20*) and is induced by classical as well as quantum noises (*24*). It is counterintuitive, based on all previous single-atom experience, because spontaneous emission is a process that obeys the half-life rule rigorously for individual atoms. But it turns out that the two-qubit correlation does not follow the one-qubit pattern. That is, the sudden death does not come from a shorter half-life; the entangled joint correlation does not even have the half-life property.

As reported in (*18*), the first experimental confirmation of ESD was made with an all-optical approach focusing on photonic polarization. It was achieved by the tomographic reconstruction of ρ(*t*), and from it the $Q(t)$ variable, and thus the concurrence $C(\rho)$. In the experiment, both amplitude and phase noises that can degrade entanglement were realized by combining beam splitters and mirrors.

Can Sudden Death Be Avoided or Delayed?

The issue of how to avoid ESD-type decorrelation in a realistic physical system is incompletely resolved at this time. A number of methods are known to provide protection against previously known types of decorrelation (*3*). Some methods have classical analogs in information theory. One engages appropriately designed redundancy and is known as quantum error correction. Another relies on using a symmetry that can isolate entanglement from noise, effectively providing a decoherence-free subspace to manage qubit evolution.

Error correction is most useful when the disturbing noise is below some threshold (*25*). In practice error correction can be complicated, because a noisy channel is a dynamical process and its physical features are often not fully understood or predictable. An example is atmospheric turbulence during open-air communication. Another issue is the cost associated with providing redundancy. Additionally, it has been reported that some quantum error correction algorithms could actually promote rather than mitigate ESD (*26*). Symmetries that avoid decoherence by providing isolation from noise during evolution (*27*) have also been examined as a way to postpone or avoid ESD, but knowledge of the noise to be combatted appears unlikely to be available because qubits remote from each other would rarely share either symmetry properties or noise descriptions.

Other methods considered use dynamic manipulation such as mode modulation (*28*) or the quantum Zeno effect (*29*), which can be regarded as extensions of the so-called bang-bang method (*30*). Another proposal is to use feedback control (*31*) to prevent ESD and other decoherence effects in the presence of hostile noise. None of these methods is perfect, but they can be more effective if designed for specific noise avoidance.

Does the Number of Noises Matter?

Nonlocal entanglement raises the issue of ESD triggered by different noise processes and can refer to more than one noise source acting together on colocated entangled qubits, or to independent noise sources acting separately on remotely located members of a qubit pair. The rate of dissipation in the presence of several noise sources is normally the sum of the individual dissipation rates. More explicitly, if decay rates Γ_1 and Γ_2 come from the action of two distinct weak noises, then when the two noises are applied together to a physical system, the resulting relaxation rate is simply given by the sum of the separate rates: $\Gamma_1 + \Gamma_2$.

However, such a long-standing result does not hold for entanglement decay. This was discovered (*16*) by examining entanglement evolution of a set of *X*-form mixed-state matrices (Eq. S3) with $d = 0$, where d is the probability that both qubits are in their ground states. Straightforward calculations for the entire class are shown by the diagrams in Fig. 3, illustrating two qubits exposed together to amplitude noise as well as phase noise. The top two time-dependent curves show that the application of either noise separately allows long-running entanglement decay of the half-life type (no ESD). By contrast, the bottom curve reaches zero in a finite time. That is, the combined effect of the two noises causes ESD. The caption explains the colored squares. This illustrates the "supervulnerability" of paired-qubit entanglement when attacked by different independent noises. This result is universal in the sense that it continues to hold (*16*) even if the two noises attack one of the qubits but not the other, and also if each of the two qubits is remotely attacked by just one of the noises.

Is There an "Anti-ESD" or Rebirth Effect?

Special circumstances are needed to see "anti-ESD," the creation or rebirth of entanglement

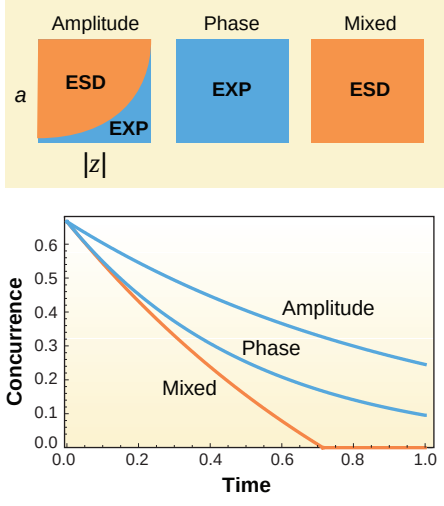

Fig. 3. The top two time-dependent curves show exponential (smooth half-life type) decay of concurrence for a qubit pair exposed to phase noise and to amplitude noise, respectively. The bottom curve shows nonsmooth decay, i.e., ESD occurs for the qubit pair when both noises are acting together. The color-coded squares apply to any two-party *X* matrix (Eq. S3) having $d = 0$. They present the predicted results for the entire accessible physical domain, which means throughout $1 \geq a \geq 0$ and $1 \geq |z| \geq 0$. The blue zones labeled EXP designate domains where smooth exponential (half-life type) evolution occurs, and the orange zones show where ESD occurs. The left and middle squares apply when amplitude and phase noises are applied separately, and have smooth decay regions, while the orange square at right shows that sudden death is universal in the entire region for any *X* matrix (Eq. S3).

from disentangled states. By imposing the right interactions almost anything can be made to happen, but we are concerned with evolution of joint information in a pure sense and focus on two-party entanglement that evolves without mutual interaction or communication.

The same two-atom situation shown in Fig. 1 can be made relevant to anti-ESD. In solving for the surface of solutions plotted in Fig. 2, the cavities were taken as fully overdamped, so that any photon emitted by either atom was irreversibly absorbed by the walls, but they could also be treated as undamped mirror-like cavities, such as used in the Jaynes-Cummings (JC) model for light-atom interactions (*32*). This situation produces a periodic sequence of perfect rebirths of atom *AB* entanglement (*33*, *34*). An early mathematical model of two-qubit evolution (*11*) can be interpreted as treating an underdamped cavity and also shows rebirths.

The panels in the top row of Fig. 4 show rebirth scenarios. They occur for states that are initially of the cat type, such that both atoms are excited and both are un-excited at the same time. The cat-type bracket for them is

$$\Phi_\alpha = [(++)\cos\alpha \Leftrightarrow (--)\sin\alpha] \qquad (2)$$

where different values of sine and cosine produce the different curves in the figure (*35*).

Starting from the photon vacuum state in each cavity, the JC-type evolution will permit only zero or one photon to reside in each cavity at any later time, so each of the two modes is a two-state system (a qubit), and counting the two atoms there are now four qubits on hand. This provides six concurrences that can be computed: C^{AB}, C^{ab}, C^{Ab}, C^{aB}, C^{Aa}, and C^{Bb}, where the capital letters identify atoms and the small letters identify the photons in cavity modes *a* or *b*. Concurrence is defined only for pairs of qubits, not quartets of them, so the label C^{AB} implies that the *a* and *b* degrees of freedom are not available to observation and have been ignored (technically, have been traced out), and for photon concurrence C^{ab} the atomic *A* and *B* properties are traced out, and so on.

This idealized model provides a convenient framework to analyze entanglement in a simplified but still multi-qubit framework. As shown in the top half of Fig. 4, ESD takes place for atom concurrence (in the left panel, almost all C^{AB} curves reach zero and remain zero for finite times). However, in the right panel, the photon concurrence C^{ab} behaves in a manner opposite to that of C^{AB}, showing anti-ESD. That is, initially C^{ab} is zero, but it immediately begins to grow. The photons jointly experience entanglement "sudden birth," but this is followed by ESD a half cycle later. All of this occurs via pure "informatics," i.e., without energy exchange or other interaction between the sites.

The reason for the rebirths is obvious—the photons emitted cannot really get lost among the few joint states available. If a larger number of cavity modes would be provided, a longer time would be needed for a rebirth to be complete, and as a limiting case, the cavities producing the curves in Fig. 2 have an infinite number of modes, so the lost quantum correlation cannot be reborn in any finite time. If there are enough states available in one mode, as is the case for coherent-state mode preparation, then ESD and true long-time revivals are also predicted (*36*).

What Are the Future Prospects?

Quantum memory banks. Clearly, ESD can be largely ignored, to a first approximation, when desirable quantum operations can be manipulated at sufficiently high speed. The key goal of memory is opposite to that of speed, i.e., to preserve quantum state features semi-indefinitely. Quantum memory networks will be sensitive to the consequences if ESD occurs. ESD will probably have to be taken into account if practical versions of quantum memories are built to operate in mixed-state configurations.

Disentanglement control. Over a given noisy channel, it appears that some entangled states may be more robust against the influence of noise than others. To control decoherence optimally, it will be useful to learn how to identify the robust states separately from the fragile ones. Control issues also include the use of external fields to manipulate qubit states (*37*) as in gate operations, to create transient decoherence-free subspaces, as mentioned already. A qualitatively different route to combat decoherence specifically of the ESD type is illustrated in Fig. 2. Two evolution tracks are highlighted to show that for qubits prepared with the same value of initial entanglement, their concurrences may evolve very differently. In that illustration, the right track is subject to ESD, while the left one is not. Decoherence per se is not avoided, because the non-ESD track shows steady dissipation, but it always remains finite. Other examples of this are known, and in some cases a purely local operation (i.e., a manipulation of only one of the two entangled qubits) can be undertaken to change the state matrix ρ without changing its degree of entanglement, but in a way that switches the evolution trajectory from ESD to non-ESD (*38*), effectively putting it on a half-life track as in the figure. Similar studies (*39*) have examined the effect of local operations at intermediate stages of evolution. Use of this method requires detailed knowledge of the state matrix ρ, which may not be practical, particularly at times late in the evolution.

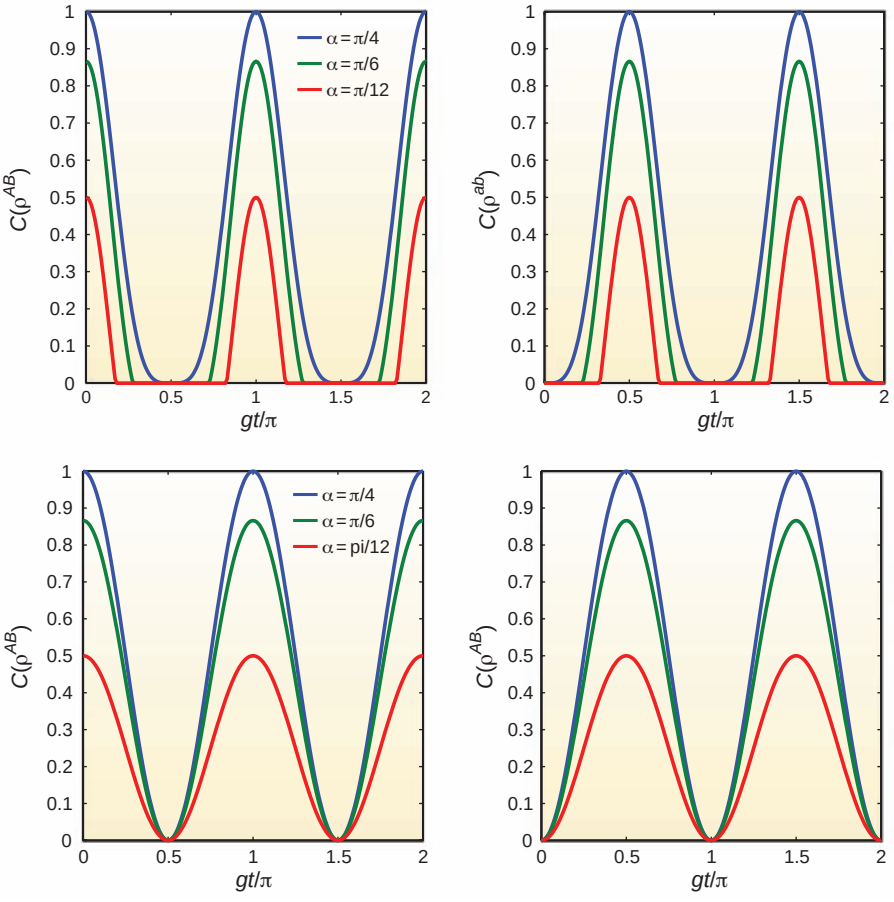

Fig. 4. Entanglement birth, death, and rebirth. [Adapted from (*35*)] In the bottom pair of panels the rise and fall of *AB* entanglement is exactly compensated by the fall and rise of *ab* entanglement. This is not the case in the top pair of panels, but a more subtle form of compensation still occurs, as reported in (*35*). It involves not concurrence but the auxiliary variable *Q*(*t*) defined in Eqs. 1 and S4.

Entanglement invariants. Entanglement flow in small reservoirs has led to the recent discovery of entanglement "invariants" (*35*) by inspection of the curves in the bottom row of Fig. 4, which repeats the top row except that a slightly different cat state is used for the atoms initially:

$$\Psi_\alpha = [(+-)\cos\alpha \Leftrightarrow (-+)\sin\alpha] \quad (3)$$

In the bottom left panel of Fig. 4, it appears that each *AB* atomic concurrence curve is compensated at all times by the corresponding *ab* photonic concurrence curve in the right panel, one going up as the other falls.

In fact, exact compensation can be confirmed analytically (*35*), but one notes that the same behavior does not appear in the top-row curves in Fig. 4, where there is no perfect compensation of *ab* for *AB*. For example, it is easy to see that the *AB* and *ab* red curves can be zero at the same time. A natural question is, where does the missing information go in that case? Because the two-site JC model is unitary, preservation of all four-qubit information is guaranteed, so it should be located "somewhere." Careful examination shows that concurrence is not conserved, but rather $Q(t)$ is conserved, spread among all six different types in that case (*35*).

This identification of four-particle memory flow channels is unusual and clearly deserves future examination (*40*, *41*). One can say about these invariants that they emerge only from a kind of analytic continuation of the bipartite concurrence function $C(t)$ to un-physically negative values, which is permitted via $Q(t)$. The entanglement flow issue (*42*) is also related to, and appears to expand considerably, the theory associated with entanglement swapping, which is under active exploration, and has been realized with particle pairs from independent sources (*43*).

Non-Markovian noises. Dissipative entanglement evolution is critically dependent on the types of the noises acting on the system. Markov environments are those for which a noise signal has no self-correlation over any time interval, and under Markov conditions noise typically results in a quantum irreversible process. Non-Markovian noise arising from a structured environment or from strong coupling appears to be more fundamental (*44*, *45*). Recent studies have suggested that correlated noises may cause new difficulties in using quantum error correction codes (*46*) and dynamic decoupling (*47*). Although some progress has been made, extending the current research on ESD into physically relevant non-Markovian situations remains a challenge. High-Q cavity QED and quantum dot systems are two possible experimental venues.

Qutrits and beyond. Many-qubit entanglement and entanglement of quantum systems that are not qubits (i.e., those having more than two states) is largely an open question, and one that is embarrassing in a sense, because the question has been open since quantum mechanics was invented in the 1920s. There is still no known finite algorithm for answering the simple-seeming question of whether a given mixed state is entangled or not, if it refers to more than two systems, and it is answerable for two mixed-state systems only in the case of pairs of qubits (as we have been discussing) and the case of one qubit and one qutrit (a three-state system such as spin-1). Investigation into ESD of qubit-qutrit systems has begun (*48*, *49*), but generalizations to many-qubit systems are daunting tasks due to both technical and conceptual difficulties (*7*–*9*).

Topological approach. *N*-party entanglement dynamics will presumably become simpler to predict if a computable entanglement measure for a mixed state of more than two qubits can be discovered. However, an alternative approach is to avoid dynamics through topological analysis (*50*). One now knows (*51*, *52*) that ESD is necessary (i.e., must occur) in arbitrary *N*-party systems of noninteracting qubits if they are exposed to thermal noise at any finite $T > 0$ temperature. The steady state of any noninteracting *N*-qubit system has a neighborhood in which every state is separable. In this case, any prearranged subsystem entanglement will inevitably be destroyed in a finite time. This is a universal result showing how entanglement evolves in the absence of external noise control.

Clearly, the holy grail for research on entanglement dynamics is to find an efficient real-time technique for tracking and controlling the entanglement evolution of a generic many-qubit system. Another important open question is to determine a generic method for direct experimental registration of entanglement, for which there is no current answer. We believe that many surprising results are awaiting discovery.

References and Notes

1. E. Schrödinger, *Naturwissenschaften* **23**, 807 (1935).
2. A. Einstein, B. Podolsky, N. Rosen, *Phys. Rev.* **47**, 777 (1935).
3. M. A. Nielsen, I. L. Chuang, *Quantum Computation and Quantum Information* (Cambridge Univ. Press, Cambridge, 2000).
4. C. H. Bennett, D. P. DiVincenzo, *Nature* **404**, 247 (2000).
5. W. H. Zurek, *Rev. Mod. Phys.* **75**, 715 (2003).
6. T. Yu, J. H. Eberly, *Phys. Rev. B* **66**, 193306 (2002).
7. C. Simon, J. Kempe, *Phys. Rev. A* **65**, 052327 (2002).
8. W. Dür, H. J. Briegel, *Phys. Rev. Lett.* **92**, 180403 (2004).
9. For an earlier review of entanglement dynamics, see (*53*).
10. T. Yu, J. H. Eberly, *Phys. Rev. Lett.* **93**, 140404 (2004).
11. K. Zyczkowski, P. Horodecki, M. Horodecki, R. Horodecki, *Phys. Rev. A* **65**, 012101 (2001).
12. A. K. Rajagopal, R. W. Rendell, *Phys. Rev. A* **63**, 022116 (2001).
13. L. Diosi, in *Irreversible Quantum Dynamics*, F. Benatti, R. Floreanini, Eds. (Springer, New York, 2003), pp. 157–163.
14. S. Daffer, K. Wodkiewicz, J. K. McIver, *Phys. Rev. A* **67**, 062312 (2003).
15. P. J. Dodd, J. J. Halliwell, *Phys. Rev. A* **69**, 052105 (2004).
16. T. Yu, J. H. Eberly, *Phys. Rev. Lett.* **97**, 140403 (2006).
17. For details, see section 1 of the Supporting Online Material.
18. M. P. Almeida *et al.*, *Science* **316**, 579 (2007).
19. J. Laurat, K. S. Choi, H. Deng, C. W. Chou, H. J. Kimble, *Phys. Rev. Lett.* **99**, 180504 (2007).
20. J. H. Eberly, T. Yu, *Science* **316**, 555 (2007).
21. Our example illustrates the distinction between entangled and nonentangled states, but quantum entanglement has the ability to encode oppositeness that goes further than the awake-asleep dichotomy of the cats or the heads-tails dichotomy of coins. One extension is the anti-alignment of the hands of a clock, not uniquely found at 6:00, but realized also at different angles of the hands, at approximately 7:05, 8:10, etc. Orthogonal photon polarizations, which may be oriented to any direction, extend the concept to continuous "opposites," exploited by Clauser and Freedman in their famous experiment showing quantum violation of a Bell Inequality (*54*).
22. Matrix encoding of the entanglement is more complicated than the bracket notation used for the cats, but it is important because we want to allow for more possibilities, which can be visualized by thinking that any of the four joint state labels ++, +−, −+, or −− can be correlated with itself or any other, making 16 basic correlation labels, and these are conventionally arranged in a 4 × 4 matrix. This is the density matrix ρ referred to in the text. See the Supporting Online Material for an example, and a sketch of the theory of time evolution of the density matrix in a noisy environment.
23. W. K. Wootters, *Phys. Rev. Lett.* **80**, 2245 (1998).
24. T. Yu, J. H. Eberly, *Opt. Commun.* **264**, 393 (2006).
25. J. Preskill, *Proc. R. Soc. Lond. A* **454**, 385 (1998).
26. I. Sainz, G. Björk, *Phys. Rev. A* **77**, 052307 (2008).
27. D. A. Lidar, K. B. Whaley, in *Irreversible Quantum Dynamics*, F. Benatti, R. Floreanini, Eds. (Springer, Berlin, 2003), pp. 83–120.
28. G. Gordon, G. Kurizki, *Phys. Rev. Lett.* **97**, 110503 (2006).
29. S. Maniscalco, F. Francica, R. L. Zaffino, N. Lo Gullo, F. Plastina, *Phys. Rev. Lett.* **100**, 090503 (2008).
30. For example, see L. Viola, S. Lloyd, *Phys. Rev. A* **58**, 2733 (1998).
31. A. R. R. Carvalho, A. J. S. Reid, J. J. Hope, *Phys. Rev. A* **78**, 012334 (2008).
32. E. T. Jaynes, F. W. Cummings, *Proc. IEEE* **51**, 89 (1963).
33. M. Yönac, T. Yu, J. H. Eberly, *J. Phys. B* **39**, S621 (2006).
34. Z. Ficek, R. Tanas, *Phys. Rev. A* **74**, 024304 (2006).
35. M. Yönac, T. Yu, J. H. Eberly, *J. Phys. B* **40**, S45 (2007).
36. M. Yönac, J. H. Eberly, *Opt. Lett.* **33**, 270 (2008).
37. H. Nha, H. J. Carmichael, *Phys. Rev. Lett.* **93**, 120408 (2004).
38. T. Yu, J. H. Eberly, *Quant. Inf. Comput.* **7**, 459 (2007).
39. A. R. P. Rau, M. Ali, G. Alber, *Eur. J. Phys.* **82**, 40002 (2008).
40. I. Sainz, G. Björk, *Phys. Rev. A* **76**, 042313 (2007).
41. D. Cavalcanti *et al.*, *Phys. Rev. A* **74**, 042328 (2006).
42. T. S. Cubitt, F. Verstraete, J. I. Cirac, *Phys. Rev. A* **71**, 052308 (2005).
43. M. Halder *et al.*, *Nat. Phys.* **3**, 692 (2007).
44. M. Ban, *J. Phys. A* **39**, 1927 (2006).
45. B. Bellomo, R. Lo Franco, G. Compagno, *Phys. Rev. Lett.* **99**, 160502 (2007).
46. E. Novais, E. R. Mucciolo, H. U. Baranger, *Phys. Rev. A* **78**, 012314 (2008).
47. K. Shiokawa, B. L. Hu, *Quant. Inf. Proc.* **6**, 55 (2007).
48. K. Ann, G. Jaeger, *Phys. Rev. B* **75**, 115307 (2007).
49. A. Checinska, K. Wodkiewicz, *Phys. Rev. A* **76**, 052306 (2007).
50. B. V. Fine, F. Mintert, A. Buchleitner, *Phys. Rev. B* **71**, 153105 (2005).
51. T. Yu, J. H. Eberly, http://arxiv.org/abs/0707.3215 (2007).
52. A. Al-Qasimi, D. F. V. James, *Phys. Rev. A* **77**, 012117 (2008).
53. F. Mintert, A. R. R. Carvalho, M. Kus, A. Buchleitner, *Phys. Rep.* **415**, 207 (2005).
54. S. J. Freedman, J. F. Clauser, *Phys. Rev. Lett.* **28**, 938 (1972).

55. T.Y. and J.H.E. acknowledge grant support from the U.S. Army Research Office (48422-PH), the NSF (PHY06-01804 and PHY07-58016), and U.S. Department of Energy, Office of Basic Energy Sciences (DE-FG02-05ER15713).

Supporting Online Material

www.sciencemag.org/cgi/content/full/323/5914/598/DC1
SOM Text
Fig. S1
References

10.1126/science.1167343

Facile Synthesis of AsP_3

Brandi M. Cossairt,[1] Mariam-Céline Diawara,[2] Christopher C. Cummins[1]*

White phosphorus consists of tetrahedral P_4 molecules and is the key industrial intermediate for most phosphorus compounds of commercial importance (*1*). In contrast, in condensed phase the corresponding arsenic molecule, As_4 (yellow arsenic), is both thermally and photochemically unstable, reverting readily to the stable gray allotrope with an infinite sheet structure (*2*). To date, essentially all that is known of the binary molecules As_nP_{4-n} (n = 1 to 3) has come from gas-phase studies wherein hot (660°C) vapors of phosphorus and arsenic mixtures under equilibrium reaction conditions were subjected to Raman spectroscopic analysis (*3*). To determine the properties of AsP_3 as a pure and isolated substance, we set out to synthesize it by using a method hinging on transition-metal chemistry.

Two salts of the $[P_3Nb(ODipp)_3]^-$ anion, of interest as a P_3^{3-} synthon, were synthesized by P_4 activation with dichloride precursor $Cl_2Nb(ODipp)_3(THF)$ in the presence of reducing agents (Fig. 1A), where Dipp indicates 2,6-$C_6H_3[CH(CH_3)_2]_2$ and THF, tetrahydrofuran (*4*). The anion $[P_3Nb(ODipp)_3]^-$ was characterized by x-ray crystallography as its sodium salt and found to contain chemically equivalent P atoms and a structure in which a $Nb(ODipp)_3$ unit replaces one vertex of the P_4 tetrahedron (*5*). Solution nuclear magnetic resonance (NMR) spectroscopy (^{31}P, ^{13}C, and ^{1}H) studies of $[P_3Nb(ODipp)_3]^-$ salts are consistent with the structural assignment, with the ^{31}P NMR data [singlets at a chemical shift, δ, of −206 and −170 parts per million (ppm) for the sodium and cobaltocenium salts, respectively] serving as spectroscopic signatures of this system (*5*).

AsP_3 itself was obtained from the reaction in THF solvent of either $[P_3Nb(ODipp)_3]^-$ salt with $AsCl_3$; dichloride $Cl_2Nb(ODipp)_3(THF)$ is regenerated in the process (Fig. 1A). Purification of AsP_3 after workup is achieved either by crystallization from ether at −35°C or by sublimation. In a typical synthesis, ~100 mg of bright white solid AsP_3 was obtained, representing a 75% yield (*5*). AsP_3 is identified with a single high-field ^{31}P NMR resonance at −484 ppm, in good agreement with the prediction given by our theoretical calculations [supporting online material (SOM) text]. Furthermore, gas chromatography–mass spectrometry (GC-MS) analysis of a toluene solution of the white powder revealed a single band of retention time of 9.1 min, corresponding to the molecular weight of AsP_3 at 168 mass/charge (m/z) (Fig. 1B). High-resolution mass spectrometry data obtained by using the electron impact technique featured a parent ion signal at 167.842 m/z (*5*).

We acquired Raman spectra of microcrystalline AsP_3 by using a solid state laser at 785 nm (Fig. 1D) (*5*). The four expected bands are prominent and compare well with theory (SOM text) and with those bands observed by Ozin for the molecule as one component of a hot gas (*3*).

AsP_3 melts without decomposition at 71° to 73°C and is thermally quite stable, withstanding temperatures of 120°C for more than 1 week in a toluene solution. No precautions against irradiation were necessary when handling isolated samples of AsP_3 in ambient light; however, much like P_4, AsP_3 must be handled anaerobically because it is pyrophoric.

For structural characterization, AsP_3 was derivatized by ligation to molybdenum in the $(AsP_3)Mo(CO)_3(PiPr_3)_2$ coordination complex, obtained as orange crystals in 63% yield (*6*). Single-crystal x-ray diffraction (Fig. 1C) revealed the AsP_3 tetrahedron bound to the metal center by a single phosphorus vertex at a distance of 2.487(1) Å. The three P–P bonds in the tetrahedron average to 2.177 Å, whereas the As–P bonds are longer, at an average of 2.305 Å (*5*). The observation of specific AsP_3 coordination to molybdenum at a phosphorus vertex is an initial example of selectivity in a reaction of AsP_3.

The synthetic strategy developed here for P_3^{3-} transfer with generation of an EP_3 tetrahedron is not limited to E = As. When using $SbCl_3$ in place of $AsCl_3$ in the synthesis, we generated the exotic SbP_3 molecule and identified it with a broadened resonance in the ^{31}P NMR spectrum at δ of −461.8 ppm (*5*).

One possible application for AsP_3 might be as a stoichiometrically exact 1:3 source of arsenic and phosphorus atoms for the synthesis of advanced materials (*7*).

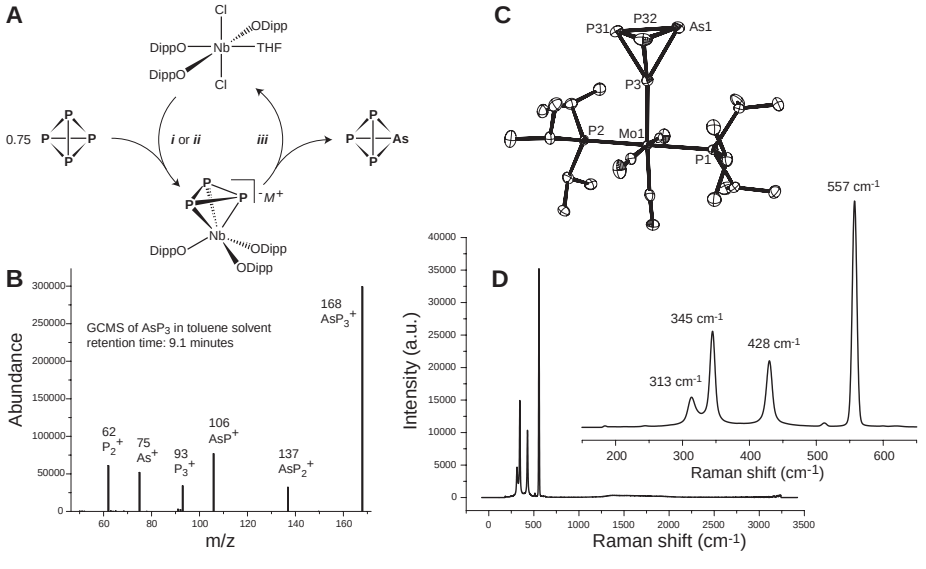

Fig. 1. (**A**) Synthetic scheme: (i) 0.5% Na/Hg, THF. (ii) 1. SmI_2, THF; 2. 2 $CoCp_2$ (M is Na or $CoCp_2$). (iii) $AsCl_3$, THF. (**B**) GC-MS spectrum of AsP_3. (**C**) Thermal ellipsoid plot of $(AsP_3)Mo(CO)_3(PiPr_3)_2$, with 50% thermal ellipsoids and hydrogen atoms omitted for clarity. (**D**) Raman spectrum of AsP_3.

References and Notes

1. J. Emsley, *The 13th Element: The Sordid Tale of Murder, Fire, and Phosphorus* (Wiley, New York, 2000).
2. N. N. Greenwood, A. Earnshaw, *Chemistry of the Elements* (Butterworth-Heinemann, Oxford, ed. 2, 1997).
3. G. A. Ozin, *J. Chem. Soc. A* **1970**, 2307 (1970).
4. J. R. Clark *et al.*, *Inorg. Chem.* **36**, 3623 (1997).
5. Materials and methods are detailed in supporting material available on *Science* Online.
6. T. Groer, G. Baum, M. Scheer, *Organometallics* **17**, 5916 (1998).
7. O. Manasreh, *Semiconductor Heterojunctions and Nanostructures* (McGraw-Hill, New York, 2005).
8. We thank the NSF (grant CHE-719157), Thermphos International, and the Massachusetts Institute of Technology for funding and N. A. Piro and H. A. Spinney for helpful discussions. Crystallographic parameters for $(Na)[P_3Nb(ODipp)_3]$, $Cl_2Nb(ODipp)_3(THF)$, and $(AsP_3)Mo(CO)_3(PiPr_3)_2$ are available free of charge from the Cambridge Crystallographic Data Centre (CCDC 704466 to 704468).

Supporting Online Material

www.sciencemag.org/cgi/content/full/323/5914/602/DC1
Materials and Methods
SOM Text
Figs. S1 to S5
References

14 October 2008; accepted 12 November 2008
10.1126/science.1168260

[1]Department of Chemistry, Massachusetts Institute of Technology, 77 Massachusetts Avenue, Room 6-435, Cambridge, MA 02139, USA. [2]École Normale Supérieure de Lyon, Université Claude Bernard Lyon 1, 46, Allée d'Italie, 69364 Lyon Cedex 07, France.

*To whom correspondence should be addressed. E-mail: ccummins@mit.edu

Anomalous Criticality in the Electrical Resistivity of $La_{2-x}Sr_xCuO_4$

R. A. Cooper,[1] Y. Wang,[1] B. Vignolle,[2] O. J. Lipscombe,[1] S. M. Hayden,[1] Y. Tanabe,[3] T. Adachi,[3] Y. Koike,[3] M. Nohara,[4]* H. Takagi,[4] Cyril Proust,[2] N. E. Hussey[1]†

The presence or absence of a quantum critical point and its location in the phase diagram of high-temperature superconductors have been subjects of intense scrutiny. Clear evidence for quantum criticality, particularly in the transport properties, has proved elusive because the important low-temperature region is masked by the onset of superconductivity. We present measurements of the low-temperature in-plane resistivity of several highly doped $La_{2-x}Sr_xCuO_4$ single crystals in which the superconductivity had been stripped away by using high magnetic fields. In contrast to other quantum critical systems, the resistivity varies linearly with temperature over a wide doping range with a gradient that scales monotonically with the superconducting transition temperature. It is maximal at a critical doping level (p_c) ~ 0.19 at which superconductivity is most robust. Moreover, its value at p_c corresponds to the onset of quasi-particle incoherence along specific momentum directions, implying that the interaction that first promotes high-temperature superconductivity may ultimately destroy the very quasi-particle states involved in the superconducting pairing.

An important theme in strongly correlated electron systems is quantum criticality and the associated quantum phase transitions that occur at zero temperature upon tuning a nonthermal control parameter, g (e.g., pressure, magnetic field H or composition), through a critical value, g_c. One feature of such a system is the influence that critical fluctuations have on the physical properties over a wide region in the (T, g) phase diagram above the quantum critical point (QCP), inside which the system shows marked deviations from conventional Landau Fermi-liquid behavior. A number of candidate non–Fermi-liquid systems have emerged, particularly in the heavy fermion family (*1*), although there are others, for example, certain transition metal oxides (*2*), that display similar characteristics.

The physics of copper-oxide high-temperature superconductors may also be governed by proximity to a QCP. The generic temperature-doping (T, p) phase diagram resembles that seen in the heavy fermions, with an apparent funnel-shaped region that either pierces or skirts the superconducting dome (*3*). Above this region, cuprates display an in-plane resistivity, ρ_{ab}, that varies linearly with temperature over a wide temperature (*4*) yet narrow doping (*5*) range. This T-linear resistivity has been widely interpreted, in tandem with other anomalous transport properties (*6*), as a manifestation of scale-invariant physics borne out of proximity to the QCP. This viewpoint has remained untested, largely because of the high upper critical field H_{c2} values in high-T_c cuprates that restrict access to the important limiting low-temperature region below $T_c(p)$. We used a combination of persistent and pulsed high magnetic fields to expose the normal state of $La_{2-x}Sr_xCuO_4$ (LSCO) over a wide doping and temperature range and studied the evolution of $\rho_{ab}(T)$ with carrier density, from the slightly underdoped (p = 0.15) to the heavily overdoped (p = 0.33) region of the phase diagram. Our analysis reveals the presence of a singular doping concentration in LSCO at which the electronic response changes, although in a manner distinct from that observed in other candidate quantum critical systems.

In-plane resistivity of $La_{2-x}Sr_xCuO_4$. A series of high-field $\rho_{ab}(T, H)$ measurements were carried out on overdoped LSCO single crystals with doping levels of p = 0.18, 0.21, and 0.23 (labeled hereafter LSCO18, LSCO21, and LSCO23, respectively) with the field aligned perpendicular to the CuO_2 planes in order to suppress the superconductivity. Figure 1A shows the $\rho_{ab}(T, H)$ data obtained on LSCO23. In order to track the temperature dependence of the zero-field resistivity $\rho(T, 0)$ below T_c, we used a simple, transparent technique to extrapolate the high-field $\rho_{ab}(T, H)$ data to the zero-field axis (Fig. 1B). The resultant $\rho(T, 0)$ values, plotted in Fig. 1C together with the zero-field $\rho_{ab}(T)$ curve below 70 K, are found to exhibit a T-linear dependence down to 1.5 K. For comparison, we also plotted the absolute values of $\rho(T, 48)$ at a fixed high field of 48 T obtained directly from the vertical dashed line in Fig. 1A. The temperature dependence of the latter (analysis-free) values is identical to that of $\rho(T, 0)$ and is consistent with earlier 60-T data taken on LSCO22 (*7*), showing that the analysis itself has not introduced any additional, artificial temperature dependence in $\rho(T, 0)$. Similar pulsed-field measurements and analysis were carried out for the two other doping levels as summarized in fig. S1.

Figure 2 shows the resultant $\rho(T, 0)$ values plus zero-field $\rho_{ab}(T)$ data for seven different concentrations ranging from optimal doping (p = 0.17) to the heavily overdoped, nonsuperconducting region (p = 0.33). The gradual crossover in the temperature dependence of $\rho_{ab}(T)$, from quasi-linear for LSCO17 to approximately quadratic for LSCO33, is evident in the raw data and is consistent with previous studies carried out above T_c (*5*, *8*, *9*). At low temperatures, however, $\rho_{ab}(T)$ develops predominantly T-linear behavior for the entire doping range $0.18 \leq p \leq 0.29$ [for p = 0.17, data exists only above $T_c(H = 0)$]. Although evidence for a low-T T-linear resistivity has emerged for single doping concentrations in both electron- (*10*) and hole-doped (*11*, *12*) cuprates, our measurements show that the low-T linearity in fact persists over a broad range of doping.

Single-component analysis. In heavy fermion systems, $\Delta\rho(T)$, the T-dependent part of $\rho(T)$, is often described by a single term $\alpha_n T^n$ whose exponent $n(T, H)$ evolves from the Fermi-liquid value n = 2 to some anomalous value less than 2 over a narrow temperature and magnetic field window (*13*–*15*). The anomalous exponent in $\Delta\rho(T)$ persists to low temperatures only at the critical field, H_c. In Fig. 3, we plotted a comparative $n(T, p) = d(\ln\Delta\rho)/d(\ln T)$ for LSCO by using the resistivity curves shown in Fig. 2.

For T > 50 K, the resultant phase diagram resembles that seen in prototypical quantum critical systems, with a narrow region in which $\rho_{ab}(T)$ is approximately (although not strictly) T-linear separated from a region where $\rho_{ab}(T)$ varies approximately as T^2. As the temperature is lowered, however, the situation becomes markedly different. Rather than collapsing to a single (critical) point, the T-linear region in LSCO fans out and dominates the low-T response. Intriguingly, this T-linear regime (or more precisely, the region where n < 1.1) is coincident with both the T_c parabola (long-dashed white line) and the superconducting fluctuation regime (short-dashed white line) and has thus been obscured until now by the veil of superconductivity.

Dual-component analysis. Previously, $\Delta\rho_{ab}(T)$ in overdoped, hole-doped cuprates has been expressed either as above, that is, as $\alpha_n T^n$ ($1 \leq n \leq 2$) (*16*), or as the sum of two components, $\alpha_1 T + \alpha_2 T^2$ (*11*, *17*, *18*). In fig. S2, we describe in detail why the latter is in fact the more appropriate expression for LSCO. In Fig. 4, A and B, we show the doping dependences of α_1 and α_2, respectively, for two different fitting protocols. The solid squares are coefficients obtained

[1]H. H. Wills Physics Laboratory, University of Bristol, Tyndall Avenue, Bristol, BS8 1TL, UK. [2]Laboratoire National des Champs Magnétiques Pulsés (LNCMP), UMR CNRS-UPS-INSA 5147, Toulouse 31400, France. [3]Department of Applied Physics, Graduate School of Engineering, Tohoku University, 6-6-05 Aoba, Aramaki, Aoba-ku, Sendai 980-8579, Japan. [4]Department of Advanced Materials Science, Graduate School of Frontier Science, University of Tokyo, Kashiwa-no-ha 5-1-5, Kashiwa-shi, Chiba 277-8651, Japan.

*Present address: Department of Physics, Okayama University, Tsushima-naka, Okayama 700-8530, Japan.

†To whom correspondence should be addressed. E-mail: n.e.hussey@bristol.ac.uk

from least-square fits of the $\rho_{ab}(T)$ curves for $T \leq 200$ K to the expression $\rho_{ab}(T) = \alpha_0 + \alpha_1 T + \alpha_2 T^2$, whereas the solid circles are obtained from fits over the same temperature range to a parallel-resistor formalism $1/\rho_{ab}(T) = 1/(\alpha_0 + \alpha_1 T + \alpha_2 T^2) + 1/\rho_{max}$, where ρ_{max} (=900 ± 100 μohm•cm) represents a maximum (saturation) resistivity value (*19*, *20*). The inclusion of ρ_{max} helps to account smoothly for the escalation of $\rho_{ab}(T)$ to higher temperatures and to make the values of α_1 and α_2 insensitive to the temperature range of fitting. [For a discussion of the physical meaning of ρ_{max} and its relevance to the data, please refer to the supporting online material (SOM).] For all samples, the parallel-resistor fits (blue dashed curves in Fig. 2) are nearly indistinguishable from the $\rho_{ab}(T)$ curves over a fitting range that extends (with the exception of LSCO17) over 2 decades in temperature and a factor of 2 in doping. The open symbols in Fig. 4 relate to coefficients obtained from corresponding fits to earlier zero-field $\rho_{ab}(T)$ data (*5*) for comparison.

For both sets of data and analysis, α_1 is seen to grow rapidly with decreasing p, attaining a maximum value of around 1 μohm cm/K at p_c = 0.185 ± 0.005. In the parallel-resistor fit, α_2 remains finite at all doping concentrations and essentially p-independent down to the same doping level, at which point it rises sharply. Without ρ_{max} in the fitting procedure, α_2 becomes negligible around p = 0.20. It is important to note that none of the main findings of this study—the ubiquity of the T-linear term, the nondivergence of α_2, the

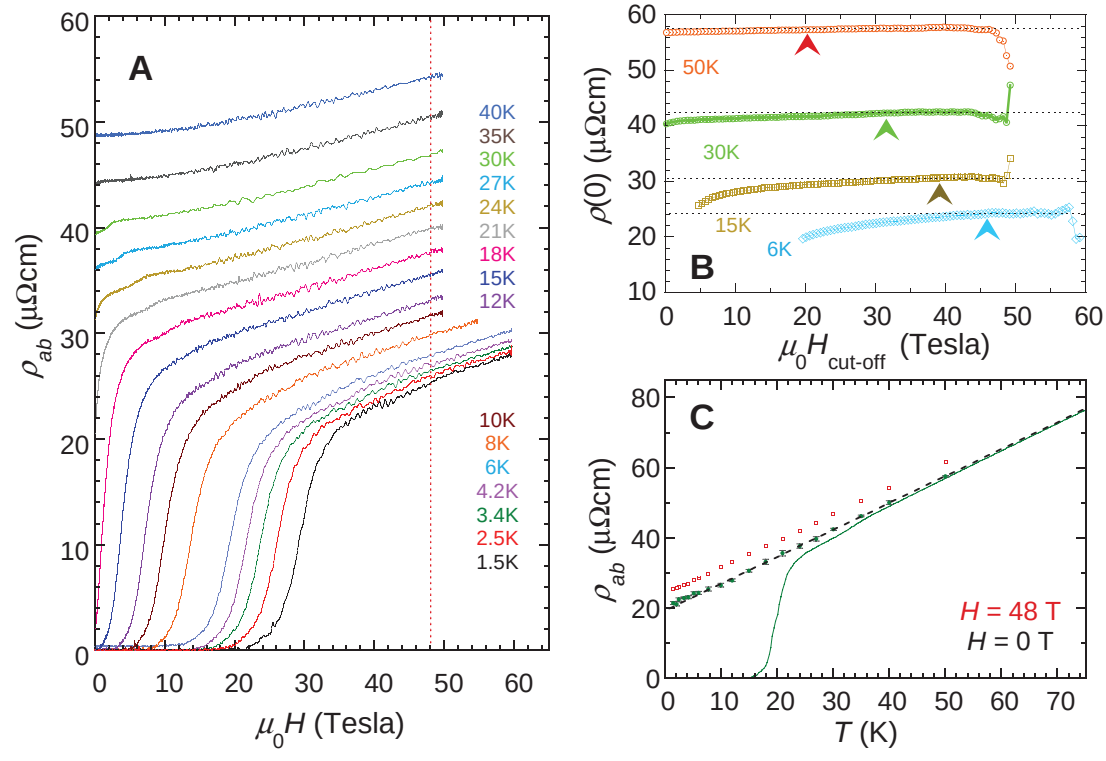

Fig. 1. Electrical resistivity of overdoped $La_{2-x}Sr_xCuO_4$ at low temperatures. (**A**) In-plane resistivity ρ_{ab} of LSCO23 as a function of temperature and magnetic field. The vertical dashed line indicates the temperature variation of ρ_{ab} at 48 T. (**B**) Mode of extraction of the zero-field resistivity $\rho(H = 0)$ for LSCO23 at each temperature. The primary data were fitted to the form $\rho(H) = \rho(0) + AH^2$ [as argued in the supporting online material (SOM) text] between some lower bound $H_{cut\text{-}off}$ and the maximum field strength used, and the deduced values of $\rho(0)$ are shown plotted as a function of these $H_{cut\text{-}off}$ values, the sample held at the various temperatures indicated. For $H_{cut\text{-}off}$ less than some indicated critical field, defined as H_{c2}, the extracted $\rho(0)$ values rise monotonically with increasing cut-off field. When $H_{cut\text{-}off}$ becomes of order H_{c2}, $\rho(0)$ reaches a plateau value. Lastly, as the field range for fitting becomes too narrow, the extrapolated value of $\rho(0)$ begins to oscillate wildly. For each temperature, $\rho(0)$ is identified by its value in the plateau region. (**C**) Zero-field $\rho_{ab}(T)$ of LSCO23 (solid green line) plotted with the extrapolated values of $\rho(0)$ (green solid squares) and of $\rho(\mu_0 H = 48$ T) (red open squares) for the various temperatures indicated. The dashed line is a guide to the eye.

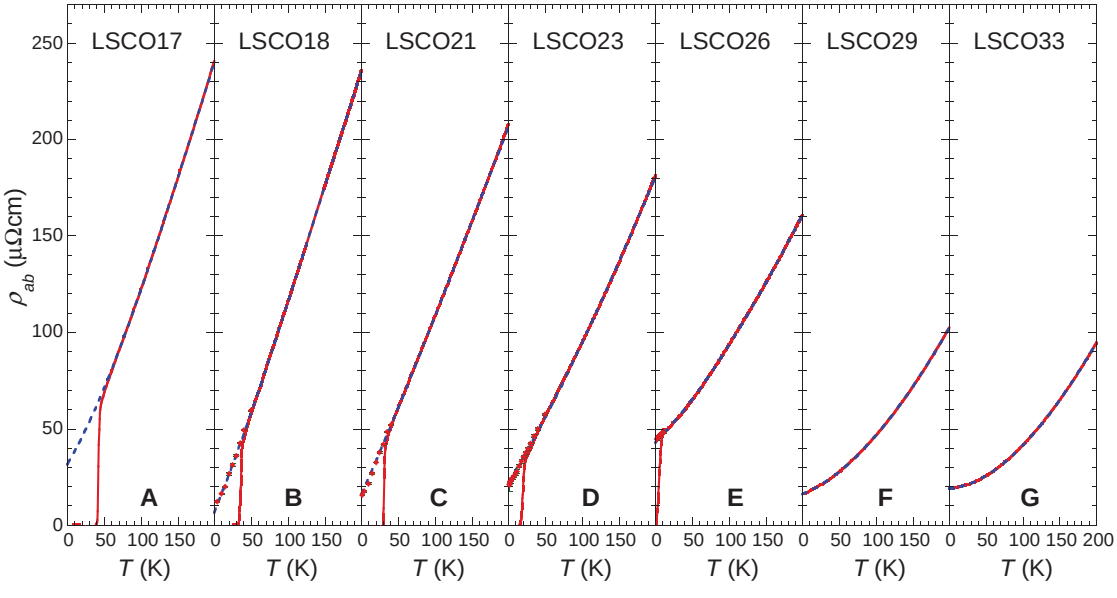

Fig. 2. Fitting of the in-plane resistivity of overdoped LSCO. Solid red lines are measured zero-field $\rho_{ab}(T)$ for (**A**) LSCO17, (**B**) LSCO18, (**C**) LSCO21, (**D**) LSCO23, (**E**) LSCO26, (**F**) LSCO29, and (**G**) LSCO33; whereas the red diamonds are corresponding extrapolated $\rho(H = 0)$ values. The blue dashed lines represent fits to the data below 200 K using the expression $1/\rho = 1/(\alpha_0 + \alpha_1 T + \alpha_2 T^2) + 1/\rho_{max}$ where ρ_{max} = 900 μohm•cm.

position of the kink, nor the value of α_1 at $p = p_c$—are dependent on the type of dual-component analysis used.

The coexistence of two distinct components to $\rho_{ab}(T)$ is suggestive of some form of two-fluid model, although the fact that the two components add in the resistivity (i.e., in series) rather than in the conductivity (in parallel) implies that the two subsystems would have to coexist on a microscopic scale. Indeed, it is well documented that cuprates possess substantial microscopic inhomogeneity (*21*), and overdoped LSCO in particular is prone to microscopic phase separation into superconducting and non-superconducting regions with a physical extent on the order of the superconducting coherence length (*22*, *23*). One might then be tempted to attribute the *T*-linear component to the superconducting region (because its value scales roughly with T_c) and the quadratic term to that portion of the sample with an effective carrier density $p > 0.27$.

An alternative approach, however, is to assign the two additive coefficients to two distinct, independent quasi-particle scattering processes that coexist on the cuprate Fermi surface. Such a picture was recently proposed on the basis of angle-dependent magnetoresistance (ADMR) measurements on overdoped $Tl_2Ba_2CuO_{6+\delta}$ (Tl2201) that revealed that the scattering rate was composed of two distinct terms, a T^2 scattering term that is isotropic within the basal plane and a *T*-linear scattering rate that is strongly anisotropic, exhibiting a maximum near the Brillouin zone boundary, where the pseudogap is maximal and vanishing along the zone diagonal (*18*). In a subsequent doping-dependent study, it was intimated that this anisotropic *T*-linear term correlates with T_c, whereas the quadratic term remains constant as a function of *p* (*24*). Both of these trends in Tl2201 now appear to be confirmed in LSCO but over a much wider range of doping.

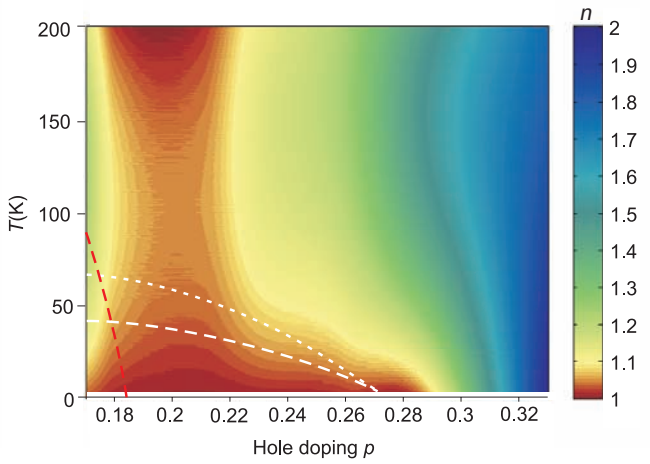

Fig. 3. Schematic of the evolution of the exponent *n* with temperature and doping in LSCO. The phase diagram is obtained directly by interpolating plots of $d[(\ln\rho_{ab} - \alpha_0)]/d(\ln T)$ versus *T* for all the resistivity curves shown in Fig. 2. In marked contrast to other quantum critical systems, the *T*-linear regime is found to grow wider with decreasing temperature. This unusual expansion of the *T*-linear region at low temperatures coincides with the superconducting dome (long dashed white line) and the region where superconducting fluctuations become significant (short dashed white line). The red dashed line represents $T^* = E_g/2$ (*36*). As stated in the text and argued in more detail in the SOM, this form of $\Delta\rho(T)$ is shown here only for comparison with the heavy-fermion compounds, but it is not the most appropriate means of describing $\Delta\rho(T)$ in LSCO or indeed other cuprates (*18*).

Anomalous criticality in LSCO. Critical fluctuations are a definitive signature of a QCP. In nearly ferromagnetic (FM) or antiferromagnetic (AFM) metals, for example, critical spin fluctuations give rise to physical properties with anomalous temperature dependences whose critical exponents depend on the nature of the spin fluctuations (FM or AFM) and on the dimensionality. For two-dimensional (2D) AFM spin fluctuations, a *T*-linear resistivity is expected that extends to very low temperatures at or near the QCP (*25*). Away from the critical point, the resistivity shows a crossover to a Fermi-liquid–like T^2 resistivity as *T* decreases. As the critical point is approached, the crossover temperature T_F decreases, and the coefficient of the T^2 resistivity diverges. Such behavior is typified by the heavy-fermion compound $YbRh_2Si_2$, where $\Delta\rho$ is found to be strictly *T*-linear over 2 decades in temperature at a critical magnetic field, H_c (*13*). Either side of H_c, $\Delta\rho$ is proportional to T^2 with a coefficient α_2 (T_F) that diverges (falls linearly) as *H* approaches H_c. Similar behavior is exhibited in the quasi-2D heavy-fermion compound $CeCoIn_5$, where the QCP coincides with the upper critical field H_{c2} (*14*), and in the bilayer ruthenate $Sr_3Ru_2O_7$ (*2*), where the QCP coincides with a metamagnetic transition.

There are three aspects of the resistivity behavior in LSCO that conflict with this conventional quantum critical picture: (i) the two

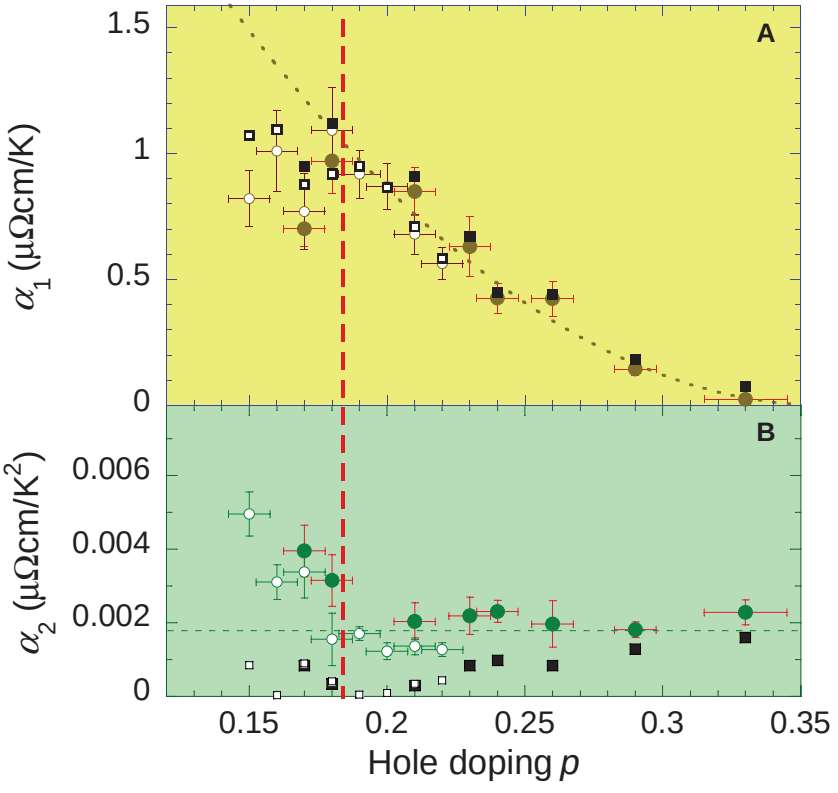

Fig. 4. Doping evolution of the temperature-dependent coefficients of $\rho_{ab}(T)$. (**A**) Doping dependence of α_1, the coefficient of the *T*-linear resistivity component. (**B**) Doping dependence of α_2, the coefficient of the T^2 resistivity component. In both panels, solid squares are coefficients obtained from least-square fits of the $\rho_{ab}(T)$ curves for $T \leq 200$ K to the expression $\rho_{ab}(T) = \alpha_0 + \alpha_1 T + \alpha_2 T^2$, whereas the solid circles are obtained from fits over the same temperature range to a parallel-resistor formalism $1/\rho_{ab}(T) = 1/(\alpha_0 + \alpha_1 T + \alpha_2 T^2) + 1/\rho_{max}$ with $\rho_{max} = 900 \pm 100$ μohm cm. The open symbols are obtained from corresponding fits made to the $\rho_{ab}(T)$ data of Ando *et al.* (*5*) between 70 K and 200 K. The dashed lines are guides to the eye. The error bars are a convolution of standard deviations in the values of α_1 and α_2 (1σ) for different temperature ranges of fitting plus systematic uncertainty in the absolute magnitude of ρ_{max}.

T-dependent coefficients appear to coexist for all *T* and *p*, rather than simply merge into one another; (ii) the coefficient of the T^2 term does not diverge—it either remains constant or diminishes as one approaches p_c from the overdoped side; and (iii) the *T*-linear scattering term in LSCO persists at low *T* over an extended doping range. This is evident not only in the evolution of α_1 (Fig. 4A) but also in the single-exponent plot (Fig. 3). This extended regime of *T*-linear resistivity is a possible manifestation of a second tuning parameter other than doping, that is, a third axis in the phase diagram (e.g., magnetic field or disorder) along which the QCP may be located. In $YbRh_2Si_2$, for example, alloying with Ge broadens the field range over which the *T*-linear resistivity extends to low *T* (*13*). Alternatively, the breadth of the critical region in LSCO suggests that the strange metal physics in cuprates is associated not with a QCP but with a novel, extended quantum phase, as seen, for example, in the itinerant ferromagnet MnSi beyond a critical pressure (*26*).

Discussion. The marked kinks in α_1 and α_2 at $p_c = 0.185 \pm 0.005$ are the most revealing findings of this study. The value of p_c coincides with that inferred from a wealth of other experimental probes (*3*) and is associated with the opening of the pseudogap, an anisotropic (nodal) gap in the normal state excitation spectrum. Below p_c, a new energy (E^*) or temperature (T^*) scale emerges, which grows sharply with decreasing doping and appears to extrapolate to a value about equal to the AFM exchange energy, *J*. There are two competing scenarios describing the effect of the pseudogap on the Fermi surface in cuprates: one involving Fermi surface reconstruction into hole and electron pockets (*27*) and the other involving Fermi surface degradation into a series of disconnected Fermi patches or arcs, centered about the zone diagonals, with an arc length that is progressively reduced upon underdoping (*28*). Although the actual doping dependence of the pseudogap has been hotly debated (*3*), the consistent and systematic analysis reported here appears to confirm that there is indeed a fundamental change in the transport properties of cuprates at this specific, well-defined doping level sandwiched between optimal doping and the upper edge of the superconducting dome (*16*, *29*).

A particular feature of Fig. 4 is the anticorrelation of α_1 and α_2 for $p < p_c$; whereas α_2 rises or recovers, α_1 falls away from its doping trajectory inferred from $p > p_c$ (thin dashed line in Fig. 4A). Recent experiments on less-disordered cuprates with $p \leq 0.1$ have shown that this trend continues well into the underdoped regime with $\rho_{ab}(T)$, becoming purely T^2 at low to intermediate temperatures (*30*). The distinct momentum dependences of the two scattering processes, suggested by the ADMR experiments on Tl2201 (*18*), provides a means to interpret qualitatively the anticorrelation of α_1 and α_2 within a scenario of progressive destruction of the underlying Fermi surface (*31*). As *p* falls below p_c, sections of Fermi surface near the Brillouin zone boundary begin to disappear. Although this may not necessarily have a detrimental effect on the isotropic term α_2, for α_1 the reduction in the total number of coherent states is more than offset by the removal of the strong scattering sinks near (π, 0), leading to an overall decrease, or at best saturation, in α_1 with further reduction in carrier density.

Recent angle-resolved photoemission spectroscopy (ARPES) studies of underdoped cuprates have hinted at a gradual erosion of the Fermi arc length with decreasing temperatures below T^* (*32*). For $0.15 \leq p \leq 0.19$, T^* is about equal to $E^*/2$ and is of the order of 100 K (*33*). Because our fitting range extends up to 200 K, the changes observed in $\alpha_1(p)$ and $\alpha_2(p)$ for $p < p_c$ imply that actually quasi-particle states are lost at temperatures $T > T^*$. Moreover, given that our fitting parameters are relatively insensitive to the temperature range, we conclude that the antinodal states must play little or no role in the conductivity at any given temperature. One hint toward understanding this lies in the absolute value of α_1 (=1 μohm•cm K^{-1}) at $p = p_c$. For a 2D metal, $d\rho_{ab}/dT = (2\pi\hbar d/e^2 v_F k_F)d(1/\tau)/dT$, where *d* is the interlayer spacing (=0.64 nm in LSCO), v_F is the Fermi velocity, and k_F the Fermi wave vector. Taking typical (*p*-independent) values of v_F ($=8.0 \times 10^4$ ms^{-1}) and k_F ($=7$ nm^{-1}) for the antinodal states in overdoped LSCO (*34*), we find that at $p = p_c$ the momentum-averaged scattering rate $\hbar/\tau \sim \pi k_B T$. Given that the anisotropic scattering rate varies as $\cos^2 2\varphi$ within the plane (φ being the angle between the *k* vector and the Cu-O-Cu bond direction) (*18*), we find that $\hbar/\tau \sim 2\pi k_B T$ for states near (π, 0). This level of scattering intensity is consistent with the so-called Planckian dissipation limit (*35*) beyond which Bloch-wave propagation becomes inhibited, that is, the quasiparticle states themselves become incoherent.

The picture that emerges then is the following. As the carrier number falls and the system approaches the Mott insulating state at $p = 0$, the effective interaction responsible for the (anisotropic) *T*-linear scattering term becomes progressively stronger. Because the strength of this term is closely correlated with T_c, the same interaction also drives up both the superconducting transition temperature and the condensation energy, the latter reaching a maximum at $p = p_c$ (*33*, *36*). At this point, however, scattering intensity is so strong that those states near (π, 0) begin to de-cohere, and, given the proportionality with temperature, incoherence occurs at all finite temperatures, not just below T^*. With further reduction in doping, the strength of the interaction continues to rise, causing yet more states to lose coherence and leading to an overall reduction or saturation in $\alpha_1(p)$ and a corresponding suppression in the condensation energy (*36*) and the superfluid density (*37*).

One is then left with the intriguing possibility that the pseudogap itself forms in response to this intense scattering, the electronic ground state lowering its energy through gapping out the incoherent, highly energetic antinodal states and, in so doing, preventing scattering of the remnant quasi-particle states into those same regions. The temperature-invariant violation of the Planckian dissipation limit then provides a possible explanation as to why the pseudogap itself is a non–states-conserving gap (*3*, *33*): In contrast to a conventional (Bardeen-Cooper-Schrieffer) superconducting gap where the full density of states is recovered above the (two-particle) gap energy, pseudogapped states near (π, 0) are effectively removed at all energies up to the bandwidth (*38*) or the Coulomb energy (*39*). Along the nodal directions, where this anisotropic scattering term is absent, however (*18*), the nodal quasi-particle states remain intact (protected) at all *T* and *p* across the entire superconducting dome.

Concluding remarks. It has been a long-standing mystery why the pseudogap in cuprates vanishes at a singular doping level, p_c, beyond optimal doping. By tracking the evolution of the in-plane resistivity from the overdoped side, we have uncovered a change in the electrical transport at $p = p_c$ that appears to coincide with the onset of incoherence (at the antinodal regions), thus offering a possible explanation for its precise location in the cuprate phase diagram and the subsequent reduction in the strength of the superconductivity with lowering carrier concentration. And although Planckian dissipation is quantum criticality of sorts, it does not appear to be consistent with any simple one-parameter scaling hypothesis (*40*) in just the same way as the doping evolution of the transport coefficients is difficult to reconcile with conventional quantum criticality.

References and Notes

1. P. Gegenwart, Q. Si, F. Steglich, *Nat. Phys.* **4**, 186 (2008).
2. S. A. Grigera *et al.*, *Science* **294**, 329 (2001).
3. J. L. Tallon, J. W. Loram, *Physica* **349C**, 53 (2001).
4. M. Gurvitch, A. T. Fiory, *Phys. Rev. Lett.* **59**, 1337 (1987).
5. Y. Ando, S. Komiya, K. Segawa, S. Ono, Y. Kurita, *Phys. Rev. Lett.* **93**, 267001 (2004).
6. D. van der Marel *et al.*, *Nature* **425**, 271 (2003).
7. G. S. Boebinger *et al.*, *Phys. Rev. Lett.* **77**, 5417 (1996).
8. H. Takagi *et al.*, *Phys. Rev. Lett.* **69**, 2975 (1992).
9. S. Nakamae *et al.*, *Phys. Rev. B* **68**, 100502(R) (2003).
10. Y. Dagan, M. M. Qazilbash, C. P. Hill, V. N. Kulkarni, R. L. Greene, *Phys. Rev. Lett.* **92**, 167001 (2004).
11. A. P. Mackenzie, S. R. Julian, D. C. Sinclair, C. T. Lin, *Phys. Rev. B* **53**, 5848 (1996).
12. R. Daou *et al.*, *Nat. Phys.* **5**, 31 (2009).
13. J. Custers *et al.*, *Nature* **424**, 524 (2003).
14. J. Paglione *et al.*, *Phys. Rev. Lett.* **91**, 246405 (2003).
15. S. Nakatsuji *et al.*, *Nat. Phys.* **4**, 603 (2008).
16. S. H. Naqib, J. R. Cooper, J. L. Tallon, C. Panagopoulos, *Physica* **387C**, 365 (2003).
17. C. Proust *et al.*, *Phys. Rev. Lett.* **89**, 147003 (2002).
18. M. Abdel-Jawad *et al.*, *Nat. Phys.* **2**, 821 (2006).
19. H. Wiesmann *et al.*, *Phys. Rev. Lett.* **38**, 782 (1977).
20. N. E. Hussey, *Eur. Phys. J. B* **31**, 495 (2003).
21. S. H. Pan *et al.*, *Nature* **413**, 282 (2001).
22. Y. Tanabe, T. Adachi, T. Noji, Y. Koike, *J. Phys. Soc. Jpn.* **74**, 2893 (2005).
23. Y. Tanabe *et al.*, *J. Phys. Soc. Jpn.* **76**, 113706 (2007).
24. M. Abdel-Jawad *et al.*, *Phys. Rev. Lett.* **99**, 107002 (2007).
25. T. Moriya, K. Ueda, *Adv. Phys.* **49**, 555 (2000).
26. N. Doiron-Leyraud *et al.*, *Nature* **425**, 595 (2003).
27. D. LeBoeuf *et al.*, *Nature* **450**, 533 (2007).
28. M. R. Norman *et al.*, *Nature* **392**, 157 (1998).

29. F. F. Balakirev *et al.*, *Phys. Rev. Lett.* **102**, 017004 (2009).
30. F. Rullier-Albenque *et al.*, *Phys. Rev. Lett.* **99**, 027003 (2007).
31. T. Senthil, *Phys. Rev. B* **78**, 035103 (2008).
32. A. Kanigel *et al.*, *Nat. Phys.* **2**, 447 (2006).
33. J. W. Loram, K. A. Mirza, J. R. Cooper, J. L. Tallon, *J. Phys. Chem. Solids* **59**, 2091 (1998).
34. T. Yoshida *et al.*, *J. Phys. Condens. Matter* **19**, 125209 (2007).
35. J. Zaanen, *Nature* **430**, 512 (2004).
36. J. W. Loram, J. Luo, J. R. Cooper, W. Y. Liang, J. L. Tallon, *J. Phys. Chem. Solids* **62**, 59 (2001).
37. C. Panagopoulos *et al.*, *Phys. Rev. B* **67**, 220502 (2003).
38. H. J. A. Molegraaf, C. Presura, D. van der Marel, P. H. Kes, M. Li, *Science* **295**, 2239 (2002).
39. S. Chakraborty, D. Galanakis, P. Phillips, http://arxiv.org/abs/0807.2854 (2008).
40. P. Phillips, C. Chamon, *Phys. Rev. Lett.* **95**, 107002 (2005).
41. We acknowledge technical and scientific assistance from S. L. Kearns, J. Levallois, and N. Mangkorntang and collaborative support from H. H. Wen. This work was supported by Engineering and Physical Sciences Research Council (UK), the Royal Society, *Laboratoire National des Champs Magnétiques Pulsés*, the French Agence Nationale de la Recherche IceNET, and EuroMagNET.

Supporting Online Material
www.sciencemag.org/cgi/content/full/1165015/DC1
Materials and Methods
Figs. S1 and S2
References

22 August 2008; accepted 21 November 2008
Published online 11 December 2008;
10.1126/science.1165015
Include this information when citing this paper.

Revealing the Maximum Strength in Nanotwinned Copper

L. Lu,[1]* X. Chen,[1] X. Huang,[2] K. Lu[1]

The strength of polycrystalline materials increases with decreasing grain size. Below a critical size, smaller grains might lead to softening, as suggested by atomistic simulations. The strongest size should arise at a transition in deformation mechanism from lattice dislocation activities to grain boundary–related processes. We investigated the maximum strength of nanotwinned copper samples with different twin thicknesses. We found that the strength increases with decreasing twin thickness, reaching a maximum at 15 nanometers, followed by a softening at smaller values that is accompanied by enhanced strain hardening and tensile ductility. The strongest twin thickness originates from a transition in the yielding mechanism from the slip transfer across twin boundaries to the activity of preexisting easy dislocation sources.

The strength of polycrystalline materials increases with decreasing grain size, as described by the well-known Hall-Petch relation (*1*, *2*). The strengthening originates from the fact that grain boundaries block the lattice dislocation motion, thereby making plastic deformation more difficult at smaller grain sizes. However, below a certain critical size, the dominating deformation mechanism may change from lattice dislocation activities to other mechanisms such as grain boundary–related processes, and softening behavior (rather than strengthening) is expected (*3*, *4*). Such a softening phenomenon has been demonstrated by atomistic simulations, and a critical grain size of maximum strength has been predicted (*5*–*7*). In pure metals, an impediment to determining the grain size that yields the highest strength is the practical difficulty of obtaining stable nanostructures with extremely small structural domains (on the order of several nanometers). The driving force for growth of nanosized grains in pure metals, originating from the high excess energy of numerous grain boundaries, becomes so large that grain growth may take place easily even at ambient temperature or below.

[1]Shenyang National Laboratory for Materials Science, Institute of Metal Research, Chinese Academy of Sciences, Shenyang 110016, P.R. China. [2]Center for Fundamental Research: Metal Structures in Four Dimensions, Materials Research Department, Risø National Laboratory for Sustainable Energy, Technical University of Denmark, DK-4000 Roskilde, Denmark.

*To whom correspondence should be addressed. E-mail: llu@imr.ac.cn

Coherent twin boundaries (TBs), which are defined in a face-centered cubic structure as the (111) mirror planes at which the normal stacking sequence of (111) planes is reversed, are known to be as effective as conventional grain boundaries in strengthening materials. Strengthening has been obtained in Cu when high densities of nanometer-thick twins are introduced into submicrometer-sized grains (*8*–*10*). In addition, coherent TBs are much more stable against migration (a fundamental process of coarsening) than conventional grain boundaries, as the excess energy of coherent TBs is one order of magnitude lower than that of grain boundaries. Hence, nanotwinned structures are energetically more stable than nanograined counterparts with the same chemical composition. The stable nanotwinned structure may provide samples for exploring the softening behavior with very small domain sizes. Here, we prepared nanotwinned pure Cu (nt-Cu) samples with average twin thickness ranging from a few nanometers to about 100 nm.

High-purity (99.995%) Cu foil samples composed of nanoscale twin lamellae embedded in submicrometer-sized grains were synthesized by means of pulsed electrodeposition. By increasing the deposition rate to 10 nm/s, we succeeded in refining the mean twin thickness (i.e., the mean spacing between adjacent TBs, hereafter referred to as λ) from a range of 15 to 100 nm down to a range of 4 to 10 nm (see supporting online material). The as-deposited Cu foils have an in-plane dimension of 20 mm by 10 mm and a thickness of 30 μm with a uniform microstructure. Shown in Fig. 1, A to C, are transmission electron microscopy (TEM) plane-view images of three as-deposited samples with λ values of 96 nm, 15 nm, and 4 nm, respectively. The TEM images indicate that some grains are irregular in shape, but low-magnification scanning electronic microscopy images, both cross section and plane view, show that the grains are roughly equiaxed in three dimensions. Grain size measurements showed a similar distribution and a similar average diameter of about 400 to 600 nm for all nt-Cu samples. Twins were formed in all grains (see the electron diffraction pattern in Fig. 1D), and observations of twins in a large number of individual grains revealed no obvious change in the twin density from grain to grain. Note that in all samples, the edge-on twins that formed in different grains are aligned randomly around the foil normal (growth) direction (*8*, *11*), in agreement with a strong [110] texture determined by x-ray diffraction (XRD). For each sample, twin thicknesses were measured from a large number of grains, which were detected from numerous TEM and high-resolution TEM (HRTEM) images, to generate a distribution. Figure 1E illustrates the 492 measurements for the sample with the finest twins; the majority yielded spacings between twins smaller than 10 nm, with a mean of 4 nm. For simplicity, each nt-Cu sample is identified by its mean twin thickness; for example, the sample with $\lambda = 4$ nm is referred to as nt-4.

Figure 2 shows the uniaxial tensile true stress–true strain curves for nt-Cu samples of various λ values. Also included are two stress-strain curves obtained from a coarse-grained Cu (cg-Cu) and an ultrafine-grained Cu (ufg-Cu) that has a similar grain size to that of nt-Cu samples but is free of twins within grains. Two distinct features are observed with respect to the λ dependence of the mechanical behavior of nt-Cu. The first is the occurrence of the λ giving the highest strength. All stress-strain curves of nt-Cu samples in Fig. 2, A and B, are above that of the ufg-Cu, indicating a strengthening by introducing twins into the submicrometer grains. However, such a strengthening does not show a linear relationship with λ. For $\lambda > 15$ nm (Fig. 2A), the stress-strain curves shift upward with decreasing λ, similar to the strengthening behavior reported previously in the nt-Cu (*9*, *11*) and nanocrystalline Cu (nc-Cu) (*12*–*15*) samples (Fig. 3A). However, with further de-

creases of λ down to extreme dimensions (i.e., less than 10 nm), the stress-strain curves shift downward (Fig. 2B). As plotted in Fig. 3A, the measured yield strength σ_y (at 0.2% offset) shows a maximum value of 900 MPa at $\lambda \approx 15$ nm.

The second feature is a substantial increase in tensile ductility and strain hardening when $\lambda < 15$ nm. As seen in Fig. 2, the tensile elongation of the nt-Cu samples increases monotonically with decreasing λ. When $\lambda < 15$ nm, the uniform tensile elongation exceeds that of the ufg-Cu sample, reaching a maximum value of 30% at the finest twin thickness. Strain-hardening coefficient (n) values were determined for each sample by fitting the uniform plastic deformation region to $\sigma = K_1 + K_2\varepsilon^n$, where K_1 represents the initial yield stress and K_2 is the strengthening coefficient (i.e., the strength increment due to strain hardening at strain $\varepsilon = 1$) (*16*, *17*). The n values determined for all the nt-Cu samples increase monotonically with decreasing λ (Fig. 3B), similar to the trend of uniform elongation versus λ. When $\lambda < 15$ nm, n exceeds the value for cg-Cu (0.35) (*16*, *17*) and finally reaches a maximum of 0.66 at $\lambda = 4$ nm. The twin refinement–induced increase in n is opposite to the general observation in ultrafine-grained and nanocrystalline materials, where n continuously decreases with decreasing grain size (Fig. 3B).

The strength of the nt-Cu samples has been considered to be controlled predominantly by the nanoscale twins via the mechanism of slip transfer across the TBs (*10*, *18*), and it increases with decreasing λ in a Hall-Petch–type relationship (*9*) similar to that of grain boundary strengthening in nanocrystalline metals (*12*). Our results show that such a relationship breaks down when $\lambda < 15$ nm, although other structural parameters such as grain size and texture are unchanged. The grain sizes of the nt-Cu samples are in the submicrometer regime, which is too large for grain boundary sliding to occur at room temperature, as expected for nanocrystalline materials with grain sizes below 20 nm (*3*). Therefore, the observed softening cannot be explained by the initiation of grain boundary–mediated mechanisms such as grain boundary sliding and grain rotation, as proposed by molecular dynamics (MD) simulations for nanocrystalline materials (*3*).

To explore the origin of the twin thickness giving the highest strength, we carried out detailed structural characterization of the as-deposited samples. HRTEM observations showed that in each sample TBs are coherent Σ3 interfaces associated with the presence of Shockley partial dislocations (as steps), as indicated in Fig. 1D. These partial dislocations have their Burgers vector parallel to the twin plane and are an intrinsic structural feature of twin growth during electrodeposition. The distribution of the preexisting partial dislocations is inhomogeneous, but their density per unit area of TBs is found to be rather constant among samples with different twin densities. This suggests that the deposition parameters and the twin refinement have a negligible effect on the nature of TBs. Therefore, as a consequence of decreasing λ, the density of such TB-associated partial dislocations per unit volume increases.

We also noticed that grain boundaries in the nt-Cu samples with $\lambda \leq 15$ nm are characterized by straight segments (facets) that are often

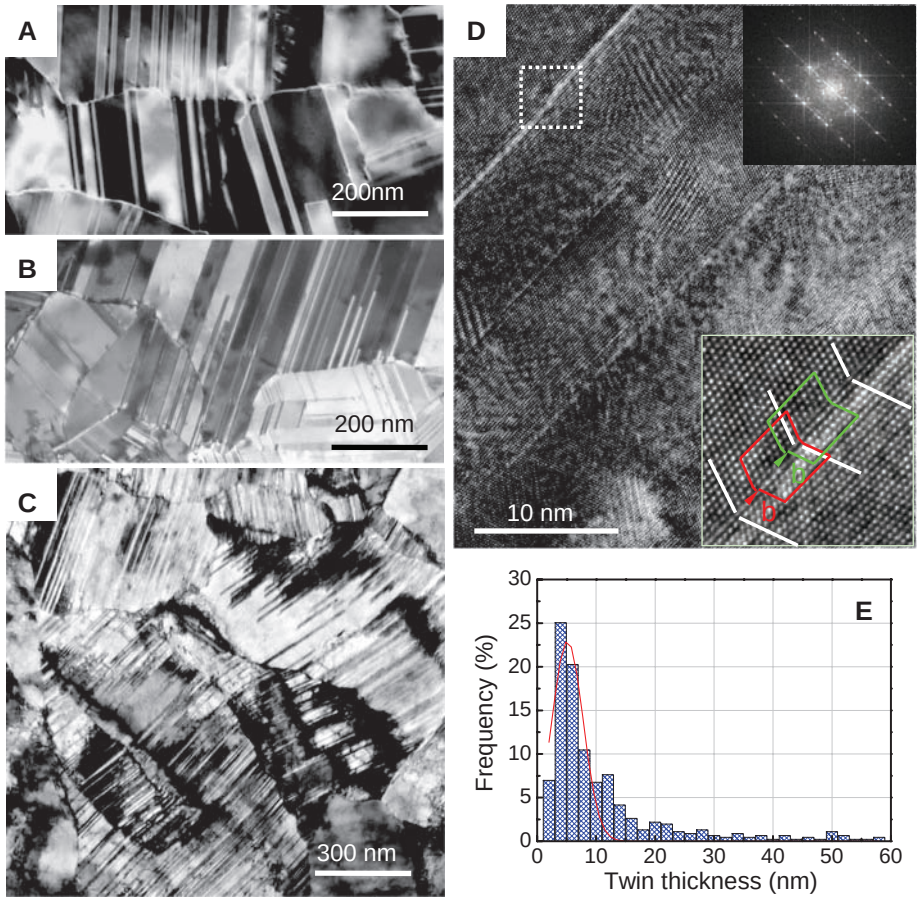

Fig. 1. TEM images of as-deposited Cu samples with various mean twin thicknesses. (**A**) $\lambda = 96$ nm. (**B**) $\lambda = 15$ nm. (**C**) $\lambda = 4$ nm. (**D**) The same sample as (C) but at higher resolution, with a corresponding electron diffraction pattern (upper right inset) and a HRTEM image of the outlined area showing the presence of Shockley partials at the TB (lower right inset). (**E**) Distribution of the lamellar twin thicknesses determined from TEM and HRTEM images for $\lambda = 4$ nm.

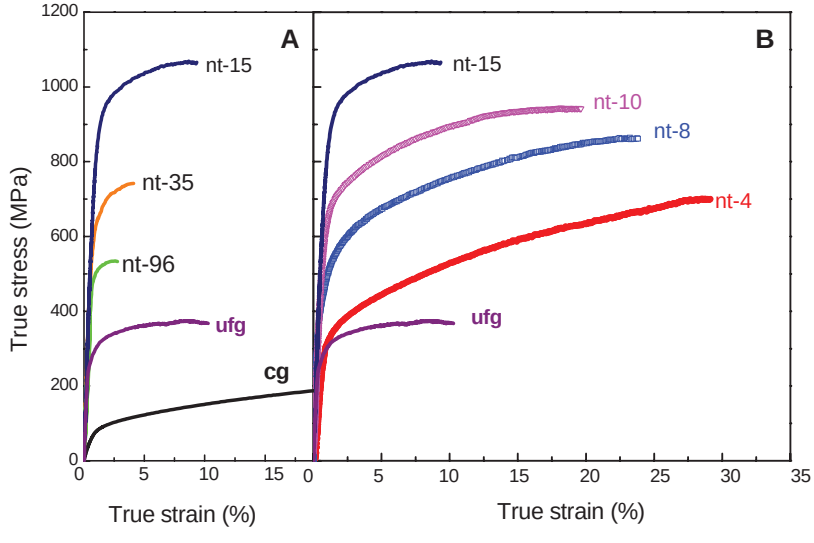

Fig. 2. Uniaxial tensile true stress–true strain curves for nt-Cu samples tested at a strain rate of 6×10^{-3} s^{-1}. (**A**) Curves for samples with mean twin thickness varying from 15 to 96 nm; (**B**) curves for samples with mean twin thickness varying from 4 to 15 nm. For comparison, curves for a twin-free ufg-Cu with a mean grain size of 500 nm and for a cg-Cu with a mean grain size of 10 μm are included.

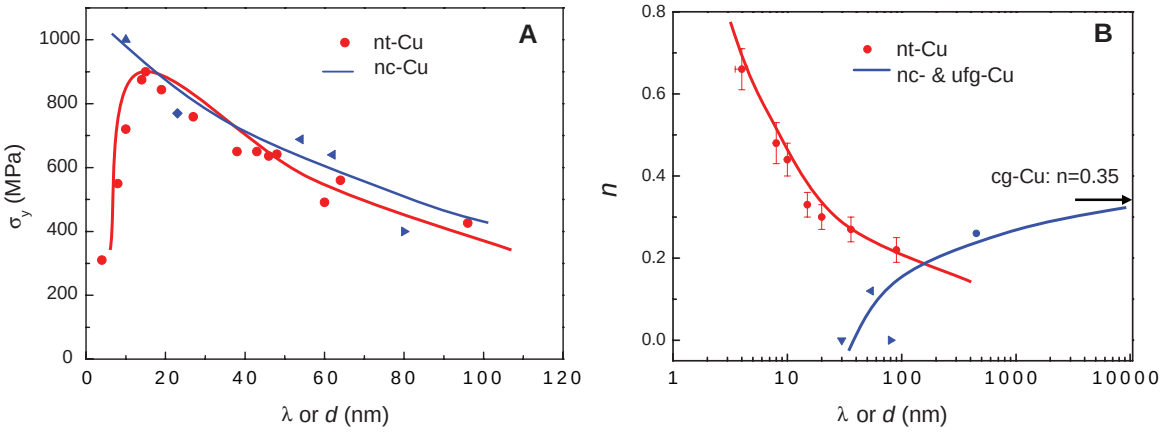

Fig. 3. Variation of (**A**) yield strength and (**B**) strain hardening coefficient *n* as a function of mean twin thickness for the nt-Cu samples. For comparison, the yield strength and *n* values for nc-Cu [▲ (*12*), ◀ (*13*), ▶ (*14*), and ◆ (*15*)], ufg-Cu [▼ (*9*)], and cg-Cu samples reported in the literature are included. A maximum in the yield stress is seen for the nt-Cu with λ = 15 nm, but this has not been observed for the nc-Cu, even when the grain size is as small as 10 nm.

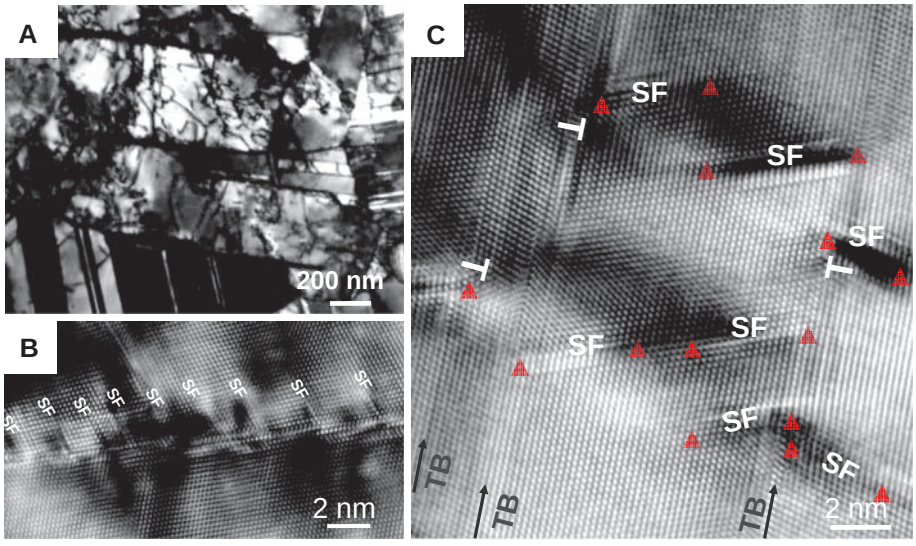

Fig. 4. (**A**) A typical bright TEM image of the deformed nt-96 sample showing the tangling of lattice dislocations. (**B**) An HRTEM image of the nt-4 sample tensile-deformed to a plastic strain of 30%, showing a high density of stacking faults (SF) at the TB. (**C**) The arrangement of Shockley partials and stacking faults at TBs within the lamellae in the nt-4 sample. Triangles, Shockley partial dislocations associated with stacking faults; ⊥, partials with their Burgers vector parallel to the TB plane.

associated with dislocation arrays (*19*), whereas in samples with coarser twins, grain boundaries are smoothly curved, similar to conventional grain boundaries. The microstrain measured by XRD was a negligible 0.01% for samples with λ ≥ 15 nm, but increased gradually from 0.038% to 0.057% when λ decreased from 10 to 4 nm, which also indicates a gradual increase in the defect density.

Recent experimental studies and MD simulations (*3*, *20*, *21*) have shown that an increase in the density of preexisting dislocations in nanoscale materials will cause softening. In the nt-Cu samples studied, both the dislocation arrays associated with the grain boundaries and the steps associated with the preexisting partial dislocations along TBs could be potential dislocation sources, which are expected to affect the initiation of plastic deformation (*22*) and to provide the dislocations required for the dislocation-TB interactions that cause work hardening. The preexisting partial dislocations can act as readily mobile dislocations, and their motion may contribute to the plastic yielding when an external stress is applied to the sample. The plastic strains induced by the motion of preexisting partial dislocations can be estimated as $\varepsilon = \rho_0 b_s d/M$ (where ρ_0 is the initial dislocation density, b_s is the Burgers vector of Shockley partial dislocation, d is the grain size, and M is the Taylor factor). Calculations showed that for the samples with λ > 15 nm, the preexisting dislocations induce a negligibly small plastic strain (<0.05%). However, for the nt-4 specimen, a remarkable amount of plastic strain, as high as 0.1 to 0.2%, can be induced just by the motions of high-density preexisting dislocations at TBs (roughly 10^{14} m^{-2}), which could control the macroscopic yielding of the sample. The above analysis suggests that for extremely small values of λ, a transition in the yielding mechanism can result in an unusual softening phenomenon in which the preexisting easy dislocation sources at TBs and grain boundaries dominate the plastic deformation instead of the slip transfer across TBs.

Shockley partial dislocations are always involved in growth of twins during crystal growth, thermal annealing, or plastic deformation. Shockley partials might be left at TBs when the twin growth is interrupted. Therefore, the presence of Shockley partials at some TBs is a natural phenomenon. Although these preexisting dislocations may have a small effect on the mechanical behavior of the samples with thick twins, the effect will be much more pronounced in the samples with nanoscale twins and/or with high preexisting TB dislocation densities such as those seen in deformation twins (*23*).

To understand the extraordinary strain hardening, we analyzed the deformation structures of the tensile-deformed samples. In samples with coarse twins, tangles and networks of perfect dislocations were observed within the lattice between the TBs (Fig. 4A), and the dislocation density was estimated to be on the order of 10^{14} to 10^{15} m^{-2}. In contrast, high densities of stacking faults and Shockley partials associated with the TBs were found to characterize the deformed structure of the nt-4 sample (Fig. 4, B and C), indicating the interactions between dislocations and TBs. Recent MD simulations (*18*, *24*, *25*) showed that when an extended dislocation (two Shockley partials connected by a stacking fault ribbon) is forced by an external stress into a coherent TB, it recombines or constricts into a perfect dislocation configuration at the coherent TB and then slips through the boundary by splitting into three Shockley partials. Two of them glide in the slip plane of the adjacent twin lamella, constituting a new extended dislocation, whereas the third one, a twinning partial, glides along the TB and forms a step. It is expected that with increasing strain, such an interaction process will generate a high density of partial dislocations (steps) along TBs and stacking faults that align with the slip planes in the twin lamellae, which may (or may not) connect to the TBs. Such a configuration of defects was observed, as shown in Fig. 4C. The density of partial dislocations in the deformed nt-4 sample

was estimated to be 5×10^{16} m^{-2} on the basis of the spacing between the neighboring partials and λ. This is two orders of magnitude higher than that of the preexisting dislocations and the lattice dislocations stored in the coarse twins. Such a finding suggests that decreasing the twin thickness facilitates the dislocation-TB interactions and affords more room for storage of dislocations, which sustain more pronounced strain hardening in the nt-Cu (*26*, *27*).

These observations suggest that the strain-hardening behavior of nt-Cu samples is governed by two competing processes: dislocation-dislocation interaction hardening in coarse twins, and dislocation-TB interaction hardening in fine twins. With a refining of λ, the contribution from the latter mechanism increases and eventually dominates the strain hardening, as revealed by the continuous increase of *n* values (Fig. 3B). However, the former hardening mechanism usually leads to an inverse trend, diminishing with size refinement (*17*).

Twins are not uncommon in nature, and they appear in various metals and alloys with different crystallographic structures. Extremely thin twin lamellae structures can possibly be achieved under proper conditions during crystal growth, plastic deformation, phase transformations, or thermal annealing of deformed structures. Our finding of the twin thickness giving maximum strength illustrates that the scale-dependent nature of plastic deformation of nanometer-scale materials is not necessarily related to grain boundary–mediated processes. This finding also provides insight into the development of advanced nanostructured materials.

References and Notes

1. E. O. Hall, *Proc. Phys. Soc. London Ser. B* **64**, 747 (1951).
2. N. J. Petch, *J. Iron Steel Inst.* **174**, 25 (1953).
3. J. Schiøtz, K. W. Jacobsen, *Science* **301**, 1357 (2003).
4. S. Yip, *Nature* **391**, 532 (1998).
5. M. A. Meyers, A. Mishra, D. J. Benson, *Prog. Mater. Sci.* **51**, 427 (2006).
6. P. G. Sanders, J. A. Eastman, J. R. Weertman, *Acta Mater.* **45**, 4019 (1997).
7. C. C. Koch, K. M. Youssef, R. O. Scattergood, K. L. Murty, *Adv. Eng. Mater.* **7**, 787 (2005).
8. L. Lu *et al.*, *Acta Mater.* **53**, 2169 (2005).
9. Y. F. Shen, L. Lu, Q. H. Lu, Z. H. Jin, K. Lu, *Scr. Mater.* **52**, 989 (2005).
10. X. Zhang *et al.*, *Acta Mater.* **52**, 995 (2004).
11. L. Lu, Y. Shen, X. Chen, L. Qian, K. Lu, *Science* **304**, 422 (2004); published online 18 March 2004 (10.1126/science.1092905).
12. J. Chen, L. Lu, K. Lu, *Scr. Mater.* **54**, 1913 (2006).
13. S. Cheng *et al.*, *Acta Mater.* **53**, 1521 (2005).
14. Y. Champion *et al.*, *Science* **300**, 310 (2003).
15. Y. M. Wang *et al.*, *Scr. Mater.* **48**, 1851 (2003).
16. A. Misra, X. Zhang, D. Hammon, R. G. Hoagland, *Acta Mater.* **53**, 221 (2005).
17. M. A. Meyers, K. K. Chawla, in *Mechanical Behavior of Materials*, M. Horton, Ed. (Prentice Hall, Upper Saddle River, NJ, 1999), pp. 112–135.
18. Z. H. Jin *et al.*, *Scr. Mater.* **54**, 1163 (2006).
19. X. H. Chen, L. Lu, K. Lu, *J. Appl. Phys.* **102**, 083708 (2007).
20. X. Huang, N. Hansen, N. Tsuji, *Science* **312**, 249 (2006).
21. Z. W. Shan, R. K. Mishra, S. A. Syed Asif, O. L. Warren, A. M. Minor, *Nat. Mater.* **7**, 115 (2008).
22. K. Konopka, J. Mizera, J. W. Wyrzykowski, *J. Mater. Process. Technol.* **99**, 255 (2000).
23. Y. S. Li, N. R. Tao, K. Lu, *Acta Mater.* **56**, 230 (2008).
24. S. I. Rao, P. M. Hazzledine, *Philos. Mag. A* **80**, 2011 (2000).
25. Z. H. Jin *et al.*, *Acta Mater.* **56**, 1126 (2008).
26. M. Dao, L. Lu, Y. Shen, S. Suresh, *Acta Mater.* **54**, 5421 (2006).
27. T. Zhu, J. Li, A. Samanta, H. G. Kim, S. Suresh, *Proc. Natl. Acad. Sci. U.S.A.* **104**, 3031 (2007).

28. Supported by National Natural Science Foundation of China grants 50431010, 50621091, 50725103, and 50890171, Ministry of Science and Technology of China grant 2005CB623604, and the Danish National Research Foundation through the Center for Fundamental Research: Metal Structures in Four Dimensions (X.H.). We thank N. Hansen, Z. Jin, W. Pantleon, and B. Ralph for stimulating discussions, X. Si and H. Ma for sample preparation, S. Zheng for TEM observations, and Y. Shen for conducting some of the tensile tests.

Supporting Online Material

www.sciencemag.org/cgi/content/full/323/5914/607/DC1
Materials and Methods
Table S1
References

24 October 2008; accepted 30 December 2008
10.1126/science.1167641

Control of Graphene's Properties by Reversible Hydrogenation: Evidence for Graphane

D. C. Elias,[1]* R. R. Nair,[1]* T. M. G. Mohiuddin,[1] S. V. Morozov,[2] P. Blake,[3] M. P. Halsall,[1] A. C. Ferrari,[4] D. W. Boukhvalov,[5] M. I. Katsnelson,[5] A. K. Geim,[1,3] K. S. Novoselov[1]†

Although graphite is known as one of the most chemically inert materials, we have found that graphene, a single atomic plane of graphite, can react with atomic hydrogen, which transforms this highly conductive zero-overlap semimetal into an insulator. Transmission electron microscopy reveals that the obtained graphene derivative (graphane) is crystalline and retains the hexagonal lattice, but its period becomes markedly shorter than that of graphene. The reaction with hydrogen is reversible, so that the original metallic state, the lattice spacing, and even the quantum Hall effect can be restored by annealing. Our work illustrates the concept of graphene as a robust atomic-scale scaffold on the basis of which new two-dimensional crystals with designed electronic and other properties can be created by attaching other atoms and molecules.

Graphene, a flat monolayer of carbon atoms tightly packed into a honeycomb lattice, continues to attract immense interest, mostly because of its unusual electronic properties and effects that arise from its truly atomic thickness (*1*). Chemical modification of graphene has been less explored, even though research on carbon nanotubes suggests that graphene can be altered chemically without breaking its resilient C-C bonds. For example, graphene oxide is graphene densely covered with hydroxyl and other groups (*2*–*6*). Unfortunately, graphene oxide is strongly disordered, poorly conductive, and difficult to reduce to the original state (*6*). However, one can imagine atoms or molecules being attached to the atomic scaffold in a strictly periodic manner, which should result in a different electronic structure and, essentially, a different crystalline material. Particularly elegant is the idea of attaching atomic hydrogen to each site of the graphene lattice to create graphane (*7*), which changes the hybridization of carbon atoms from sp^2 into sp^3, thus removing the conducting π-bands and opening an energy gap (*7*, *8*).

Previously, absorption of hydrogen on graphitic surfaces was investigated mostly in conjunction with hydrogen storage, with the research focused on physisorbed molecular hydrogen (*9*–*11*). More recently, atomic hydrogen chemisorbed on carbon nanotubes has been studied theoretically (*12*) as well as by a variety of experimental techniques including infrared (*13*), ultraviolet (*14*, *15*), and x-ray (*16*) spectroscopy and scanning tunneling microscopy (*17*). We report the reversible hydrogenation of single-layer graphene and observed dramatic changes in its transport properties and in its electronic and atomic structure, as evidenced by Raman spectroscopy and transmission electron microscopy (TEM).

Graphene crystals were prepared by use of micromechanical cleavage (*18*) of graphite on top of an oxidized Si substrate (300 nm SiO_2) and then identified by their optical contrast (*1*, *18*) and distinctive Raman signatures (*19*). Three types of samples were used: large (>20 μm) crystals for Raman studies, the standard Hall bar devices 1 μm in width (*18*), and free-standing membranes (*20*, *21*) for TEM. For details of sample fabrication, we refer to earlier work (*18*, *20*, *21*).

[1]School of Physics and Astronomy, University of Manchester, M13 9PL, Manchester, UK. [2]Institute for Microelectronics Technology, 142432 Chernogolovka, Russia. [3]Manchester Centre for Mesoscience and Nanotechnology, University of Manchester, M13 9PL, Manchester, UK. [4]Department of Engineering, Cambridge University, 9 JJ Thomson Avenue, Cambridge CB3 OFA, UK. [5]Institute for Molecules and Materials, Radboud University Nijmegen, 6525 ED Nijmegen, Netherlands.

*These authors contributed equally to this work.
†To whom correspondence should be addressed. E-mail: Kostya@manchester.ac.uk

We first annealed all samples at 300°C in an argon atmosphere for 4 hours in order to remove any possible contamination (for example, resist residues). After their initial characterization, the samples were exposed to a cold hydrogen plasma. We used a low-pressure (0.1 mbar) hydrogen-argon mixture (10% H_2) with dc plasma ignited between two aluminum electrodes. The samples were kept 30 cm away from the discharge zone in order to minimize any possible damage by energetic ions. We found that it typically required 2 hours of plasma treatment to reach the saturation in measured characteristics. As a reference, we used graphene samples exposed to a pure Ar plasma under the same conditions, which showed little changes in their transport and Raman properties (*22*).

Typical changes induced by the hydrogenation in electronic properties of graphene are illustrated in Fig. 1. Before plasma exposure, our devices exhibited the standard ambipolar field effect with the neutrality point (NP) near zero gate voltage (*18*). For the device shown in Fig. 1, mobility μ of charge carriers was ≈14,000 cm^2 V^{-1} s^{-1}. This device exhibits a weak temperature dependence of its resistivity at all gate voltages (not visible on the scale of Fig. 1A). We observed metallic dependence close to the NP below 50 K (*23*) and the half-integer quantum Hall effect (QHE) at cryogenic temperatures (Fig. 1B), both of which are hallmarks of single-layer graphene [(*1*) and references therein].

This behavior completely changed after the devices were treated with atomic hydrogen (Fig. 1, C and D). The devices exhibited an insulating behavior such that the resistivity ρ grew by two orders of magnitude with decreasing temperature T from 300 to 4 K (Fig. 1C). Carrier mobility decreased at liquid-helium temperatures down to values of ~10 cm^2 V^{-1} s^{-1} for typical carrier concentrations n of the order of 10^{12} cm^{-2}. The quantum Hall plateaus, so marked in the original devices, completely disappeared, with only weak signatures of Shubnikov–de-Haas oscillations remaining in magnetic field B of 14 T (Fig. 1D). In addition, we observed a shift of NP to gate voltages $V_g \approx +50$ V, which showed that graphene became doped with holes in concentration of $\approx 3 \times 10^{12}$ cm^{-2} (probably due to adsorbed water). At carrier concentrations of less than 3×10^{12} cm^{-2}, the observed temperature dependences $\rho(T)$ can be well fitted by the function $\exp[(T_0/T)^{1/3}]$ (T_0 is the parameter that depends on V_g) (Fig. 2), which is a signature of variable-range hopping in two dimensions (*24*). T_0 exhibits a maximum at NP of ~250 K and strongly decreases away from NP (Fig. 2B). At $n > 4 \times 10^{12}$ cm^{-2} (for both electrons and holes), changes in ρ with T became small (similar to those in pristine graphene), which indicates a transition from the insulating to the metallic regime.

The hydrogenated devices were stable at room T for many days and showed the same characteristics during repeated measurements. However, we could restore the original metallic state by annealing (we used 450°C in Ar atmosphere for 24 hours; higher annealing T damaged graphene). After the annealing, the devices returned practically to the same state as before hydrogenation: ρ as a function of V_g reached again a maximum value of $\approx h/4e^2$, where h is Planck's constant and e is the electron charge, and became only weakly T-dependent (Figs. 1E and 2). Also, μ recovered to ~3500 cm^2 V^{-1} s^{-1}, and the QHE reappeared (Fig. 1F). Still, the recovery was not complete: Graphene remained p-doped, the QHE did not restore at filling factors ν larger than ±2 (compare Figure 1, B and F), and zero–B field conductivity σ (=1/ρ) became a sublinear function of n, which indicates an increased number of short-range scatterers (*23*). We attribute the remnant features to vacancies induced by plasma damage or residual oxygen during annealing. To this end, after annealing, the distance (as a function of V_g) between

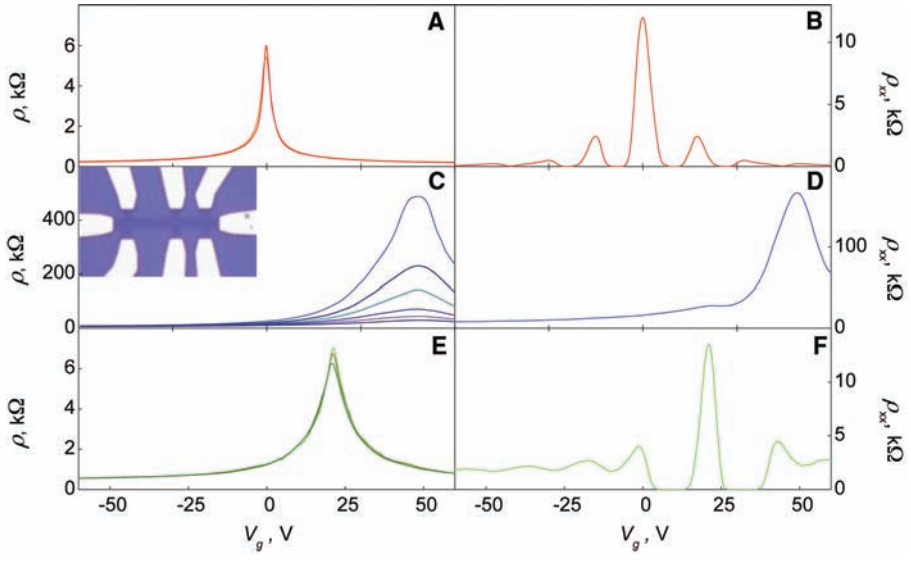

Fig. 1. Control of the electronic properties of graphene by hydrogenation. The electric field effect for one of our devices at zero B at various temperatures T (left column) and in B = 14 T at 4 K (right). (**A** and **B**) The sample before its exposure to atomic hydrogen; curves in (A) for three temperatures (40, 80, and 160 K) practically coincide. (**C** and **D**) After atomic hydrogen treatment. In (C), temperature increases from the top; T = 4, 10, 20, 40, 80, and 160 K. (**E** and **F**) The same sample after annealing. (E) T = 40, 80, and 160 K, from top to bottom. (Inset) Optical micrograph of a typical Hall bar device. The scale is given by its width of 1 μm.

Fig. 2. Metal-insulator transition in hydrogenated graphene. (**A**) Temperature dependence of graphene's resistivity at NP for the sample shown in Fig. 1. Red circles, blue squares, and green triangles are for pristine, hydrogenated, and annealed graphene, respectively. The solid line is a fit by the variable-range hopping dependence $\exp[(T_0/T)^{1/3}]$. (**B**) Characteristic exponents T_0 found from this fitting at different carrier concentrations.

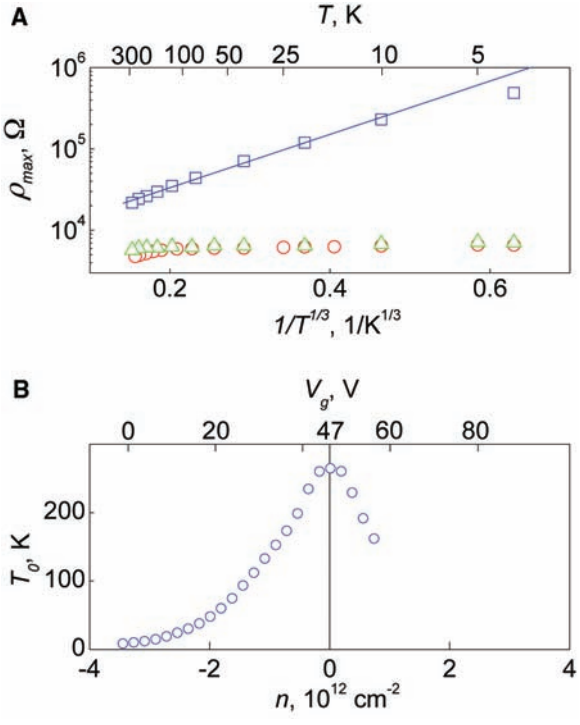

the peaks in ρ_{xx} at $\nu = 0$ and $\nu = \pm 4$ became notably greater (~40%) than that between all the other peaks for both annealed and original devices. The greater distance indicates the presence of mid-gap states (*25*) [such as vacancies (*26*)] that were induced during the processing, which was in agreement with the observed sublinear behavior of the conductivity. The extra charge required to fill these states (*25*) yields their density as of about 1×10^{12} cm^{-2} (with an average spacing of ≈10 nm).

The changes induced by hydrogenation have been corroborated by Raman spectroscopy. The main features in the Raman spectra of carbon-based materials are the G and D peaks that lie at around 1580 and 1350 cm^{-1}, respectively. The G peak corresponds to optical E_{2g} phonons at the Brillouin zone center, whereas the D peak is caused by breathing-like modes (corresponding to transverse optical phonons near the K point) and requires a defect for its activation via an intervalley double-resonance Raman process (*19*, *27*–*29*). Both the G and D peaks arise from vibrations of sp^2-hybridized carbon atoms. The D peak intensity provides a convenient measure for the amount of disorder in graphene (*27*–*29*). Its overtone, the 2D peak, appears around 2680 cm^{-1} and its shape identifies monolayer graphene (*19*). The 2D peak is present even in the absence of any defects because it is the sum of two phonons with opposite momentum. In Fig. 3, there is also a peak at ~1620 cm^{-1}, called D′, which occurs via an intravalley double-resonance process in the presence of defects.

Figure 3A shows the evolution of Raman spectra for graphene crystals that are hydrogenated and annealed simultaneously with the device in Fig. 1 (the use of different samples for Raman studies was essential to avoid an obscuring contribution to the D and D′ peaks caused by the edges of the Hall bars, which were smaller than our laser spot size of about 1 μm). Hydrogenation resulted in the appearance of sharp D and D′ peaks, slight broadening and a decrease of the height of the 2D peak relative to the G peak, and the onset of a combination mode (D + D′) around 2950 cm^{-1}, which, unlike the 2D and 2D′ bands, requires a defect for its activation because it is a combination of two phonons with different momentum. The D peak in hydrogenated graphene is observed at 1342 cm^{-1} and is very sharp, as compared with that in disordered or nanostructured carbon-based materials (*29*). We attribute the activation of this sharp D peak in our hydrogenated samples to breaking of the translational symmetry of C-C sp^2 bonds after the formation of C-H sp^3 bonds. Although the majority of carbon bonds in hydrogenated graphene are expected to acquire sp^3 hybridization, we do not expect to see any Raman signature of C-C sp^3 bonds because their cross section at visible light excitation is negligible as compared with that of the resonant C-C sp^2 bonds, and therefore even a small residual sp^2 phase should generally dominate our spectra, as happens in other diamondlike compounds (*22*, *29*).

After annealing, the Raman spectrum recovered to almost its original shape, and all of the

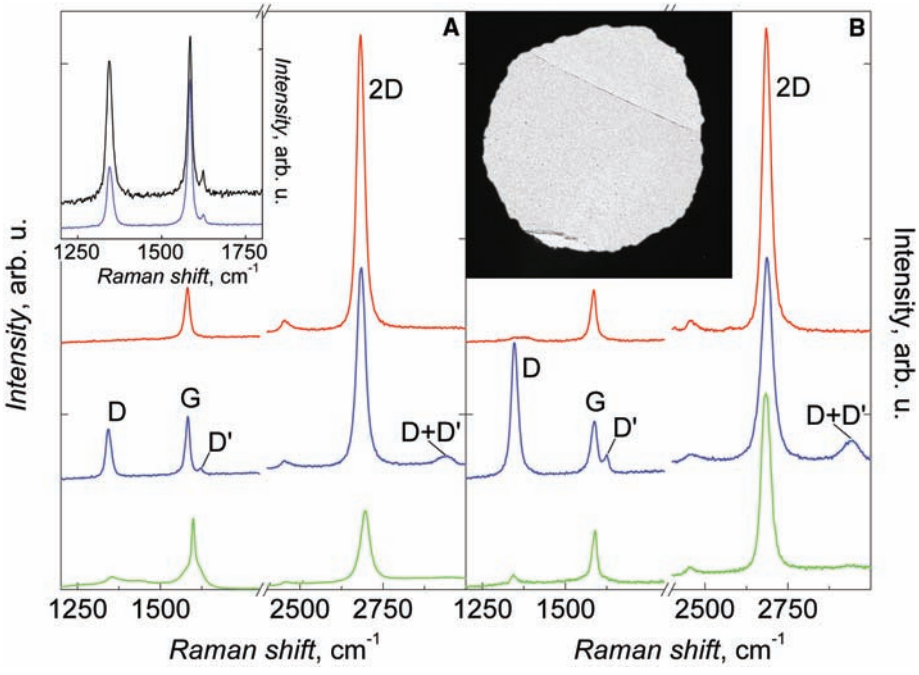

Fig. 3. Changes in Raman spectra of graphene caused by hydrogenation. The spectra are normalized to have a similar intensity of the G peak. (**A**) Graphene on SiO_2. (**B**) Free-standing graphene. Red, blue, and green curves (top to bottom) correspond to pristine, hydrogenated, and annealed samples, respectively. Graphene was hydrogenated for ~2 hours, and the spectra were measured with a Renishaw spectrometer at wavelength 514 nm and low power to avoid damage to the graphene during measurements. (Left inset) Comparison between the evolution of D and D′ peaks for single- and double-sided exposure to atomic hydrogen. Shown is a partially hydrogenated state achieved after 1 hour of simultaneous exposure of graphene on SiO_2 (blue curve) and of a membrane (black curve). (Right inset) TEM image of one of our membranes that partially covers the aperture 50 μm in diameter.

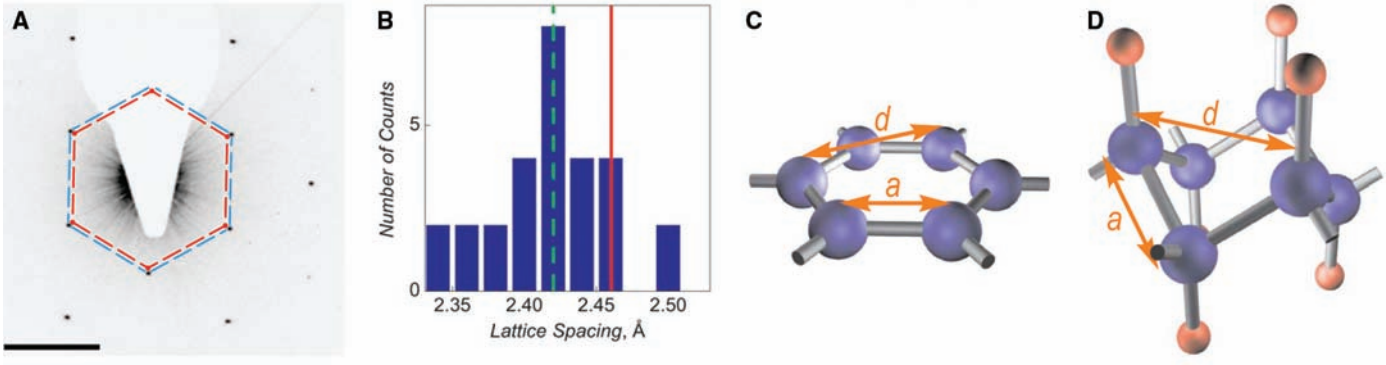

Fig. 4. Structural studies of graphane via TEM [we used a Tecnai F30 (FEI, Eindhoven, the Netherlands)]. (**A**) Changes in the electron diffraction after ~4 hours exposure of graphene membranes to atomic hydrogen. Scale bar, 5 nm^{-1}. The blue hexagon is a guide to the eye and marks positions of the diffraction spots in graphane. The equivalent diffraction spots in graphene under the same conditions are shown by the red hexagon. (**B**) Distribution of the lattice spacing *d* found in hydrogenated membranes. The green dashed line marks the average value, whereas the red solid line shows *d* always observed for graphene (both before hydrogenation and after annealing). (**C** and **D**) Schematic representation of the crystal structure of graphene and theoretically predicted graphane. Carbon atoms are shown as blue spheres, and hydrogen atoms are shown as red spheres.

defect-related peaks (D, D′, and D+D′) were strongly suppressed. However, two broad low-intensity bands appeared, overlapping a sharper G and residual D peaks. These bands are indicative of some residual structural disorder (*29*). The 2D peak remained relatively small with respect to the G peak when compared with the same ratio in the pristine sample, and both became shifted to higher energies, indicating that the annealed graphene is p-doped (*30*). The observed changes in Raman spectra are in broad agreement with our transport measurements.

For graphene on a substrate, only one side is accessible to atomic hydrogen, and the plasma exposure is not expected to result in graphane (which assumes hydrogen atoms attached on both sides). For more effective hydrogenation, we employed free-standing graphene membranes (Fig. 3B, inset) (*20*, *21*). The experiments described below refer to membranes that had some free edges to facilitate the relaxation of strain induced by hydrogenation [membranes with all the sides fixed to a metal scaffold are discussed in (*22*)]. Raman spectra for hydrogenated and subsequently annealed membranes (Fig. 3B) were rather similar to those described above for graphene on SiO_2, but with some notable differences. If hydrogenated simultaneously and before reaching the saturation, the D peak for a membrane was by a factor of two greater than that for graphene on a substrate (Fig. 3A, inset), which indicates the formation of twice as many C-H bonds in the membrane. This result agrees with the general expectation that atomic hydrogen attaches to both sides of membranes. Moreover, the D peak could become up to three times greater than the G peak after prolonged exposures of membranes to atomic hydrogen (Fig. 3B).

Further information about hydrogenated membranes was obtained with TEM. For graphene, the electron-diffraction (ED) patterns observed on dozens of the studied membranes were always the same, exhibiting the hexagonal symmetry with the lattice constant $d = 2.46 \pm 0.02$ Å. Prolonged exposure to atomic hydrogen preserved the hexagonal symmetry and hence crystallinity, but led to drastic changes in the lattice constant d, which could decrease by as much as 5% (Fig. 4A). Generally, the compression was not uniform, and different parts of membranes exhibited locally different in-plane periodicities (Fig. 4B; diameters of the selected area for the ED and studied membranes were 0.3 μm and 30 to 50 μm, respectively). Such nonuniformity is generally not unexpected because the crystals were fixed to the scaffold (Fig. 3) that restricted their isotropic shrinkage. We found that the more extended free edges a membrane had, the more uniformly it became hydrogenated (*22*). In the extreme case of all the edges being fixed to the scaffold, even domains with a stretched lattice could be observed (*22*). Annealing led to complete recovery of the original periodicity observed in TEM.

The in-plane compression of graphene's lattice can only be the result of chemical modification as opposed to physical forces, because any compression that is not stabilized on an atomic scale should cause the membranes to buckle. Furthermore, strains of the order of a few percent would result in massive variations of the Raman peaks, which was not the case. The most obvious candidate for the modified crystal lattice is graphane (*7*, *8*). In this until-now-theoretical material, hydrogen attaches to graphene's sublattices A and B from the two opposite sides, and carbon atoms in A and B move out of the plane ("buckle"), as shown in Fig. 4D. The in-plane periodicity probed by TEM would then substantially shrink if the length a of the C-C bond were to remain the same as in graphene (1.42 Å). However, the change in hybridization from sp^2 to sp^3 generally results in longer C-C bonds, which is the effect opposing to the lattice shrinkage by atomic-scale buckling. Recent calculations (*8*) predicted a in graphane to be ≈1.53 Å (near that of diamond) and the in-plane periodicity d to be ≈1% smaller than in graphene. Although the maximum in the observed distribution of d occurs at ≈2.42 Å (that is, near the theoretical value for graphane) (Fig. 4B), the observation of more compressed areas (such as in Fig. 4A) suggests that the equilibrium d (without strain imposed by the scaffold) should be smaller. The latter implies either shorter or stronger buckled C-C bonds, or both, are present. Alternatively, the experimentally produced graphane may have a more complex hydrogen bonding than the one suggested by theory.

Finally, let us return to the graphene hydrogenated on a substrate (Figs. 1 and 3). Single-sided hydrogenation of ideal graphene would create a material that is thermodynamically unstable (*7*, *8*), and therefore our experiments seem to be in conflict with the theory [for the case of graphene on a substrate, we can exclude the possibility of double-sided hydrogenation because the diffusion of hydrogen along the graphene-SiO_2 interface is negligible (*31*)]. However, realistic graphene samples are not microscopically flat but always rippled (*20*, *21*), which should facilitate their single-sided hydrogenation. Indeed, attached hydrogen is expected to change the hybridization of carbon from sp^2 to (practically) sp^3 with angles of ~110° acquired between all of the bonds (*7*). These constraints necessitate the movement of carbon atoms out of the plane in the direction of the attached hydrogen, at the cost of an increase in elastic energy. However, for a convex surface, the lattice is already deformed in the direction that favors sp^3 bonding, which lowers the total energy. As shown in (*22*), single-sided hydrogenation becomes energetically favorable for a typical size of ripples observed experimentally (*20*). Because of the random nature of ripples, single-sided graphane is expected to be a disordered material, similar to graphene oxide, rather than a new graphene-based crystal. The formation of a disordered material also explains the observation of variable-range hopping in our transport experiments. The importance of ripples for hydrogenation of graphene on a substrate is further evidenced in experiments involving bilayer samples, which show a substantially lower level of hydrogenation than monolayers under the same conditions (*22*). We attribute this observation to the fact that bilayer graphene is less rippled (*20*).

The distinct crystal structure of hydrogenated graphene and pronounced changes in its electronic and phonon properties reveal two new graphene derivatives, one crystalline and the other disordered. The results show that conversion of graphene into other giant molecules with a regular structure is possible.

References and Notes

1. A. K. Geim, K. S. Novoselov, *Nat. Mater.* **6**, 183 (2007).
2. S. Stankovich *et al.*, *J. Mater. Chem.* **16**, 155 (2006).
3. S. Stankovich *et al.*, *Nature* **442**, 282 (2006).
4. X. Wang, L. Zhi, K. Mullen, *Nano Lett.* **8**, 323 (2008).
5. S. Gilje, S. Han, M. Wang, K. L. Wang, R. B. Kaner, *Nano Lett.* **7**, 3394 (2007).
6. C. Gomez-Navarro *et al.*, *Nano Lett.* **7**, 3499 (2007).
7. J. O. Sofo, A. S. Chaudhari, G. D. Barber, *Phys. Rev. B* **75**, 153401 (2007).
8. D. W. Boukhvalov, M. I. Katsnelson, A. I. Lichtenstein, *Phys. Rev. B* **77**, 035427 (2008).
9. A. C. Dillon *et al.*, *Nature* **386**, 377 (1997).
10. F. L. Darkrim, P. Malbrunot, G. P. Tartaglia, *Int. J. Hydrogen Energy* **27**, 193 (2002).
11. A. Züttel *et al.*, *Int. J. Hydrogen Energy* **27**, 203 (2002).
12. T. Yildirim, O. Gulseren, S. Ciraci, *Phys. Rev. B* **64**, 075404 (2001).
13. B. N. Khare, M. Meyyappan, A. M. Cassell, C. V. Nguyen, J. Han, *Nano Lett.* **2**, 73 (2002).
14. P. Ruffieux *et al.*, *Phys. Rev. B* **66**, 245416 (2002).
15. D. Neumann *et al.*, *Appl. Phys. A* **55**, 489 (1992).
16. A. Nikitin *et al.*, *Phys. Rev. Lett.* **95**, 225507 (2005).
17. L. Hornekær *et al.*, *Phys. Rev. Lett.* **96**, 156104 (2006).
18. K. S. Novoselov *et al.*, *Science* **306**, 666 (2004).
19. A. C. Ferrari *et al.*, *Phys. Rev. Lett.* **97**, 187401 (2006).
20. J. C. Meyer *et al.*, *Nature* **446**, 60 (2007).
21. T. J. Booth *et al.*, *Nano Lett.* **8**, 2442 (2008).
22. Supporting online material is available on *Science* Online.
23. S. V. Morozov *et al.*, *Phys. Rev. Lett.* **100**, 016602 (2008).
24. N. F. Mott, *Philos. Mag.* **19**, 835 (1969).
25. T. O. Wehling *et al.*, *Nano Lett.* **8**, 173 (2008).
26. V. M. Pereira, F. Guinea, J. M. B. Lopes dos Santos, N. M. R. Peres, A. H. Castro Neto, *Phys. Rev. Lett.* **96**, 036801 (2006).
27. A. C. Ferrari, *Solid State Commun.* **143**, 47 (2007).
28. F. Tuinstra, J. L. Koenig, *J. Chem. Phys.* **53**, 1126 (1970).
29. A. C. Ferrari, J. Robertson, *Phys. Rev. B* **61**, 14095 (2000).
30. A. Das *et al.*, *Nat. Nanotechnol.* **3**, 210 (2008).
31. J. S. Bunch *et al.*, *Nano Lett.* **8**, 2458 (2008).

32. This work was supported by Engineering and Physical Sciences Research Council (UK), the Royal Society, the European Research Council (programs "Ideas" and "New and Emerging Science and Technology," project "Structural Information of Biological Molecules at Atomic Resolution"), Office of Naval Research, and Air Force Research Office of Scientific Research. D.C.E. acknowledges financial support from the National Council for Scientific and Technological Development (Brazil). The authors are grateful to Nacional de Grafite for providing high-quality crystals of natural graphite.

Supporting Online Material

www.sciencemag.org/cgi/content/full/323/5914/610/DC1
SOM Text
Figs. S1 to S7
References

13 October 2008; accepted 10 December 2008
10.1126/science.1167130

Dynamical Quorum Sensing and Synchronization in Large Populations of Chemical Oscillators

Annette F. Taylor,[1] Mark R. Tinsley,[2] Fang Wang,[2] Zhaoyang Huang,[2] Kenneth Showalter[2]*

Populations of certain unicellular organisms, such as suspensions of yeast in nutrient solutions, undergo transitions to coordinated activity with increasing cell density. The collective behavior is believed to arise through communication by chemical signaling via the extracellular solution. We studied large, heterogeneous populations of discrete chemical oscillators (~100,000) with well-defined kinetics to characterize two different types of density-dependent transitions to synchronized oscillatory behavior. For different chemical exchange rates between the oscillators and the surrounding solution, increasing oscillator density led to (i) the gradual synchronization of oscillatory activity, or (ii) the sudden "switching on" of synchronized oscillatory activity. We analyze the roles of oscillator density and exchange rate of signaling species in these transitions with a mathematical model of the interacting chemical oscillators.

From the periodic firing of neurons to the flashing of fireflies, the synchronization of rhythmic activity plays a vital role in the functioning of biological systems (*1*–*3*). The mechanisms by which single cells or whole organisms coordinate their activity continue to inspire research over a range of disciplines (*4*–*6*). Synchronization may occur by global coupling, where each oscillator is connected to every other oscillator through a common (mean) field. With this mechanism, mathematically formalized by Kuramoto (*7*), oscillators are regulated by the average activity of the population (the mean field) and a collective rhythm emerges above a critical coupling strength. A number of oscillatory systems are thought to synchronize by this mechanism (*8*, *9*), such as stirred suspensions of the cellular slime mold *Dictyostelium discoidium* (*10*), but it has been experimentally characterized only recently in a system of coupled electrochemical oscillators (*11*).

A distinctly different type of transition to synchronized oscillatory behavior has been observed in suspensions of yeast cells (*12*). The density-dependent transition, discovered by Aldridge and Pye (*13*) more than 30 years ago, recently has been studied in a stirred-flow reactor configuration (*14*). Relaxation experiments reveal that slightly below the critical cell density, the system is made up of a collection of quiescent cells rather than unsynchronized oscillatory cells, whereas slightly above the critical density, the cells oscillate in nearly complete synchrony (*12*). This type of transition is much like quorum-sensing transitions in bacteria populations, where each member of a population undergoes a sudden change in behavior with a supercritical increase in the concentration of a signaling molecule (autoinducer) in the extracellular solution (*15*). Many examples of quorum-sensing transitions have been found, such as the appearance of bioluminescence in populations of *Vibrio fischeri* (*16*–*18*) and biofilm formation in *Pseudomonas aeruginosa* (*19*).

We studied a population of chemical oscillators to characterize the transition to synchronization as a function of population density and transport rate of signaling species to the surrounding solution. We used porous catalytic particles (~100 μm in radius) that were suspended in a fixed volume of catalyst-free Belousov-Zhabotinsky (BZ) reaction mixture (*20*, *21*). The catalyst for the reaction, $Fe(phen)_3^{2+}$ (ferroin), is immobilized on the cation exchange particles (*22*, *23*). Reagents in the solution react with the ferroin to produce an activator, $HBrO_2$, which catalyzes its own production, and an inhibitor, Br^-, which inhibits autocatalysis. A catalyst-loaded particle changes from red to blue as ferroin is oxidized and $HBrO_2$ is produced. The oxidized metal catalyst reacts with solution reagents to regenerate the reduced form of the catalyst and Br^-. The cycle repeats when the inhibitor level falls sufficiently. Each catalyst-loaded particle has its own oscillatory period, on the order of 1 min (45 ± 13 s), which depends on the catalyst loading and the particle size. The period distribution (fig. S1) is obtained by monitoring the color change associated with the oxidation of the ferroin catalyst on each particle in unstirred solutions (*21*, *24*).

A sketch of the experimental setup is shown in Fig. 1. Both the activator $HBrO_2$ and inhibitor Br^- are exchanged between the catalyst particles and the surrounding solution, with the exchange rate depending on the stirring rate (*21*). The surrounding solution is monitored with a Pt electrode, where the potential increases with an increasing concentration of $HBrO_2$ relative to Br^-, and the oxidation state of the particles is monitored by high-speed video (*21*). The first time series in Fig. 1 illustrates the change in amplitude of the potential as the oscillator density is increased. The second time series shows the corresponding average intensity obtained from the mean of the individual particle intensities in each image (scaled by the average intensity of fully oxidized particles). When all particles are simultaneously oxidized, the scaled average intensity increases from 0 (all particles red) to 1 (all particles blue), and the value is less than 1 when a fraction of the population is oxidized. The coherence of the population can be seen in images of the stirred particles (Fig. 1).

We observed two distinct types of transitions to synchronous activity, depending on the stirring rate. One type occurs at low stirring rates, as

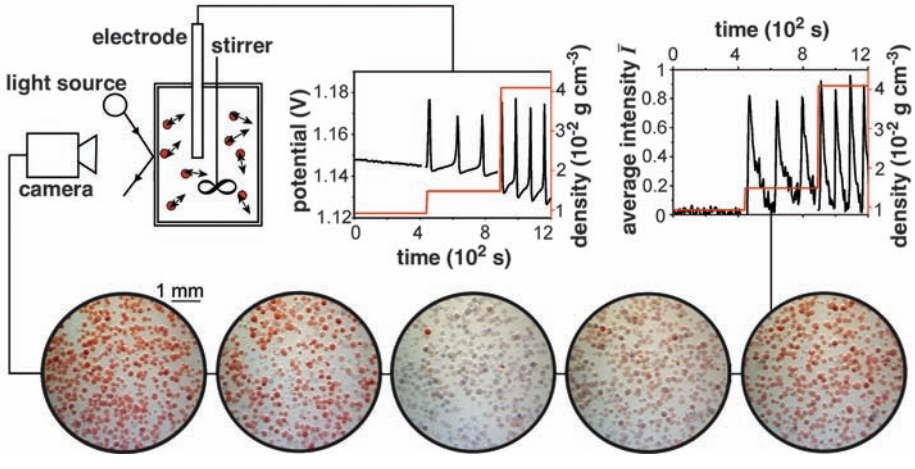

Fig. 1. Experimental setup (*21*). Catalytic microparticles are globally coupled by exchange of species with the surrounding catalyst-free BZ reaction solution. Electrochemical time series illustrates the change in oscillatory amplitude and period with increasing particle density (red line) for a stirring rate of 600 rpm. A typical series of images obtained during one oscillation is shown, from which the (normalized) average intensity of the particles is calculated as a function of time. The associated time series illustrates the change in oscillatory amplitude and period with increasing particle density (red line) for a stirring rate of 600 rpm. A density of 0.02 g cm^{-3} corresponds to ~1.3×10^4 particles cm^{-3}.

[1]School of Chemistry, University of Leeds, Leeds LS2 9JT, UK. [2]C. Eugene Bennett Department of Chemistry, West Virginia University, Morgantown, WV 26506, USA.

*To whom correspondence should be addressed. E-mail: kshowalt@wvu.edu

shown in Fig. 2A for 300 rpm. At low particle densities, the global electrochemical signal is noisy with no regular oscillations. There are also no oscillations in the average intensity of the particle images; however, an approximately constant fraction of oxidized catalyst particles is observed (~20%), representing the fraction of the oscillatory cycle in the oxidized state. As the density is increased, small-amplitude oscillations emerge, and there is a gradual growth in the amplitude of the global electrochemical signal. Corresponding oscillations are also observed in the average image intensity. With a density of 0.02 g cm^{-3}, ~50% of the particles are simultaneously oxidized in an oscillation, and this approaches 100% for densities greater than 0.04 g cm^{-3}, as shown by the maximum average intensity as a function of particle density. Also shown is the period of the oscillations decreasing slightly with increasing particle density.

The other type of transition to synchronous activity occurs at high stirring rates. At low particle density, there is no oscillatory signal in the electrochemical potential and there are no oxidized catalyst particles in the associated images, as shown in Fig. 2B for 600 rpm. As the density is increased beyond a threshold value, large-amplitude oscillations in the global signal suddenly appear, and analysis of the average image intensity shows that ~80% of the particles are simultaneously oxidized each oscillation. As the density is increased further, the maximum fraction of oxidized particles during an oscillation approaches a constant value. The period of oscillation, which is greater than in the low stirring rate case, decreases with increasing density.

Insights into these transitions to synchronized oscillatory behavior can be gained by examining a model of the oscillatory particle system (*20*, *21*). A sketch of the exchange between the particles and the surrounding solution is shown in Fig. 3. The model is based on the three-variable ZBKE scheme (*25*) for the ferroin-catalyzed BZ reaction (*26*), with variables X for the autocatalyst, Y for the inhibitor, and Z for the oxidized form of the metal ion catalyst. The concentration of the autocatalyst for the ith particle ($i = 1, \ldots N$) is given by

$$\frac{dX_i}{dt} = -k_{ex}(X_i - X_s) + f(X_i, Y_i, Z_i) \quad (1)$$

and in the surrounding solution

$$\frac{dX_s}{dt} = \frac{\overline{V}}{V_s}\sum_i N k_{ex}(X_i - X_s) + g(X_s, Y_s) \quad (2)$$

where $f(X_i, Y_i, Z_i)$ represents the chemical reaction on the particle, and $g(X_s, Y_s)$ represents the reaction in the surrounding solution (*21*). The exchange rate of the autocatalyst between the particle and the surrounding solution is given by the term $-k_{ex}(X_i - X_s)$, where the value of the exchange rate constant k_{ex} increases with increasing stirring rate (*21*). The sum of the contributions from each particle gives the concentration in the surrounding solution, with the dilution factor $\overline{V}/V_s$, where V_s is the total volume of solution and $\overline{V}$ is the average volume of a particle. The particle dynamics is periodic for $k_{ex} = 0$ and depends on the number density and the exchange rate for nonzero k_{ex}. There is no mechanism for oscillation in the surrounding solution in the absence of particles; however, in the presence of oscillatory particles, oscillations in X_s and Y_s arise from the exchange between the particles and the solution.

The coherence of the population of oscillators is determined for a sample of $N = 1000$ using the order parameter K introduced by Shinomoto and Kuramoto (*27*):

$$K = \left\langle \left| N^{-1}\sum_j^N \exp(i\theta_j) - \left\langle N^{-1}\sum_j^N \exp(i\theta_j) \right\rangle \right| \right\rangle \quad (3)$$

where θ_j is the phase of the jth oscillator and angle brackets indicate the time average. This coherence measure is 0 when all particles oscillate out of phase with each other (or when the particles are not oscillating) and 1 when all particles oscillate in perfect synchrony. For $k_{ex} = 0$, the particles have a broad distribution of natural periods (38 ± 6 s).

The surface plot in Fig. 3A shows the amplitude of the activator species X_s in the surrounding solution as a function of the number density of particles n, where $n = N/V_s$, and the exchange rate constant k_{ex}. The growth in the amplitude of X_s with increasing n depends on the value of k_{ex}. For $k_{ex} = 0.3$, there is a distribution in the natural period for low n (Fig. 3B). There is a corresponding gradual increase in the coherence parameter K with increasing particle density as the individual oscillators gradually align their frequencies and phases. For $k_{ex} = 3.0$, the catalyst particles are not oscillatory for low values of n (Fig. 3C); however, when n is increased beyond a threshold value, the particles suddenly begin to oscillate in perfect synchrony. The coherence parameter switches from 0 to 1. The gradual transition from unsynchronized to synchronized oscillations at low values of k_{ex}, and the sharp switching transition from steady-state behavior to synchronized oscillations at high values of k_{ex} can be seen in the surface plot of the global signal X_s (Fig. 3A).

The gradual synchronization of particles for low k_{ex} can be understood within the framework of the Kuramoto model, with X_s playing the role of the mean-field coupling. The time variation of X_i, X_s, and the exchange rate $-k_{ex}(X_i - X_s)$ for a particle are shown in Fig. 4A for one cycle, with $k_{ex} = 0.3$ and $n = 4000$. The value of X_s increases when several of the oscillators fire together (Fig. 4A, top). This increase in turn influences the individual oscillators through the exchange rate, which becomes positive for a particle when the concentration is higher in the solution (Fig. 4A, middle), leading to an increase in X_i. When X_i crosses a threshold value, the particle fires in synchrony with the others (Fig. 4A, bottom). For low n, particles with frequencies that differ from that of the global oscillation are little affected by the weak signal in X_s; however, as n is increased, the magnitude of

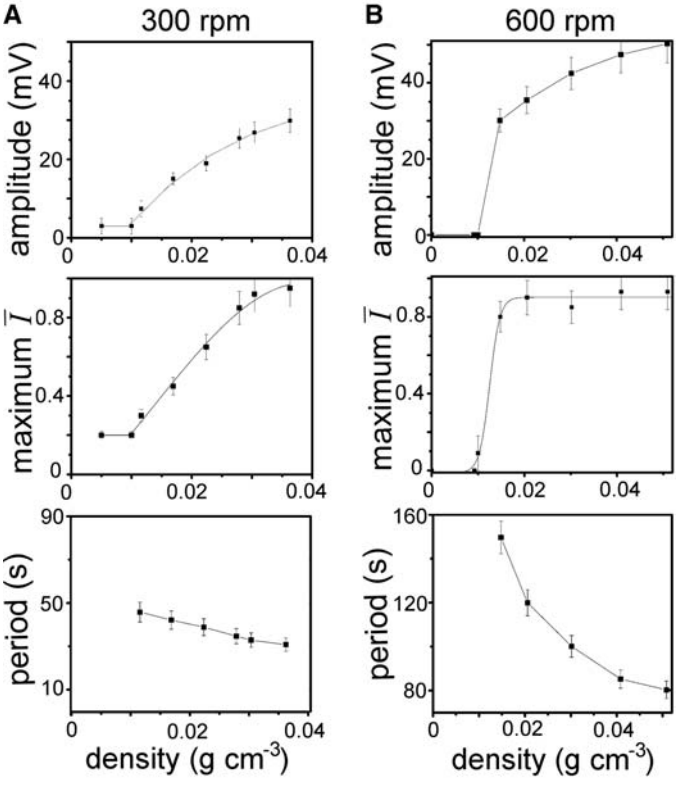

Fig. 2. Dynamical transitions with increasing particle density at low stirring rate (**A**) and high stirring rate (**B**). From top to bottom: Amplitude of oscillation in the surrounding solution from the electrochemical signal; maximum of the average particle intensity, corresponding to the degree of coherence of the oscillators; and period of oscillation.

the X_s signal increases, and more of the oscillators join the rhythm. In this way, the particles are synchronized by an internally generated signal.

The exchange rate for all particles averaged over one cycle is negative and therefore constitutes an overall loss rate in X_i, shown as a function of k_{ex} in Fig. 4B. As k_{ex} increases for fixed n, the average concentration of activator in the surrounding solution X_s increases (blue line), but the loss rate also increases (red line), and hence the average concentration of X_i on a particle decreases (black line). When it decreases below a threshold value, oscillations are no longer supported and a sudden transition to the steady state is observed. The X_i loss rate increases slightly as k_{ex} is further increased.

The model predicts that both a dynamical quorum-sensing transition and a desynchronization transition will be observed upon decreasing the stirring rate (Fig. 4C, upper panel). The oscillations suddenly appear and then decrease in amplitude with decreasing k_{ex} because of the loss of synchronization until a noisy nonoscillatory signal corresponding to out-of-phase oscillators is observed. The transition to the desynchronized state is best observed at low particle densities, as can be seen in Fig. 3A for $n = 1.8 \times 10^4$ cm^{-3}. The transition from steady-state to oscillatory behavior followed by a gradual desynchronization is also observed experimentally (Fig. 4C, lower panel).

For high k_{ex} and low n, the catalyst particles are quiescent, as oscillations are not supported because of the high loss rate of X_i. As the number density is increased, the concentration both in the surrounding solution X_s and on the individual particles X_i increases, with a corresponding slight decrease in the average loss rate of X_i on the particles (Fig. 4D). At a critical density n, the value of X_i on the individual particles reaches the threshold for the transition from steady-state behavior to oscillatory behavior. Although there is a considerable spread in oscillator frequencies, the transition is sharp, with all particles oscillating synchronously, indicating cooperative behavior in the transition (*21*). The time series in Fig. 1 show experimental measurements of the dynamical quorum-sensing transition from steady-state to oscillatory behavior with increasing particle density, with a Pt electrode giving the global signal and video images giving the average particle intensity.

We have shown that there are two distinct types of transitions to synchronized oscillatory behavior with increasing oscillator density, where coupling occurs by exchange of signaling species through the surrounding solution. For low exchange rates, the oscillators gradually synchronize their rhythms via a weak coupling through the low solution concentration of activator. For high exchange rates, the oscillators are quiescent below a critical density, as the activator concentration on the particles is not sufficient to support oscillatory behavior. Higher exchange rates give rise to lower activator concentrations on individual particles, because only activator-consuming processes occur in the surrounding solution. As the density is increased, the activator concentration in the surrounding solution and on each particle increases until a threshold concentration is reached, and synchronous oscillations sudden-

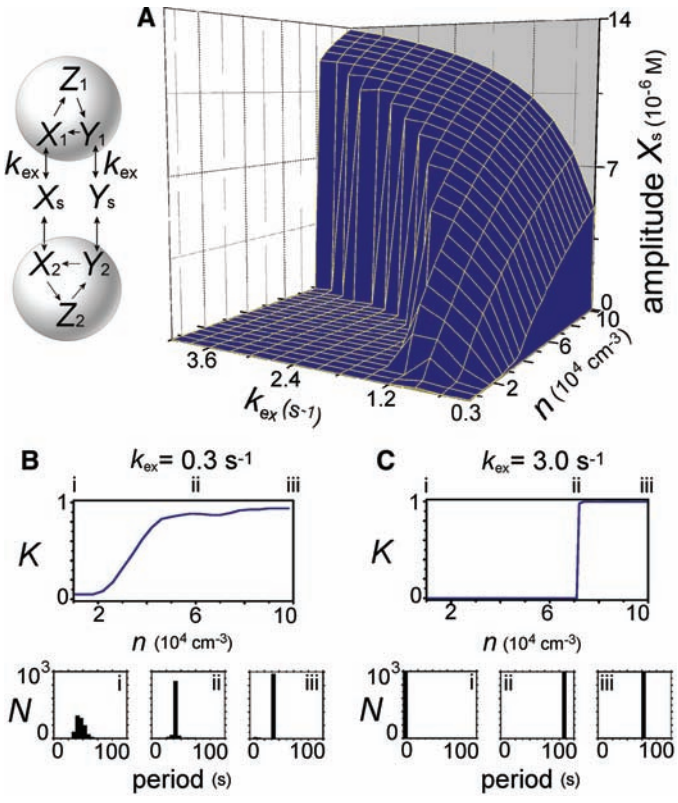

Fig. 3. Behavior of BZ particle population model (*20*, *21*) with oscillators coupled by exchange of species with the surrounding solution (see table S1 for parameter values). (**A**) The amplitude of the oscillations in autocatalyst in the surrounding solution as a function of number density of oscillators and exchange rate constant. (**B**) The order parameter K as a function of n for low exchange rates. Lower plots show the distribution of oscillator periods at indicated densities (i to iii). (**C**) The order parameter K at high exchange rates and corresponding oscillator periods.

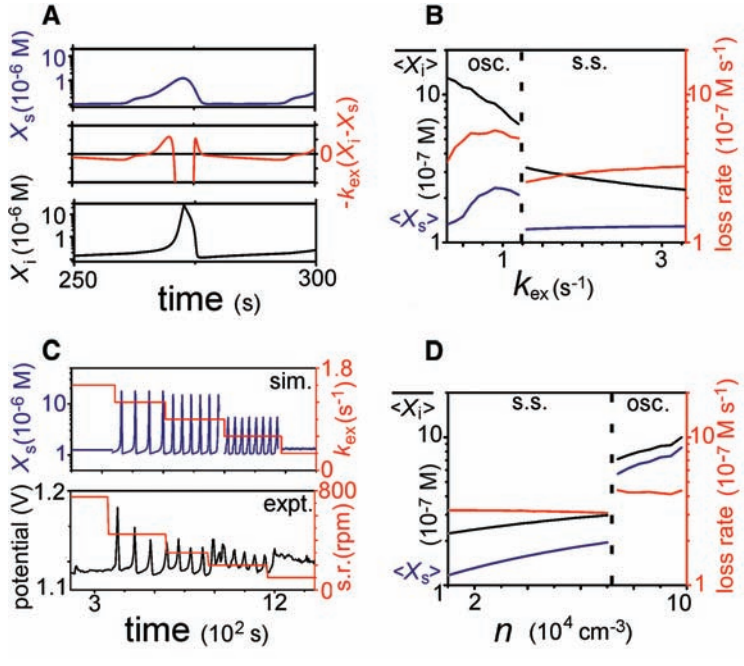

Fig. 4. Influence of exchange rate $-k_{ex}(X_i - X_s)$ on model dynamics. (**A**) Variation of autocatalyst in solution (blue line), on a particle (black line), and the exchange rate (red line) during one oscillation, with $n = 1.8 \times 10^4$ cm^{-3} and $k_{ex} = 0.3$ s^{-1}. (**B**) Transition from oscillations to steady state with increasing k_{ex} ($n = 1.8 \times 10^4$ cm^{-3}). Time-averaged autocatalyst on the particles (black line), in solution (blue line), and loss rate of autocatalyst from the particles (red line = $\langle k_{ex}(X_i - X_s)\rangle$). (**C**) Appearance and desynchronization of oscillations in autocatalyst in solution (blue line) and electrode potential (black line) with decreasing k_{ex} ($n = 1.8 \times 10^4$ cm^{-3}) and stirring rate (density = 0.0162 g cm^{-3}) shown as red lines. (**D**) Transition from steady state to oscillations with increasing n ($k_{ex} = 3.0$ s^{-1}). Color coding is same as in (**A**).

ly appear at the critical density. The sudden transition has features that are suggestive of an "oscillator death" transition (*28*); however, the coupling between particles occurs through the surrounding solution in which there is an additional decay of the activator species.

The exchange rate of the activator $HBrO_2$ and the inhibitor Br^- determines whether the transition to synchronized oscillatory behavior occurs by a synchronization mechanism or a dynamical quorum-sensing mechanism. It is possible that suspensions of cellular organisms, such as yeast or *D. discoidium*, may also undergo both types of transitions with different efficacies of molecular signaling. Our system of chemical oscillators suspended in a stirred solution is an idealized configuration of oscillators interacting by global coupling.

References and Notes

1. A. T. Winfree, *The Geometry of Biological Time* (Springer, New York, ed. 2, 2001).
2. A. Goldbeter, *Biochemical Oscillations and Cellular Rhythms: The Molecular Bases of Periodic and Chaotic Behaviour* (Cambridge Univ. Press, Cambridge, 1996).
3. L. Glass, M. C. Mackey, *From Clocks to Chaos: The Rhythms of Life* (Princeton Univ. Press, Princeton, NJ, 1988).
4. S. Strogatz, *Sync: The Emerging Science of Spontaneous Order* (Hyperion, New York, 2003).
5. A. S. Pikovsky, M. Rosenblum, J. Kurths, *Synchronization: A Universal Concept in Nonlinear Sciences* (Cambridge Univ. Press, Cambridge, 2001).
6. S. C. Manrubia, A. S. Mikhailov, D. H. Zanette, *Emergence of Dynamical Order: Synchronization Phenomena in Complex Systems* (World Scientific, Singapore, 2004).
7. Y. Kuramoto, *Chemical Oscillations, Waves and Turbulence* (Springer, Berlin, 1984).
8. A. T. Winfree, *Science* **298**, 2336 (2002).
9. J. Garcia-Ojalvo, M. B. Elowitz, S. H. Strogatz, *Proc. Natl. Acad. Sci. U.S.A.* **101**, 10955 (2004).
10. G. Gerisch, B. Hess, *Proc. Natl. Acad. Sci. U.S.A.* **71**, 2118 (1974).
11. I. Z. Kiss, Y. Zhai, J. L. Hudson, *Science* **296**, 1676 (2002).
12. S. De Monte, F. d'Ovidio, S. Danø, P. G. Sørensen, *Proc. Natl. Acad. Sci. U.S.A.* **104**, 18377 (2007).
13. J. Aldridge, E. K. Pye, *Nature* **259**, 670 (1976).
14. S. Danø, P. G. Sørensen, F. Hynne, *Nature* **402**, 320 (1999).
15. A. Camilli, B. L. Bassler, *Science* **311**, 1113 (2006).
16. E. P. Greenberg, *ASM News* **63**, 371 (1997).
17. A. Eberhard *et al*., *Biochemistry* **20**, 2444 (1981).
18. J. Engebrecht, K. Nealson, M. Silverman, *Cell* **32**, 773 (1983).
19. G. M. Patriquin *et al*., *J. Bacteriol.* **190**, 662 (2008).
20. R. Toth, A. F. Taylor, M. R. Tinsley, *J. Phys. Chem. B* **110**, 10170 (2006).
21. See supporting material on *Science* Online.
22. J. Maselko, K. Showalter, *Nature* **339**, 609 (1989).
23. J. Maselko, J. S. Reckley, K. Showalter, *J. Phys. Chem.* **93**, 2774 (1989).
24. K. Yoshikawa, R. Aihara, K. Agladze, *J. Phys. Chem. A* **102**, 7649 (1998).
25. A. M. Zhabotinsky, F. Buchholtz, A. B. Kiyatkin, I. R. Epstein, *J. Phys. Chem.* **97**, 7578 (1993).
26. A. Zaikin, A. Zhabotinsky, *Nature* **225**, 535 (1970).
27. S. Shinomoto, Y. Kuramoto, *Prog. Theor. Phys.* **75**, 1105 (1986).
28. G. B. Ermentrout, *Physica D* **41**, 219 (1990).

29. Supported by UK Engineering and Physical Sciences Research Council grant GR/T11036/01 (A.F.T.) and by NSF grant CHE-0809058. We dedicate this paper to the memory of Anatol M. Zhabotinsky, a pioneer of modern research in oscillations and pattern formation in chemical systems.

Supporting Online Material

www.sciencemag.org/cgi/content/full/323/5914/614/DC1
Materials and Methods
SOM Text
Figs. S1 and S2
Table S1
References

22 September 2008; accepted 17 December 2008
10.1126/science.1166253

Single Nanocrystals of Platinum Prepared by Partial Dissolution of Au-Pt Nanoalloys

Marc Schrinner,[1] Matthias Ballauff,[1]* Yeshayahu Talmon,[2] Yaron Kauffmann,[3] Jürgen Thun,[4] Michael Möller,[4] Josef Breu[4]

Small metal nanoparticles that are also highly crystalline have the potential for showing enhanced catalytic activity. We describe the preparation of single nanocrystals of platinum that are 2 to 3 nanometers in diameter. These particles were generated and immobilized on spherical polyelectrolyte brushes consisting of a polystyrene core (diameter of ~100 nanometers) onto which long chains of a cationic polyelectrolyte were affixed. In a first step, a nanoalloy of gold and platinum (a solid solution) was generated within the layer of cationic polyelectrolyte chains. In a second step, the gold was slowly and selectively dissolved by cyanide ions in the presence of oxygen. Cryogenic transmission electron microscopy, wide-angle x-ray scattering, and high-resolution transmission electron microscopy showed that the resulting platinum nanoparticles are faceted single crystals that remain embedded in the polyelectrolyte-chain layer. The composite systems of the core particles and the platinum single nanocrystals exhibit an excellent colloidal stability, as well as high catalytic activity in hydrogenation reactions in the aqueous phase.

Metallic nanoparticles (NPs) of controlled size and shape have been of great interest recently for a number of possible applications in electronic or optical materials, as well as in catalysis (*1*–*8*). Particle morphology can play a central role in catalysis. For example, faceted Pt crystals can exhibit higher catalytic activity than spherical particles (*9*, *10*), and the activity of the exposed facets may vary considerably (*11*, *12*). The reactivity and selectivity of NPs can be tuned by controlling their morphology; for example, amorphous Pt NPs have exhibited a much reduced catalytic activity (*13*).

However, faceted nanocrystals (NCs) with a well-developed shape and a narrow size distribution that have been reported generally were in the size range of 100 nm and more. For instances, Sun and Xia obtained well-defined Au and Ag crystals with sizes on the order of 100 nm (*4*). Nanoprisms of Ag with dimensions around 100 nm were prepared by Jin *et al*. by photochemical conversion of Ag spheres (*3*). Anisotropic Ag NPs of similar size were synthesized by Liz-Marzan and co-workers through careful choice of a suitable surfactant (*14*), and Pt NPs with high-index facets were obtained recently by Tian and co-workers (*6*). Again, the typical sizes ranged between 50 and 200 nm. The only reported route to faceted single crystals in the size range of a few nanometers was the synthesis of well-defined clusters, for example, Au_{55} cluster, and a subsequent heat treatment (*15*).

Platinum NPs have been of particular interest because of their role in many catalytic reactions and because the growth of specific surfaces can be controlled by amphiphilic polymers or suitable surfactants (*9*, *16*–*19*). However, downsizing the Pt NPs to a few nanometers is often accompanied by a broadening of their size distribution and partial loss of the control of the particle shape (*5*). The reduction of the metal ions and the generation of the NPs seem to proceed very rapidly and leads to disordered structures and distorted crystal shapes.

We present a simple synthesis of faceted, well-defined Pt single NCs with a typical size of 2 to 3 nm. As shown in Fig. 1, the Pt NCs are obtained by partial dissolution of nanoalloys of Pt and Au. In case of larger nanoalloy particles, this procedure leads to spongelike or hollow structures (*20*, *21*). We found that the dissolution of the Au component of the nanoalloy leads to reorganization of the Pt atoms and the formation of well-defined, faceted NCs. We started from a nanoalloy of Au and Pt generated on the surface of a spherical polyelectrolyte brush (SPB), as described recently (*22*). These particles consist of a solid polystyrene (PS) core with colloidal dimensions (diameter ~ 100 nm) onto which long charged polymer chains are grafted. Spherical polyelectrolyte brushes are well suited for the

[1]Physikalische Chemie I, University of Bayreuth, 95440 Bayreuth, Germany. [2]Department of Chemical Engineering, Technion-Israel Institute of Technology, Haifa 32000, Israel. [3]Department of Materials Engineering, Technion-Israel Institute of Technology, Haifa 3200, Israel. [4]Anorganische Chemie I, University of Bayreuth, 95440 Bayreuth, Germany.

*To whom correspondence should be addressed. E-mail: Matthias.Ballauff@uni-bayreuth.de

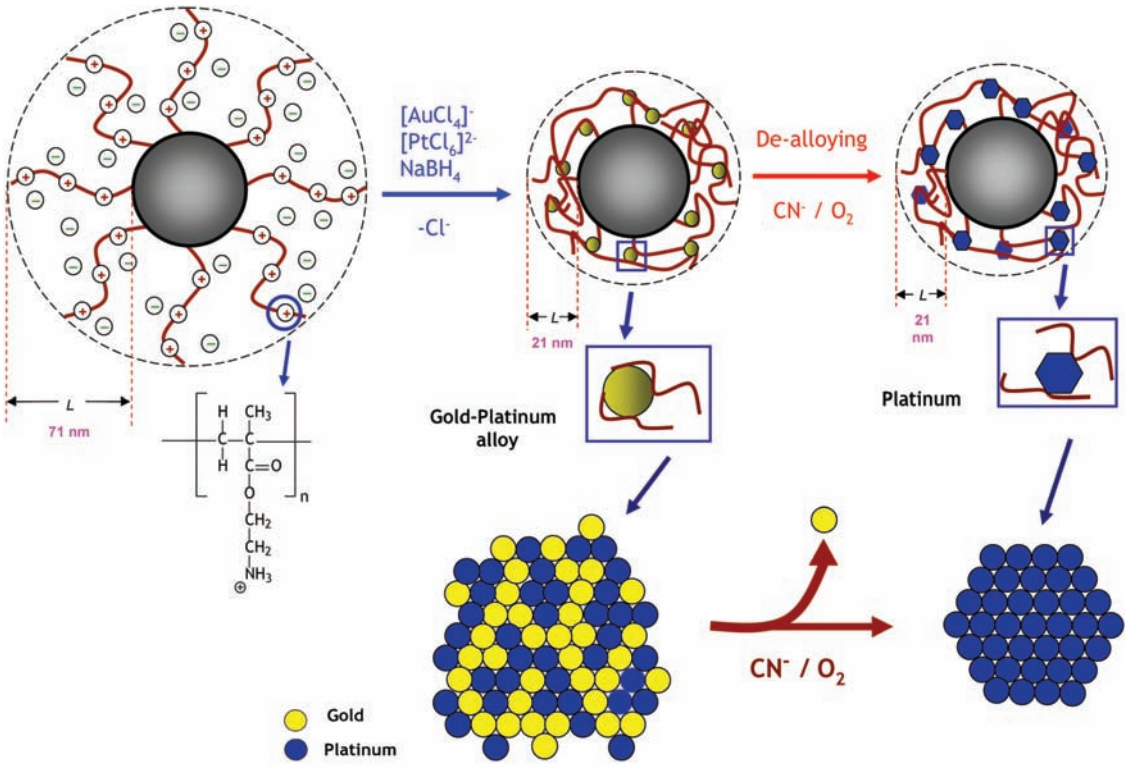

Fig. 1. Synthesis scheme of Pt NCs by de-alloying of a Au-Pt nanoalloy. The carrier particles are SPBs that consist of a solid PS core (R_H = 50 nm) onto which cationic polyelectrolyte chains of 2-aminoethylmethacrylate (2-AEMH) are attached. In a first step, the chloride counterions were exchanged against $AuCl_4^-$ ions; in a second step the rest of Cl^- ions were exchanged against $PtCl_4^{2-}$ ions. Bimetallic $Au_{45}Pt_{55}$ nanoalloy particles were generated by reduction of the mixture of these ions by $NaBH_4$ (*22*). The composition of the resulting nanoalloy can be adjusted by the ratio of the metal ions in the brush layer. In the final step, cyanide ions and oxygen were used to leach out the Au atoms from the nanoalloy under very mild conditions. This procedure leads to faceted Pt NCs with a few nanometers in diameter embedded in the surface layer of polyelectrolyte chains.

generation and immobilization of metallic NPs in the aqueous phase (*23*, *24*) because anionic complex ions of metals, like Au, Ag, Pd, or Pt, can be immobilized in the surface layer of cationic SPB. The confinement of these ions was attributed to the strong electrostatic interaction of the counterion with the highly charged macro-ion. The complex metal ions like $PtCl_6^{2-}$ are thus localized solely in the layer of polyelectrolyte chains of the SPB, so that virtually no metal salt is released into the aqueous phase. Subsequent reduction with $NaBH_4$ under mild conditions led to the formation of metallic NPs, firmly embedded in a dense layer of polyelectrolyte chains.

In the same way, particles of nanoalloys (*25*) can be synthesized and immobilized on the surface layer of SPB particles. We demonstrated this approach by reducing a mixture of the $AuCl_4^-$ and $PtCl_6^{2-}$ ions in the surface layer of a cationic SPB (*22*). High-resolution transmission electron microscopy (HR-TEM) has shown that the nanoalloy particles do not exhibit a core-shell structure [compare with the discussion of this point in (*25*)] but form homogeneous solid solutions (*22*). The composition of the metals can be varied continuously without disturbing the structure of the particles that consist of a random mixture of Au and Pt (*22*). Moreover, the final composition is within narrow limits, determined by the ratio of the metal ions introduced into the brush layer earlier (*22*). The composite particles that consist of the carriers and the metallic NPs exhibit excellent colloidal stability in aqueous solution, which arises from the strong interaction

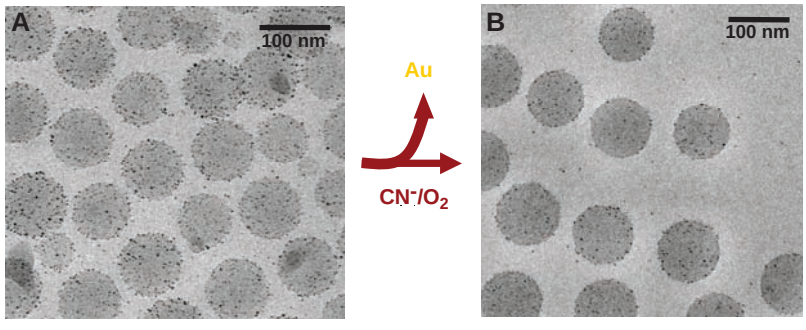

Fig. 2. (**A**) Cryo-TEM micrographs of the Au-Pt-nanoalloy particles (composition: $Au_{45}Pt_{55}$) generated on the surface of the spherical polyelectrolyte brushes. (**B**) Composite particles after complete removal of the gold atoms from the Au-Pt-nanoalloy by a mixture of CN^- ions and O_2.

of the alloy NPs with the polyelectrolyte chains affixed to their surface. As depicted in Fig. 1, the cationic polymer chains are interwoven with the NPs and form a dense mesh on the surface of the core particles. This model is supported by careful measurements of the hydrodynamic radius, R_H, by dynamic light scattering [see the discussion of this point in (*26*)]. The thickness, L, of the surface layer is given by $L = R_H - R$, where R denotes the radius of the cores. As will be shown below, the colloidal stability of the composites allows us to transform the NPs while keeping them on the surface of the core particles.

We prepared composite particles containing Au-Pt NPs with the composition $Au_{45}Pt_{55}$, as shown by elemental analysis. Partial dissolution of these alloy NPs then leads to pure Pt NCs. The Au atoms were slowly dissolved by a treatment of the alloy NPs with cyanide ions in presence of oxygen (Fig. 1). In a typical experiment, 4 ml of a 1.9×10^{-5} M NaCN solution was added dropwise within 25 min to 13 ml of a AuPt-SPB suspension [0.04 weight % (wt. %)] at room temperature under air with vigorous stirring. The high dilution of the cyanide ions is crucial for avoiding coagulation or complete dissolution of the NPs. Air was bubbled slowly through the solution to achieve complete removal of the Au atoms. After 3 hours, the dispersion turned blue, indicating the formation of pure Pt NCs (*26*).

The de-alloying of the Au-Pt-nanoalloy proceeded surprisingly smoothly. Micrographs of the composite particles before and after the leaching process (Fig. 2) were obtained by cryogenic transmission electron microscopy (cryo-TEM) that allow us to analyze the NPs in their native

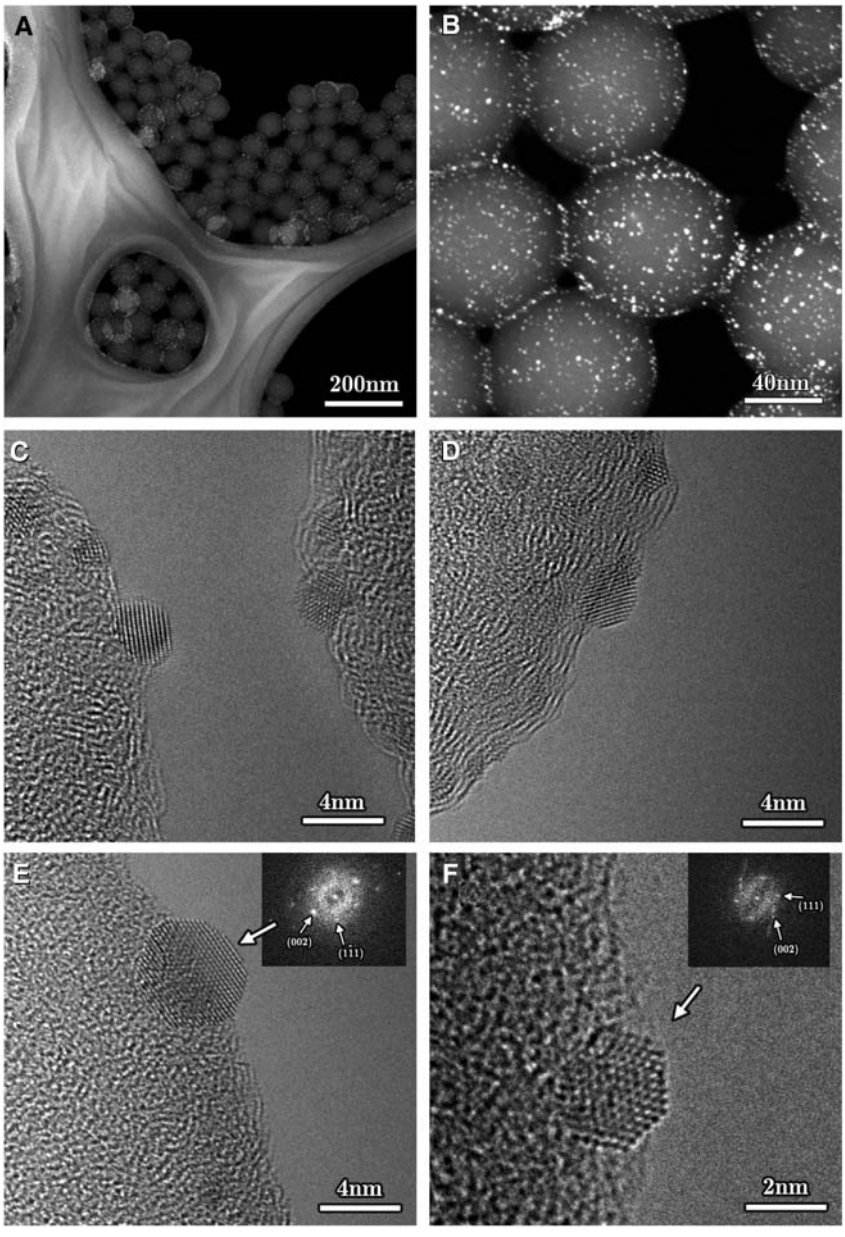

Fig. 3. (**A** and **B**) HAADF-STEM micrographs of the Pt NPs (bright spots) embedded and uniformly dispersed on a surface layer of the spherical polyelectrolyte. (**C**) HR-TEM micrograph of NPs on the surface of two adjacent carrier particles. (**D**) HR-TEM micrograph of several NCs. (**E** and **F**) HR-TEM micrographs of two different Pt single NCs of sizes 4.6 and 2.8 nm, respectively, showing well-defined facets. All micrographs were acquired at 300 keV. (Insets) The Fourier transforms of the images.

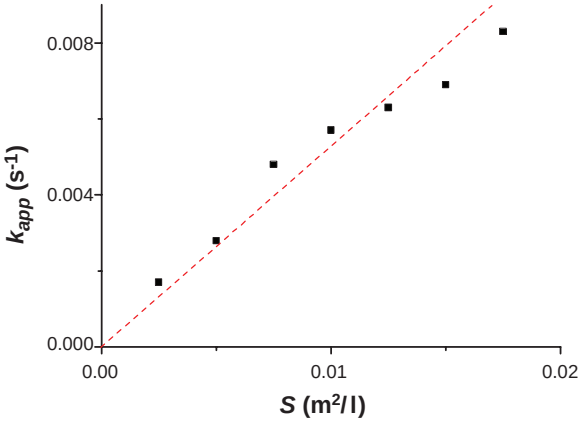

Fig. 4. Catalytic activity of the Pt NCs. k_1 (Eq. 1), obtained for the catalytic reduction of *p*-nitrophenol to *p*-aminophenol is plotted against the specific surface, S, of the Pt NCs in the solution. S is the total surface of all particles per unit volume.

state (*27*). Thus, a small drop of the suspension of the composite particles is shock-frozen and analyzed by TEM (see supporting online material for details). The Pt NCs can be seen in Fig. 2B as black dots distributed over the SPB. Both the alloy NPs as well as the Pt NCs are distributed more or less uniformly over the carrier particles. The alloy NPs have a rather narrow size distribution that is preserved during the leaching process (fig. S3 histogram).

The formation of the cyanide complex is selective for Au (*28*). Energy-dispersive x-ray spectroscopy (EDX) (figs. S1 and S2) shows that the NPs resulting from de-alloying consist only of Pt. The Pt NPs are still embedded on the surface of the SPB-carrier particles. The colloidal stability of the composite particles was not lost during the reaction with the cyanide ions, nor is any coagulation of the NPs on the surface of the carrier particles observed during this process. We reiterate that rapid addition or high concentrations of the cyanide ions lead to coagulation and coarsening of the metal NPs on the surface.

The structure of the Pt NPs was analyzed by combining high-angle annular dark-field scanning TEM (HAADF-STEM) and HR-TEM with electron diffraction (ED) and wide-angle x-ray scattering (WAXS). A low-magnification HAADF-STEM micrograph of the PS spheres on the supporting holey carbon film is shown in Fig. 3A, and Fig. 3B (from the same area at higher magnification) shows the uniform distribution of the Pt NPs on the PS spheres. In order to avoid any disturbance of this analysis by the core particles, only NPs sitting on the periphery of the carrier spheres were analyzed by HR-TEM (Fig. 3, C to F). The HR-TEM shows that the Pt NPs contain no grain boundaries and are single crystals. In several cases, the facets can be indexed because the NCs are aligned by chance; in Fig. 3, E and F, the electron diffraction shows directly the hexagonal symmetry of the cubic crystal.

The lattice spacing derived from the (200) reflection as seen in ED (d_{200} = 0.20 nm) is in good agreement with the bulk value [d_{200} = 0.196 nm; spacing 0.392 nm (*29*, *30*)]. The overall size of the Pt NCs lies within the range estimated from the volume contraction caused by Au leaching. Our results are consistent with the Au-Pt nanoparticles converted individually into Pt NCs, without coagulation or exchange between different alloy NPs having taken place. Some of the NPs moved under the intense electron beam and rolled on the surface of the PS spheres, but their shape remained stable (no melting was observed).

The high crystallinity observed by HR-TEM might have been induced by the electron beam through local heating and subsequent crystallization. To rule out this possibility, we examined powders of the dried composite particles before and after leaching by WAXS (fig. S4). The average crystallite sizes as derived from the Rietveld analysis were 7.01 ± 0.003 [7.01(3)] nm for the $Au_{45}Pt_{55}$-NPs and 3.80(4) nm for the resulting Pt NCs. These values agree quite well with crystal sizes as observed by HR-TEM showing that the

particles are single-domain NCs. Also, the lattice parameter of 0.401 (± 0.001) nm obtained for the alloy NPs agrees very well with the value expected from Vegard's law, that is, a linear interpolation of the lattice parameters of Au and Pt [see the discussion of this point in (*22*)], if a solid solution had formed. After the Au leaching step, the lattice parameter decreased to 0.391 (± 0.001) nm, in agreement with the known lattice parameter of pure Pt [0.392 nm (*29*)]. Thus, full dealloying of the Au-Pt-nanoalloy could be achieved. We note that a partial dealloying by an electrochemical method has been recently reported by Koh and Strasser (*31*).

As a final point, we discuss the catalytic activity of the Pt NCs affixed to the surface of the SPBs. Previous work (*23*, *32*, *33*) showed that the catalytic reduction of *p*-nitrophenol to *p*-aminophenol can be used for the analysis of the catalytic activity of Pt NPs. We assumed that reduction rates were independent of the concentration of sodium borohydride because it was in excess compared to *p*-nitrophenol. Moreover, the apparent rate constant, k_{app}, was found to be proportional to the surface *S* of the Pt NPs present in the system (*32*, *33*):

$$-\frac{dc_t}{dt} = k_{app}c_t = k_1 S c_t \qquad (1)$$

where c_t is the concentration of *p*-nitrophenol at time *t* and k_1 is the rate constant normalized to *S*, the surface area normalized to the unit volume of the system. k_1 is plotted against the specific surface *S* of the Pt NCs in the systems in Fig. 4 (*32*). The Pt NCs exhibit a high catalytic activity and turnover numbers as high as 1580 ± 50, which are among the highest turnover numbers measured so far for this reaction (*23*, *32*, *33*). Hence, the composite particles consisting of the SPBs and the Pt NCs present a system with high colloidal stability that may be used for catalysis in an aqueous environment.

References and Notes

1. C. Burda, X. Chen, R. Narayanan, M. A. El-Sayed, *Chem. Rev.* **105**, 1025 (2005).
2. S. K. Ghosh, T. Pal, *Chem. Rev.* **107**, 4797 (2007).
3. R. Jin *et al.*, *Science* **294**, 1901 (2001).
4. Y. Sun, Y. Xia, *Science* **298**, 2176 (2002).
5. R. Narayanan, M. A. El-Sayed, *J. Am. Chem. Soc.* **126**, 7194 (2004).
6. N. Tian, Z.-Y. Zhou, S.-G. Sun, Y. Ding, Z. L. Wang, *Science* **316**, 732 (2007).
7. S. C. Warren *et al.*, *Science* **320**, 1748 (2008).
8. E. Sulman *et al.*, *Top. Catal.* **39**, 187 (2006).
9. T. S. Ahmadi, Z. L. Wang, T. C. Green, A. Henglein, M. A. El-Sayed, *Science* **272**, 1924 (1996).
10. R. Narayanan, M. A. El-Sayed, *J. Am. Chem. Soc.* **126**, 7194 (2004).
11. R. Narayanan, M. A. El-Sayed, *J. Phys. Chem. B* **107**, 12416 (2003).
12. R. Narayanan, M. A. El-Sayed, *Nano Lett.* **4**, 1343 (2004).
13. Y. Sun, L. Zhuang, J. Lu, X. Hong, P. Liu, *J. Am. Chem. Soc.* **129**, 15465 (2007).
14. I. Pastoriza-Santos, L. Liz-Marzan, *Nano Lett.* **2**, 903 (2002).
15. M. Turner *et al.*, *Nature* **454**, 981 (2008).
16. H. Lee *et al.*, *Angew. Chem. Int. Ed.* **45**, 7824 (2006).
17. S. Kinge, H. Bönnemann, *Appl. Organomet. Chem.* **20**, 784 (2006).
18. J. Ren, R. D. Tilley, *Small* **3**, 1508 (2007).
19. E. Ramirez, L. Eradés, K. Philippot, P. Lecante, B. Chaudret, *Adv. Funct. Mater.* **17**, 2219 (2007).
20. S. Guo, Y. Fang, S. Dong, E. Wang, *J. Phys. Chem. C* **111**, 17104 (2007).
21. J. Snyder, P. Asanithi, A. B. Dalton, J. Erlebacher, *Adv. Mater.* **20**, 4883 (2008).
22. M. Schrinner *et al.*, *Adv. Mater.* **20**, 1928 (2008).
23. M. Ballauff, *Prog. Polym. Sci.* **32**, 1135 (2007).
24. Y. Lu *et al.*, *J. Phys. Chem. C* **111**, 7676 (2007).
25. R. Ferrando, J. Jellinek, R. L. Johnston, *Chem. Rev.* **108**, 845 (2008).
26. M. Schrinner *et al.*, *Macromol. Chem. Phys.* **208**, 1542 (2007).
27. Z. Li, E. Kesselman, Y. Talmon, M. A. Hillmyer, T. P. Lodge, *Science* **306**, 98 (2004).
28. J. E. Huheey, *Inorganic Chemistry: Principles of Structure and Reactivity* (Pearson/Addison-Wesley, Boston, ed. 5, 2004).
29. D. Brooksbank, K. W. Andrews, *J. Iron Steel Inst. London* **206**, 595 (1968).
30. T. Swanson, *Natl. Bur. Stand. (U.S.) Circ.* **31**, 539 (1953).
31. S. Koh, P. Strasser, *J. Am. Chem. Soc.* **129**, 12624 (2007).
32. Y. Mei, Y. Lu, F. Polzer, M. Ballauff, F. Polzer, *Chem. Mater.* **19**, 1062 (2007).
33. Y. Mei *et al.*, *Langmuir* **21**, 12229 (2005).

34. Financial support by the Deutsche Forschungsgemeinschaft, SFB 481, Bayreuth; by the BASF SE; and by the Fonds der Chemischen Industrie is gratefully acknowledged. M.S. thanks the Minerva Foundation, the German Academic Exchange Service (DAAD), and the Technion Russell Berrie Nanotechnology Institute (RBNI) for the support during a stay at the Technion in Haifa. Y.T. thanks the von Humboldt Foundation for the support, through a von Humboldt–Meitner Prize, of the collaboration with the University of Bayreuth. Cryo-TEM was performed at the Hannah and George Krumholz Laboratory for Electron Microscopy of Soft Matter, part of the Technion Project on Complex Liquids, Microstructure, and Macromolecules. The HR-TEM work was done at the Electron Microscopy Center at the Department of Materials Engineering, the Technion.

Supporting Online Material

www.sciencemag.org/cgi/content/full/323/5914/617/DC1
Materials and Methods
Figs. S1 to S4
Table S1
References

2 October 2008; accepted 15 December 2008
10.1126/science.1166703

Cascadia Tremor Located Near Plate Interface Constrained by *S* Minus *P* Wave Times

Mario La Rocca,[1]* Kenneth C. Creager,[2] Danilo Galluzzo,[1] Steve Malone,[2] John E. Vidale,[2] Justin R. Sweet,[2] Aaron G. Wech[2]

Nonvolcanic tremor is difficult to locate because it does not produce impulsive phases identifiable across a seismic network. An alternative approach to identifying specific phases is to measure the lag between the *S* and *P* waves. We cross-correlate vertical and horizontal seismograms to reveal signals common to both, but with the horizontal delayed with respect to the vertical. This lagged correlation represents the time interval between vertical compressional waves and horizontal shear waves. Measurements of this interval, combined with location techniques, resolve the depth of tremor sources within ±2 kilometers. For recent Cascadia tremor, the sources locate near or on the subducting slab interface. Strong correlations and steady *S-P* time differences imply that tremor consists of radiation from repeating sources.

Deep nonvolcanic tremor (NVT) has been observed in several tectonically active regions. In Cascadia and Japan, a relation with the subduction dynamics is inferred by the contemporaneous occurrence of slow slip detected geodetically (*1*–*3*). In these regions, the occurrence of major episodic tremor and slip (ETS) events is surprisingly periodic (*2*). Minor NVT has been triggered by the stresses imposed by low-frequency seismic waves radiated by major distant earthquakes (*4*–*6*), and NVT is modulated by ocean tidal loading (*7*), indicating that small stress perturbations trigger it. NVT is characterized by low amplitudes, a lack of energy at high frequency, emergent onsets, an absence of clear impulsive phases, and durations from minutes to days. The lack of impulsive phases identifiable across seismic networks in Cascadia hinders accurate source location by conventional techniques.

NVT recorded in Shikoku, Japan, contains identifiable low-frequency earthquakes (LFEs) (*8*, *9*), suggesting that tremor is primarily made up of many back-to-back LFEs. On individual seismograms, *S* waves are sometimes identified. Stacking seismograms of repeating events recorded at a given station after aligning them on the *S* waves produces a clear *P* wave. The *S* minus *P* times allow an accurate depth to be determined. Such Japanese tremor locations are found to be near the subduction plate interface (*8*, *10*). Individual LFEs have not yet been reported in tremor recorded in Cascadia.

Tremor episodes that continue for several days are accompanied by geodetically observed slow slip in both Cascadia and Shikoku, leading

[1]Istituto Nazionale di Geofisica e Vulcanologia–Osservatorio Vesuviano, Via Diocleziano 328, 80124 Napoli, Italy. [2]Department of Earth and Space Science, University of Washington, Box 351310, Seattle, WA 98195, USA.

*To whom correspondence should be addressed. E-mail: mlarocca@ov.ingv.it

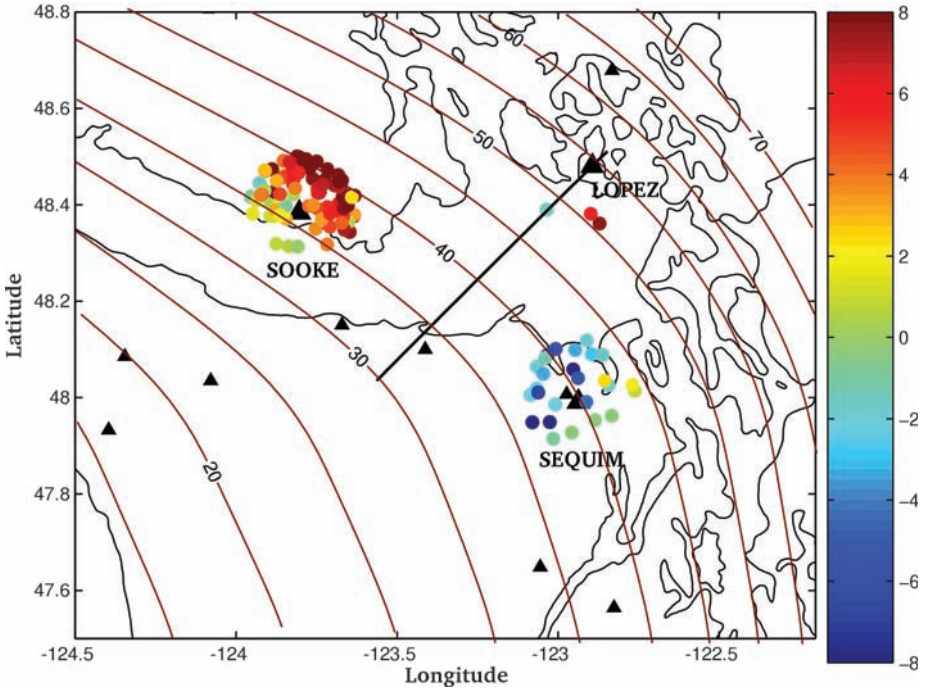

Fig. 1. Map showing locations of the three seismic arrays (large triangles), other stations used for location (small triangles), depth (km) to the plate interface [assumed to be 7 km above the slab Moho (*20*)], and location of cross section on Fig. 4 (black line) and tremor epicenters (dots), color-coded by distance above (red) and below (blue) the plate interface. Tremor epicenters are determined from cross-correlations of seismogram envelopes, and depths come from additional $t_{s\text{-}p}$ constraints. Theoretical ray incident angles at the arrays are restricted to be less than 15°.

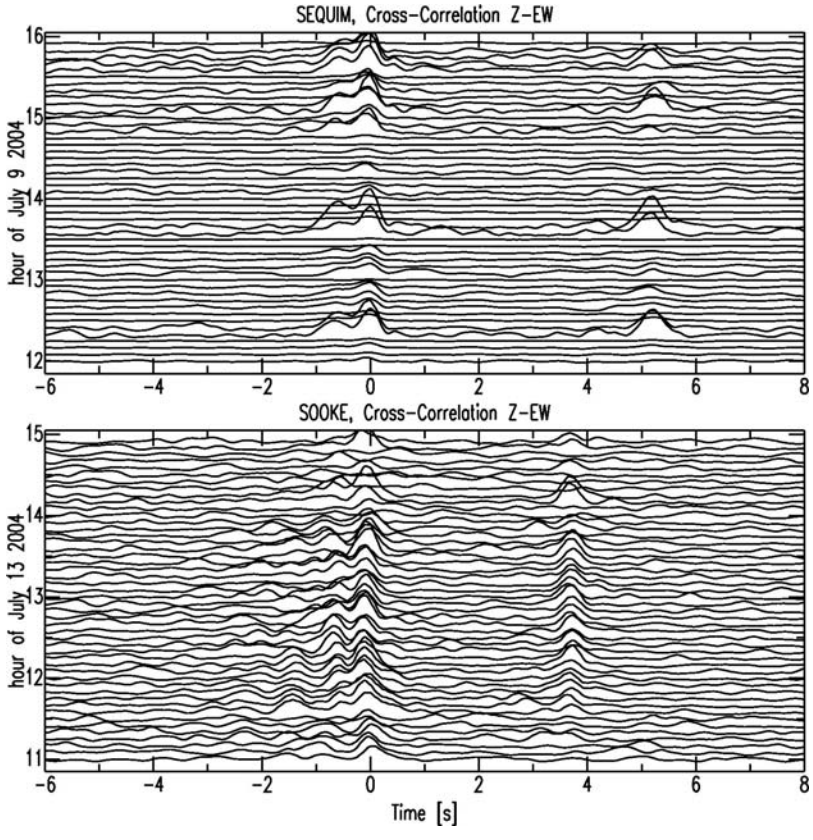

Fig. 2. Envelopes of the cross-correlations between vertical and east components for 5-min windows recorded at Sequim array (**top**) and Sooke array (**bottom**).

to the widely accepted interpretation for Japan that tremor and slow slip are manifestations of the same process. In contrast, attempts to locate tremor in Cascadia have resulted in a broad, 40-km-thick, distribution in depth, leading to the interpretation that much of the tremor is related to fluids throughout a large volume above the plate interface (*11*, *12*). Three different location techniques for tremor in Cascadia produce depth estimates over a range of 40 km. One technique uses the arrival times of seismic signal envelopes (*12*–*14*) and conventional location techniques based on an *S*-wave velocity model. A second technique, the Source Scanning Algorithm (*15*), stacks seismograms such that theoretical *S*-wave time delays correspond to a grid of possible source locations. Formal uncertainties are as small as 5 km but still show a wide depth range (*11*, *16*). A third technique uses small-aperture arrays to compute slowness vectors for seismic wavefronts and back projects those for a common source (*17*). In all of these cases, common signal shapes are processed under the assumption that they are direct *S* phases.

Cascadia tremor depth estimates likely have a greater uncertainty than the reported formal errors of 10 km in epicenter and more in depth. We tested this assumption by using two of the techniques to locate earthquakes in the same region as the tremor. The differences between the more accurately determined catalog earthquake depths and those we computed are much greater than the formal errors, sometimes tens of kilometers different (*14*, *17*). In the case of back projection of slowness vectors, unmodeled lateral velocity variations may bend the wave fronts sufficiently to explain these large errors in estimated tremor depths. Errors in depth determined from arrival times of seismogram envelopes are caused largely by unmodeled variations in *S*-wave coda duration. Here, we apply a new location procedure that greatly improves the depth resolution of the tremor sources.

Our data come from low-noise stations of the Pacific Northwest Seismograph Network and from three dense arrays composed of six three-component short-period seismic stations that were deployed specifically to record the July 2004 ETS event in Cascadia (*18*) (Fig. 1). Tremor periods with depths from 20 to 60 km have been reported (*12*, *16*, *17*). Polarization analysis of array data indicates that most of the signal has *S*-wave polarization (*13*) with apparent velocity higher than 5 km/s, as expected for shear waves from a deep source (*17*). *P*-wave polarization is observed in some of the tremor signals (*18*).

To improve the signal-to-noise ratio, we first stacked the seismograms over all the stations for each component of each array. Such stacks emphasize signals arriving with a steep incidence angle, i.e., from sources directly below an array. Then we computed the cross-correlations between the vertical and each horizontal stacked trace by using 300-s windows bandpass-filtered from

2 to 8 Hz. On many traces, the cross-correlogram envelopes show a distinct and persistent peak at positive lag times of 3.5 to 6.0 s, and no such peaks at negative lag times (Fig. 2). Positive lags correspond to the vertical component leading the horizontal component. These are particularly evident at the Sequim and Sooke arrays, where they were observed in many 5-min windows every day from 9 to 18 July. At the Lopez array, similar lags were visible only sporadically on 9 and 10 July, when tremor was nearest the array.

The distinct peaks at positive lags are consistent with the arrival of first vertical *P* waves and then horizontal *S* waves. The sequential correlations are characterized by tens of minutes with almost constant *S* minus *P* times ($t_{s\text{-}p}$). In several cases, when these peaks are most evident, visual inspection of the stacked seismograms revealed many subtle individual *P*- and *S*-wave arrival pairs with the same $t_{s\text{-}p}$ (Fig. 3). This pattern implies that at least some Cascadia tremor is made up of individual LFEs from a single source region occurring rapidly one after another in a sporadic sequence such as observed in Japan (*9*).

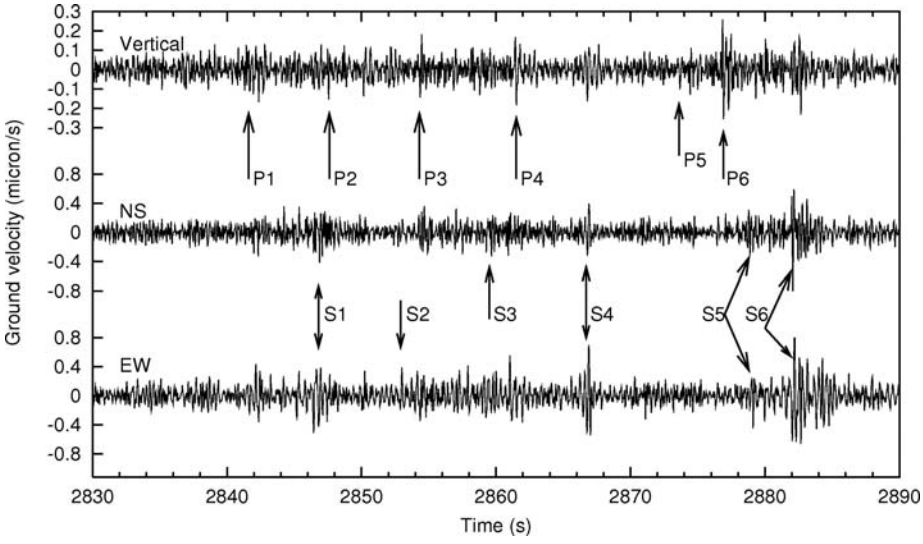

Fig. 3. Three-component seismograms in which several *P* waves, marked by arrows on the vertical component, are followed by *S* waves 5.1 ± 0.2 s later, as marked by arrows on the horizontal components. Seismograms are the stacked signals of Sequim array bandpass filtered between 2 and 10 Hz. The reference time is 15:00 GMT of 9 July 2004.

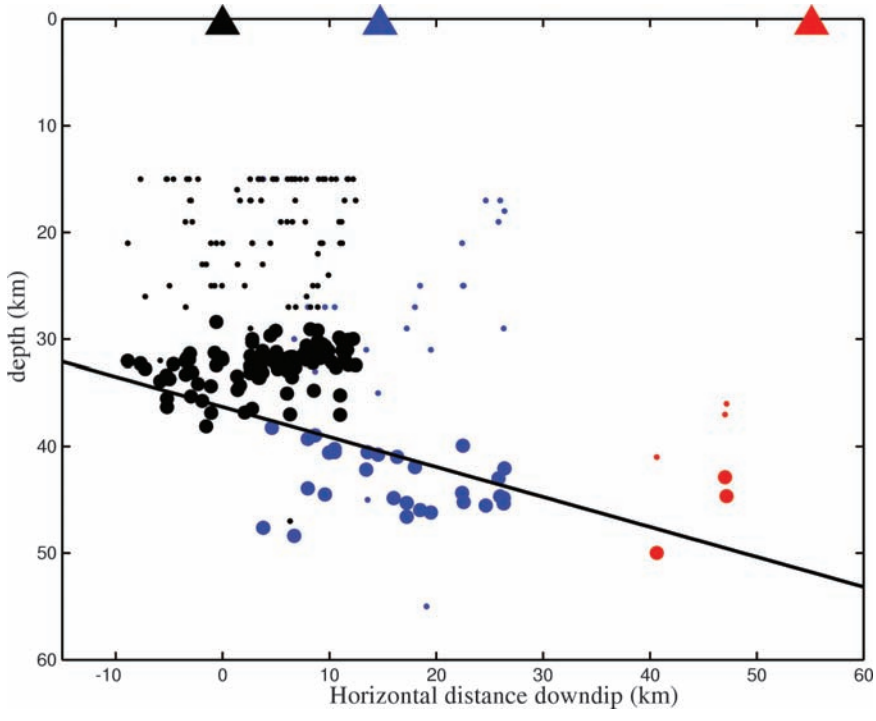

Fig. 4. Cross-section of tremors shown in Fig. 1 along the southwest-northeast profile. Small dots show hypocenters determined solely from envelope cross correlations. Large dots are hypocenters of the identical set of tremor periods, but with their depths shifted to satisfy the additional $t_{s\text{-}p}$ constraints from the Sooke (black), Sequim (blue), and Lopez (red) arrays.

Figure 2 shows lag times of 5.2 s at Sequim and of 3.7 s at Sooke. At Sequim, there were no intervals during the entire tremor period with $t_{s\text{-}p}$ less than 4.5 s. The low horizontal slowness measured at this array during times corresponding to $t_{s\text{-}p}$ near 4.5 s indicate that the sources were directly beneath the array. In contrast, higher slowness and back-azimuths to the north systematically correspond to $t_{s\text{-}p}$ = 5.0 to 5.4 s. At the Sooke array, all *S*-*P* times were between 3.7 and 4.4 s. The smallest value of $t_{s\text{-}p}$ = 3.7 s (Fig. 2) is consistent with sources located almost directly beneath the array. At the Lopez array, there were only a few periods of tremor with clear cross-correlation peaks, and those had $t_{s\text{-}p}$ = 5.5 s.

Combining the $t_{s\text{-}p}$-determined distances with slowness determined by array analysis allows an accurate estimate of the source depth. Based on a standard layered Earth model (*19*), tremor below the Sequim array ($t_{s\text{-}p}$ = 4.5 s) was located at a depth of 39 ± 2 km, whereas it was 31 ± 2 km below the Sooke array ($t_{s\text{-}p}$ = 3.7 s). To better compare the range of depths determined with and without the $t_{s\text{-}p}$ constraints, we applied an envelope cross-correlation tremor location method (*14*) to the same periods of time for which good *S*-*P* cross-correlation times are available. We located these tremor bursts both with and without the constraints of distance based on array measurements of $t_{s\text{-}p}$ and show the resulting epicenters in Fig. 1 and cross-section in Fig. 4. We kept all observations for which the theoretical ray angles at the arrays were less than 15° from the vertical. Depths are shown relative to the plate interface depth as determined from slab-Moho reflections (*20*). The depth range for locations determined with just envelope cross-correlations is large (small circles) as compared with those of the same tremor located with the additional $t_{s\text{-}p}$ constraints (large circles). At Lopez and Sequim, the refined depths are close to the plate interface. On average, the tremor beneath Sooke appears to be farther above the slab interface than that beneath Sequim and Lopez. This is likely an artifact of unmodeled high wave speeds associated with the Crescent Basalts beneath Sooke (*21*). Taken together, out of 128 observations, the mean source distance above the plate interface is 3 km and the standard deviation is ±5 km.

The clear correlations and stable $t_{s\text{-}p}$ in the signals suggest that, as was the case in Shikoku, where individual low-frequency events are found in the tremor and precisely located (*8*), at least some of the deep tremor in Cascadia consists of highly repetitive, continuous sequences of individual events, which radiate both *P*- and *S*-wave

energy from a volume small enough to give almost constant $t_{s\text{-}p}$ over periods of tens of minutes or more. We cannot locate all tremor with this method for two reasons. First, the stable determination of $t_{s\text{-}p}$ depends on tremor over an extended period coming from only one place, which is not always the case. Second, our technique is most sensitive to tremor beneath each array where the *P* and *S* waves are clearly separated into vertical and horizontal components. There are many periods of time, particularly at the Lopez array, in which tremor was located some distance from an array. In these cases, there was likely too much *S*-wave energy on the vertical component and *P* energy on the horizontal to get a strong cross-correlation. Although we cannot determine the depth of all observed tremor, the tremor under each array occurred near the subduction zone interface, and we see no evidence for shallow tremor, in contrast to other studies (*11*, *12*, *16*, *17*). Our method is ideally suited to find shallow tremor if it existed beneath an array.

If our results are representative of most NVT in Cascadia, then the contemporaneous occurrence of Global Positioning System–detected slow slip (*22*) indicates that deep tremor and slow slip are two manifestations of the same source process in Cascadia, as has been inferred for Japan (*8*, *10*, *23*). This hypothesis is further supported by the polarization characteristics of tremor signals, which are in good agreement with the expected polarization of signals produced by fault slip along the subduction megathrust (*13*).

References and Notes

1. K. Obara, *Science* **296**, 1679 (2002).
2. G. Rogers, H. Dragert, *Science* **300**, 1942 (2003).
3. K. Obara, H. Hirose, *Tectonophysics* **417**, 33 (2006).
4. J. L. Rubinstein *et al*., *Nature* **448**, 579 (2007).
5. J. Gomberg *et al*., *Science* **319**, 173 (2008).
6. M. Miyazawa, J. Mori, *Geophys. Res. Lett.* **32**, L10307 (2005).
7. J. L. Rubinstein, M. La Rocca, J. E. Vidale, K. C. Creager, A. G. Wech, *Science* **319**, 186 (2008).
8. D. R. Shelly, G. C. Beroza, S. Ide, S. Nakamula, *Nature* **442**, 188 (2006).
9. D. R. Shelly, G. C. Beroza, S. Ide, *Nature* **446**, 305 (2007).
10. Shelly D. R., G. C. Beroza, S. Ide, *Geochem. Geophys. Geosys.* **8** (2007).
11. H. Kao *et al*., *Nature* **436**, 841 (2005).
12. W. McCausland, S. Malone, D. Johnson, *Geophys. Res. Lett.* **32**, L24311 (2005).
13. Wech A. G., K. C. Creager, *Geophys. Res. Lett.* **34**, L22306 (2007).
14. A. G. Wech, K. C. Creager, *Geophys. Res. Lett.* **35**, L20302 (2008).
15. H. Kao, S.-J. Shan, *Geophys. J. Int.* **157**, 589 (2004).
16. H. Kao *et al*., *J. Geophys. Res.* **111**, B03309 (2006).
17. M. La Rocca *et al*., *Bull. Seismol. Soc. Am.* **98**, 620 (2008).
18. M. La Rocca *et al*., *Geophys. Res. Lett.* **32**, L21319 (2005).
19. R. S. Crosson, *J. Geophys. Res.* **81**, 3047 (1976).
20. L. A. Preston, K. C. Creager, R. S. Crosson, T. M. Brocher, A. M. Trehu, *Science* **302**, 1197 (2003).
21. K. Ramachandran, R. D. Hyndman, T. M. Brocher, *J. Geophys. Res.* **111**, B12301 (2006).
22. T. I. Melbourne, W. M. Szeliga, M. M. Miller, V. M. Santillan, *Geophys. Res. Lett.* **32**, L04301 (2005).
23. Ide S., D. R. Shelly, G. C. Beroza, *Geophys. Res. Lett.* **34**, L03308 (2007).

24. Istituto Nazionale di Geofisica e Vulcanologia and IRIS/PASSCAL provided instruments for the arrays; other seismograms were provided by the Pacific Northwest Seismic Network. Discussions with T. Pratt, J. Gomberg, H. Houston, A. Ghosh, E. Del Pezzo and comments from two anonymous reviewers improved this manuscript. Funding was provided by INGV, NSF and the U.S. Geological Survey.

13 October 2008; accepted 12 December 2008
10.1126/science.1167112

Divergent Evolution of Duplicate Genes Leads to Genetic Incompatibilities Within *A. thaliana*

David Bikard,[1] Dhaval Patel,[2] Claire Le Metté,[1] Veronica Giorgi,[1] Christine Camilleri,[1] Malcolm J. Bennett,[2] Olivier Loudet[1]*

Genetic incompatibilities resulting from interactions between two loci represent a potential source of postzygotic barriers and may be an important factor in evolution when they impair the outcome of interspecific crosses. We show that, in crosses between strains of the plant *Arabidopsis thaliana*, loci interact epistatically, controlling a recessive embryo lethality. This interaction is explained by divergent evolution occurring among paralogs of an essential duplicate gene, for which the functional copy is not located at the same locus in different accessions. These paralogs demonstrate genetic heterogeneity in their respective evolutionary trajectories, which results in widespread incompatibility among strains. Our data suggest that these passive mechanisms, gene duplication and extinction, could represent an important source of genetic incompatibilities across all taxa.

When crossing individuals from different species is feasible, offspring often have reduced viability or fertility (*1*, *2*). The Bateson-Dobzhansky-Muller model explains such incompatibilities on the basis of the synergistic interaction of genes that have functionally diverged among the respective parents (*3*–*5*). Elucidating the molecular basis of such genetic incompatibilities is of great importance to the science of evolution as well as to plant breeding. Whether these incompatibilities mostly appear concurrently with speciation (arising, for example, in geographically isolated populations) or after speciation has occurred as a consequence of their divergence remains a considerable question (*4*); it is now known that such incompatibilities can segregate within species first (*5*, *6*). A limited number of genes interacting to cause hybrid incompatibility have been identified at the molecular level, such as the *Lhr*/*Hmr* system responsible for lethality of male F1s from a cross between two *Drosophila* species (*7*). Recently, an interaction between *zeel-1* and *peel-1* loci was discovered to cause widespread genetic incompatibility among *Caenorhabditis elegans* strains (*8*). Also at the intraspecific scale, a typical dominant case of incompatibility in *Arabidopsis thaliana* has been identified that may establish a link between hybrid necrosis and the plant immune system (*9*).

While generating homozygous progeny from crosses between *A. thaliana* wild strains, it is frequently witnessed that physically unlinked loci do not always segregate independently and that, often, one homozygous allelic combination at two independent loci is rare or totally absent in the descendants of a specific cross (*10*, *11*). This phenomenon explains part of the segregation distortion inherited in such material and is viewed as the recessive version of Bateson-Dobzhansky-Muller–type incompatibilities, although other models than functional divergence could apply (*12*, *13*). Such epistasis-based recessive incompatibilities could result in reduced fitness in the progeny and limit the extent of rearrangements among parental genomes. Furthermore, if several incompatibilities were to segregate within a cross they should lead to conflicts between the genomes of diverged strains, which could result in isolating barriers and, ultimately, speciation (*14*, *15*).

A cross between the *Arabidopsis* reference accession Columbia-0 (Col) and the Cape Verde Island accession Cvi-0 (Cvi) was generated, and 367 F6 recombinant inbred lines (RILs) were genotyped, revealing that two pairs of unlinked loci did not segregate independently from each other (*10*). For both of these pairs, a specific combination of Col and Cvi alleles was not found in the RIL set, resulting in a transchromosomal linkage disequilibrium pattern (pseudo-LD) and exhibiting segregation distortion (fig. S1). By focusing on one of these two-locus interactions (labeled LD1 in fig. S1), we realized that a homozygous combination of the Col allele at the LD1.1

[1]Genetics and Plant Breeding, INRA, SGAP UR254, F-78026 Versailles, France. [2]Centre for Plant Integrative Biology, Division of Plant Sciences, School of Biosciences, University of Nottingham, Sutton Bonington Campus, Loughborough LE12 5RD, UK.

*To whom correspondence should be addressed. E-mail: loudet@versailles.inra.fr

locus (bottom of chromosome 1) and the Cvi allele at the LD1.5 locus (top of chromosome 5) caused arrested embryo development, resulting in seed abortion (Fig. 1 arrows). A large F2 population generated from the same cross recapitulated this recessive incompatibility (Fig. 1) and showed complete penetrance. We also noted that, in one intermediate heterozygous combination, the embryo developed normally but the primary root of the resulting seedling was shortened to ~one-third of its regular size, adding a quantitative phenotype we named "weak root" to the complexity of this epistasis. Taking advantage of heterogeneous inbred families [HIFs; (*16*)] derived from F6 RILs segregating for each locus while being fixed for the appropriate (incompatible) genotype at the other locus, we fine-mapped the LD1 epistatic interaction (*17*), reducing the candidate intervals of LD1.1 and LD1.5 to 65 and 15 kb, containing 11 and 4 annotated genes, respectively.

Gene annotation within these intervals revealed a candidate gene pair; the histidinol-phosphate amino-transferase gene codes for a protein (HPA) that catalyzes an important step in the biosynthetic pathway leading to histidine (His), an essential amino acid incorporated into proteins and hence required in many aspects of plant growth and development (*18*). Two paralogous copies of this gene are found in the Col genome; one (*HPA1*/*HISN6A*/At5g10330) lies within the LD1.5 candidate interval, and the other (*HPA2*/*HISN6B*/At1g71920) lies within the LD1.1 candidate interval. These paralogs appear to have arisen from a recent single gene duplication event resulting in a dispersed duplicate pair, a mode of gene duplication that typically affects fewer genes than tandem or segmental duplication events in *A. thaliana* (*19*). In Col, At1g71920 and At5g10330 coding sequences differ by two synonymous single nucleotide polymorphisms (SNPs). Intraspecific sequence analyses and comparison to *A. lyrata* show that the ancestral locus is represented by At1g71920 (*19*) and that At5g10330 arose from a 3.3-kb duplication centered on At1g71920. In the Col background, transferred DNA (T-DNA)–insertion mutants in At5g10330 are embryo-lethal at the homozygous state [*emb2196*; (*20*)], and we have confirmed this result in other mutant lines, including SALK_089516. Recently, a weak point mutation allele of At5g10330 (*hpa1*) was shown to affect the maintenance of the root meristem and primary root elongation (*21*), an effect typically associated with the lack of free His in the plant. Both arrested embryo development and root growth impairment have been complemented by supplying *emb2196* and *hpa1* plants with exogenous histidine (*18*, *21*).

The SNPs in the coding sequence were used to distinguish between the two paralogs' mRNA, confirming that there is no detectable transcriptional activity from At1g71920 in Col, whereas At5g10330 is expressed in both shoot and root [fig. S2; (*19*)]. Sequence and reverse transcription polymerase chain reaction (RT-PCR) analyses in Cvi showed that the gene at LD1.1 (At1g71920) was expressed, whereas there were no traces of an HPA coding sequence at LD1.5 in this background (fig. S2). Instead, according to sequence results, a 6.4-kb region appears to be deleted in Cvi (compared with the Col sequence) that encompasses the entire Col duplication stretching to 3 kb beyond the Col duplicated region on one side. Furthermore, the borders of this additional 3-kb deletion contained traces of transposable elements: ATGP9-LTR and VANDAL-18NA. The region homologous to LD1.5 in *A. lyrata* lacks a *HPA* gene but is also slightly different from Cvi, with deletions and insertions of hundreds of base pairs at the locus. Then, the possibility that the LD1.5 locus might have undergone multiple rearrangements makes it difficult to determine whether the *HPA* gene was deleted in Cvi or whether it was ever present in this background.

The situation at each paralog is summarized in Fig. 1, with Col and Cvi retaining alternate functional copies of the essential *HPA* gene. The combination of the two silenced copies in a progeny homozygous for the Col allele at LD1.1 and the Cvi allele at LD1.5 leads to arrested seed development, presumably because the embryo is unable to synthesize His. Similarly, the limited primary root growth in weak-root plants could be explained by a reduced His quantity in these plants because they have a single functional *HPA* copy originating from the Col LD1.5 locus (Fig. 1). Given that the Col LD1.5 allele is less expressed than the Cvi LD1.1 allele (fig. S2), this allelic combination may be specifically limiting for the root, an organ particularly sensitive to a shortage in His (*21*). All other genotypes should result in greater HPA activity, enough to sustain normal

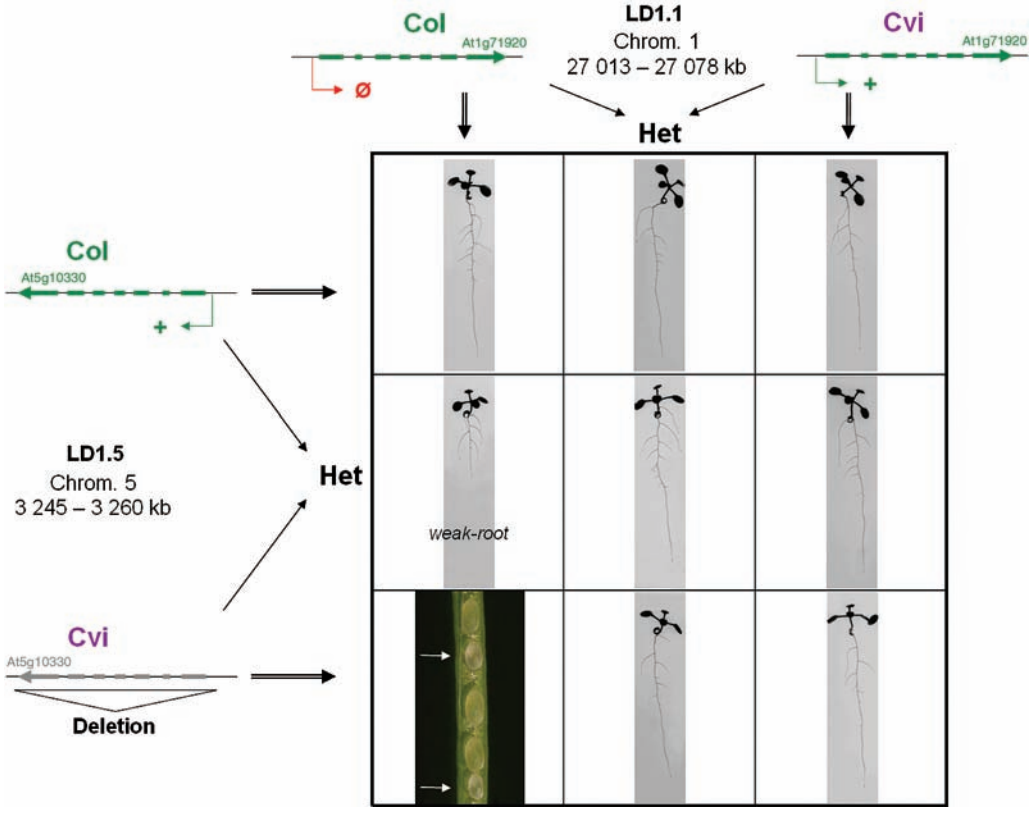

Fig. 1. Genetic mechanism underlying LD1 interaction and incompatibility. All combinations of alleles at LD1.5 and its interactor LD1.1 result in phenotypically normal plants, except for the combination Col at LD1.1/Heterozygous (Het) at LD1.5, which shows a reduced primary root length (weak-root phenotype), and another combination (Col at LD1.1/Cvi at LD1.5), which shows embryo lethality at an early stage in the silique (seeds under development containing lethal embryos are indicated by arrows). Fine-mapping identified a duplicate gene for which Col and Cvi show reciprocal gene loss explaining the interaction and incompatibility.

embryo and root development. Moreover, limited root growth in weak-root individuals can be explained by an alteration of the cell production rate because cell elongation remains normal in these plants (fig. S3), which is consistent with the lack of His and its associated defect in root meristem maintenance (*21*).

One way to prove the link between LD1 and *HPA* genes is to show that LD1 can be complemented by adding exogenous His. Weak-root plants were gradually and quantitatively rescued to the phenotype of the control by growing the plants on increasing concentrations of His in vitro (Fig. 2). Furthermore, watering heterozygous plants from the bolting stage with sufficient amounts of His restored the viability of embryos with incompatible allelic combinations (*17*), providing complementation of the embryo lethality phenotype as well. From these experiments, we concluded that the LD1 incompatibility results from a shortage of His in certain genotypes.

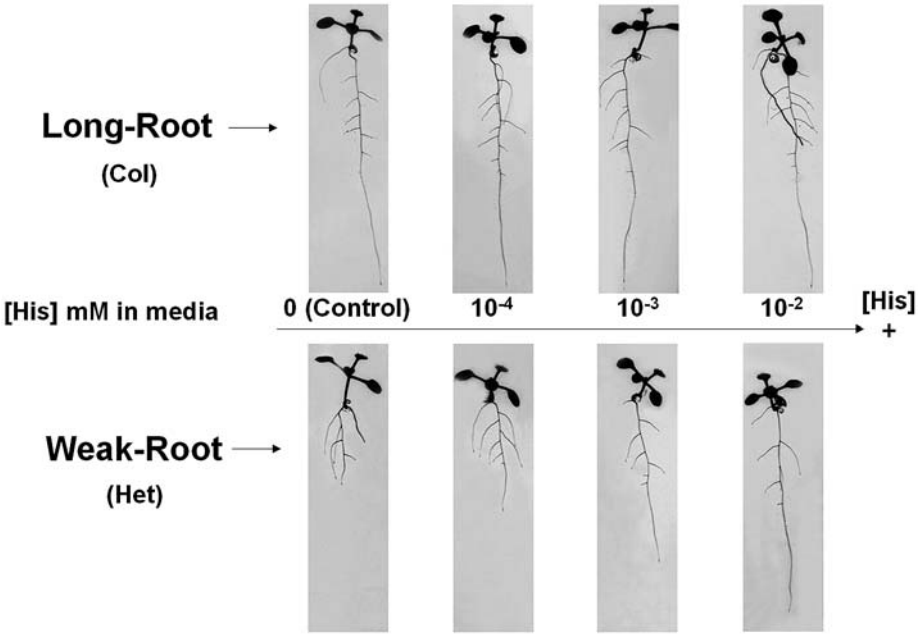

Fig. 2. The weak-root phenotype is quantitatively complemented by exogenous His. Typical phenotypes of descendants from a plant segregating at the LD1.5 locus when grown on media supplemented with different histidine concentrations. Plants were identified on the basis of their genotype at the LD1.5 locus. The complementation of the expected weak-root phenotype was complete when supplied with 10^{-2} mM His.

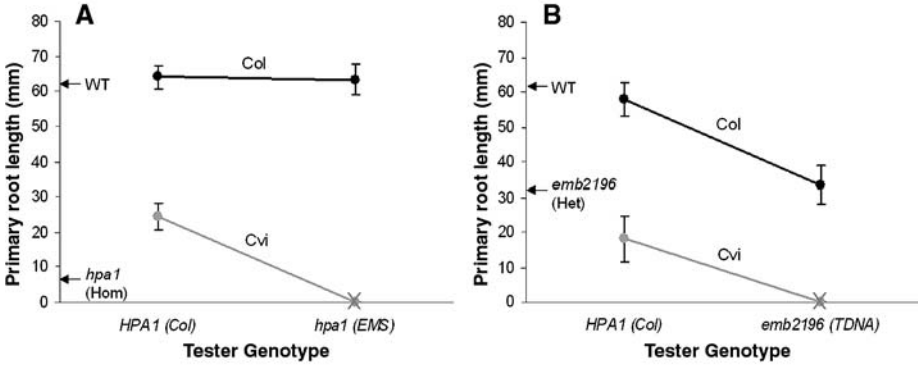

Fig. 3. Allelic complementation of LD1 interaction. Quantitative complementation tests were performed by combining different alleles at LD1 loci in F1 backgrounds. The relative complementation of either (**A**) an EMS mutant allele (*hpa1*) or (**B**) a T-DNA insertion mutant allele (*emb2196*) at At5g10330 by a Col or Cvi allele at LD1.5 was measured through both the length of the primary root (shown in mm) and embryo lethality. Individuals with a phenotype depicted on the *x* axis (null) underwent seed abortion. All plants are Col at LD1.1. Arrows along the *y* axis represent the typical root length of control genotypes [WT indicates wild-type Col plants; *hpa1* (Hom), homozygous *hpa1* mutant plants; and *emb2196* (Het), heterozygous individuals for the *emb2196* mutation]. Each data point represents the mean ± standard error of about 40 plants. The LD1.5 allele × *HPA1* genotype interaction term as tested by analysis of variance is significant in crosses to *hpa1* ($P < 0.0001$) and crosses to *emb2196* ($P < 0.05$).

To prove the causative role of *HPA* genes on LD1, we performed an allelic (quantitative) complementation test by combining different alleles at LD1.5 and At5g10330 in an identical F1 background. Crossing segregating HIF lines to different mutants (*hpa1* and *emb2196*) revealed how the different alleles at the two duplicate genes interact to qualitatively control embryo development and quantitatively limit primary root growth (Fig. 3). From crosses with the *hpa1* mutant (Fig. 3A), we observed that a Cvi allele at LD1.5 is unable to complement the EMS mutant allele at At5g10330 (whereas a Col allele does). This genotype (Cvi/*hpa1*) leads to embryo lethality, a phenotype even stronger than homozygous *hpa1* mutants (these embryos survive), indicating that the causative Cvi allele at LD1.5 is more deleterious than the EMS mutation (which fits well with the gene being completely deleted in Cvi). The significant interaction between the LD1.5 alleles and *HPA* genotypes argues that *HPA* is involved in LD1 epistasis. Crosses to the *emb2196* mutant led to the same conclusion when Col and Cvi alleles were compared versus the stronger *emb2196* allele (Fig. 3B). However, a heterozygous seedling for *emb2196* mutation (Col/*emb2196* at At5g10330) had a significantly ($P < 0.01$) longer primary root than a heterozygous seedling with a Cvi/Col genotype at LD1.5 (Fig. 3B). This, together with the fact that another T-DNA line in the same gene (SALK_089516) has a shorter root than *emb2196* in the heterozygous state (similar to weak-root plants), indicated that the *emb2196* T-DNA insertion is probably not a complete null allele (in contrast to SALK_089516). From these experiments, we concluded that epistasis at LD1 is most likely explained by allelic variation at *HPA* genes as depicted in Fig. 1 and that the incompatibility observed between Col and Cvi represents an example of intraspecific divergence of a duplicate gene pair.

Similar patterns of segregation distortion involving regions at the bottom of chromosome 1 and top of chromosome 5 were detected in a RIL set derived from the cross between Cvi and Landsberg *erecta* (L*er*), indicating that there may be a similar interaction between these loci (*22*). Nearly isogenic lines derived from this population (*23*) confirmed epistasis and incompatibility by showing a specific pattern of segregation and the weak-root phenotype. Both *HPA* genes were expressed in L*er*; however, the chromosome 1 paralog contains a premature stop codon (Fig. 4). This encouraged us to analyze the extent of functional natural variation at those loci and further characterize intraspecific evolution of these genes in *A. thaliana*.

We analyzed 30 accessions derived from distinct natural populations representing most known variation in *Arabidopsis* (*24*) for the expression of each gene copy, potential deletions,

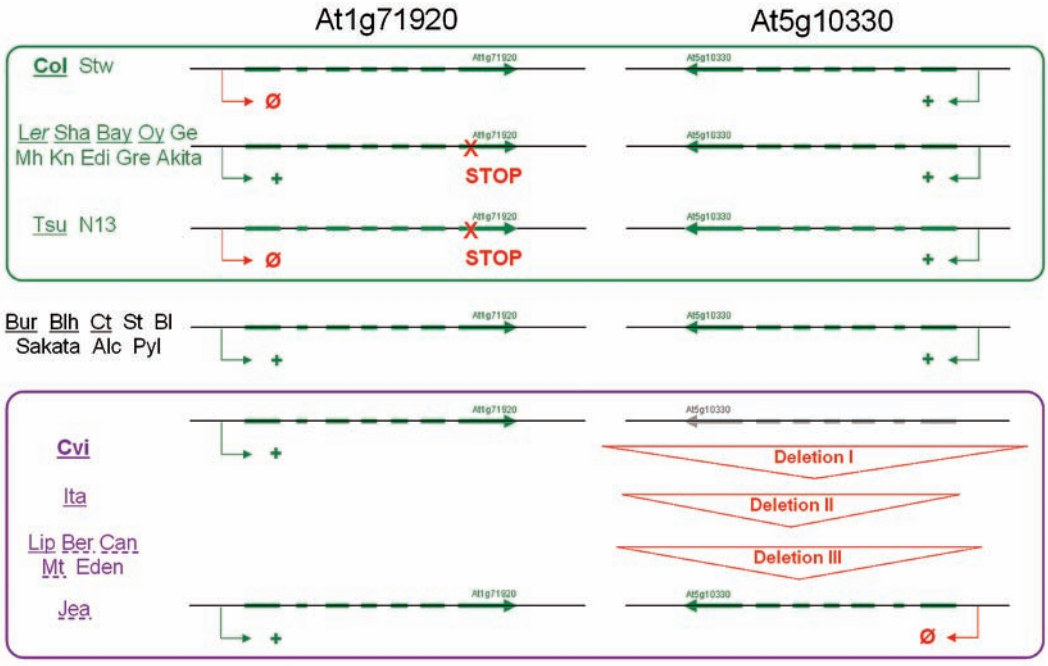

Fig. 4. Divergent evolution of duplicate genes among *A. thaliana* accessions. Groups of accessions are presented according to At5g10330 and/or At1g71920 genotypes and transcript accumulation phenotypes. Accessions (underlined) from each group were crossed to Col and/or Cvi and tested for LD1 incompatibility and compatibility to confirm the loss of function of one or the other duplicate gene. Dash-underlined accessions show conditional incompatibility (table S1). The incompatible groups are circled: green-circled genotypes are incompatible with Cvi; purple-circled genotypes are incompatible with Col. Genotypes not circled are fully compatible with both Col and Cvi.

and deleterious mutations. We also looked for LD1.1/LD1.5 genetic incompatibilities (accompanied by segregation of the weak-root phenotype) in 28 of the possible crosses to Col or Cvi (either in RIL sets or F2 populations) to confirm the relevance of variation detected at the nucleotide and/or expression level. Divergent evolution of the *HPA* gene pair was dramatic and widespread (Fig. 4 and table S1) because most (22/30) of the accessions tested have silenced one or the other copy in at least six different ways (early stop, no expression, a combination of both, and different deletions). Cvi- and Col-incompatible groups represent 14 and 8 accessions, respectively, and, on the basis of these data, we estimate that at least one-fourth of all possible crosses among these 30 strains would show *HPA* incompatibility. We observed no particular correlation with geographical population structure (*25*). Most of the four structure groups defined previously (*26*) included strains belonging to the two incompatibility groups as well as compatible accessions.

We confirmed that the rapid and common evolution of duplicate genes provides an important source of Bateson-Dobzhansky-Muller–like epistatic interactions after paralogs have been reciprocally silenced or lost in diverged strains, as proposed (*27*, *28*). Depending on the function and essential nature of the gene, this may result in hybrid and/or F2 defective fitness in the descendants of certain intraspecific crosses and could contribute to reproductive isolation (*29*). Passive gene loss is recognized as the most probable fate of duplicate genes and is especially likely at early stages after small-scale duplication events (*12*, *30*). However, direct evidence of gene loss as a neutral mechanism generating postzygotic isolating barriers within existing species with no prior fitness consequences in the parental strains (because only the location of the functional copy changes) has been lacking (*4*, *31*, *32*). Staal *et al*. (*33*) described how a transposition of a resistance gene found in the L*er* strain of *Arabidopsis* was responsible for variation in disease susceptibility in crosses to Col. Similarly, transposition of an essential gene has recently been associated with the sterility of a hybrid between two *Drosophila* species (*29*), and descriptive work on three related yeast species indicated that divergent resolution events after whole-genome duplication may have contributed to their speciation (*34*). Our study extends these observations in demonstrating the link between gene duplication and genetic incompatibility.

References and Notes

1. K. Bomblies, D. Weigel, *Nat. Rev. Genet.* **8**, 382 (2007).
2. J. Mallet, *Trends Ecol. Evol.* **21**, 386 (2006).
3. T. Dobzhansky, *Genetics and the Origin of Species* (Columbia Univ. Press, New York, 1937).
4. J. A. Coyne, H. A. Orr, *Speciation*, M. A. Sunderland, Ed. (Sinauer, Sunderland, MA, 2004).
5. K. Bomblies, D. Weigel, *Curr. Opin. Genet. Dev.* **17**, 500 (2007).
6. A. Kopp, A. Frank, *Genetica* **125**, 55 (2005).
7. N. J. Brideau *et al*., *Science* **314**, 1292 (2006).
8. H. S. Seidel, M. V. Rockman, L. Kruglyak, *Science* **319**, 589 (2008); published online 10 January 2008 (10.1126/science.1151107).
9. K. Bomblies *et al*., *PLoS Biol.* **5**, e236 (2007).
10. M. Simon *et al*., *Genetics* **178**, 2253 (2008).
11. O. Törjék *et al*., *Theor. Appl. Genet.* **113**, 1551 (2006).
12. M. Lynch, J. S. Conery, *Science* **290**, 1151 (2000).
13. H. A. Orr, J. P. Masly, N. Phadnis, *J. Hered.* **98**, 103 (2007).
14. H. A. Orr, M. Turelli, *Evolution* **55**, 1085 (2001).
15. H. A. Orr, J. P. Masly, D. C. Presgraves, *Curr. Opin. Genet. Dev.* **14**, 675 (2004).
16. O. Loudet, V. Gaudon, A. Trubuil, F. Daniel-Vedele, *Theor. Appl. Genet.* **110**, 742 (2005).
17. Materials and methods are available as supporting material on *Science* Online.
18. R. Muralla, C. Sweeney, A. Stepansky, T. Leustek, D. Meinke, *Plant Physiol.* **144**, 890 (2007).
19. R. C. Moore, M. D. Purugganan, *Proc. Natl. Acad. Sci. U.S.A.* **100**, 15682 (2003).
20. I. Tzafrir *et al*., *Plant Physiol.* **135**, 1206 (2004).
21. X. Mo *et al*., *Plant Physiol.* **141**, 1425 (2006).
22. C. Alonso-Blanco *et al*., *Plant J.* **14**, 259 (1998).
23. J. J. Keurentjes *et al*., *Genetics* **175**, 891 (2007).
24. H. I. McKhann *et al*., *Plant J.* **38**, 193 (2004).
25. M. Nordborg *et al*., *PLoS Biol.* **3**, e196 (2005).
26. M. F. Ostrowski *et al*., *Mol. Ecol.* **15**, 1507 (2006).
27. M. Lynch, A. G. Force, *Am. Nat.* **156**, 590 (2000).
28. C. R. Werth, M. D. Windham, *Am. Nat.* **137**, 515 (1991).
29. J. P. Masly, C. D. Jones, M. A. F. Noor, J. Locke, H. A. Orr, *Science* **313**, 1448 (2006).
30. S. Maere *et al*., *Proc. Natl. Acad. Sci. U.S.A.* **102**, 5454 (2005).
31. M. Lynch, J. S. Conery, *J. Struct. Funct. Genomics* **3**, 35 (2003).
32. M. Semon, K. H. Wolfe, *Curr. Opin. Genet. Dev.* **17**, 505 (2007).
33. J. Staal, M. Kaliff, S. Bohman, C. Dixelius, *Plant J.* **46**, 218 (2006).
34. D. R. Scannell, K. P. Byrne, J. L. Gordon, S. Wong, K. H. Wolfe, *Nature* **440**, 341 (2006).

35. We thank K. Bomblies and D. Weigel for providing F2 seeds for specific test crosses (Bay-0 × Cvi and Tsu-0 × Cvi), X. Mo for hpa1 seeds, and R. Mercier and F. Roux for discussion and critical reading of the manuscript. Funded partly by an INRA–Département de Génétique et d'Amélioration des Plantes Innovative Project grant to C.C. and O.L. Funding by the University of Nottingham to D.P. and the Biotechnology and Biological Sciences Research Council/ Engineering and Physical Sciences Research Council Centres for Integrative Systems Biology program to M.J.B. Sequences have been deposited in GenBank under accessions FJ436446 and FJ436447.

Supporting Online Material

www.sciencemag.org/cgi/content/full/323/5914/623/DC1
Materials and Methods
Figs. S1 to S3
Table S1
References

15 September 2008; accepted 25 November 2008
10.1126/science.1165917

Serotonin Mediates Behavioral Gregarization Underlying Swarm Formation in Desert Locusts

Michael L. Anstey,[1]* Stephen M. Rogers,[1,2]*† Swidbert R. Ott,[2] Malcolm Burrows,[2] Stephen J. Simpson[1,3]

Desert locusts, *Schistocerca gregaria*, show extreme phenotypic plasticity, transforming between a little-seen solitarious phase and the notorious swarming gregarious phase depending on population density. An essential tipping point in the process of swarm formation is the initial switch from strong mutual aversion in solitarious locusts to coherent group formation and greater activity in gregarious locusts. We show here that serotonin, an evolutionarily conserved mediator of neuronal plasticity, is responsible for this behavioral transformation, being both necessary if behavioral gregarization is to occur and sufficient to induce it. Our data demonstrate a neurochemical mechanism linking interactions between individuals to large-scale changes in population structure and the onset of mass migration.

Phenotypic plasticity, the differential expression of alternative phenotypes from a single genotype depending upon environmental conditions, is of considerable evolutionary importance, but controlling mechanisms remain elusive (*1*). Changes in population density can be a substantial source of environmental variability and can trigger phenotypic changes that equip animals for increased competition for resources as well as for dispersal or migration (*1*–*3*). Desert locusts undergo an extreme and economically devastating form of this kind of phenotypic plasticity, changing reversibly between two extreme forms or phases (*4*–*6*). These differ extensively in morphology and physiology, but behavior is the key to both establishing and maintaining each phase (*7*). Swarming begins with a rapidly induced switch from mutual repulsion in solitarious locusts to attraction and aggregation after just a few hours of forced crowding (*7*, *8*). Although the sensory stimuli triggering behavioral gregarization have recently been identified (*9*–*11*), it was unknown how they mediated their effect.

Solitarious locusts acquire full gregarious behavioral characteristics within the first 2 hours of forced crowding [Fig. 1, A to C, fig. S1, and supporting online material (SOM) text]. This period coincides with a substantial but transient (<24 hours) increase in the amount of serotonin [5-hydroxytryptamine (5-HT)] specifically in one region of the central nervous system (CNS), the thoracic ganglia, but not the brain (*12*) (Fig. 1D). To determine whether this increase caused gregarization, we first analyzed the relationship between the degree of behavioral gregarization and the amount of serotonin in individual locusts crowded for different times (*13*). Behavior was characterized by using a binary logistic regression model (*8*), which produced a single probabilistic metric of gregariousness P_{greg} that encompassed four different variables (table S1). A P_{greg} of 0 meant an animal behaved solitariously, whereas a P_{greg} of 1 indicated fully gregarious behavior. Amounts of serotonin in the thoracic ganglia were measured by using high-performance liquid chromatography (HPLC).

We crowded solitarious locusts for 0, 1, or 2 hours to generate the entire gamut of behavior, from solitarious to gregarious (Fig. 2A). The amount of serotonin was significantly positively correlated with the extent of gregarious behavior across this entire range (analysis of covariance, 5-HT $\log_e$ transformed; $F_{1,35} = 21.817$, $r^2 = 0.429$, $P < 0.001$). Locusts that behaved the most gregariously ($P_{greg} > 0.8$) had approximately three times more serotonin (12.78 ± 1.85 pmol; mean ± SD, $n = 10$ locusts) than more solitariously behaving ($P_{greg} < 0.2$) locusts (4.18 ± 0.27 pmol; $n = 7$ locusts). Furthermore, the amount of serotonin only corresponded with the degree of gregarization but not the duration of crowding, per se ($F_{3,35} = 1.218$, $P = 0.318$).

Behavioral gregarization can be acquired via two distinct sensory pathways: a thoracic pathway driven by mechanosensory stimulation of the hind legs as locusts jostle each other and a cephalic pathway in which the combined sight and smell of other locusts is the necessary stimulus (*9*–*11*). Locusts stimulated via either sensory pathway displayed similar levels of gregarious behavior after 2 hours (Fig. 1C, fig. S1, and SOM text). We tested whether gregarization induced by these separate pathways showed the same relationship between serotonin and behavior that we saw in crowded solitarious locusts. The thoracic pathway was activated by either stroking a hind femur (*10*) or electrically stimulating metathoracic nerve 5, which simulated mechanosensory stimulation (*11*). In both instances, the amount of serotonin in the thoracic ganglia significantly increased and was correlated with the extent of

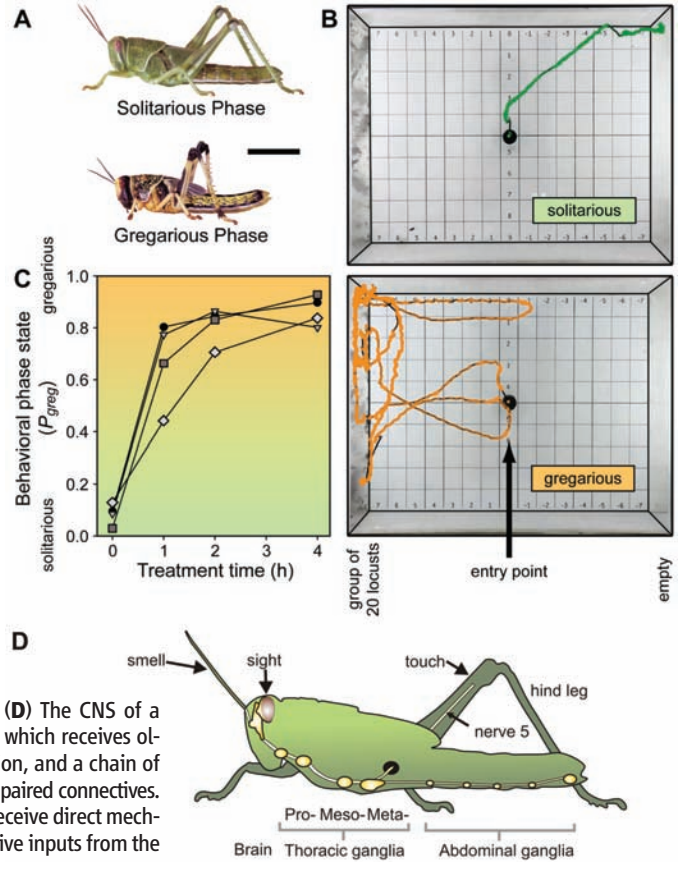

Fig. 1. (**A**) Final larval instar solitarious and gregarious locusts. Scale bar, 1 cm. (**B**) Trajectories (over 500 s) of a solitarious (upper) and gregarious (lower) locust in the behavioral arena. A group of 20 long-term gregarious-phase locusts was placed behind a clear partition on the left. (**C**) Solitarious locusts undergo rapid behavioral gregarization with appropriate stimulation; median P_{greg} of locusts treated for 0 to 4 hours by either forced crowding with gregarious locusts (circles), stroking a hind femur (squares), electrically stimulating the principal hind-leg nerve (diamonds), or exposure to the sight and smell of other locusts (triangles). See SOM text for analysis. (**D**) The CNS of a locust consists of the brain, which receives olfactory and visual information, and a chain of segmental ganglia linked by paired connectives. The three thoracic ganglia receive direct mechanosensory and proprioceptive inputs from the legs.

[1]Department of Zoology, University of Oxford, South Parks Road, Oxford, OX1 3PS, UK. [2]Department of Zoology, University of Cambridge, Downing Street, Cambridge, CB2 3EJ, UK. [3]School of Biological Science, University of Sydney, Sydney, NSW 2006, Australia.

*These authors contributed equally to this work.
†To whom correspondence should be addressed. E-mail: smr34@cam.ac.uk

gregarization [linear regressions; in stroked locusts, $F_{1,24} = 15.027$, $P = 0.001$, $r^2 = 0.39$ (Fig. 2B); in electrically stimulated locusts, $F_{1,13} = 7.457$, $P = 0.017$; $r^2 = 0.37$ (Fig. 2C)]. Likewise, gregarization through exposure to just the sight and smell of other locusts led to an increase in the amount of serotonin in the thoracic ganglia that correlated with the degree of behavioral gregarization [$F_{1,11} = 23.065$, $P = 0.001$, $r^2 = 0.7$ (Fig. 2D)]. These results indicate that gregarizing stimuli from both sensory pathways converge in the thoracic ganglia, but it is unknown whether they have a cumulative effect on serotonin production.

This strong correlation between phase state and serotonin levels in the thoracic ganglia led us to ask whether blocking the action of serotonin could prevent behavioral gregarization. A mixture of two 5-HT receptor antagonists, ketanserin (1 mM) (*14*, *15*) and methiothepin (1 mM) (*16*, *17*), or a saline control were injected directly into the meso- and metathoracic ganglia of solitarious locusts. The locusts then received either mechanosensory or olfactory and visual gregarizing stimuli for 1 hour. The locusts injected with the antagonists failed to gregarize in response to either stimulus regime (Fig. 3A), in contrast to the saline-injected controls [analysis of variance (ANOVA) of normal rank transformed data, $F_{1,49} = 17.169$, $P < 0.0005$; there was no interaction between stimulus regime and degree of gregarization, $F_{1,49} = 0.001$, $P = 0.987$]. Median P_{greg} in the antagonist-injected locusts was 0.27 for the thoracic and 0.07 for the cephalic pathways (Fig. 3A). By contrast, the median P_{greg} values of the saline-injected controls were 0.91 and 0.74, respectively. Next, we inhibited serotonin synthesis by using α-methyltryptophan (AMTP), a competitive antagonist of tryptophan hydroxylase (*18*, *19*). Locusts were given repeated systemic injections of either 40 μl of 0.1 mM AMTP in locust saline or just saline (controls) over 5 days (*13*). The AMTP-injected locusts (Fig. 3B) showed little behavioral gregarization after having their hind-femora stroked for 2 hours (median $P_{greg} = 0.13$), in strong contrast to the controls (median $P_{greg} = 0.91$; Mann-Whitney $U = 30.500$, $n = 23$ locusts, $P = 0.032$).

We next determined whether serotonin or serotonin receptor agonists were sufficient to induce behavioral gregarization in the absence of stimuli associated with other locusts. Serotonin (1 mM) in saline or a saline control were topically applied to the exposed thoracic ganglia over 2 hours. Serotonin-treated locusts (Fig. 4A) were significantly more gregarious in behavior (median $P_{greg} = 0.6$) than control animals, which remained highly solitarious (median $P_{greg} = 0.07$; Mann-Whitney $U = 41$, $n = 30$ locusts, $P = 0.004$). In a second experiment, animals injected in the thoracic ganglia with a mixture of two serotonin receptor agonists, 1 mM α-methylserotonin (*20*, *21*) and 1 mM 5-carboxamidotryptamine (*16*), showed a significant shift toward gregarious behavior (median $P_{greg} = 0.4$) as compared with saline-injected controls after 1 hour [median $P_{greg} = 0.13$; Mann-Whitney $U = 63$, $n = 30$ locusts, $P = 0.042$ (Fig. 4B)].

Gregarizing stimuli cause serotonin to increase in the thoracic CNS, and exogenous serotonin increases the likelihood of locusts behaving gregariously. We next asked whether enhanced endogenous serotonin synthesis could amplify the effect of stimuli presented for a brief period. Locusts were given single 40-μl injections in the thoracic haemocoel of either the serotonin precursor 5-hydroxytryptophan (5-HTP) (10 mM) (*22*, *23*) or saline controls, and their behavior was assayed after either 30 min of further solitude or 30 min of crowding. Treatment regime had a significant effect on behavior [ANOVA of normal rank transformed P_{greg} data; $F_{3,59} = 5.6$, $P = 0.002$ (Fig. 4C)]. Control locusts that just received saline and were kept in isolation remained highly solitarious in behavior (median $P_{greg} = 0.17$). The median P_{greg} of crowded saline-injected locusts was 0.46, suggesting some change in

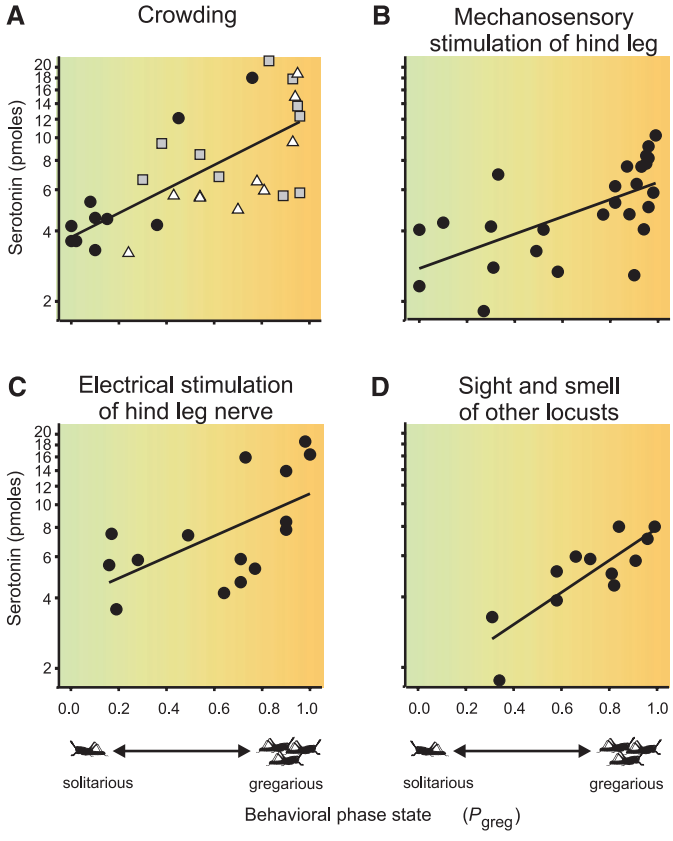

Fig. 2. The amount of serotonin in the thoracic CNS is correlated with the degree of behavioral gregarization. Relationships between the amount of serotonin in the thoracic CNS ($\log_e$ scale) and the degree of behavioral gregarization (P_{greg}) after solitarious locusts have been (**A**) crowded for 1 hour (triangles), 2 hours (squares), or unstimulated controls (circles); (**B**) stroked on the left hind femur for 2 hours; (**C**) given patterned electrical stimulation to metathoracic nerve 5, simulating the effect of mechanosensory stimulation for 2 hours; or (**D**) presented with the sight and smell of ~1000 locusts for 2 hours.

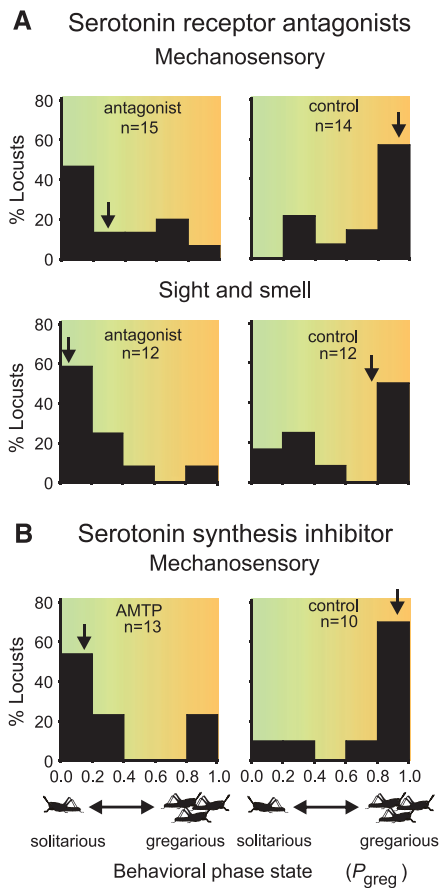

Fig. 3. Serotonin is necessary to induce behavioral gregarization. Behavior of locusts injected with substances that block either the action or the synthesis of serotonin and then exposed to sensory stimuli that normally induce gregarization (left column) is shown. Saline-injected controls are shown in the right column. (**A**) Locusts injected with serotonin-receptor antagonists ketanserin and methiothepin (1 mM) and given either 1 hour of femoral mechanosensory stimulation or 1 hour of olfactory and visual stimulation from other locusts. (**B**) Locusts injected with 0.1 mM AMTP, an inhibitor of serotonin synthesis coupled with 2 hours of mechanosensory stimulation. Arrows indicate median P_{greg} values.

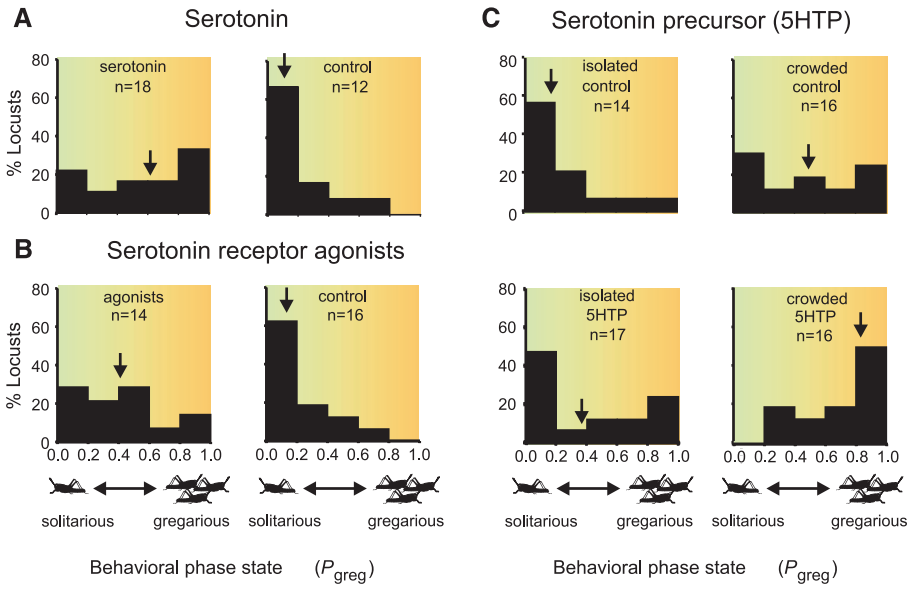

Fig. 4. Serotonin is sufficient to induce gregarious behavior. Behavior of locusts after they have been treated with (**A**) serotonin topically applied to the thoracic ganglia (left column) and paired saline controls (right column); (**B**) a mixture of serotonin agonists (1 mM α-methylserotonin and 1 mM 5-carboxamidotryptamine) and paired saline-injected controls; and (**C**) the serotonin precursor 5-HTP, either with or without 30 min of crowding with other locusts.

behavior; however, the distribution was not significantly different from isolated saline-injected locusts (Dunnet's post-hoc test, $P = 0.383$), which indicates that 30 min was too brief a period of crowding to induce full behavioral gregarization. Locusts that received an injection of 5-HTP but were not crowded also showed a similar but also nonsignificant increase in P_{greg} (median 0.38; $P = 0.448$), which indicates that this treatment was also insufficient to induce full behavioral gregarization. However, locusts that had received both the serotonin precursor and had also been exposed to a brief period of crowding became highly gregarious (median $P_{greg} = 0.81$, $P = 0.001$ as compared with undrugged and uncrowded controls). Thus, 5-HTP can potentiate the effect of gregarizing stimuli applied for a brief period. Unlike the direct application of serotonin, this experiment suggests that endogenous serotonin synthesis driven by sensory stimuli is mechanistically responsible for inducing behavioral gregarization. There are few serotonergic neurons in the locust CNS (*24*), which suggests that the individual neurons driving behavioral gregarization can be identified.

Serotonin and other monoamines have been implicated in changing behavior after social interactions in a number of contexts, including intraspecific aggression, status, and courtship in many species, including crickets (*25*), crustaceans (*26*, *27*), and rats (*28*). All of these interactions, including behavioral gregarization in locusts, require the interpretation of complex signals from conspecifics leading to long-lasting changes in the way individuals interact during future encounters. Behavioral gregarization therefore resembles memory formation, with specific sensory experiences altering future behavior; in the case of locusts, this entails a suite of changes that creates an integrated behavioral phenotype adapted to a changed biotic environment. Locusts that have been reared gregariously for many generations have lower titers of serotonin than long-term solitarious animals, (*12*) which strongly suggests that gregarious behavior is not maintained by a long-term serotonergic modulation of neuronal circuits. Furthermore, solitarious behavior is acquired more slowly on the isolation of long-term gregarious phase locusts (*8*) than gregarious behavior is acquired by solitarious locusts, implying that gregarious behavior becomes more ingrained during prolonged crowding. This ingraining process may entail serotonin-mediated gene transcription and/or translation-dependent mechanisms similar to those associated with other serotonin-mediated neuronal plasticity (*29*, *30*). Although serotonin clearly mediates the critical change in behavior that drives the early process of gregarization, we do not know whether it directly initiates the full and complex suite of changes associated with the full gregarious phenotype. Serotonin, by providing a rapidly acquired and stable behavioral substrate for group living, may enable slower but fully independent mechanisms of phenotypic change to activate through a process of environmental feedback (*4*, *5*, *7*, *31*).

Could serotonin antagonists be effective locust control agents? Given the ubiquity of serotonin signaling in the animal kingdom, any agent would have to be specific for the serotonin receptor mediating phase change, which is yet to be characterized. To be effective, it would have to be targeted at regions of incipient swarm formation to prevent locusts coalescing further into groups.

The whole multilayered process of phase change depends upon a simple behavioral decision whether to avoid other locusts or band together. Without this initial behavioral choice, no further physiological and morphological change can occur (*12*, *31*), and there is no possibility of further escalation in group size. Our data demonstrate a mechanism by which sensory signals gauging population density alter neuronal circuits underlying this fundamental decision. The consequences ramify upwards into population structure and ultimately provide the essential conditions for mass migration and swarming. Phase change is the defining character of locust biology and is the reason why they make such devastating pests. Serotonin-mediated behavioral plasticity is a pivotal mechanism in this transformation.

References and Notes

1. M. J. West-Eberhard, *Developmental Plasticity and Evolution* (Oxford Univ. Press, Oxford, 2003).
2. J. Buhl *et al.*, *Science* **312**, 1402 (2006).
3. S. Bazazi *et al.*, *Curr. Biol.* **18**, 735 (2008).
4. B. Uvarov, *Grasshopper and Locusts*, vol. 1 (Cambridge Univ. Press, Cambridge, 1966).
5. M. P. Pener, Y. Yerushalmi, *J. Insect Physiol.* **44**, 365 (1998).
6. M. Enserink, *Science* **306**, 1880 (2004).
7. S. J. Simpson, A. R. McCaffery, B. F. Hagele, *Biol. Rev. Camb. Philos. Soc.* **74**, 461 (1999).
8. P. Roessingh, S. J. Simpson, S. James, *Proc. R. Soc. London B Biol. Sci.* **252**, 43 (1993).
9. P. Roessingh, A. Bouaichi, S. J. Simpson, *J. Insect Physiol.* **44**, 883 (1998).
10. S. J. Simpson, E. Despland, B. F. Hagele, T. Dodgson, *Proc. Natl. Acad. Sci. U.S.A.* **98**, 3895 (2001).
11. S. M. Rogers *et al.*, *J. Exp. Biol.* **206**, 3991 (2003).
12. S. M. Rogers *et al.*, *J. Exp. Biol.* **207**, 3603 (2004).
13. Materials and methods are available as supporting material on *Science* Online.
14. D. Parker, *J. Neurophysiol.* **73**, 923 (1995).
15. L. Gatellier, T. Nagao, R. Kanzaki, *J. Exp. Biol.* **207**, 2487 (2004).
16. A. J. Tierney, *Comp. Biochem. Physiol.* **128A**, 791 (2001).
17. N. Spitzer, D. H. Edwards, D. J. Baro, *J. Exp. Biol.* **211**, 92 (2008).
18. B. D. Sloley, S. Orikasa, *J. Neurochem.* **51**, 535 (1988).
19. P. A. Stevenson, H. A. Hofmann, K. Schoch, K. Schildberger, *J. Neurobiol.* **43**, 107 (2000).
20. G. Molaei, A. B. Lange, *J. Insect Physiol.* **49**, 1073 (2003).
21. J. F. Colas, J. M. Launay, O. Kellermann, P. Rosay, L. Maroteaux, *Proc. Natl. Acad. Sci. U.S.A.* **92**, 5441 (1995).
22. M. Ureshi, M. Dainobu, M. Sakai, *J. Comp. Physiol. A* **188**, 767 (2002).
23. N. N. Osborne, V. Neuhoff, *Brain Res.* **74**, 366 (1974).
24. N. M. Tyrer, J. D. Turner, J. S. Altman, *J. Comp. Neurol.* **227**, 313 (1984).
25. H. A. Hofmann, P. A. Stevenson, *Nature* **403**, 613 (2000).
26. R. Huber, K. Smith, A. Delago, K. Isaksson, E. A. Kravitz, *Proc. Natl. Acad. Sci. U.S.A.* **94**, 5939 (1997).
27. E. A. Kravitz, R. Huber, *Curr. Opin. Neurobiol.* **13**, 736 (2003).
28. K. A. Miczek *et al.*, *J. Neurosci.* **27**, 11803 (2007).
29. C. Pittenger, E. R. Kandel, *Philos. Trans. R. Soc. London B* **358**, 757 (2003).
30. C. A. Hoeffer, S. Sanyal, M. Ramaswami, *J. Neurosci.* **23**, 6362 (2003).
31. A. I. Tawfik *et al.*, *Proc. Natl. Acad. Sci. U.S.A.* **96**, 7083 (1999).

32. We thank J. Niven, G. Sutton, and G. Sword for reading and commenting upon the manuscript; C. de la Riva at the Babraham Institute (UK) for technical support with the HPLC and K. Kendrick for permission to use the

facility; T. Dodgson and E. Miller for locust rearing and technical support; and M. Ungless for advice and support to M.A. This work is supported by grants from the Biotechnology and Biological Sciences Research Council, UK (to M.B, S.S., and S.O.), and a University Research Fellowship from the Royal Society, UK, to S.O. M.A. was supported by the Natural Sciences and Engineering Research Council of Canada, an Overseas Research Student Award, UK, and the Hope Studentship in Entomology from Jesus College and the University of Oxford, UK. S.S. is supported by an Australian Research Council Federation Fellowship.

Supporting Online Material

www.sciencemag.org/cgi/content/full/323/5914/627/DC1
Materials and Methods
SOM Text
Fig. S1
Table S1
References

15 September 2008; accepted 14 November 2008
10.1126/science.1165939

Survival from Hypoxia in *C. elegans* by Inactivation of Aminoacyl-tRNA Synthetases

Lori L. Anderson,[1] Xianrong Mao,[1] Barbara A. Scott,[1] C. Michael Crowder[1,2]*

Hypoxia is important in a wide range of biological processes, such as animal hibernation and cell survival, and is particularly relevant in many diseases. The sensitivity of cells and organisms to hypoxic injury varies widely, but the molecular basis for this variation is incompletely understood. Using forward genetic screens in *Caenorhabditis elegans*, we isolated a hypoxia-resistant reduction-of-function mutant of *rrt-1* that encodes an arginyl–transfer RNA (tRNA) synthetase, an enzyme essential for protein translation. Knockdown of *rrt-1*, and of most other genes encoding aminoacyl-tRNA synthetases, rescued animals from hypoxia-induced death, and the level of hypoxia resistance was inversely correlated with translation rate. The unfolded protein response was induced by hypoxia and was required for the hypoxia resistance of the reduction-of-function mutant of *rrt-1*. Thus, translational suppression produces hypoxia resistance, in part by reducing unfolded protein toxicity.

Oxygen requirements of cells and organisms have wide-ranging implications in behavior and disease. Forward genetic screens offer the possibility of discovering genes not previously known to control hypoxic sensitivity. Such genes are likely to play an important role in emergent organismal traits such as habitat range and ability to hibernate. Additionally, these genes may lead to the development of novel therapies for conditions where cellular hypoxic sensitivity is a pathological determinant, such as stroke, myocardial infarction, and cancer. Wild-type *C. elegans* when placed in a severe hypoxic environment (oxygen concentration <0.3 volume percent) become immobile but fully recover when returned to normoxia within 4 hours (*1*). After 4 hours, permanent behavioral deficits and cellular death ensue, and after a 22-hour hypoxic incubation, >99% of wild-type animals are dead. To identify genes that control hypoxic sensitivity, we screened for ethylmethane sulfonate (EMS)–derived mutants that survived a 22-hour hypoxic incubation. In a screen of 3884 F_1 mutant worm genomes, we recovered 14 mutants that had a hypoxia-resistant phenotype (table S1). These mutants fell into 13 complementation groups. We selected *gc47*, one of the strongest hypoxia-resistant mutants, for further characterization and mapping.

After outcrossing to the wild-type strain N2, the hypoxia resistance of *gc47* was quantified. Immediately after removal from a 20-hour hypoxic incubation, both N2 and *gc47* were paralyzed, but the *gc47* worms recovered the ability to move completely over the next 1 to 2 hours. After a 24-hour recovery, essentially all of the *gc47* animals were alive, whereas almost all wild-type worms failed to survive (Fig. 1, A and B); *gc47* prolonged the hypoxic incubation time required for complete killing by a factor of >3 (Fig. 1C). The hypoxia-resistant phenotype was fully recessive and segregated as a single locus in a Mendelian fashion (Fig. 1D) (*2*). *gc47* was mapped to a 106-kb interval on the left arm of chromosome III (Fig. 2A) (*2*). Double-stranded RNA interference (RNAi) of 29 of the 32 genes in the interval identified only one gene, *rrt-1*, whose knockdown produced high-level hypoxia resistance (Fig. 2B). Simultaneously, five fosmids that together spanned the entire interval were individually injected to attempt transformation rescue of *gc47*. Only one fosmid restored normal hypoxia sensitivity to *gc47* (Fig. 2C); the rescuing fosmid contained the *rrt-1* gene implicated by RNAi. Sequencing *rrt-1* in *gc47* found a single G → A transition, resulting in a change of amino acid residue 271 from an aspartate to an asparagine in *gc47* (D271N, Fig. 2A). Thus, *gc47* is an allele of *rrt-1* and behaves like a reduction-of-function allele.

rrt-1 encodes an arginyl-tRNA synthetase, one of the aminoacyl-tRNA synthetases (AARSs). AARSs catalyze the adenosine triphosphate (ATP)–dependent acylation of their cognate tRNA(s) with a specific amino acid (*3*). AARSs

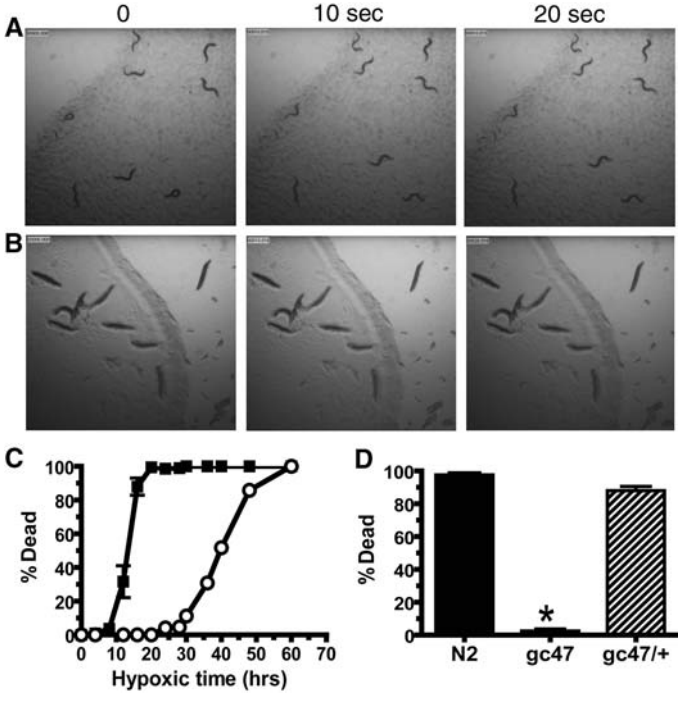

Fig. 1. *gc47* is a potent regulator of hypoxic cell death in *C. elegans*. (**A** and **B**) Time-lapse images (magnification 4×) of *gc47* (A) and N2 (B) adult worms after a 24-hour recovery from a 20-hour hypoxic insult. (**C**) Percent dead animals for N2 (squares) and *gc47* (circles) after a 24-hour recovery as a function of length of hypoxic insult. (**D**) Percent death among homozygous *gc47* (open bar, 13 trials), heterozygous *gc47*/+ (hatched bar, 9 trials), and N2 (solid bar, 16 trials) animals; the results show that *gc47* is recessive. Data are means ± SEM with >30 animals per trial; *$P < 0.01$ (two-tailed *t* test).

[1]Department of Anesthesiology, Washington University School of Medicine, St. Louis, MO 63110, USA. [2]Department of Developmental Biology, Washington University School of Medicine, St. Louis, MO 63110, USA.

*To whom correspondence should be addressed. E-mail: crowderm@morpheus.wustl.edu

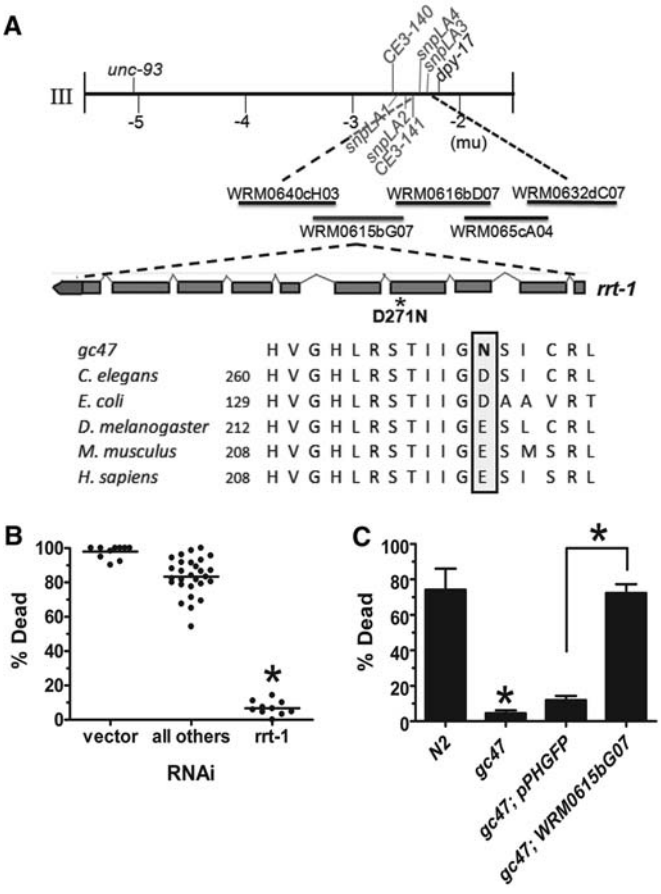

Fig. 2. *gc47* is an allele of *rrt-1*. (**A**) Genetic mapping of *gc47*. Three-factor mapping with the indicated visible markers (black text) and single-nucleotide polymorphisms (gray text) placed *gc47* in a 106-kb interval on chromosome III between CE3-141 and snpLA3. Fosmids injected for transformation rescue are shown. Amino acid alignment is with *rrt-1* orthologs; the *gc47* mutation is boxed. Amino acid abbreviations: A, Ala; C, Cys; D, Asp; E, Glu; G, Gly; H, His; I, Ile; L, Leu; M, Met; N, Asn; R, Arg; S, Ser; T, Thr; V, Val. (**B**) RNAi of genes within the 106,000–base pair mapping interval. Death was induced by hypoxia in animals treated with 29 of 32 predicted genes within the mapping interval. *rrt-1* RNAi conferred highly significant hypoxia resistance relative to empty vector (*$P < 0.01$; two-tailed *t* test, $n = 30$ animals per data point). (**C**) Transformation rescue of *gc47*. Hypoxia-induced animal death was scored for N2, *gc47* [full genotype: *rrt-1(gc47) dpy-17(e164)*], and *gc47* transformed with the transformation marker pPHGFP alone or in addition to the rescuing fosmid WRM0615bG07. Data are means ± SEM of at least two trials, >20 animals per trial; *$P < 0.01$ (two-tailed *t* test).

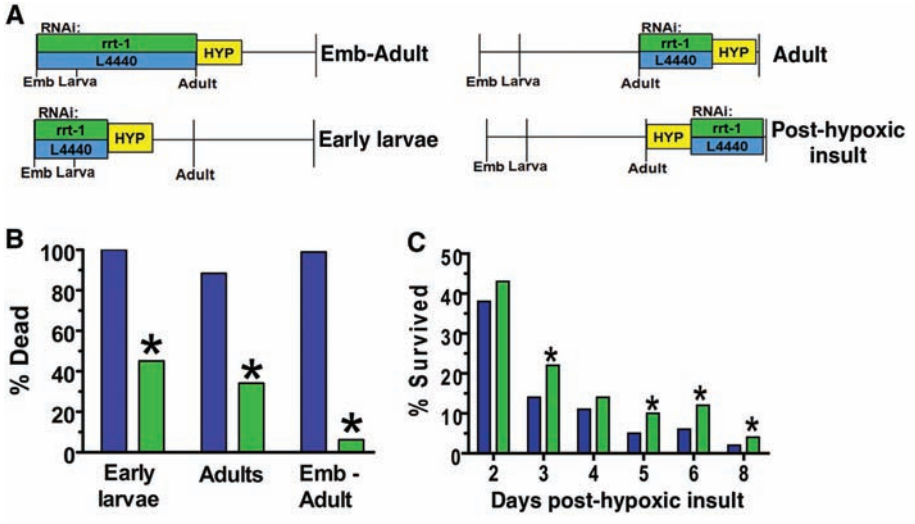

Fig. 3. *rrt-1* acutely controls hypoxic sensitivity, both during and after the insult. (**A**) Schematic of the experimental protocol. Wild-type animals were exposed to *rrt-1* or L4440 empty vector RNAi at the developmental stages indicated, and were then treated with a 20-hour (**B**) or 16-hour (**C**) hypoxic incubation (HYP, yellow boxes); Emb, embryo. (B) Hypoxia resistance by *rrt-1(RNAi)* is not dependent on developmental stage [$n = 40$ animals per condition; *$P < 0.05$ versus L4440 (Fisher's exact test, two-sided)]. (C) Inhibition of *rrt-1* is effective after hypoxic insult. Percent survived = [(number of animals alive at day of interest)/(number of animals alive initially after 24-hour recovery)] × 100; *$P < 0.05$ versus L4440 (Fisher's exact test, two-sided); $n > 300$ initially alive worms per RNAi over three independent trials.

fall into two distinct structural classes. RRT-1 is a class I enzyme, characterized by HIGH and MRSK domains (*4*, *5*). In higher eukaryotes, the RRT-1 ortholog has been isolated in a cytoplasmic complex with six other AARSs and three accessory subunits (*6*, *7*). Some AARSs are specific for mitochondrial DNA, and besides their role in translation, a subset has been implicated in non–translation-related functions (*8*, *9*). To test whether control of hypoxic sensitivity is a general function of AARSs or is restricted to a particular subset, we used feeding RNAi constructs against 23 of the 33 predicted AARSs in the *C. elegans* genome. All but one of the 23 RNAi constructs conferred significant hypoxia resistance (table S2). Thus, most, if not all, AARSs control hypoxic sensitivity. Knockdown of some AARSs produced stronger hypoxia-resistant phenotypes than others, which was not explained by the class of AARSs or whether the tRNA substrate was cytoplasmic or mitochondrial. Although the degree of RNAi knockdown was variable (table S2), RNAi efficacy did not explain all of the phenotypic variance. To examine whether the variable levels of hypoxia resistance could be explained by differences in translational suppression, we measured [^{35}S]methionine incorporation in animals treated with select AARS RNAi constructs as well as in *rrt-1(gc47)* (fig. S1). The level of hypoxia resistance had a strong inverse correlation with the relative translation rate. However, the absolute amount of translational suppression was relatively modest even in the strongest hypoxia-resistant animals, where the [^{35}S]methionine incorporation was about half that of vector controls. Thus, hypoxic sensitivity appears to be exquisitely sensitive to even small changes in translation rate. Consistent with translational suppression as the proximate mechanism of hypoxia resistance, treatment with cycloheximide also conferred hypoxia resistance (fig. S2).

Reduced translation has been shown to lengthen life span in *C. elegans* and other organisms (*10*–*12*) and a known, long-lived mutant was also found to be highly hypoxia-resistant (*1*). Thus, we hypothesized that *rrt-1(gc47)* would be long-lived. Indeed, *rrt-1(gc47)* had a small but significantly increased life span (fig. S3). Although this further links hypoxia resistance and long life span, the difference in the strength of the two phenotypes suggests that their mechanisms downstream of RRT-1 are distinct or that hypoxic sensitivity is much more responsive than life span to alterations in the translation machinery. Other phenotypes seen in *gc47* were a modest decrease in fecundity, a small but significant level of embryonic lethality, a reduction in speed of movement to about half that of wild-type animals, and a slight developmental delay (table S3). Thus, as expected for a gene with such an essential function, *rrt-1(gc47)* has a pleiotropic phenotype but the strongest observed phenotype was hypoxia resistance.

RRT-1 presumably functions in all cells to mediate translation. However, because of their

high metabolic activity, germ cells might be particularly vulnerable to hypoxic injury and thereby determine the hypoxic sensitivity of the whole organism. To examine this issue, we made use of a mutation in the *rrf-1* gene, which encodes an RNA-directed RNA polymerase required for the somatic but not germline actions of RNAi (*13*). The hypoxia resistance of *rrt-1(RNAi)* was greatly reduced in an *rrf-1* mutant versus wild-type background (fig. S4), indicating that RRT-1 acts in both somatic and germline cells to mediate hypoxic sensitivity. Myocytes and neurons are two major somatic cell types where hypoxia produces characteristic pathological changes (*1*, *14*). Hypoxia-induced myocyte nuclear fragmentation and neuron axonal degeneration were both abated in *rrt-1(gc47)* (fig. S5).

To determine when RRT-1 functions to regulate hypoxic sensitivity, we applied RNAi to wild-type animals early in development, early in adulthood before the hypoxic insult, or in adulthood after the hypoxic insult (Fig. 3A). RNAi either during early development or during early adulthood protected equally well from subsequent hypoxic death (Fig. 3B). Thus, the hypoxia-resistant phenotype of *rrt-1* reduction of function is not dependent on developmental stage and can be induced after development is complete. Exposure to *rrt-1(RNAi)* only after the hypoxic insult also increased survival from delayed hypoxic death (Fig. 3C).

The reduction-of-function mutant *rrt-1(rf)* reduces global translation rate and consequently should reduce oxygen consumption. Indeed, the rate of paralysis by hypoxia, which should correlate with oxygen consumption, is decreased in *rrt-1(gc47)* (fig. S6). Reduced oxygen consumption by translational arrest is a logical and established mechanism for reducing cellular injury during hypoxia but not after (*15*–*17*). Thus, the mechanism of protection by *rrt-1* knockdown, at least that functioning after the hypoxic insult, appears to be more complex than a global reduction in oxygen consumption by translational arrest.

Hypoxia produces intracellular misfolded proteins and thereby induces the unfolded protein response (UPR) (*18*). One effect of UPR induction is phosphorylation of the translation initiation factor eIF2-α, thereby suppressing translation (*19*); this has been proposed as an adaptive mechanism to reduce the load of newly synthesized and unfolded proteins, particularly in the context of cancer cell biology. To determine whether the hypoxia-resistant phenotype of *rrt-1(rf)* may be due to a reduction in unfolded proteins, we used strains carrying a transgene, P*hsp-4*::GFP, consisting of a fusion between the *hsp-4* promoter and GFP (green fluorescent protein). P*hsp-4*::GFP expression has been shown to be a reliable indicator of the level of unfolded proteins and of activation of the UPR (*20*–*22*). Hypoxia induced a significant increase in expression of P*hsp-4*::GFP that peaked 4 hours after recovery from hypoxia and was dependent on the length of hypoxic incubation (Fig. 4, A to C). The glycosylation inhibitor tunicamycin, which increases the level of unfolded proteins, also induced P*hsp-4*::GFP expression. Induction of P*hsp-4*::GFP expression by either hypoxia or tunicamycin was blocked virtually completely by a loss-of-function mutation in *ire-1* [*ire-1(lf)*], which encodes an endoplasmic reticulum transluminal kinase essential for the UPR (*22*, *23*) (Fig. 4, A and B). Consistent with a reduction in unfolded protein load, *rrt-1(RNAi)* completely blocked hypoxic induction of P*hsp-4*::GFP (Fig. 4, A and B); however, it did not diminish induction by tunicamycin. Thus, the level of translational suppression by *rrt-1(RNAi)* does not preclude synthesis of the GFP marker under strong inducing conditions. Further supporting the hypothesis that *rrt-1(rf)* reduces the load of unfolded proteins, *rrt-1(gc47)* was highly resistant to tunicamycin-induced developmental arrest (Fig. 4D). Finally, we found that *ire-1(lf)* and its downstream target *xbp-1(lf)* (*22*) significantly suppressed the hypoxia resistance produced by *rrt-1(RNAi)*, but neither *ire-1(lf)* nor *xbp-1(lf)* induced hypersensitivity in *rrt-1*(+) animals (Fig. 4E). Rather, the *ire-1(lf)* and *xbp-1(lf)* animals were weakly resistant. These data indicate that inhibition of translation by *rrt-1(lf)* and the UPR interact synergistically to reduce hypoxic sensitivity, but that in the absence of translational suppression by *rrt-1(lf)*, an intact UPR can promote death after a severe hypoxic insult.

Translational repression is a well-established mechanism of survival for hibernating animals in a prolonged hypoxic environment (*24*). Translational mechanisms are important in the tumori-

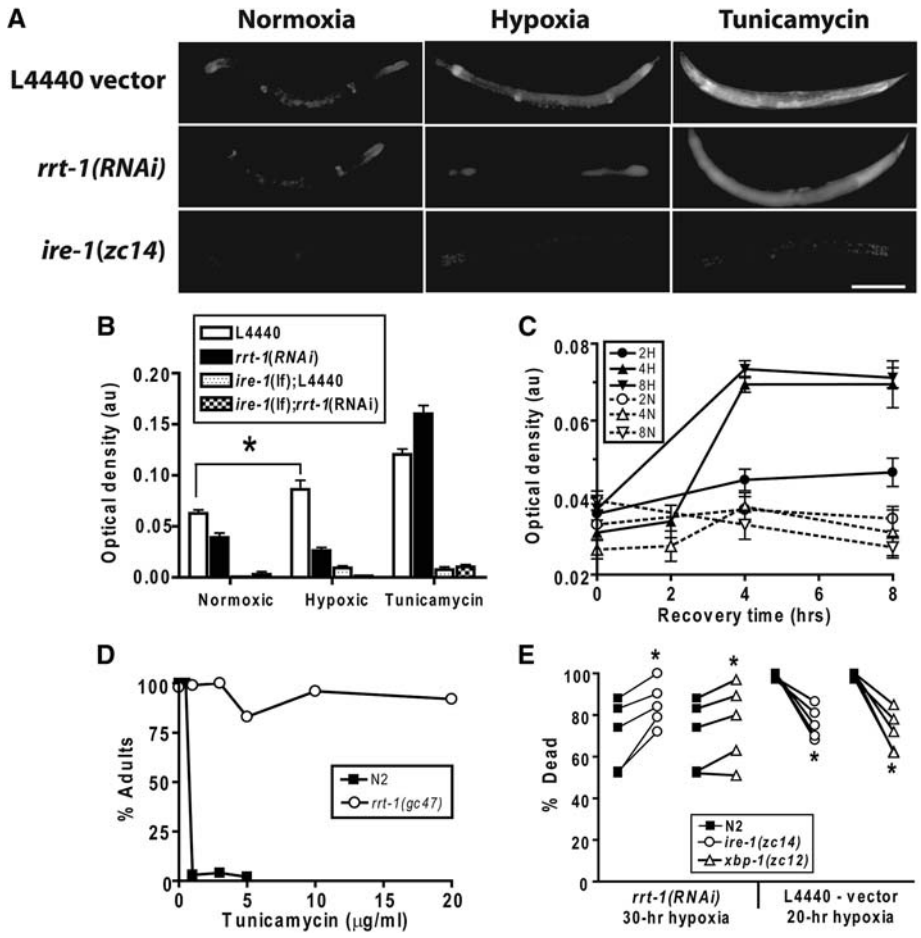

Fig. 4. The unfolded protein response is induced by hypoxia and is required for high-level hypoxia resistance of *rrt-1(RNAi)*. (**A**) P*hsp-4*::GFP expression in age-matched young adult *C. elegans* after incubation for 6 hours in M9 buffer in a normoxic or hypoxic environment or with tunicamycin (25 μg/ml). *zcIs4*[P*hsp-4*::GFP] animals were raised on empty vector or *rrt-1(RNAi)* bacteria; *ire-1(zc14);zcIs4* animals were raised on empty vector. Scale bar, 200 μm. (**B**) Quantification of P*hsp-4*::GFP expression. **P* < 0.01, unpaired two-sided *t* test; au, arbitrary units. (**C**) Time course of P*hsp-4*::GFP induction after hypoxic (H) or normoxic (N) incubations of 2, 4, or 8 hours. (**D**) Sensitivity to developmental arrest by tunicamycin in N2 and *rrt-1(gc47)* animals. Freshly laid eggs were allowed to develop on agar plates containing the indicated concentrations of tunicamycin; percent of animals reaching adulthood after 7 days of development was scored. (**E**) Hypoxic sensitivity of wild-type or UPR pathway mutant animals exposed to *rrt-1(RNAi)* (30-hour hypoxic incubation) or empty vector control (20-hour hypoxic incubation). **P* < 0.05, paired *t* test.

genicity of cancer cells (*25*) and are increasingly implicated in the sensitivity of normal cell types to hypoxic and ischemic injury (*15*, *26*). In these diverse scenarios, translational repression results in several secondary changes in the biology of the cell, including decreases in ATP consumption and protein aggregates and an alteration of the proteome. Our data show that a modest suppression of translation that allows relatively normal growth and physiology can produce a profound hypoxia resistance that requires the UPR for its full phenotypic expression. One effect of UPR activation is translational suppression, which occurs by a mechanism distinct from limiting aminoacylated tRNA levels. A logical model is that a reduction in translation rate by a decrement in AARS activity reduces the unfolded protein load to a level that is manageable by the UPR and may synergize with the translational suppression produced by the UPR itself. However, without translational inhibition, the activity of the UPR may be maladaptive in the context of hypoxic injury. This interaction between translational activity and the UPR may be exploited to regulate hypoxic cell death.

References and Notes

1. B. A. Scott, M. S. Avidan, C. M. Crowder, *Science* **296**, 2388 (2002); published online 13 June 2002 (10.1126/science.1072302).
2. See supporting material on *Science* Online.
3. M. Ibba, D. Soll, *Annu. Rev. Biochem.* **69**, 617 (2000).
4. C. Landes *et al.*, *Biochimie* **77**, 194 (1995).
5. B. Delagoutte, D. Moras, J. Cavarelli, *EMBO J.* **19**, 5599 (2000).
6. S. V. Kyriacou, M. P. Deutscher, *Mol. Cell* **29**, 419 (2008).
7. J. M. Han, J. Y. Kim, S. Kim, *Biochem. Biophys. Res. Commun.* **303**, 985 (2003).
8. P. Sampath *et al.*, *Cell* **119**, 195 (2004).
9. S. G. Park, K. L. Ewalt, S. Kim, *Trends Biochem. Sci.* **30**, 569 (2005).
10. P. Syntichaki, K. Troulinaki, N. Tavernarakis, *Nature* **445**, 922 (2007).
11. K. Z. Pan *et al.*, *Aging Cell* **6**, 111 (2007).
12. M. Hansen *et al.*, *Aging Cell* **6**, 95 (2007).
13. T. Sijen *et al.*, *Cell* **107**, 465 (2001).
14. N. Dasgupta, A. M. Patel, B. A. Scott, C. M. Crowder, *Curr. Biol.* **17**, 1954 (2007).
15. W. Paschen, C. G. Proud, G. Mies, *Curr. Pharm. Des.* **13**, 1887 (2007).
16. B. G. Wouters *et al.*, *Semin. Cell Dev. Biol.* **16**, 487 (2005).
17. D. J. DeGracia, R. Kumar, C. R. Owen, G. S. Krause, B. C. White, *J. Cereb. Blood Flow Metab.* **22**, 127 (2002).
18. C. Koumenis *et al.*, *Methods Enzymol.* **435**, 275 (2007).
19. C. Koumenis *et al.*, *Mol. Cell. Biol.* **22**, 7405 (2002).
20. T. Yoneda *et al.*, *J. Cell Sci.* **117**, 4055 (2004).
21. F. Urano *et al.*, *J. Cell Biol.* **158**, 639 (2002).
22. M. Calfon *et al.*, *Nature* **415**, 92 (2002).
23. X. Shen *et al.*, *Cell* **107**, 893 (2001).
24. K. B. Storey, J. M. Storey, *Biol. Rev. Camb. Philos. Soc.* **79**, 207 (2004).
25. T. van den Beucken, M. Koritzinsky, B. G. Wouters, *Cancer Biol. Ther.* **5**, 749 (2006).
26. D. J. DeGracia, B. R. Hu, *J. Cereb. Blood Flow Metab.* **27**, 875 (2007).

27. We thank M. Mabon for early efforts on screen design, L. Metz for technical help, and M. Hansen for advice and strains. Supported by the National Institute of Neurological Disorders and Stroke, a Neuroscience of Brain Disorders Award from the McKnight Endowment Fund for Neuroscience, and an American Heart Association Established Investigator Award. Some of the strains used in this work were provided by the *Caenorhabditis* Genetics Center, which is funded by the NIH National Center for Research Resources.

Supporting Online Material

www.sciencemag.org/cgi/content/full/323/5914/630/DC1
Materials and Methods
Figs. S1 to S6
Tables S1 to S4
References

19 September 2008; accepted 2 December 2008
10.1126/science.1166175

Ligand-Dependent Equilibrium Fluctuations of Single Calmodulin Molecules

Jan Philipp Junker,[1] Fabian Ziegler,[1] Matthias Rief[1,2]*

Single-molecule force spectroscopy allows superb mechanical control of protein conformation. We used a custom-built low-drift atomic force microscope to observe mechanically induced conformational equilibrium fluctuations of single molecules of the eukaryotic calcium-dependent signal transducer calmodulin (CaM). From this data, the ligand dependence of the full energy landscape can be reconstructed. We find that calcium ions affect the folding kinetics of the individual CaM domains, whereas target peptides stabilize the already folded structure. Single-molecule data of full length CaM reveal that a wasp venom peptide binds noncooperatively to CaM with 2:1 stoichiometry, whereas a target enzyme peptide binds cooperatively with 1:1 stoichiometry. If mechanical load is applied directly to the target peptide, real-time binding/unbinding transitions can be observed.

Single-molecule mechanical methods have made it possible to study and control biomolecular conformations with unprecedented precision (*1*–*6*). Whereas classical methods such as changes in temperature or chemical environment act globally and rather unspecifically on the energy landscape, forces can be applied locally to precisely manipulate selected structural elements of a protein and thus explore protein energy landscapes in a controlled manner (*5*). Due to limited resolution, single-molecule mechanical studies of protein folding and protein/ligand interactions have so far almost exclusively been carried out in nonequilibrium and have thus been restricted to the study of unfolding and unbinding reactions (*7*–*9*). Hence, half of the energy landscape (the part that controls re-folding or ligand re-binding) has been mostly inaccessible to these experiments. We have used a low-drift atomic force microscope (AFM) (*10*) to observe folding/unfolding fluctuations of single calmodulin proteins (CaM) under equilibrium conditions in the presence of Ca^{2+} and target peptides. Ligand-dependent folding/unfolding fluctuations, as well as ligand binding/unbinding fluctuations, can be induced mechanically and observed in real time.

CaM is the most prominent Ca^{2+} sensor in eukaryotic cells (*11*). When Ca^{2+} binds to CaM, the flexible Ca^{2+}-free apo conformation converts into a rigid and stable holo conformation (*12*). Holo CaM binds to specific target sequences in downstream regulatory proteins, thus altering their signaling properties. To date, more than one hundred target proteins for CaM have been described (*11*). Little is known about the folding of CaM, but temperature-jump experiments have shown that folding of apo CaM occurs on the submillisecond time scale (*13*).

The experimental scheme, including a sketch of Ca^{2+}-CaM, is shown in Fig. 1A. Following previously described methods, we have sandwiched a single CaM molecule between immunoglobulin domains from *Dictyostelium discoideum* filamin that serve as attachment points for the AFM tip and the surface. CaM consists of two structurally similar domains, a ~75-residue N-terminal (DomN, red) and a ~70-residue C-terminal (DomC, blue) globular domain, that each bind two Ca^{2+} ions. A typical force extension trace of CaM at a pulling velocity of 1 nm/s and 10 mM Ca^{2+} is shown in Fig. 1B. At pulling velocities generally used in force spectroscopy of ~1 μm/s, unfolding events of CaM are buried in the thermal noise (*14*). Low instrumental drift allows us to achieve the slow pulling velocity (1 nm/s) necessary for the required force resolution of ~2 pN (*15*). Two distinct peaks (marked in red and blue, respectively) correspond to the unfolding of the two globular CaM domains. To allow for a structural interpretation of the unfolding traces, we introduced a disulfide bond between residues 128 and 144 of DomC to shorten the extensible backbone of this domain (CaM 128×144). Ligand binding properties of the shortened version were indistinguishable from the wild type. The length gain upon un-

[1]Physik Department E22, Technische Universität München, James-Franck-Strasse, 85748 München, Germany. [2]Munich Center for Integrated Protein Science, 81377 München, Germany.

*To whom correspondence should be addressed. E-mail: mrief@ph.tum.de

folding of the domains can be measured using the wormlike chain model of polymer elasticity (*16*) (black solid lines in Fig. 1B, main graph). The average values are $\Delta L_I = 25.7 \pm 0.4$ nm and $\Delta L_{II} = 17.6 \pm 0.7$ nm. This result suggests that the red unfolding peak marks unfolding of DomN (expected value $\Delta L = 25.0$ nm), whereas in the second peak DomC unfolds (expected value $\Delta L = 18.7$ nm) (*17*). Closer inspection of the unfolding peaks reveals rapid transitions between the folded and unfolded states in both unfolding peaks. The insets above the peaks in Fig. 1B show time traces of the transition regions. Such transitions are the hallmark of thermodynamic equilibrium, and a kinetic analysis now allows extracting both equilibrium and nonequilibrium parameters and, hence, the energy landscape of CaM folding from a single molecule.

In agreement with experiments using single-domain CaM constructs, our results suggest that the two domains fold and unfold independently from each other (*18*). Therefore, we investigated single-domain constructs of both DomN and DomC. A sample time trace of the unfolding fluctuations of isolated DomC is shown in Fig. 1C. Due to the large spring constant of the AFM probe (6 pN/nm), the fluctuations do not occur at constant load. Unfolding occurs at high loads (12 pN), whereas refolding occurs from the relaxed state (6 pN). The slope of the broken lines marking the folded and unfolded levels, respectively, reflects the slow force ramp imposed during the experiment. To analyze the fluctuation kinetics, we define the characteristic transition rate as the averaged folding and unfolding rate in the whole transition region (DomC: 11.7/s, number of molecules analyzed $n = 23$). Using a Monte-Carlo simulation, we adjusted the unfolding and folding rates at zero force so that the characteristic transition rate matched our experiment [for details, see the supporting online material (SOM) text]. Independent measurements of the speed dependence of the nonequilibrium unfolding forces at higher pulling velocities yielded a distance of the transition state from the folded state of $\Delta x_{N\text{-}TS} = 2$ nm, which is a typical value for an all–α helical protein (SOM text and fig. S1A). Combining these results, we can now draw an energy landscape for the folding of CaM at 10 mM Ca^{2+} (Fig. 1D). A zero-force folding rate of ~2×10^5/s under these conditions makes CaM one of the fastest folding proteins known to date (*19*).

To investigate the influence of ligand binding on the folding dynamics of DomC in greater detail, we performed concentration scans of Ca^{2+} and mastoparan (Mas), a wasp venom peptide known to bind to CaM (*20*). Figure 2A shows equilibrium time traces of the transition region at varying Mas concentrations with Ca^{2+} kept fixed at 10 mM. The most obvious influence of Mas binding is the decreased speed of the transition kinetics with increasing Mas concentration. We plotted the characteristic transition rate as a function of Mas concentration in Fig. 2B. The effect of Mas on the midpoint unfolding force (the average value of the unfolding forces in the transition region) is shown in the inset. As expected, higher concentrations of Mas increase the stability of DomC and, hence, its midpoint unfolding force. The effect of Mas on both force and kinetics can be readily explained by assuming that Mas binding exclusively slows the unfolding rate k_u, as depicted in Fig. 2C for two sample concentrations. In the narrow force range where we observe folding/unfolding transitions, both unfolding rates (green) and folding rates (purple) will depend in good approximation exponentially on the applied force (*21*–*23*). The slopes of the green and purple lines are determined by the distance of the transition state from the native and unfolded states, respectively (*21*, *22*). At 1 μM Mas, the midpoint force of the transition region, where unfolding and folding occur at the same rates, is defined by the intersection of the thin green line and the purple line. Because Mas binding acts on the unfolding rate, increasing the

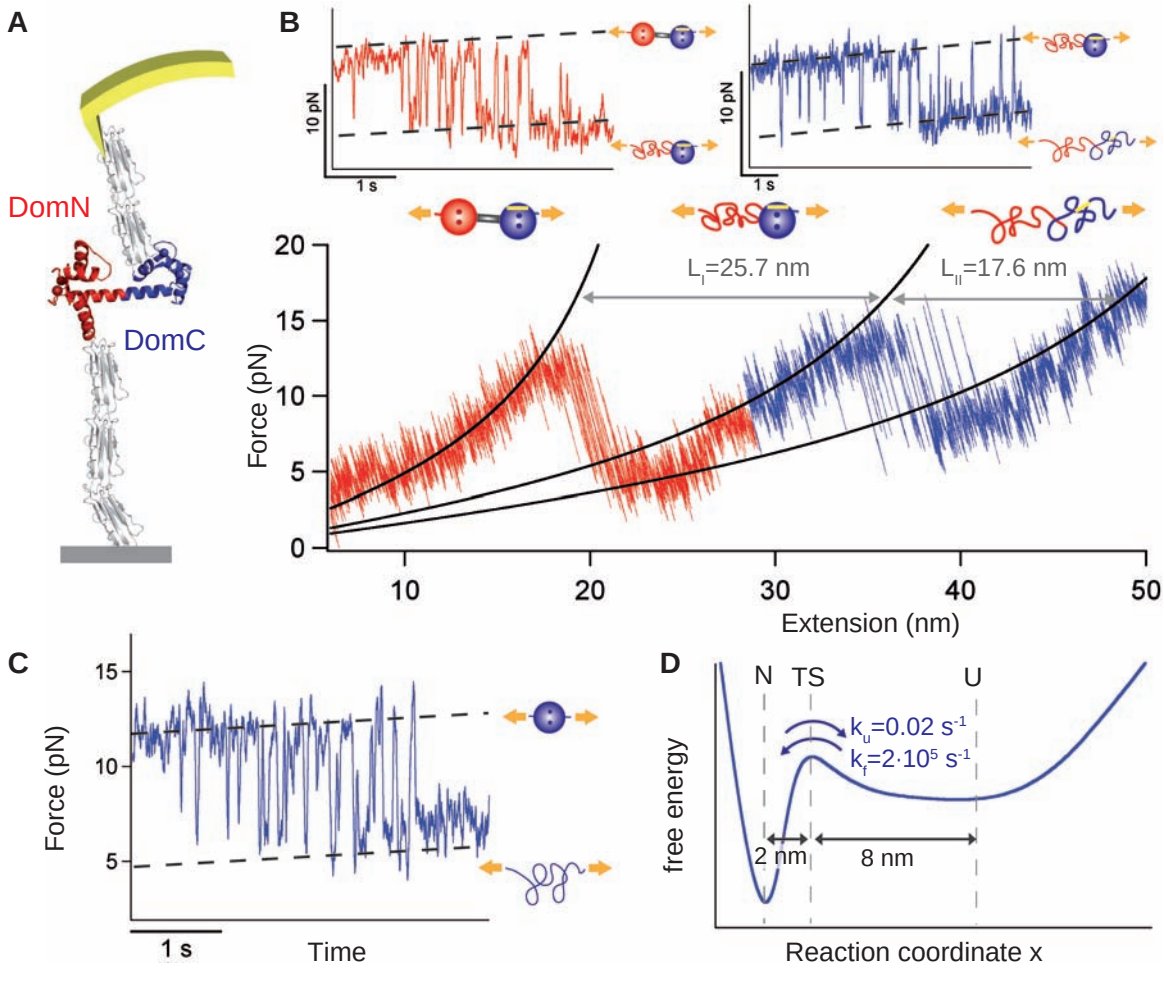

Fig. 1. (**A**) Sketch of the experimental setup, showing CaM attached to AFM cantilever tip and surface by means of filamin domains that serve as handles (not to scale). (**B**) Sample trace of CaM 128×144 at 10 mM Ca^{2+}. The folding/unfolding transitions of DomN are shown in red, and those of DomC are shown in blue. Worm-like chain fit curves (black traces) allow determining the contour length increase upon unfolding ΔL and thus identifying the individual domains. In the insets above the peaks, time traces of the transition region are depicted. (**C**) Time traces of the transition region of isolated DomC at 10 mM Ca^{2+}. (**D**) Potential energy landscape for the folding of DomC at 10 mM Ca^{2+}. N, native state; TS, transition state; U, unfolded state.

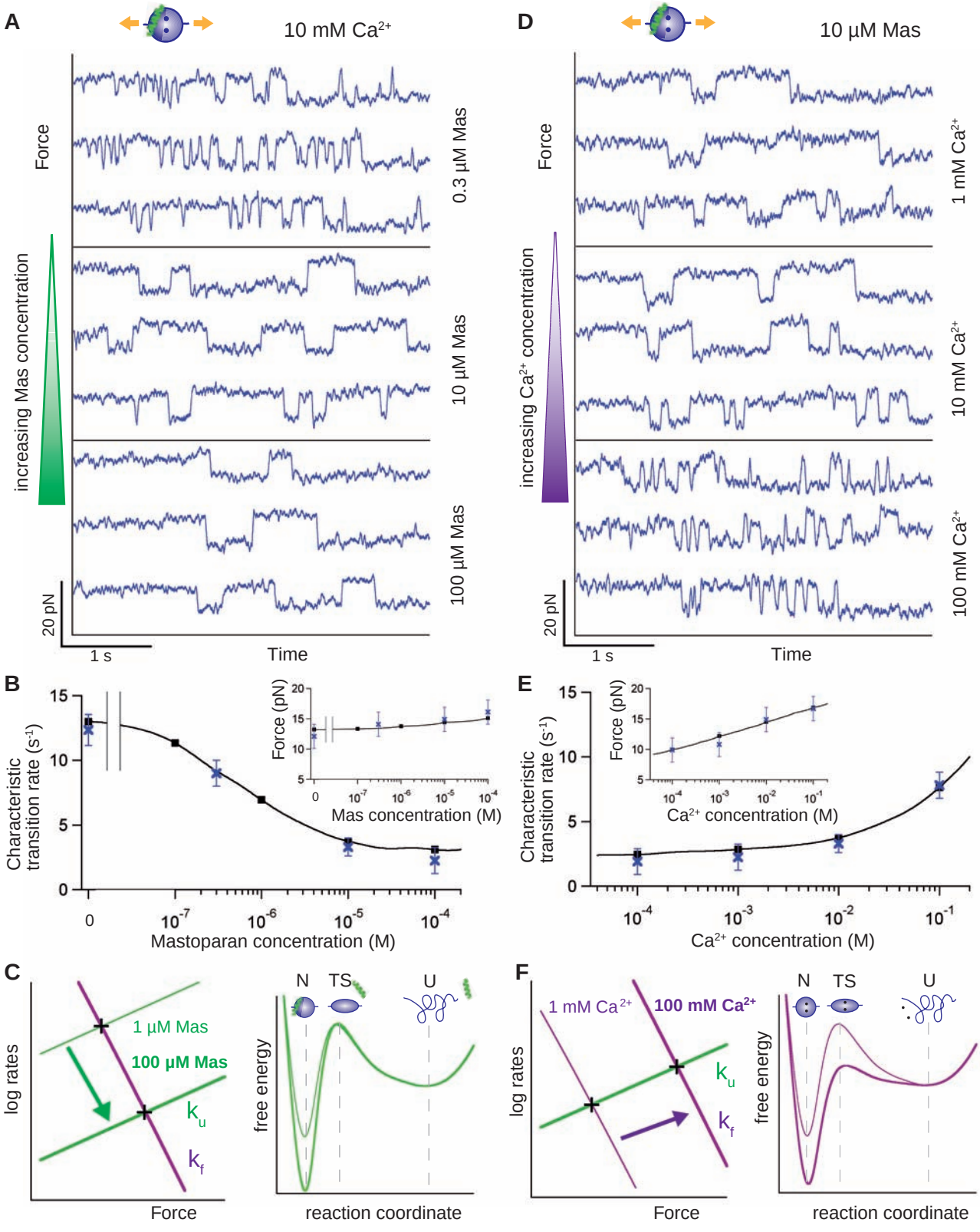

Fig. 2. (**A**) Time traces of isolated DomC at 10 mM Ca^{2+} and varying Mas concentrations. (**B**) Characteristic transition rate and unfolding force at different Mas concentrations (blue symbols). The ligand effect can be fully reproduced by Monte Carlo simulations (black symbols and black interpolation curve). (**C**) (Left) Force dependence of folding rate (purple) and unfolding rate (green). An increase in Mas from 1 µM (thin green line) to 100 µM (thick green line) moves the intersection point (transition region) to higher forces and lower rates. (Right) Potential energy landscape at low (thin green line) and high (thick green line) Mas. (**D**) Time traces of isolated DomC at 10 µM Mas and varying Ca^{2+} concentrations. (**E**) Transition rate and unfolding force at different Ca^{2+} concentrations (blue symbols). Results of a Monte Carlo simulation are shown in black. (**F**) (Left) Increase in Ca^{2+} from 1 mM Ca^{2+} (thin purple line) to 100 mM Ca^{2+} (thick purple line) moves the intersection point to higher forces and higher rates. (Right) Potential energy landscape for folding at low (thin purple line) and high (thick purple line) Ca^{2+}.

concentration to 100 μM will shift the green line down (thick green line). The new intersection point now lies at an increased force as well as a reduced characteristic transition rate. A detailed modeling of k_u and k_f in dependence of ligand concentration and force in a Monte Carlo simulation could reproduce the full effect of Mas concentration on midpoint unfolding forces and transition rates (solid lines in Fig. 2B; for details, see SOM text). This simulation includes equilibrium constants for Mas binding to the native, unfolded, and transition state, respectively.

Similarly, we investigated the effect of Ca^{2+} on midpoint unfolding forces and kinetics (Fig. 2D). From the data traces taken at three sample concentrations, it can be readily seen that unlike Mas, Ca^{2+} increases the characteristic transition rate of DomC. Forces and transition rates are quantified in Fig. 2E. Despite the increase in transition rates, the midpoint unfolding force (see inset) also increases (*24*). Increased transition rates, together with increased stability, can only be explained by Ca^{2+} raising predominantly the folding rate (see the scheme in Fig. 2F). Increasing the Ca^{2+} concentration from 1 mM to 100 mM will shift up the folding rate (purple lines) but leave the unfolding rate unaffected. The new intersection point lies at both higher forces and higher rates. Again, a Monte Carlo simulation incorporating the Ca^{2+} dependence of k_u and k_f can fully explain the data (solid lines in Fig. 2E; for details, see SOM text).

Thus, the two CaM ligands, Ca^{2+} and Mas, act on folding in different ways (see energy landscapes in Fig. 2, C and F). Mas stabilizes the already folded form but does not interact with the transition state structure or the unfolded protein because it leaves the folding rate unaffected. Hence, the transition state has only negligible affinity to Mas (Fig. 2C) (*8*). In contrast, at the concentrations measured (100 μM to 100 mM), Ca^{2+} predominantly acts on the folding rate. Hence, Ca^{2+} binding stabilizes both the transition state and the folded state, indicating a dissociation constant of Ca^{2+} binding to the transition state of ~1 mM (see energy landscape in Fig. 2F and SOM text). At very low Ca^{2+}, CaM folds into the flexible and highly dynamic apo structure that undergoes a large conformational change upon addition of Ca^{2+} (*12*). Higher Ca^{2+} opens a new folding pathway directly to the holo form via a transition state that has already bound Ca^{2+} ions. At high Ca^{2+}, this pathway prevails over the apo folding route (see scheme in fig. S3 and SOM text). Along this holo folding route, the Ca^{2+} binding sites might act as nucleation seeds for folding because Ca^{2+} binding appears to occur early on the folding pathway.

Our mechanical folding/unfolding assay now offers the possibility to study CaM-target peptide interaction modes of full-length CaM directly on the single-molecule level. Figure 3A (upper trace) shows a mechanical unfolding curve of CaM 128×144 in the presence of 100 μM Mas. In comparison to peptide-free CaM, a mechanical stabilization of both DomN and DomC becomes obvious, which manifests itself in higher forces as well as slower transition rates (Table 1). In the full-length construct, the stabilizations of the in-

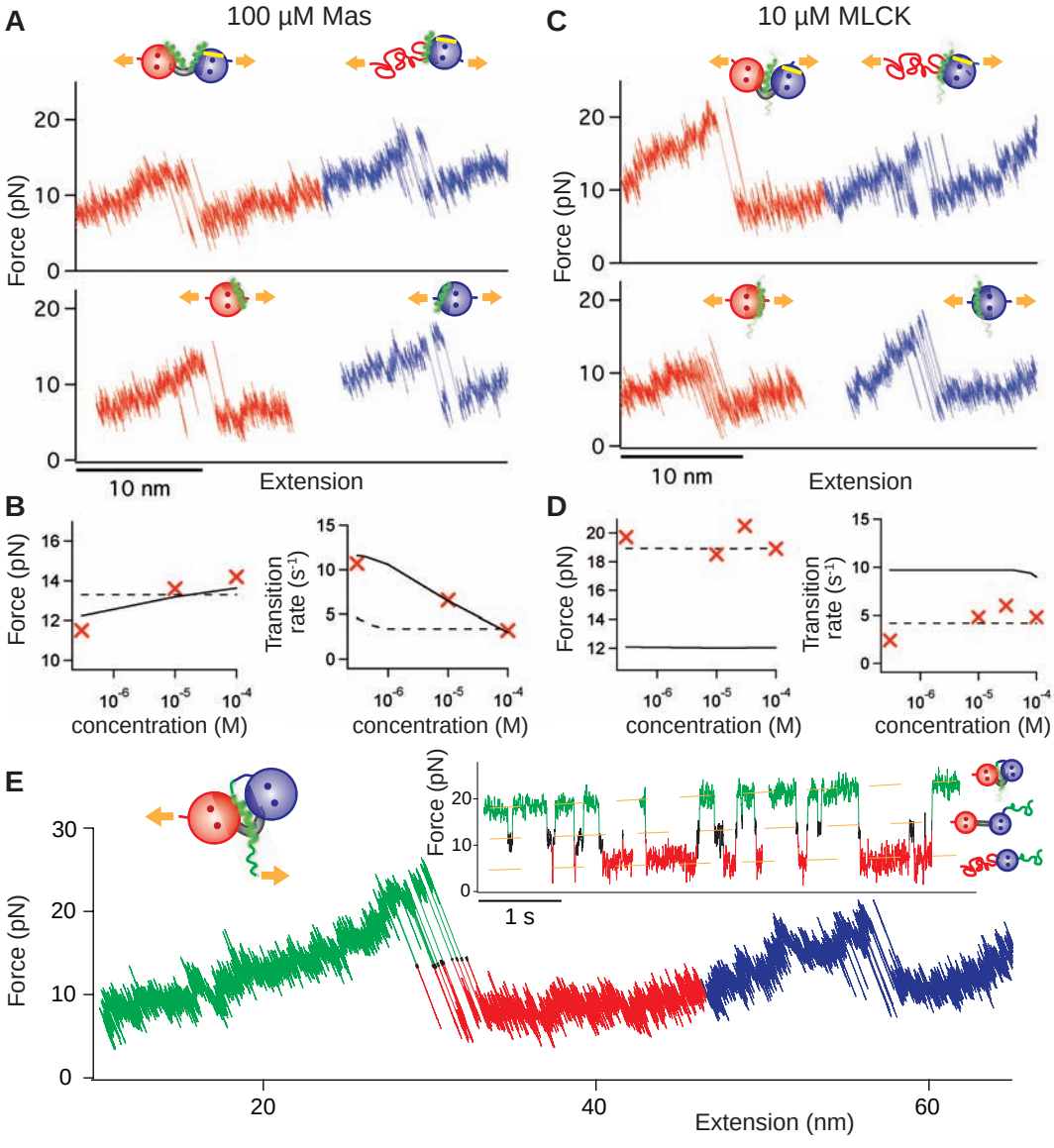

Fig. 3. (**A**) (Upper trace) Sample trace of CaM 128 × 144 at 10 mM Ca^{2+} and 100 μM Mas. DomN (red) and DomC (blue) are stabilized approximately equally by Mas. (Lower traces) Isolated DomN (red) and DomC (blue) at 100 μM Mas. (**B**) Unfolding forces and transition rates of DomN of CaM 128×144 at different Mas concentrations (red). Solid lines, concentration dependence in the case of a 1:2 stoichiometry; broken lines, 1:1 stoichiometry (Monte Carlo simulations). (**C**) (Upper trace) Sample trace of CaM 128×144 at 10 mM Ca^{2+} and 10 μM MLCK. DomN (red) is stabilized considerably more strongly than DomC (blue). (Lower traces) Isolated DomN (red) and DomC (blue) at 10 μM MLCK. (**D**) Unfolding forces and transition rates of DomN of CaM 128×144 at different MLCK concentrations (red). Solid lines, concentration dependence for a 1:2 stoichiometry; broken lines, 1:1 stoichiometry. (**E**) Sample trace of CaM with MLCK fused to the C terminus at 10 mM Ca^{2+}. The protein construct is shown in the scheme. (Inset) Time traces of first unfolding peak. An intermediate state, corresponding to CaM with unbound peptide (black level), appears.

Table 1. Midpoint unfolding forces and characteristic transition rates (10 mM Ca^{2+}).

Peptides	Isolated DomN		Isolated DomC		DomN (CaM 128x144)		DomC (CaM 128x144)	
	Force	Rate	Force	Rate	Force	Rate	Force	Rate
No peptide	12.6 pN	11.5 s^{-1}	12.1 pN	11.7 s^{-1}	11.8 pN	11.9 s^{-1}	14.2 pN	19.5 s^{-1}
100 μM Mas	14.0 pN	4.0 s^{-1}	16.1 pN	2.1 s^{-1}	14.2 pN	3.2 s^{-1}	18.2 pN	2.8 s^{-1}
10 μM MLCK	12.2 pN	12.2 s^{-1}	14.9 pN	2.6 s^{-1}	19.5 pN	4.9 s^{-1}	15.5 pN	5.4 s^{-1}

dividual domains obviously occur independently from each other because they behave identical to single-domain constructs at the same Mas concentration (Fig. 3A, lower traces, and Table 1). This result is surprising, given that Mas binding to CaM is discussed in the literature almost exclusively in the context of a binding stoichiometry of 1:1 (*25*). Cooperative binding of both domains simultaneously to a single Mas peptide should occur with a higher energy than the sum of the interaction energies of the individual domains. Our result indicates that full-length CaM binds Mas noncooperatively in a 1:2 stoichiometry where each peptide interacts with only one CaM domain. The 1:2 stoichiometry can be confirmed by analyzing the single-molecule thermodynamics of ligand binding to CaM (SOM text). The Mas dependence of forces and transition rates of the first unfolding peak (DomN) of CaM 128×144 is shown in Fig. 3B. A 1:1 stoichiometry is not consistent with our data (dashed black line obtained from the Monte Carlo simulation), whereas a 1:2 stoichiometry fits our data well (solid black line) (*26*).

Because binding of the venom peptide Mas to CaM probably has a very different physiological role than binding to target enzymes, we also investigated binding of CaM to the interaction site peptide of its target enzyme skeletal muscle myosin light chain kinase (MLCK) (*27*). As expected for a strongly and cooperatively binding peptide (*28*), the stabilization of full-length CaM upon MLCK peptide binding is dramatic at concentrations of 10 μM (Fig. 3C, upper trace, and Table 1). The unfolding peak of DomN is increased to ~19 pN, whereas DomC is stabilized to an extent similar to Mas. For comparison, the unfolding traces of the isolated domains are shown in the lower traces of Fig. 3C. In contrast to Mas, isolated DomN seems to exhibit almost no affinity for the MLCK peptide. In agreement with the literature, we find a binding stoichiometry of 1:1 for this peptide (Fig. 3D).

The large interaction energy of CaM and MLCK peptide, together with a diffusion-limited on-rate (*29*), suggests that the exchange of the bound peptide from the complex may be slow. Mechanical force can be used as control parameter to affect the peptide off-rates directly and bring them into an observable regime while still leaving the structure of CaM intact. To this end, we fused the MLCK peptide directly to the C terminus of CaM (*30*), enabling us to apply force to the peptide directly (see sketch in Fig. 3E). Again, the observed traces exhibit near equilibrium fluctuations. In the first unfolding peak, rapid transitions between three levels can be observed: peptide bound (green), peptide unbound (black), and DomN unfolded (red) (Fig. 3E). For clarity, the inset shows time traces of those fluctuations taken from three independent molecules. This data directly reveals the thermodynamic hierarchy of the folding/peptide-binding process. The black level (CaM folded and peptide unbound) seems to be obligatory both on the folding/binding pathway and on the unfolding/unbinding pathway. Even though the stabilization due to peptide binding (~20 k_BT as estimated from the area enclosed by the green and black levels) is higher than the folding free energy of the individual domains (~15 k_BT), binding/unbinding and folding/unfolding are still separate processes.

At forces of ~20 pN, the peptide-bound state still has a long lifetime on a time scale of seconds (green levels). Using a transition state position of 1 nm for peptide unbinding, we estimated a zero-force lifetime for the bound peptide of 10^2 to 10^3 s. Such a long lifetime may be essential for proper functioning of the CaM signaling pathway, specifically because typical free cellular Ca^{2+}-CaM concentrations are lower than the overall concentration of target sites (*31*).

We demonstrated that single-molecule force spectroscopy by AFM allows online observation of the interaction dynamics of a signaling protein with its target. How CaM binding kinetics and mechanics are affected by full-length target proteins and how their activity is modulated will be an important question for future experiments. We anticipate that direct single-molecule measurements of equilibrium fluctuations, as presented in this study, will provide an important tool to measure protein-target interaction dynamics in real time.

References and Notes

1. W. J. Greenleaf, K. L. Frieda, D. A. N. Foster, M. T. Woodside, S. M. Block, *Science* **319**, 630 (2008); published online 2 January 2008 (10.1126/science.1151298).
2. C. Cecconi, E. A. Shank, C. Bustamante, S. Marqusee, *Science* **309**, 2057 (2005).
3. A. P. Wiita *et al*., *Nature* **450**, 124 (2007).
4. S. P. Ng *et al*., *Proc. Natl. Acad. Sci. U.S.A.* **104**, 9633 (2007).
5. H. Dietz, F. Berkemeier, M. Bertz, M. Rief, *Proc. Natl. Acad. Sci. U.S.A.* **103**, 12724 (2006).
6. E. M. Puchner *et al*., *Proc. Natl. Acad. Sci. U.S.A.* **105**, 13385 (2008).
7. E.-L. Florin, V. T. Moy, H. E. Gaub, *Science* **264**, 415 (1994).
8. Y. Cao, T. Yoo, H. Li, *Proc. Natl. Acad. Sci. U.S.A.* **105**, 11152 (2008).
9. Y. Cao, M. M. Balamurali, D. Sharma, H. Li, *Proc. Natl. Acad. Sci. U.S.A.* **104**, 15677 (2007).
10. Materials and methods are available as supporting material on *Science* Online.
11. A. P. Yamniuk, H. J. Vogel, *Mol. Biotechnol.* **27**, 33 (2004).
12. M. Zhang, T. Tanaka, M. Ikura, *Nat. Struct. Biol.* **2**, 758 (1995).
13. C. R. Rabl, S. R. Martin, E. Neumann, P. M. Bayley, *Biophys. Chem.* **101–102**, 553 (2002).
14. M. Carrion-Vazquez *et al*., *Prog. Biophys. Mol. Biol.* **74**, 63 (2000).
15. The low instrumental drift now allows a force resolution of AFM that comes close to optical traps. In our experience, AFM offers a better length resolution, whereas optical tweezers, due to the much softer spring constants, have advantages if constant force conditions are required.
16. C. Bustamante, J. F. Marko, E. D. Siggia, S. Smith, *Science* **265**, 1599 (1994).
17. The expected contour length increase upon unfolding of a protein domain consisting of N amino acid residues can be calculated as $\Delta L = 0.365N - d_{folded}(I) + d_{folded}(II)$, where $d_{folded}(I)$ and $d_{folded}(II)$ are the end-to-end distances of the folded structure before and after the unfolding event, respectively (SOM text). Due to the α-helical linker between DomN and DomC, the domain boundaries of CaM are not precisely defined, which may account for the small deviations from the expected values.
18. L. Masino, S. R. Martin, P. M. Bayley, *Protein Sci.* **9**, 1519 (2000).
19. V. Munoz, *Annu. Rev. Biophys. Biomol. Struct.* **36**, 395 (2007).
20. D. A. Malencik, S. R. Anderson, *Biochem. Biophys. Res. Commun.* **114**, 50 (1983).
21. G. I. Bell, *Science* **200**, 618 (1978).
22. M. Schlierf, F. Berkemeier, M. Rief, *Biophys. J.* **93**, 3989 (2007).
23. R. B. Best, G. Hummer, *J. Am. Chem. Soc.* **130**, 3706 (2008).
24. The increase in force upon an increase in Ca^{2+} is, in fact, stronger than with an increase in Mas (insets in Fig. 2, B and E). This difference directly reflects the binding of 2 Ca^{2+} ions to CaM, whereas it only binds 1 molecule of Mas (SOM text).
25. S. Linse, T. Drakenberg, S. Forsen, *FEBS Lett.* **199**, 28 (1986).
26. A simple thermodynamic argument can readily explain why a 1:1 stoichiometry should lead to concentration independent forces and transition rates (dashed lines in Fig. 3B). In our assay, the fully folded CaM is transformed to CaM with unfolded DomN in the first unfolding peak. Because at all Mas concentrations used (>0.3 μM), both intact CaM and DomC alone are fully saturated with Mas, changes in concentration cannot affect the energetics of this transition any further (SOM text).
27. M. Ikura *et al*., *Science* **256**, 632 (1992).
28. P. M. Bayley, W. A. Findlay, S. R. Martin, *Protein Sci.* **5**, 1215 (1996).
29. S. E. Brown, S. R. Martin, P. M. Bayley, *J. Biol. Chem.* **272**, 3389 (1997).
30. A. Miyawaki *et al*., *Nature* **388**, 882 (1997).
31. M. N. Teruel, W. Chen, A. Persechini, T. Meyer, *Curr. Biol.* **10**, 86 (2000).

32. We thank P. M. Bayley for inspiring discussions and A. Bausch, H. Gaub, M. Bertz, and M. Schlierf for helpful comments on the manuscript. This work was supported by Deutsche Forschungsgemeinschaft grant RI 990/3-1. J.P.J. was supported by the International Graduate School "Materials Science of Complex Interfaces."

Supporting Online Material

www.sciencemag.org/cgi/content/full/323/5914/633/DC1
Materials and Methods
SOM Text
Figs. S1 to S4
References

19 September 2008; accepted 5 December 2008
10.1126/science.1166191

Stretching Single Talin Rod Molecules Activates Vinculin Binding

Armando del Rio,[1] Raul Perez-Jimenez,[1] Ruchuan Liu,[2] Pere Roca-Cusachs,[1] Julio M. Fernandez,[1] Michael P. Sheetz[1]*

The molecular mechanism by which a mechanical stimulus is translated into a chemical response in biological systems is still unclear. We show that mechanical stretching of single cytoplasmic proteins can activate binding of other molecules. We used magnetic tweezers, total internal reflection fluorescence, and atomic force microscopy to investigate the effect of force on the interaction between talin, a protein that links liganded membrane integrins to the cytoskeleton, and vinculin, a focal adhesion protein that is activated by talin binding, leading to reorganization of the cytoskeleton. Application of physiologically relevant forces caused stretching of single talin rods that exposed cryptic binding sites for vinculin. Thus in the talin-vinculin system, molecular mechanotransduction can occur by protein binding after exposure of buried binding sites in the talin-vinculin system. Such protein stretching may be a more general mechanism for force transduction.

Force sensing by cells is critical for their proper function; however, how cells transform a force stimulus into a chemical response remains unclear. Forces have been shown to open ion channels, activate phosphorylation, and cause catch bond formation. These could all be mechanisms for force transduction [reviewed in (*1*)]. Another mechanism that has been postulated but never demonstrated experimentally is that stretching of single force-bearing cytoplasmic molecules might expose binding sites for other proteins. We characterized at a single-molecule level the interaction of two cytoskeletal proteins, talin, the adhesion force–bearing protein, and vinculin, its binding partner, in the absence and presence of a physiologically relevant force.

Talin and vinculin are key players in cell signaling, adhesion, and migration (*2*) and are localized at the sites of cell-matrix adhesion (*3*). They are ideal candidates for mechanotransduction because the binding of vinculin to focal adhesion complexes was shown to increase upon the application of force (*4*). Talin couples the cytoskeleton to the extracellular matrix through membrane integrins and can activate signaling through vinculin binding, for assembly and reorganization of the actin cytoskeleton (*3*, *5*). The globular head of talin contains a FERM (4.1/ezrin/radixin/moesin) domain that binds and activates β-integrin cytodomains (*6*), whereas the talin rod (TR) contains up to 11 vinculin binding sites (VBSs) (*7*). A portion of the TR spanning residues 482 to 889 (Fig. 1A) contains a five-helix bundle with a cryptic VBS in helix four, followed by a seven-helix bundle containing four additional VBSs (helices 6, 9, 11, and 12). The x-ray structures of VBSs reveal that they are defined by six turns of an α helix and that they are often buried because of extensive hydrophobic interactions with other amphipathic helices (*8*, *9*). VBSs trigger conformational changes in the vinculin head (Vh), in a process of helical bundle conversion: α helices of Vh reorganize to surround the VBS from the TR, burying 50% of its solvent accessible area (*5*, *10*). Figure 1, B and C, shows the proposed sequential unfolding of the helical bundles in the TR and Vh binding to the helix 12, which is exposed in steered molecular dynamic simulations (*11*).

[1]Department of Biological Sciences, Columbia University, New York, NY 10027, USA. [2]Department of Physics, National University of Singapore, Singapore 117542, Singapore.

*To whom correspondence should be addressed. E-mail: ms2001@columbia.edu

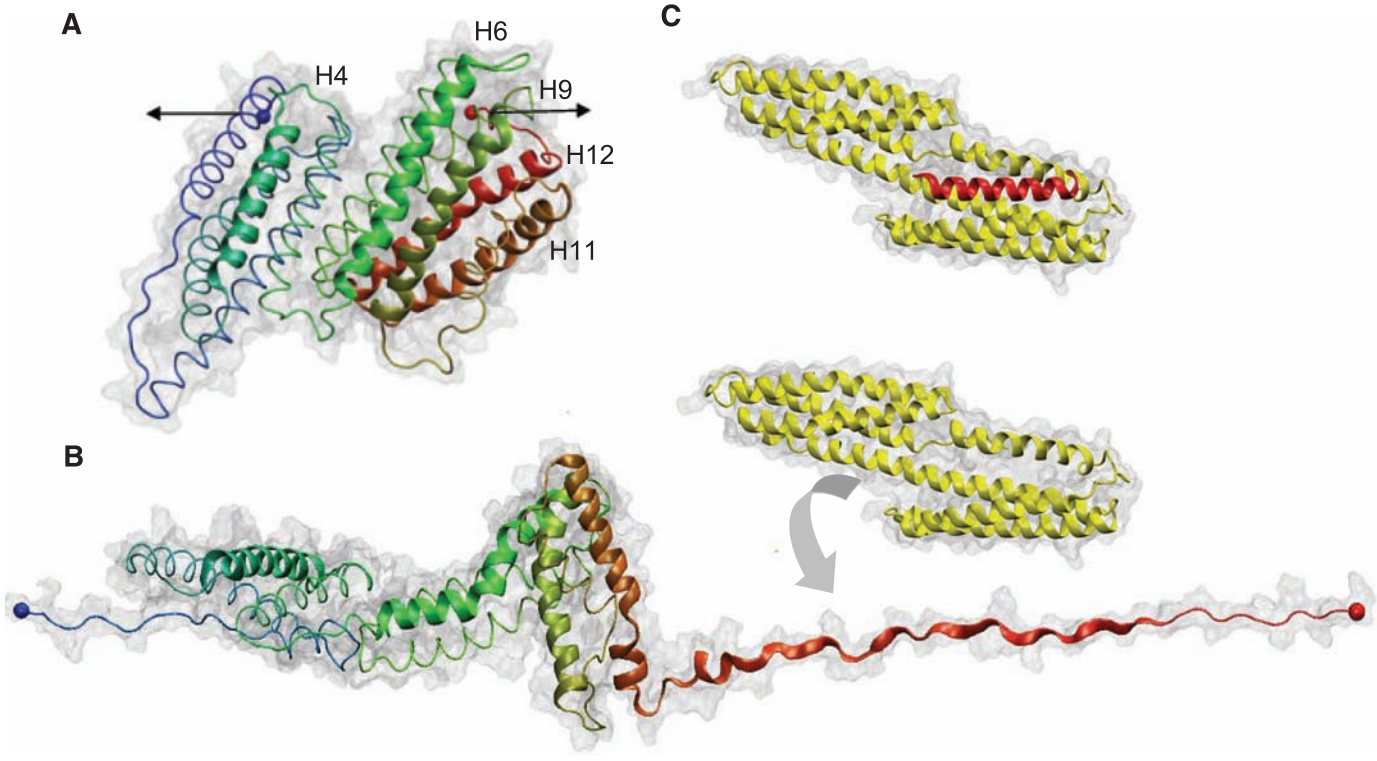

Fig. 1. (**A**) Structure of the 12 helices that form the TR 482 to 889 [Protein Data Bank (PDB) 1xwx]. Color coding: blue, N terminus; green, middle; and red, C terminus. VBS helices are numbered and represented with cartoon models, and the rest of the protein is shown with tube models. (**B**) Under the application of a force in the direction indicated by the black arrows in (A), TR starts to unfold. Once helix 12 exposed its VBS, Vh (PDB 1u6h), represented in yellow, reorganizes to bind to it. (**C**) X-ray structure of the complex Vh-VBS-helix 12, PDB 1u6h. Images were generated by using the VMD (Visual Molecular Dynamics) program (www.ks.uiuc.edu/research/vmd/).

Previous studies have shown that four of five VBSs in TR residues 482 to 889 are inactive for binding in the native molecule (*8*, *12*). What activates the VBSs in TR is still unknown. The facts that mechanical force increases vinculin recruitment to focal adhesions (*4*) and that talin can bind to the actin cytoskeleton suggest that force induced by actomyosin contraction could stretch the TR, exposing the cryptic VBSs to Vh (*2*). The mechanical stretching of cytoskeletally attached proteins by applied force is documented for the case in which stretch activates tyrosine phosphorylation by Src family kinases (*13*). Moreover, it has been shown that stretching of DNA leads to changes in the binding of DNA-interacting proteins (*14*). Molecular dynamics simulations have supported the ability of force-induced conformational changes to expose the cryptic residues of VBSs in the TR (*15*). In addition, another recent steered molecular dynamic study provided a model in which mechanical force gradually breaks the 12 helices of the TR into three smaller sub-bundles (*11*).

To experimentally test the hypothesis that force-induced stretching of the TR can open the helical bundles and enable Vh binding, we used a combination of magnetic tweezers to enable stretching of single TR molecules and total internal reflection fluorescence (TIRF) microscopy to observe fluorescent Vh binding (Fig. 2).

Three DNA constructs encoding monomeric TR, dimeric tandem TR, and full-length α-actinin were designed with His and Avi tags at their N- and C-termini, respectively. The dimeric tandem TR served as a positive control because it should have twice the number of binding sites that are in a single TR. Because α-actinin has an active binding site for Vh (*10*), it served as a negative control; we would not expect to see any difference in the number of Vh molecules bound to α-actinin with and without force-induced stretching. All expressed proteins had 6×His and a biotin at their N- and C-termini, respectively (fig. S1). The N-terminal was used to attach the protein to a Ni–nitrilotriacetic acid (NTA) glass surface, whereas avidinated magnetic beads were coupled to the biotinylated C-terminus. The molecule attached to the glass was stretched by applying a magnetic force to the beads in a vertical direction with the magnetic tweezers apparatus described previously (*16*).

The criterion for deciding that beads were bound to a single talin molecule was to observe a random motion of the bead around a single point close to the surface. The Vh was labeled with the fluorophore Alexa 488 at a molar ratio of 1:1 and further incubated with the TR. This incubation was performed in presence or absence of force depending on whether or not stretching of TR was pursued. Then, all unbound Alexa 488–Vh was washed, and TIRF intensity was measured over time. The number of Alexa 488–Vh molecules bound to the TR was determined by single-molecule fluorescence photobleaching events. The fluorescence intensity abruptly decreased in a standard step if a single fluorophore was bleached. The same protocol was used to measure Vh binding to TR tandem fragment and α-actinin controls.

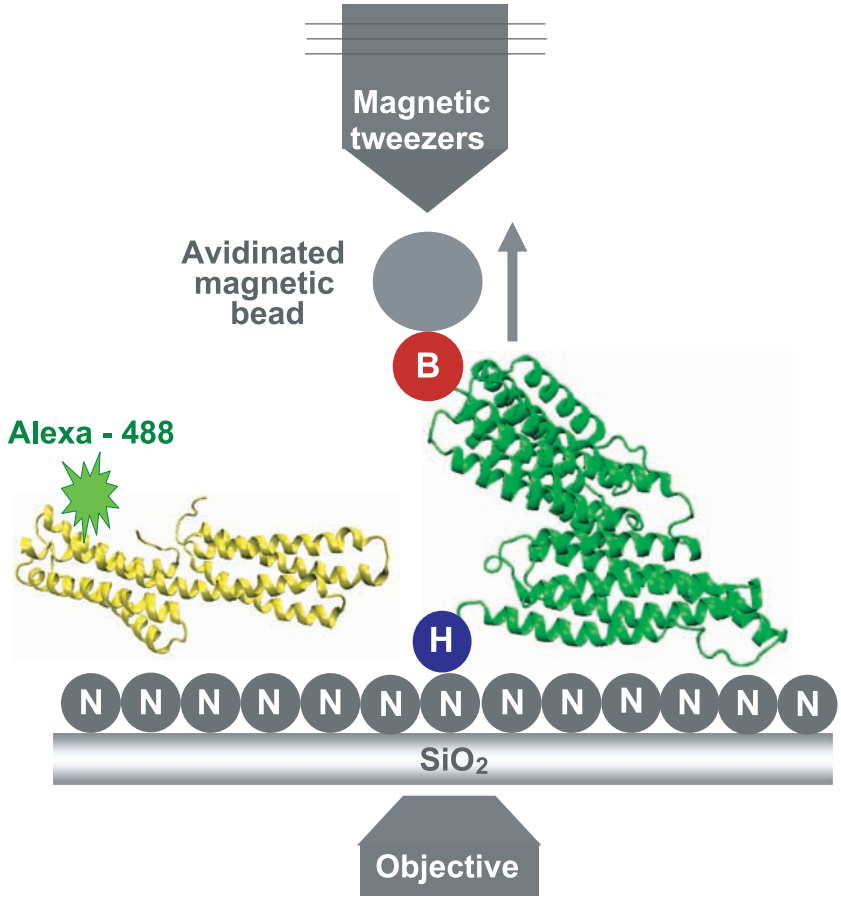

Fig. 2. Representation of the device used to measure the binding events. The Ni-NTA (labeled N) grafted slides containing the TR fixed through its 6×His N terminus (labeled H) to the glass and with the avidinated magnetic bead bound to its biotinylated C terminus (labeled B) was placed over the objective. Alexa 488–Vh was added to the slides for the period of the incubation. The TR and Vh structures are represented in green and yellow, respectively. The arrow shows the direction of the movement of the beads when they are pulled using the magnetic tweezers.

With monomeric TR in the absence of force, we observed (Fig. 3A) one or no photobleaching events of the Alexa 488–Vh fluorescence for each bead attached to a TR. After the application of 12 pN of force to the beads, as many as three photobleaching events were observed, each the size of a single bleaching event. The histogram next to each graph represents the distribution of photobleaching events for all the analyzed beads. Although fewer than half of the diffusing beads showed binding and individual bleaching events, the percentage of vinculin bound to beads was greater upon application of force. Because each Alexa 488–Vh was labeled with one fluorophore molecule, each photobleaching event was associated with the binding of one Vh molecule to the TR. We suggest that force applied to the beads caused mechanical unfolding of TR, exposing up to two additional VBSs. When 2 pN of force was applied to the beads, the percentage of vinculin bound to beads was larger than in the case of no force but smaller than when 12 pN of force was applied, which supports the hypothesis that the number of vinculin molecules bound to the TR depends on the stretching force applied to the TR.

The analysis of the photobleaching events for the experiments performed using the tandem TR as the positive control (Fig. 3B) revealed up to two Vh binding events to the tandem TR in the absence of force. When 12 pN of force was applied to the beads, up to six binding events were observed. In all experiments performed using α-actinin as the negative control (Fig. 3C), one or no binding event was observed with and without the application of 12 pN of force.

In order to measure the pattern of force-dependent stretching of TR, we designed a DNA construct encoding for $I27_2$-T_R-$I27_2$ [TR flanked by two molecules of the I27 (27th immunoglobular domain of human cardiac titin), which has well-characterized mechanical properties (*17*) (Fig. 4A)]. The protein $I27_2$-T_R-$I27_2$ was manipulated by using single-molecule force extension spectroscopy (*18*). Figure 4B shows a characteristic force extension curve corresponding to the unfolding of $I27_2$-T_R-$I27_2$. In this trace, the four equally spaced peaks at ~200 pN with

contour length increments of ~28.5 nm correspond to the unfolding of the four flanking I27 handles (*17*). The largest peak at the right of Fig. 4B represents the detachment of the cantilever from the polyprotein. Before the four force peaks for the I27 domains, there are several smaller peaks over a distance of about 160 nm, which corresponds closely to the expected length of the fully stretched 407-residue TR domain. Distances between the unfolding peaks were determined by using the contour length measured by fits of the wormlike chain model (green lines in Fig. 4B). [The contour length of a fully stretched protein is about 0.4 nm per amino acid (*19*).] A histogram of positions for each of the five TR force peaks (Fig. 4C, n = 120 traces) with the resting length of the protein as reference (163 nm minus the measured distance to the first I27 module) showed that the unfolding pattern was very regular. Five unfolding peaks with average forces of 29 ± 19, 31 ± 19, 36 ± 22, 42 ± 22, and 51 ± 26 pN were identified at 24 ± 7, 81 ± 9, 107 ± 3, 129 ± 6, and 152 ± 5 nm, respectively. Histograms showing the force distribution for each peak can be found in fig. S2.

The force extension experiment provides a mechanical description for TR, that is, unfolding forces and contour lengths. To study the unfolding rate of TR, we used force-clamp spectroscopy, a technique that allows us to apply a constant calibrated force to a single TR for determining the unfolding trajectory as a function of time (*20*). A double pulse protocol was used in order to separate the unfolding of TR from those of I27 modules. The first force pulse was set up at forces ranging from 20 to 50 pN to allow for the unfolding of TR. A second pulse of force of 150 pN was applied to capture the unfolding of the I27 modules, represented with the four identical steps of 24 nm (Fig. 4D). Only those recordings showing at least three I27 unfolding events were analyzed. The portion of the traces containing the TR unfolding was extracted, averaged, and fitted to a single exponential with a time constant, τ, which provides the unfolding rate, $r = 1/\tau$ (Fig. 4E). Considering the number of traces collected per force (~20 traces), the exponential fitting provides a good approximation for the unfolding rate that adequately describes the process over the entire range of forces. The unfolding rate versus the applied force is presented in Fig. 4F. The extrapolation at 12 pN, the unfolding force value used in the binding experiments, yields a constant rate of 2.7 s^{-1}.

Taking together the results of the atomic force spectroscopy and the binding experiments of Vh to the TR, it is possible to make some conclusions. First, the fact that only one binding event was observed in the absence of force-induced stretching indicates that, in its intact state, TR contains one active VBS, as was predicted in previous studies using several biophysical techniques (*9*, *12*). This active VBS could be located in the helix 6, 9, 11, or 12, most likely helix 9, where the trypsin cleavage site is found (*12*) and which is likely the initial vinculin interaction site in cells. Second, stretching the TR with 12 pN of force can increase the Vh binding events from one to three. Thus, force-induced stretching of the TR caused conformational changes in its helical bundle, exposing two of the four remaining buried VBSs, which become available to bind Vh.

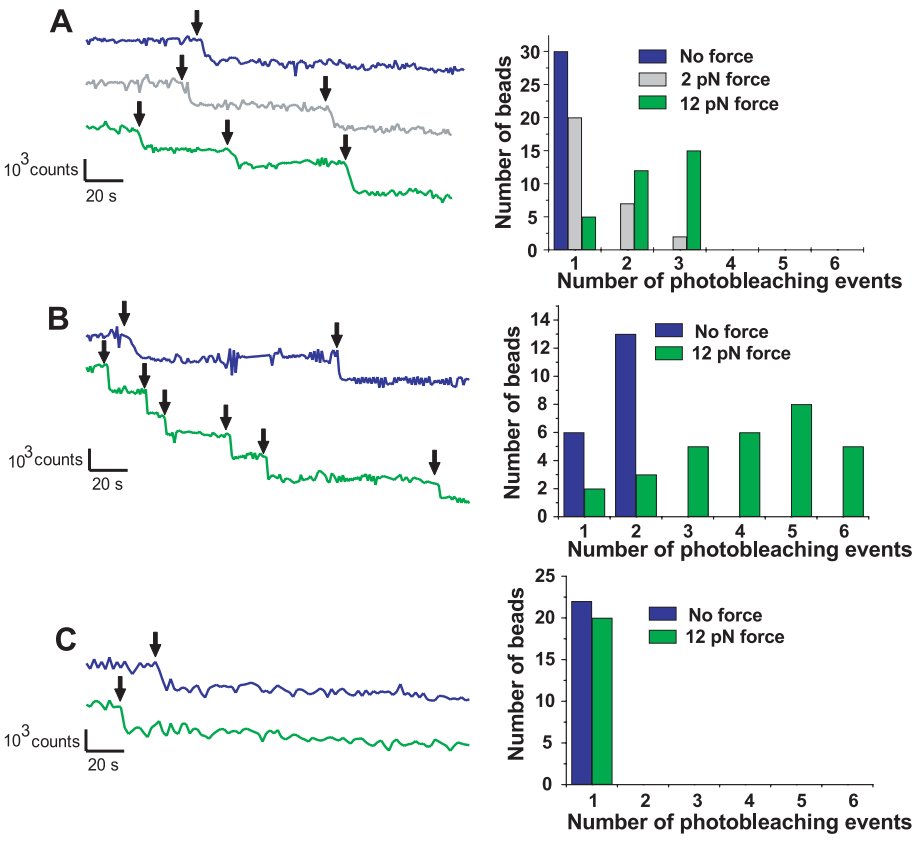

Fig. 3. Diagram of photobleaching events of Alexa 488–Vh bound to (**A**) TR, (**B**) dimeric tandem TR, and (**C**) α-actinin. Histograms show the number of beads per photobleaching event. In all cases, blue, gray, and green colors correspond with no force, 2-pN force, and 12-pN force applied, respectively. The TR, talin dimeric tandem (positive control), and α-actinin (negative control) showed maximally 1 and 3, 2 and 6, and 1 and 1 photobleaching events (black arrows) when no force and 12 pN force, respectively, was applied.

Previous steered molecular dynamic calculations potentially provide insights into the number of VBSs activated by force-induced stretching (*11*). Because the mechanical stabilities of the domains that form the TR are different (*8*, *12*), force applied across the H1-H12 fragment will sequentially break the rod into smaller helix bundles. In the calculations, force first splits the fragments H1-H8 from H9-H12, and then H1-H8 breaks into the sub-bundles H1-H5 and H6-H8. The formation of these two intermediate states is in agreement with the unfolding pattern that we obtained by using force extension spectroscopy, because the subsequent unfolding of the three domains would give five mechanical transition states as observed. The predicted fragmentation pattern involves the sequential exposure of VBSs in TR, and this could explain why we observed up to three instead of five Vh binding events when force is applied. Although the 12-pN force used in the binding experiments is lower than the average unfolding forces in the atomic force microscopy (AFM) experiments, it is applied for a much longer time and could be as effective. More experimentation is needed to define the partial unfolding of the TR to intermediate states, in which the cryptic VBSs become exposed but the secondary structure of helices enables recognition by Vh. Similarly, lower unfolding forces have been used in AFM force-clamp unfolding of polyubiquitins (*21*) as compared with AFM force extension experiments (*22*). Furthermore, it is known that at constant low force (i.e., 12 pN), the unfolding and refolding processes may compete with each other, leading to situations such as that reported by Cecconi *et al*. (*23*) in which only up to three VBSs are available. Higher forces might stretch the VBS helices and reduce the binding probability; however, a new experimental setup is needed to generate the higher forces.

These findings establish that force-induced stretching can expose previously buried binding sites for vinculin in the TR. The consensus sequence for the 11 VBSs in the TR indicates that they have extensive hydrophobic interactions with adjacent amphipathic helices (*7*). If this scenario is correct, the proposed mechanotransduction mechanism for the VBSs in TR

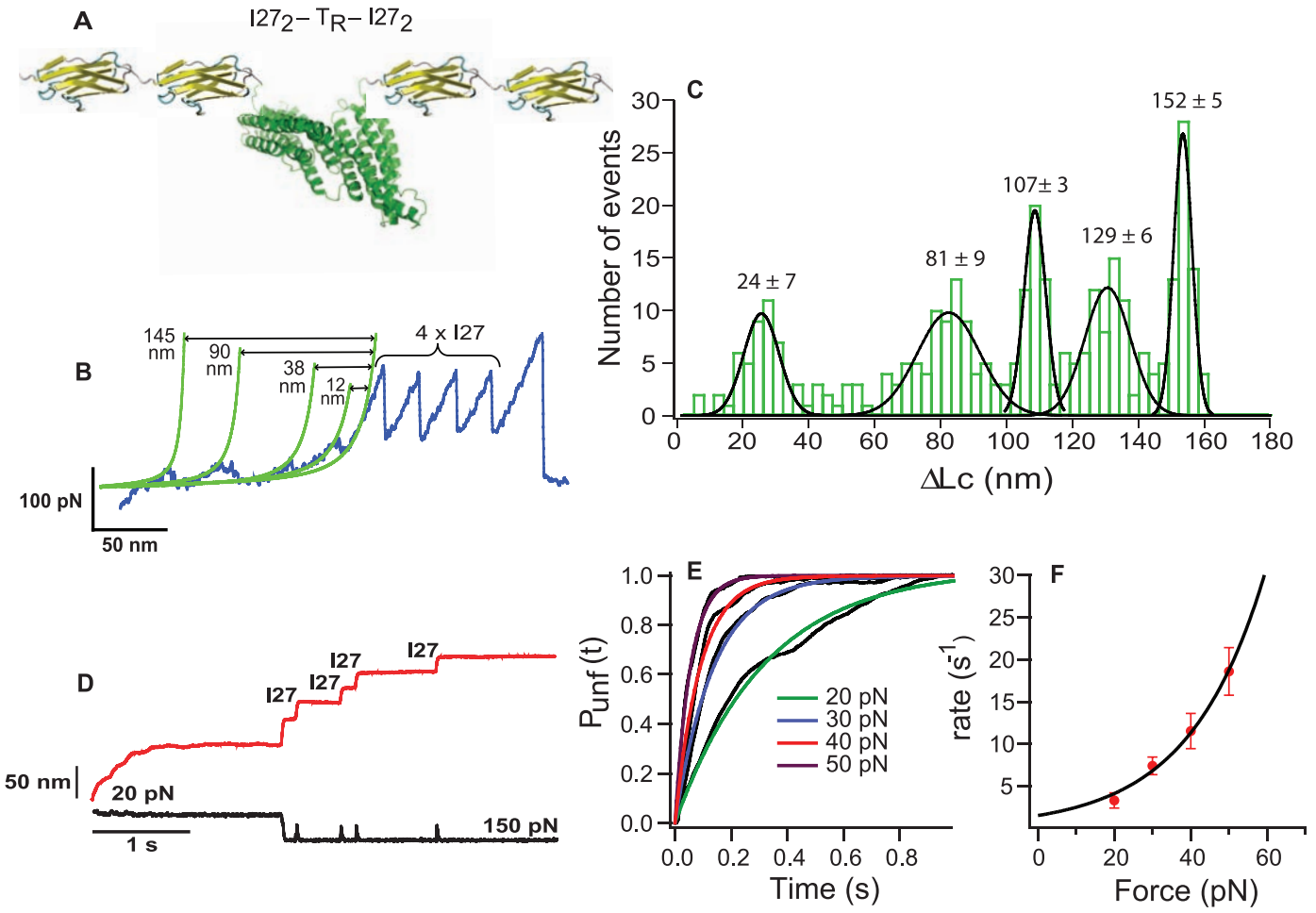

Fig. 4. AFM experiments. (**A**) Diagram of the polyprotein designed for AFM, $I27_2$–TR–$I27_2$. (**B**) Force extension trace for $I27_2$-TR-$I27_2$. (**C**) Histogram of the contour length increments (ΔL_c) for the unfolding peaks of the TR (120 traces). (**D**) Force-clamp trace obtained by stretching $I27_2$-TR-$I27_2$ at 20 and 150 pN of force. The red and black lines represent extension and force, respectively. (**E**) Probability of unfolding versus time for TR. Average recordings of TR unfolding at 20 pN (15 traces), 30 pN (14 traces), 40 pN (17 traces), and 50 pN (22 traces). A single exponential (colored smooth lines) is fitted to each average trace (in black). (**F**) The rate constant of unfolding as a function of force. Data are represented as mean ± SD; error bars were calculated by using the bootstrapping method (*26*).

may be a general pathway used by the talin molecule to amplify biochemical signals upon activation by force. Indeed, talin head interacts with membrane integrins while its tail binds actin filaments, so that force transmitted to the matrix from the actin cytoskeleton would logically be borne by talin. Actomyosin contraction could develop force-dependent talin unfolding that may cause vinculin binding and activation, leading to several intracellular responses. Although the force per integrin is 1 to 2 pN on average, the bond between integrin and fibronectin is able to withstand a force of about 20 pN before breaking (*24*). Thus, forces used in this study are in a physiological range.

Talin stretching may provide a prototype for a wide range of signaling events in cells because there are many multidomain proteins that link cytoskeleton with membrane sites (*25*). Learning the mechanism by which stretching forces activate binding may broaden our understanding of the fundamental workings of mechanosensory systems in cells.

References and Notes

1. V. Vogel, M. Sheetz, *Nat. Rev. Mol. Cell Biol.* **7**, 265 (2006).
2. D. R. Critchley, *Biochem. Soc. Trans.* **33**, 1308 (2005).
3. D. R. Critchley, *Curr. Opin. Cell Biol.* **12**, 133 (2000).
4. C. G. Galbraith, K. M. Yamada, M. P. Sheetz, *J. Cell Biol.* **159**, 695 (2002).
5. T. Izard, C. Vonrhein, *J. Biol. Chem.* **279**, 27667 (2004).
6. D. A. Calderwood, V. Tai, G. Di Paolo, P. De Camilli, M. H. Ginsberg, *J. Biol. Chem.* **279**, 28889 (2004).
7. A. R. Gingras *et al.*, *J. Biol. Chem.* **280**, 37217 (2005).
8. E. Papagrigoriou *et al.*, *EMBO J.* **23**, 2942 (2004).
9. I. Fillingham *et al.*, *Structure* **13**, 65 (2005).
10. T. Izard *et al.*, *Nature* **427**, 171 (2004).
11. V. P. Hytonen, V. Vogel, *PLOS Comput. Biol.* **4**, e24 (2008).
12. B. Patel *et al.*, *J. Biol. Chem.* **281**, 7458 (2006).
13. Y. Sawada *et al.*, *Cell* **127**, 1015 (2006).
14. Y. Harada *et al.*, *Biophys. J.* **76**, 709 (1999).
15. S. E. Lee, R. D. Kamm, M. R. Mofrad, *J. Biomech.* **40**, 2096 (2007).
16. M. Tanase, N. Biais, M. Sheetz, *Methods Cell Biol.* **83**, 473 (2007).
17. M. Carrion-Vazquez *et al.*, *Proc. Natl. Acad. Sci. U.S.A.* **96**, 3694 (1999).
18. A. F. Oberhauser, P. E. Marszalek, H. P. Erickson, J. M. Fernandez, *Nature* **393**, 181 (1998).
19. S. R. Ainavarapu *et al.*, *Biophys. J.* **92**, 225 (2007).
20. J. M. Fernandez, H. Li., *Science* **303**, 1674 (2004).
21. M. Schlierf, H. B. Li, J. M. Fernandez, *Proc. Natl. Acad. Sci. U.S.A.* **101**, 7299 (2004).
22. M. Carrion-Vazquez *et al.*, *Nat. Struct. Biol.* **10**, 738 (2003).
23. C. Cecconi, E. A. Shank, C. Bustamante, S. Marqusee, *Science* **309**, 2057 (2005).
24. G. Jiang, G. Giannone, D. R. Critchley, E. Fukumoto, M. P. Sheetz, *Nature* **424**, 334 (2003).
25. D. A. Calderwood, M. H. Ginsberg, *Nat. Cell Biol.* **5**, 694 (2003).
26. Materials and methods are available as supporting material on *Science* Online.

27. We thank D. Critchley and N. Bate for Vh and TR monomer constructs, C. Badilla-Fernandez for advisement with constructs, and V. Hytonen for contribution to Fig. 1. This work was supported by NIH grants to J.M.F. and M.P.S., an NIH award to A.d.R., a grant from the Spanish Ministry of Science and Education to R.P.-J., and a Marie Curie international fellowship to P.R.-C.

Supporting Online Material

www.sciencemag.org/cgi/content/full/323/5914/638/DC1
Materials and Methods
Figs. S1 to S4
References

8 July 2008; accepted 10 December 2008
10.1126/science.1162912

Mechanically Activated Integrin Switch Controls $\alpha_5\beta_1$ Function

Julie C. Friedland,[1,2]* Mark H. Lee,[1,2]* David Boettiger[1,2,3]†

The cytoskeleton, integrin-mediated adhesion, and substrate stiffness control a common set of cell functions required for development and homeostasis that are often deranged in cancer. The connection between these mechanical elements and chemical signaling processes is not known. Here, we show that $\alpha_5\beta_1$ integrin switches between relaxed and tensioned states in response to myosin II–generated cytoskeletal force. Force combines with extracellular matrix stiffness to generate tension that triggers the integrin switch. This switch directly controls the $\alpha_5\beta_1$-fibronectin bond strength through engaging the synergy site in fibronectin and is required to generate signals through phosphorylation of focal adhesion kinase. In the context of tissues, this integrin switch connects cytoskeleton and extracellular matrix mechanics to adhesion-dependent motility and signaling pathways.

Integrins are expressed on the surface of most cells in the body, and their primary function is to maintain a dynamic adhesion between the cell and its microenvironment (*1*). Integrin-mediated cell adhesion controls critical intracellular signals that regulate cell differentiation, proliferation, and survival (*2*–*4*). Recent analyses have found that tissue stiffness and the ability of cells to generate tension also control the same signaling pathways (*5*, *6*). How the mechanical properties of the cell's microenvironment are transmitted to intracellular biochemical pathways is not known. However, several intracellular signaling molecules, including src, Cas, and vinculin, show tension-dependent conformational changes that affect kinase activity, availability of phosphorylation sites, or intracellular localization (*7*–*9*). Binding proteins to the extracellular and cytoplasmic domains of integrins forges a link between the extracellular matrix and the actin cytoskeleton that is tensioned by myosin II motors acting on actin filaments (*7*). This complex contains the major mechanical elements that have been associated with the mechano-sensing capabilities of the cell (*10*). Integrins are necessary elements for most mechano-sensing models and lie at the beginning of the sensing pathway. Here, we investigate the mechano-responsive properties of $\alpha_5\beta_1$ integrin bound to surface-attached fibronectin.

[1]Institute for Medicine and Engineering, University of Pennsylvania, Philadelphia, PA 19104, USA. [2]Department of Microbiology, University of Pennsylvania, Philadelphia, PA 19104, USA. [3]Department of Pharmacology, University of Pennsylvania, Philadelphia, PA 19104, USA.

*These authors contributed equally to the work.
†To whom correspondence should be addressed: E-mail: boettige@upenn.edu

HT1080 cells plated on a stiff fibronectin-coated substrate attach through $\alpha_5\beta_1$ integrin, and these adhesive bonds are then tensioned by actin and myosin II (*11*). To analyze the role of tension for $\alpha_5\beta_1$-fibronectin adhesive bonds, we used pharmacological inhibitors of myosin II function and activation (*12*). The effects of these inhibitors on adhesive $\alpha_5\beta_1$-fibronectin bonds were measured by chemical cross-linking. In previous analyses, the fraction of total $\alpha_5\beta_1$ integrin that cross-linked was proportional to the number of adhesive bonds (*11*). This assay demonstrated a dose-dependent decrease in cross-linked $\alpha_5\beta_1$ integrin for cells treated with the myosin light-chain kinase inhibitor, ML-7 (Fig. 1A), and the myosin II inhibitors 2,3-butanedione monoxime (BDM) and blebbistatin (fig. S1, A to C) [supporting online text (SOM text), note S1]. Similar decreases were observed with the actin assembly inhibitors cytochalasin D and latrunculin A (fig. S1, D and E). Thus, blocking the ability of the cell to apply tension reduced the number of cross-linkable $\alpha_5\beta_1$-fibronectin bonds. In contrast, these inhibitors had no effect on the chemical binding of soluble fibronectin to $\alpha_5\beta_1$ integrin on cells in suspension (fig. S2, A and B). Another approach to measuring adhesive bonds is to measure the force required to detach the cell. We developed a spinning disc device for this purpose and demonstrated that the cell detachment force was proportional to the number of adhesive bonds (*11*, *13*, *14*). This measure of adhesive bonds was not affected by inhibiting actin-myosin–induced cell tension (Fig. 1B). Hence, we hypothesized that there were two distinct forms of the $\alpha_5\beta_1$-fibronectin adhesive bonds: one that formed in the absence of cell tension (relaxed bonds) that could not be cross-linked and one that formed in

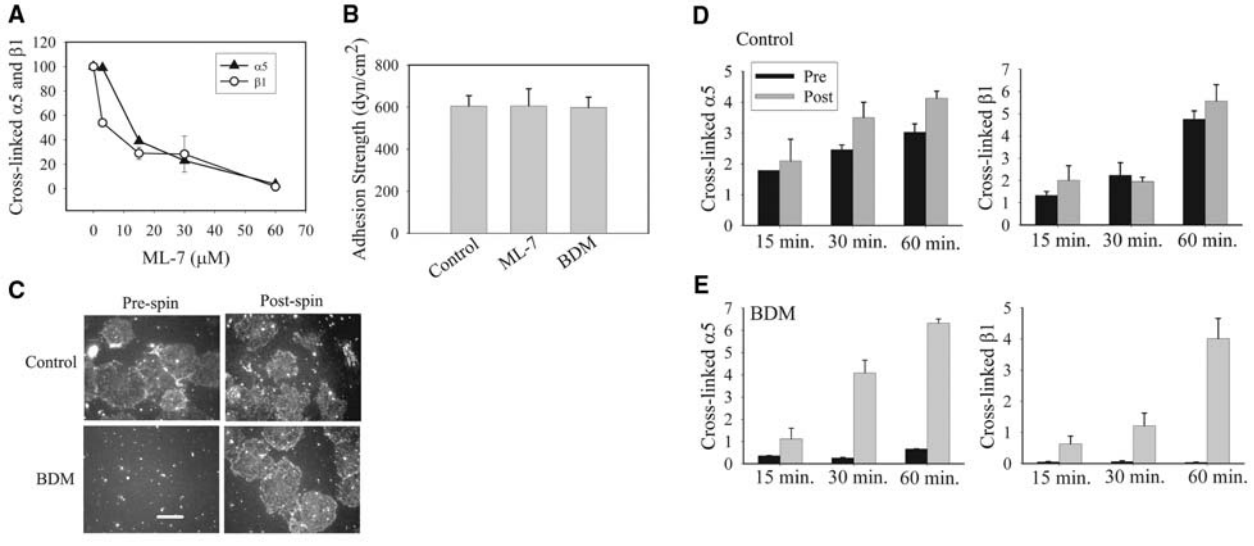

Fig. 1. Analysis of adhesive $\alpha_5\beta_1$-fibronectin bonds by chemical cross-linking before and after application of external force. (**A**) Proportion of cross-linked α_5 and β_1 integrin in ML-7–treated cells. (**B**) Tension-inhibited cells were analyzed by using the spinning disc: [ML-7] = 15 μM; [BDM] = 10 mM. (**C**) Distribution of cross-linked $\alpha_5\beta_1$ integrin 60 min after plating, before and after spinning ±10 mM BDM. Nonspecific aggregates of secondary antibody provide an internal focus or exposure control. Scale bar, 25 μm. (**D**) Prespin represents tensioned bonds, and post spin represents total bonds; the difference between the two represents relaxed bonds. Data show percentage of total α_5 and β_1 cross-linked as a function of time. (**E**) BDM-treated cells, the same as (D). Means ± SEM; n = 3.

the presence of cell tension (tensioned bonds) that could be cross-linked. Tension involves holding one end of the bond and pulling on the other. This can have two outcomes; either the bond separates or the bond switches to a new, stronger state that resists more tension.

To determine whether a state shift occurred when tension was applied, cells were allowed to adhere for 60 min (prespin) or incubated for 60 min and spun 5 min, which would apply tension to adhesive bonds by pulling on the cell (post spin) (Fig. 1C). The control showed considerable cross-linked $\alpha_5\beta_1$ integrin prespin and only a slight increase post spin, particularly toward the centers of the cells. The BDM-inhibited cells showed no detectable cross-linking before spinning, in agreement with the earlier result, but post spin, the levels of cross-linking were similar to those of the control. Thus, external force could substitute for intracellular force. The resulting tension switched the relaxed (non–cross-linkable) $\alpha_5\beta_1$-fibronectin bonds to the tensioned (cross-linkable) state. To expand this result, a quantitative analysis of cross-linkable $\alpha_5\beta_1$ was performed at 15, 30, and 60 min after plating, both before and after a 5-min spin (Fig. 1, D and E, and fig. S2C). The prespin values represent tensioned bonds; the spinning would convert all bonds to tensioned bonds, and hence, the post spin values represent total bonds; and the difference represents the relaxed bonds. Control cells showed a progressive increase in the level of tensioned bonds with time. In the BDM-treated cells, there was very little increase in tensioned bonds, although the total number of bonds increased with similar kinetics and extent as the control. Thus, in the absence of tension, adhesive $\alpha_5\beta_1$-fibronectin bonds accumulated at a rate similar to that in the presence of tension, but the bonds remained in a relaxed state. Because it is necessary to generate the linkage from substrate through $\alpha_5\beta_1$-fibronectin bonds to actin and myosin before tension can be exerted, the relaxed bond is a necessary, logical precursor to the tensioned bond. It is unlikely that the increase in bonds observed after spinning could be caused by the spinning itself because: (i) the extent of the increase depended on the time of the prespin incubation and not on the spinning time, and (ii) $\alpha_5\beta_1$-fibronectin bonds accumulate relatively slowly because of issues of diffusion and the requirements for complex formation; 5 min is not sufficient time for the observed increases (fig. S2D and Fig. 1C).

If tension converts $\alpha_5\beta_1$ integrin–fibronectin bonds from the relaxed to the tensioned state rather than causing the bond to dissociate, the intermolecular contacts that form the two states must be distinct (*15*). The relaxed state can be approximated by the chemical binding between fibronectin [the fragment containing the 7th to 10th type II repeats (Fn7-10), including both the Arg-Gly-Asp (RGD) and synergy sites (*16*) (Fig. 2A)] and the purified extracellular domain of $\alpha_5\beta_1$ integrin, because these reactions were done with purified components, the bonds could not be tensioned (*17*). A combination of electron microscopy and surface plasmon resonance analyses demonstrated that the binding interface includes the RGD but not the synergy site. To determine the intermolecular contacts for tensioned bonds, the spinning disc was used to analyze fibronectin mutants. Bonds were allowed to form for 60 min to approximate steady-state adhesion (fig. S2D). When RGD was deleted, the relaxed bonds could not form and no cells attached. Individual synergy site mutations in which Ala replaced Arg at residue 1374 and 1379 (R1374A and R1379A, respectively) produced weaker bonds that required less force to rupture, and this effect was roughly additive in the double R1374/1379A mutant (Fig. 2B). Thus, the relaxed bonds involved only the RGD site, but the tensioned bonds required also R1374 and R1379 in the synergy site. The reduction of ~90% in adhesion strength for the double R1374/1379A mutant implies that most of the bond strength depended on synergy-site contacts. Both molecular docking and the presence of epitopes for inhibitory monoclonal antibodies suggest that the synergy site would contact the β-propeller in α_5 (*18*). The differential cross-linking observed for the relaxed and tensioned states can be explained by the resulting change in intermolecular distance.

The generation of tension involves pulling against a resistance, which is provided by the substrate to which the fibronectin is attached. Up to this point, the experiments have used very stiff

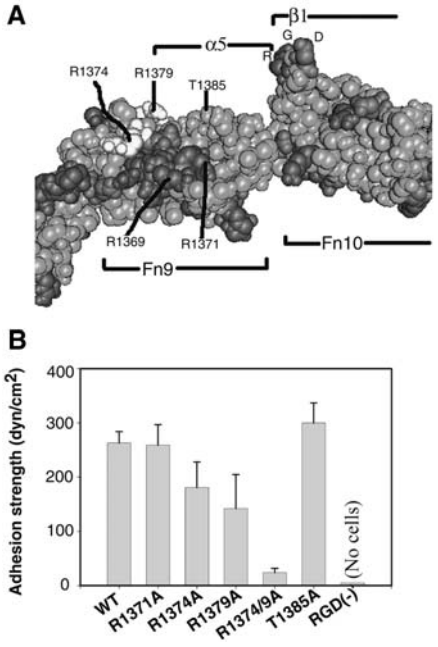

Fig. 2. Tensioned $\alpha_5\beta_1$-fibronectin bonds engage the synergy site of fibronectin. (**A**) Crystal structure of fibronectin type III repeats 9 and 10. $\alpha_5\beta_1$ integrin binds from the top overlapping Fn9 and Fn10 surfaces. The RGD extended loop in Fn10 acts as the recognition sequence. Synergy-site R1374 and R1379 (white) binds near the edge of the β-propeller of α5. Charged residues (black). (**B**) Spinning disc analysis of mutant Fn7-10. Means ± SEM; $n = 3$.

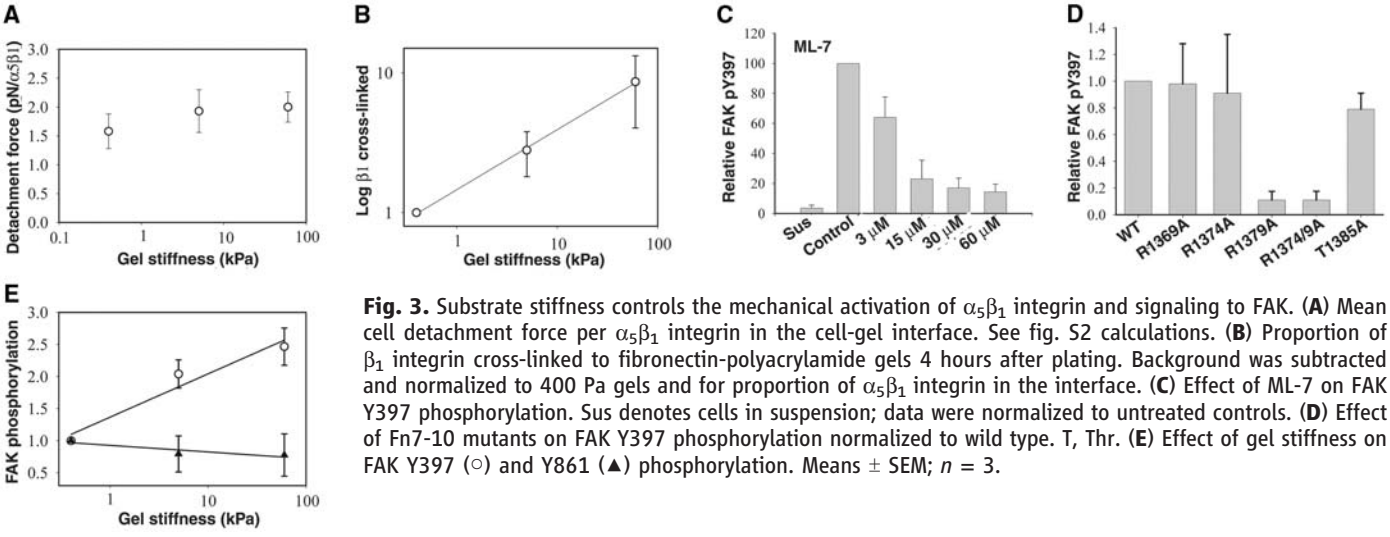

Fig. 3. Substrate stiffness controls the mechanical activation of $\alpha_5\beta_1$ integrin and signaling to FAK. (**A**) Mean cell detachment force per $\alpha_5\beta_1$ integrin in the cell-gel interface. See fig. S2 calculations. (**B**) Proportion of β_1 integrin cross-linked to fibronectin-polyacrylamide gels 4 hours after plating. Background was subtracted and normalized to 400 Pa gels and for proportion of $\alpha_5\beta_1$ integrin in the interface. (**C**) Effect of ML-7 on FAK Y397 phosphorylation. Sus denotes cells in suspension; data were normalized to untreated controls. (**D**) Effect of Fn7-10 mutants on FAK Y397 phosphorylation normalized to wild type. T, Thr. (**E**) Effect of gel stiffness on FAK Y397 (○) and Y861 (▲) phosphorylation. Means ± SEM; $n = 3$.

substrates that provide strong resistance to forces applied to the cell or cytoskeleton. On these substrates, most $\alpha_5\beta_1$ integrin–fibronectin bonds were tensioned, but softer substrates in the range of that found in tissues (0.2 to 20 kPa) provide less resistance, and the proportion of adhesive bonds in the relaxed state should increase. Fibronectin was attached to polyacrylamide gel substrates with different stiffness and $\alpha_5\beta_1$ integrin–fibronectin bonds were measured by using both spinning disc and chemical cross-linking methods (Fig. 3, A and B). Note that corrections were made for cell spreading and shape differences (see fig. S3, A and B, and SOM text, note S2). Spinning disc analysis showed that the total number of adhesive bonds that formed was independent of substrate stiffness. In contrast, the cross-linking assay showed a strong dependence of the number of tensioned bonds on substrate stiffness. Thus, as the substrate stiffness increased, the proportion of $\alpha_5\beta_1$-fibronectin adhesive bonds in the tensioned state increased. If only tensioned bonds generated downstream signals, this would provide a mechanism for cells to sense microenvironmental stiffness. Inhibitors of myosin II and actin that blocked the conversion of relaxed to tensioned bonds exhibited a parallel dose-dependent reduction in phosphorylation of the focal adhesion kinase FAK on Y397 (Fig. 3C and fig. S4, A and B). The R1379A mutant that had the largest effect on synergy-site engagement was sufficient to block FAK Y397 phosphorylation, but the weaker R1374A mutant was below the tension threshold (Fig. 3D). Finally, FAK Y397 exhibited a stiffness-dependent increase in phosphorylation, whereas FAK Y861, which is tethering-independent (*11*), showed no stiffness-dependent change in phosphorylation in the same cells (Fig. 3E).

$\alpha_5\beta_1$ integrin functions both to adhere cells to a fibronectin substrate and to mediate downstream signals that control cell physiology and cell fates (*1*, *3*). Previous analyses have associated those functions with integrin activation and clustering (*19*, *20*). The current models for integrin activation are based on analyses in which tension was not applied (*17*, *21*). This activation switches the integrin into a state that can bind ligand and is necessary for the clustering of integrins and the formation of focal complexes (*22*). Although these processes were required to form adhesion complexes, they were insufficient to generate either strong adhesion or downstream signals (fig. S5). The initial $\alpha_5\beta_1$-fibronectin bond is equivalent to the previously described activated-bound state (*17*, *19*). Application of force switches the relaxed state to a new tensioned state, which has increased bond strength. Bonds that undergo tension-strengthening have been called "catch-bonds" and have been previously reported for leukocyte selectin and *Escherichia coli* FimH adhesion receptors (*23*, *24*). A catch-bond can function as a molecular clutch that is engaged under tension and that will release when tension is released. Thus, $\alpha_5\beta_1$-fibronectin bonds provide mechanical clutches for cell migration (*25*). For $\alpha_5\beta_1$ integrin, the catch-bond mechanism depended on the synergy-site engagement, which raises the question of whether synergy sites exist more broadly in integrin ligands.

Mechano-responsive proteins undergo functional conformational transitions, in response to tension, that alter binding properties and/or enzymatic functions (*8*, *10*). Intracellular proteins, like src, that have this property require cytoskeletal structure and integrin-mediated adhesion for mechanical activation (*9*). Thus, the mechanical activation of src would depend on the mechanical activation of integrins, which suggests a model that contains multiple intra- and extracellular mechano-sensitive nodes to generate intracellular signaling responses. Control of intracellular signals by mechanical triggers provides a mechanism for spatial distribution of signals within cells. This is important for the cells' capability to sense and respond to differences in microenvironmental stiffness and generates a need for mechanisms to control the cell's "tensional" homeostasis (*5*).

References and Notes

1. R. O. Hynes, *Cell* **69**, 11 (1992).
2. A. S. Menko, D. Boettiger, *Cell* **51**, 51 (1987).
3. C. K. Miranti, J. S. Brugge, *Nat. Cell Biol.* **4**, E83 (2002).
4. A. K. Fournier *et al.*, *J. Cell Sci.* **121**, 226 (2008).
5. M. J. Paszek *et al.*, *Cancer Cell* **8**, 241 (2005).
6. D. E. Discher, P. Janmey, Y. L. Wang, *Science* **310**, 1139 (2005).
7. D. Riveline *et al.*, *J. Cell Biol.* **153**, 1175 (2001).
8. Y. Sawada *et al.*, *Cell* **127**, 1015 (2006).
9. S. Na *et al.*, *Proc. Natl. Acad. Sci. U.S.A.* **105**, 6626 (2008).
10. T. Shemesh, B. Geiger, A. D. Bershadsky, M. M. Kozlov, *Proc. Natl. Acad. Sci. U.S.A.* **102**, 12383 (2005).
11. Q. Shi, D. Boettiger, *Mol. Biol. Cell* **14**, 4306 (2003).
12. Materials and methods are available as supporting material on *Science* Online.
13. A. J. Garcia, F. Huber, D. Boettiger, *J. Biol. Chem.* **273**, 10988 (1998).
14. D. Boettiger, *Methods Enzymol.* **426**, 1 (2007).
15. B. C. Cunningham, J. A. Wells, *J. Mol. Biol.* **234**, 554 (1993).
16. D. J. Leahy, I. Aukhil, H. P. Erickson, *Cell* **84**, 155 (1996).
17. J. Takagi, K. Strokovich, T. A. Springer, T. Walz, *EMBO J.* **22**, 4607 (2003).
18. M. J. Humphries, E. J. Symonds, A. P. Mould, *Curr. Opin. Struct. Biol.* **13**, 236 (2003).
19. R. O. Hynes, *Cell* **110**, 673 (2002).
20. S. Miyamoto, S. K. Akiyama, K. M. Yamada, *Science* **267**, 883 (1995).
21. J. P. Xiong *et al.*, *Science* **296**, 151 (2002).
22. C. Cluzel *et al.*, *J. Cell Biol.* **171**, 383 (2005).
23. O. Yakovenko *et al.*, *J. Biol. Chem.* **283**, 11596 (2008).
24. B. T. Marshall *et al.*, *Nature* **423**, 190 (2003).
25. Y. L. Wang, *Sci. STKE* **2007**, e10 (2007).

26. This work was supported by grant GM57388 from the National Institutes of Health to D.B. We thank S. Akiyama (NIH) for 13G12 antibody, H. Erickson (Duke) for mutant fibronectin constructs, and Qi Shi for technical assistance.

Supporting Online Material

www.sciencemag.org/cgi/content/full/323/5914/642/DC1
Materials and Methods
SOM Text
Figs. S1 to S5
References

12 November 2008; accepted 24 November 2008
10.1126/science.1168441

A Human Telomerase Holoenzyme Protein Required for Cajal Body Localization and Telomere Synthesis

Andrew S. Venteicher,[1,2] Eladio B. Abreu,[3]* Zhaojing Meng,[4]* Kelly E. McCann,[1,5] Rebecca M. Terns,[3] Timothy D. Veenstra,[4] Michael P. Terns,[3] Steven E. Artandi[1,2,5]†

Telomerase is a ribonucleoprotein (RNP) complex that synthesizes telomere repeats in tissue progenitor cells and cancer cells. Active human telomerase consists of at least three principal subunits, including the telomerase reverse transcriptase, the telomerase RNA (TERC), and dyskerin. Here, we identify a holoenzyme subunit, TCAB1 (telomerase Cajal body protein 1), that is notably enriched in Cajal bodies, nuclear sites of RNP processing that are important for telomerase function. TCAB1 associates with active telomerase enzyme, established telomerase components, and small Cajal body RNAs that are involved in modifying splicing RNAs. Depletion of TCAB1 by using RNA interference prevents TERC from associating with Cajal bodies, disrupts telomerase-telomere association, and abrogates telomere synthesis by telomerase. Thus, TCAB1 controls telomerase trafficking and is required for telomere synthesis in human cancer cells.

The telomerase reverse transcriptase (TERT) and the telomerase RNA component (TERC) comprise the minimal catalytic core of the telomerase enzyme (*1*), whereas dyskerin is an RNA-binding protein that recognizes the H/ACA sequence motif shared by TERC and two groups of noncoding RNAs involved in RNA modification: small Cajal body RNAs (scaRNAs) and small nucleolar RNAs (snoRNAs) (*2*, *3*). Dyskerin functions in part

to support telomerase ribonucleoprotein (RNP) biogenesis and TERC stability (*4*, *5*). TERT, TERC, and dyskerin are all components of active telomerase (*6*), and mutations in any of these genes can cause the human stem cell disorder dyskeratosis congenita (*7*). Other potential components of active telomerase include three evolutionarily conserved dyskerin-associated proteins, nucleolar protein 10 (NOP10), nonhistone protein 2 (NHP2), and glycine/arginine–rich domain containing protein 1 (GAR1) (*8*–*10*), and ever-shorter telomeres 1A (EST1A), a homolog of the yeast telomerase protein Est1p (*11*, *12*). However, the size of active human telomerase, estimated in the 0.65-to-2-MDa range (*6*, *13*, *14*), suggests the existence of additional components. We reasoned that other dyskerin-associated proteins may be telomerase components, and we therefore sought to purify dyskerin complexes.

To study dyskerin, we expressed tagged dyskerin protein at endogenous levels in the absence of competing endogenous protein (fig. S1) and isolated dyskerin complexes by using a dual-affinity chromatography strategy. Purified dyskerin complexes were analyzed by SDS–polyacrylamide gel electrophoresis (SDS-PAGE) and nano–liquid chromatography–tandem mass spectrometry (nanoLC-MS/MS) for identification of copurifying proteins (Fig. 1, A and B). Dense peptide coverage was obtained for dyskerin and for the dyskerin-associated adenosine triphosphatases (ATPases) pontin and reptin (*14*). Each of the evolutionarily conserved dyskerin-binding proteins NHP2, NOP10, and GAR1 was detected, as were the dyskerin-associated proteins nucleolar and coiled-body phosphoprotein of 140 kD. (Nopp140) and nuclear assembly factor 1 (NAF1), a nucleoplasmic factor required for the assembly of H/ACA RNPs, including telomerase (Fig. 1B) (*15*). In addition, this approach identified WD repeat domain 79 (WDR79) (Fig. 1B), a protein that had not been previously implicated in dyskerin or telomerase function.

We further characterized WDR79, hereafter referred to as TCAB1 (telomerase Cajal body protein 1) (fig. S2). Endogenous TCAB1 was specifically bound to Flag-dyskerin that was immunoprecipitated from Flag-dyskerin^{+shRNA} HeLa cells (shRNA, short hairpin RNA), as were endogenous pontin, NAF1, TERT, and TERC (Fig. 1C). Interactions between TERT and dyskerin were disrupted by ribonuclease A (RNase A) treatment of the extract, which degraded TERC. In contrast, dyskerin interactions with TCAB1, NAF1, and pontin were not RNase A–sensitive, indicating that these associations occur through protein-protein contacts (Fig. 1C). Reciprocal immunoprecipitation (IP) of Flag-TCAB1 from Flag-TCAB1^{+shRNA} HeLa cells showed that Flag-TCAB1 not only associates with endogenous dyskerin but also with TERT and TERC, the catalytic core of telomerase (Fig. 1D). Like the TERT-dyskerin association, the binding of TERT to Flag-TCAB1 was RNase A–sensitive, suggesting that the interaction of TCAB1 with telomerase is dependent on TERC (Fig. 1D). Thus, TCAB1 interacts specifically with dyskerin, TERT, and TERC, all three known components of active telomerase.

Although TCAB1 associated with TERT, TERC, and dyskerin, it did not interact with the assembly factors NAF1, pontin, or reptin (Fig. 1D), suggesting that TCAB1 may be a component of the enzymatically active telomerase complex rather than a pre-telomerase complex. To test this hypothesis, we asked to what extent telomerase activity in cell extracts was associated with overexpressed TCAB1. Flag-tagged TCAB1, dyskerin, and NAF1 were depleted from extracts by IP (Fig. 2A, lanes 14 to 21). Flag-TCAB1 and Flag-dyskerin immunoprecipitates were associated with high telomerase activity (Fig. 2A,

[1]Department of Medicine, Stanford School of Medicine, Stanford, CA 94305, USA. [2]Program in Biophysics, Stanford School of Medicine, Stanford, CA 94305, USA. [3]Department of Biochemistry and Molecular Biology and Department of Genetics, University of Georgia, Athens, GA 30602, USA. [4]Laboratory of Proteomics and Analytical Technologies, Advanced Technology Program, Science Applications International Corporation (SAIC)–Frederick, National Cancer Institute (NCI)–Frederick, Frederick, MD 21702, USA. [5]Program in Cancer Biology, Stanford School of Medicine, Stanford, CA 94305, USA.

*These authors contributed equally to this work.
†To whom correspondence should be addressed. E-mail: sartandi@stanford.edu

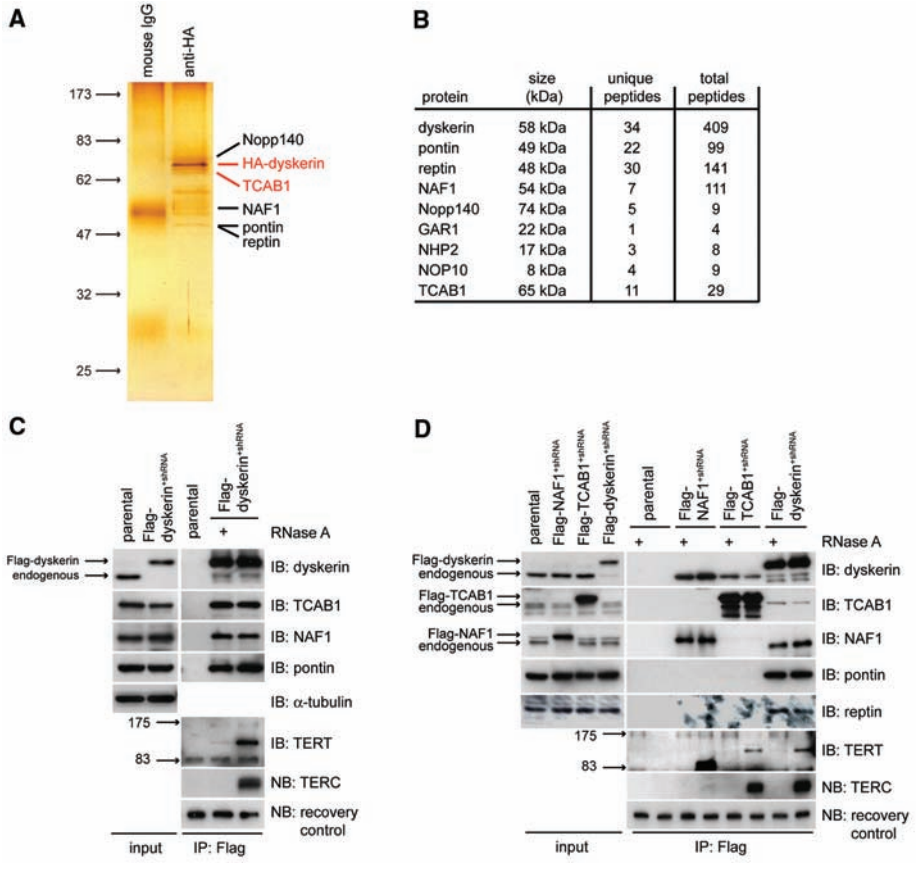

Fig. 1. Identification of TCAB1 as a dyskerin- and telomerase-interacting protein. (**A**) Dual affinity–purified dyskerin complexes fractionated by SDS-PAGE and silver-stained. (**B**) Unique and total peptides corresponding to dyskerin-associated proteins identified by nanoLC-MS/MS. (**C**) Flag-dyskerin interactions with endogenous TCAB1 and telomerase components and (**D**) Flag-TCAB1 and Flag-NAF1 interactions with endogenous telomerase components. IP–Western blot using extracts from Flag-dyskerin^{+shRNA} cells, Flag-TCAB1^{+shRNA} cells, or Flag-NAF1^{+shRNA} cells is shown. IB, immunoblot; NB, Northern blot; parental, HeLa cells. Plus sign indicates treatment of extracts with RNase A during IP. Recovery control was exogenous RNA spiked into samples after IP to control for differential RNA recovery.

lanes 12 and 13). Moreover, purification of either Flag-TCAB1 or Flag-dyskerin depleted these extracts of telomerase activity, indicating that both Flag-TCAB1 and Flag-dyskerin were associated with nearly all telomerase activity in the extract. In contrast, Flag-NAF1 bound only a small percentage of telomerase and did not deplete telomerase activity from cell extracts (Fig. 2A, lanes 1 to 8). Furthermore, IP of either Flag-TCAB1 or Flag-dyskerin depleted TERC but not unrelated RNAs such as U1 from cell extracts (Fig. 2A, lanes 14 to 21). Flag-TCAB1 and Flag-dyskerin were associated with similar amounts of endogenous TERT and TERC, further suggesting that TCAB1 and dyskerin reside together in the same active telomerase complexes (Fig. 2A, lanes 24 to 25).

To understand the composition of endogenous telomerase, IPs were performed using antibodies to TCAB1 and NAF1, each of which efficiently depleted its cognate protein from cell extracts (Fig. 2B, lanes 9 to 13). High telomerase activity was associated with TCAB1 immunoprecipitates, and antibodies to TCAB1 quantitatively depleted telomerase activity from cell extracts (Fig. 2B, lanes 1 to 8, and fig. S4). In contrast, antibodies to NAF1 pulled down only a small percentage of telomerase activity. Assessing the TCAB1 immunoprecipitates for telomerase components revealed that TCAB1 interacts with endogenous dyskerin, TERT, and TERC (Fig. 2B, lanes 14 to 16). IP of TCAB1 effectively depleted cell extracts of TERC by use of Northern blot (Fig. 2B, lanes 9 to 13, and figs. S4 and S5). We conclude that TCAB1, like dyskerin, associates stably with a vast majority of active telomerase and TERC and therefore is a component of a human telomerase holoenzyme.

Using immunofluorescence (IF), we found that stably overexpressed hemagglutinin (HA)–tagged TCAB1 (HA-TCAB1) was distributed weakly throughout the nucleoplasm but was strongly enriched within nuclear foci resembling Cajal bodies, sites of RNP processing shown to contain dyskerin and TERC (*16*–*18*). IF showed that the HA-TCAB1 foci overlapped with p80-coilin and were therefore Cajal bodies (Fig. 3A). Endogenous TCAB1 was also highly enriched in Cajal bodies, with smaller amounts distributed in the nucleoplasm (Fig. 3B). Although dyskerin accumulates in both Cajal bodies and nucleoli, the Cajal body–restricted localization of TCAB1 suggested that TCAB1 may function specifically with telomerase and with other noncoding RNAs found in Cajal bodies.

Immunoprecipitates of Flag-TCAB1 (Fig. 3C) and endogenous TCAB1 (Fig. 3D) were assayed for scaRNAs and representatives of other classes of nuclear noncoding RNAs by Northern blot. Both overexpressed TCAB1 and endogenous TCAB1 specifically bound H/ACA scaRNAs but associated with neither snoRNAs nor splicing RNAs. In contrast, Flag-dyskerin specifically bound both H/ACA scaRNAs and

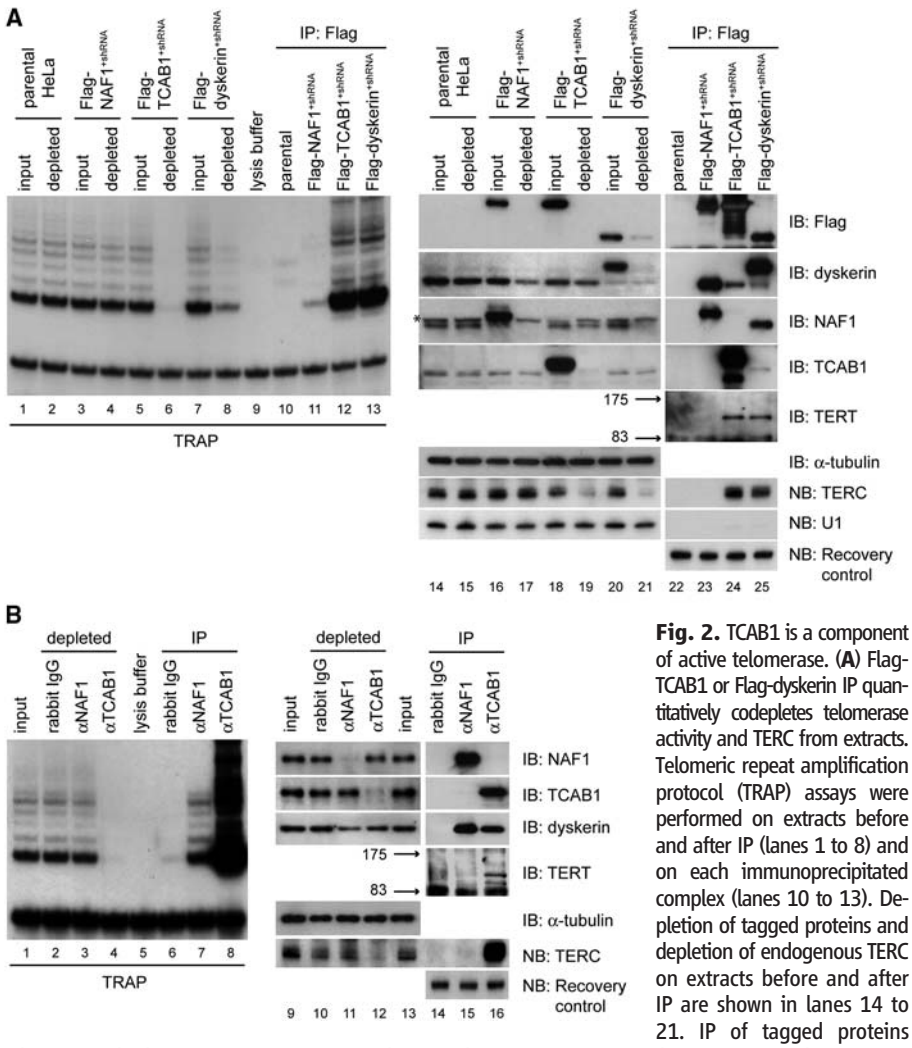

Fig. 2. TCAB1 is a component of active telomerase. (**A**) Flag-TCAB1 or Flag-dyskerin IP quantitatively codepletes telomerase activity and TERC from extracts. Telomeric repeat amplification protocol (TRAP) assays were performed on extracts before and after IP (lanes 1 to 8) and on each immunoprecipitated complex (lanes 10 to 13). Depletion of tagged proteins and depletion of endogenous TERC on extracts before and after IP are shown in lanes 14 to 21. IP of tagged proteins and associated telomerase components are shown in lanes 22 to 25. U1-splicing RNA was the negative control. (**B**) IP of endogenous TCAB1 codepletes telomerase activity and TERC. TRAP assays were performed on extracts before and after each IP (lanes 1 to 4) and on the IP (lanes 6 to 8). Depletion of endogenous NAF1 or endogenous TCAB1 and depletion of TERC are shown in lanes 9 to 13. Association of NAF1 and TCAB1 with telomerase components is shown in lanes 14 to 16. Recovery control was exogenous RNA spiked into samples after IP to control for differential RNA recovery.

H/ACA snoRNAs, whereas NAF1 did not associate stably with any noncoding RNAs studied. For each H/ACA scaRNA tested, a substantial proportion was depleted from the extract by IP of TCAB1 (Fig. 3, C, lanes 5 to 6, and D, lanes 1 to 5). Thus, TCAB1 specifically binds scaRNAs, which share a Cajal body (CAB) box sequence that controls Cajal body localization, and provides a potential mechanism to explain how scaRNAs, including TERC, are retained in Cajal bodies.

TCAB1 depletion by using retroviral-encoded shRNAs reduced neither telomerase activity nor TERC levels, in contrast to dyskerin depletion, which markedly diminished TERC and telomerase activity (Fig. 4A). Thus, TCAB1 may be required in vivo for a step after the assembly of a catalytically competent telomerase complex. To determine the role of TCAB1 in Cajal body localization of telomerase, TERC localization was measured by RNA fluorescence in situ hybridization (FISH) in TCAB1-depleted HeLa cells. FISH revealed that TCAB1 knockdown substantially reduced the percentage of cells in which TERC was found in Cajal bodies (Fig. 4, B and C) without affecting overall TERC RNA levels (Fig. 4A). Cajal bodies have been directly implicated in the delivery of TERC to telomeres during *S* phase (*19*–*21*). Therefore, we also examined the effect of TCAB1 knockdown on the localization of TERC to telomeres, using FISH for TERC and IF for telomere repeat binding factor 2 (TRF2). Depletion of TCAB1 substantially reduced the presence of TERC at telomeres during *S* phase (Fig. 4, B and C). Thus, TCAB1 is required for TERC localization in Cajal bodies and for delivery of TERC to telomeres during *S* phase.

To determine whether TCAB1 is required for telomere addition by telomerase, we first induced

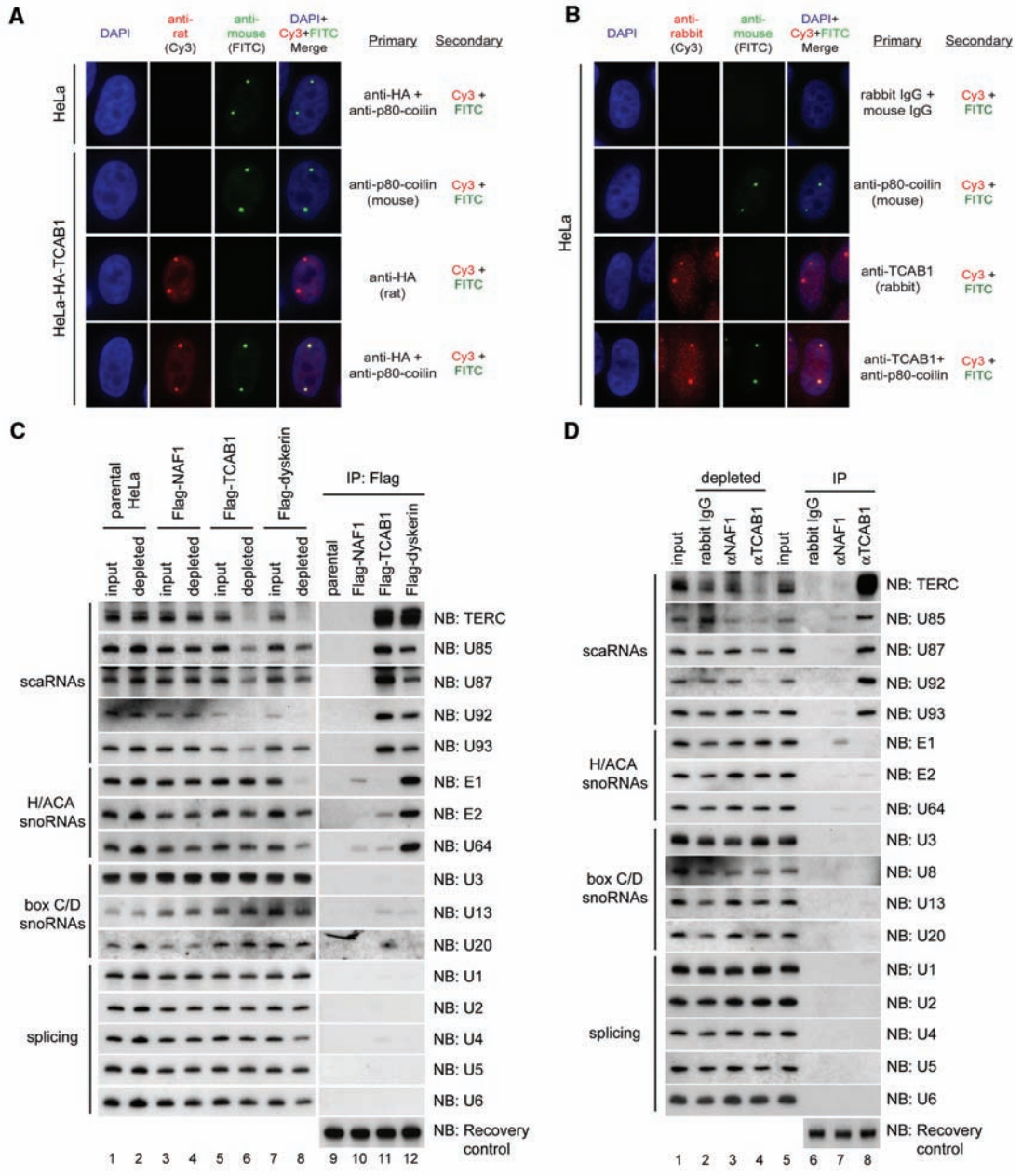

Fig. 3. TCAB1 is enriched in Cajal bodies and associates specifically with scaRNAs. (**A**) HA-TCAB1 colocalizes with the Cajal body marker p80-coilin. IF using antibodies to HA (rat) and p80-coilin (mouse) on fixed HeLa cells stably overexpressing HA-TCAB1 is shown. (**B**) Colocalization of endogenous TCAB1 with p80-coilin. IF using antibodies to TCAB1 (rabbit) and p80-coilin (mouse) on fixed HeLa cells. (**C**) Flag-TCAB1 associates specifically with scaRNAs by IP–Northern blot. Cell extract from parental HeLa cells, Flag-NAF1^{+shRNA} cells, Flag-TCAB1^{+shRNA} cells, or Flag-dyskerin^{+shRNA} cells was incubated with resin coated with antibodies to Flag. RNA was isolated from extracts before (input) and after (depleted) antibody treatment. Two micrograms of total RNA was fractionated by urea-PAGE (lanes 1 to 8), representing 2% of the input. RNAs from IPs are shown in lanes 9 to 12. (**D**) Endogenous TCAB1 associates specifically with scaRNAs. Antibodies to NAF1 or TCAB1, or the immunoglobulin G control, were used in assays at the same scale as in (C). RNAs from input and depleted extracts are shown in lanes 1 to 5. RNAs from IPs are shown in lanes 6 to 8. Recovery control was exogenous RNA spiked into samples after IP to control for differential RNA recovery.

telomere elongation through TERC overexpression in HTC75 fibrosarcoma cells. Overexpression of wild-type TERC lengthened telomeres with cell passage, but telomere lengthening was inhibited in cells overexpressing a CAB box–mutant TERC that fails to accumulate in Cajal bodies, as previously shown (*19*). Depletion of TCAB1 in cells overexpressing wild-type TERC substantially inhibited telomere elongation, mimicking the effect of the CAB box mutation (Fig. 4D and fig. S6). To determine whether TCAB1 is required for telomere synthesis by endogenous telomerase, we assayed telomere lengths with serial passage in HTC75 cells transduced with TCAB1 shRNAs or with the empty vector. Both shRNAs targeting TCAB1 led to progressive telomere shortening as compared with that of the empty vector control (Fig. 4E and fig. S7), indicating that TCAB1 is required for telomere synthesis in human cancer cells.

Our data identify TCAB1 as a Cajal body–enriched protein that associates with TERC and other scaRNAs and explains how TERC, and perhaps other scaRNAs, localize in Cajal bodies. TCAB1 functions as a telomerase holoenzyme component in the telomere synthesis pathway at a step after the assembly of a minimal telomerase complex containing TERT, TERC, and dyskerin. NAF1 and the ATPases pontin and reptin are required for assembly of the catalytically competent complex (*14*, *15*). In contrast, TCAB1 stably associates with active telomerase enzyme and directs it through Cajal bodies to telomeres. In this manner, TCAB1 may act as a Cajal body–targeting or –retention factor, may facilitate additional assembly steps of the enzyme in Cajal bodies, and/or may facilitate translocation of telomerase to telomeres (Fig. 4F). The interaction of telomerase with telomeres and the activity of the telomerase holoenzyme may be enhanced by the telomere-binding proteins TPP1 and protection of telomeres 1 (POT1) (*22*, *23*), as well as other factors that remain to be discovered.

References and Notes

1. K. Collins, *Nat. Rev. Mol. Cell Biol.* **7**, 484 (2006).
2. U. T. Meier, *Chromosoma* **114**, 1 (2005).
3. A. G. Matera, R. M. Terns, M. P. Terns, *Nat. Rev. Mol. Cell Biol.* **8**, 209 (2007).
4. J. R. Mitchell, E. Wood, K. Collins, *Nature* **402**, 551 (1999).

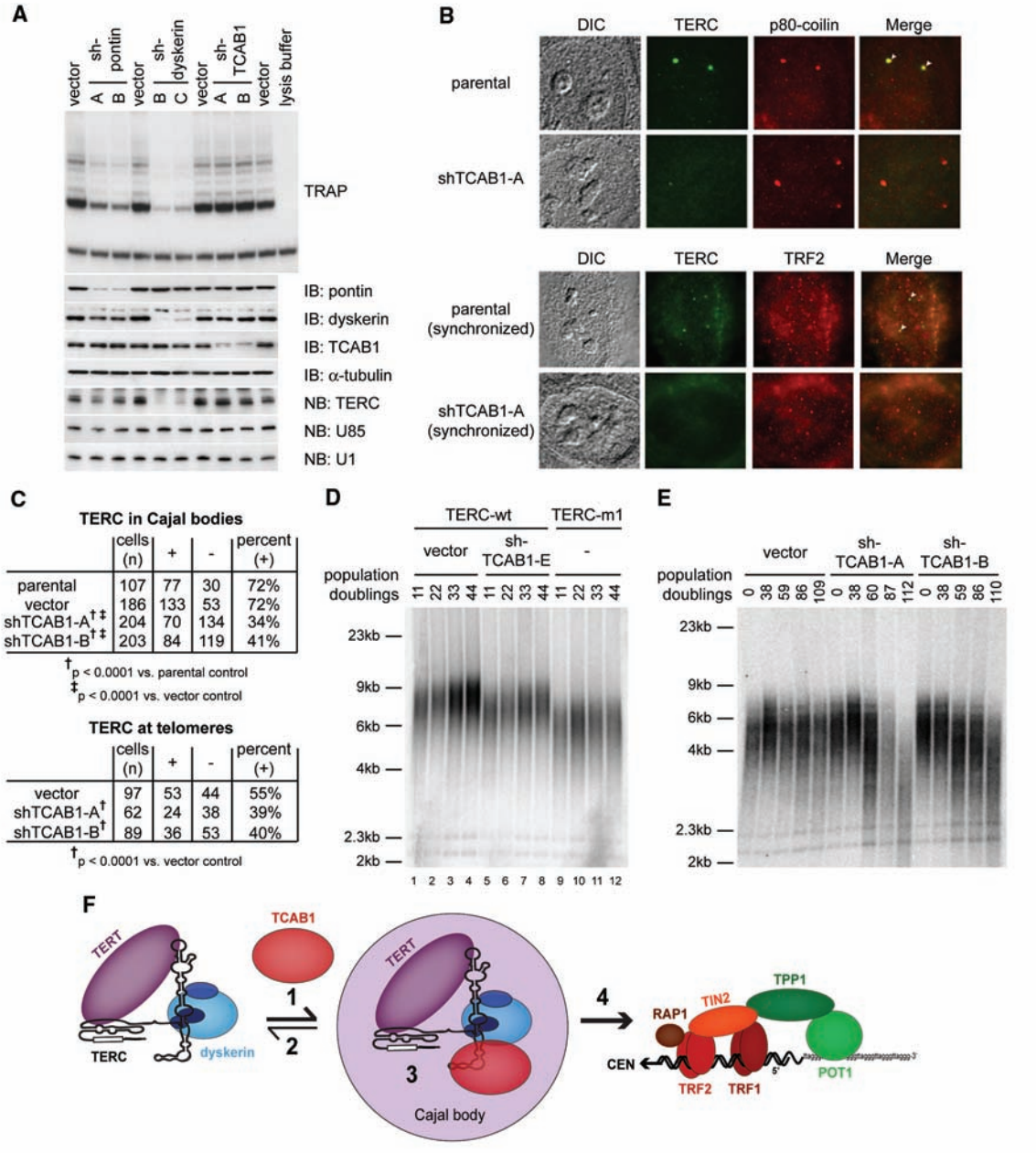

TERC in Cajal bodies	cells (n)	+	-	percent (+)
parental	107	77	30	72%
vector	186	133	53	72%
shTCAB1-A†‡	204	70	134	34%
shTCAB1-B†‡	203	84	119	41%

†p < 0.0001 vs. parental control
‡p < 0.0001 vs. vector control

TERC at telomeres	cells (n)	+	-	percent (+)
vector	97	53	44	55%
shTCAB1-A†	62	24	38	39%
shTCAB1-B†	89	36	53	40%

†p < 0.0001 vs. vector control

Fig. 4. TCAB1 is essential for TERC localization to Cajal bodies and for telomere synthesis by telomerase. (**A**) HeLa cells were transduced with retroviruses expressing independent shRNA sequences targeting the indicated proteins or with empty vector control. Telomerase activity was measured by TRAP assay. (**B**) TERC colocalization with p80-coilin was determined by RNA FISH for TERC (green) and IF for p80-coilin (red) (top). Cells synchronized in *S* phase were assayed for TERC by RNA FISH (green) and for telomeres with antibody to TRF2 (red) to assess trafficking of TERC to telomeres (bottom). (**C**) Quantification of data in (B). (Top) Cells in which TERC colocalized with p80-coilin (+) versus cells in which TERC was not detected in Cajal bodies (–) ($P < 0.0001$, Fisher's exact test). (Bottom) Cells in which TERC colocalized with telomeres (+) versus cells in which TERC was not detected at telomeres (–) ($P < 0.0001$, Fisher's exact test). (**D**) Telomere lengths were measured using terminal restriction fragment (TRF) Southern blot in HTC75 cells overexpressing wild-type TERC (lanes 1 to 8) or mutant TERC-m1 (lanes 9 to 12). Cells overexpressing wild-type TERC were transduced with shRNA retroviruses targeting TCAB1 or with the empty vector. (**E**) Effect of TCAB1 depletion on endogenous telomerase was assessed by TRF Southern blot in parental HTC75 cells that were transduced with the empty vector or retroviruses expressing independent TCAB1 shRNAs. Cells were counted at each passage and population doublings are indicated. (**F**) Model for TCAB1 function in the telomere synthesis pathway.

5. Y. Mochizuki, J. He, S. Kulkarni, M. Bessler, P. J. Mason, *Proc. Natl. Acad. Sci. U.S.A.* **101**, 10756 (2004).
6. S. B. Cohen *et al.*, *Science* **315**, 1850 (2007).
7. M. Kirwan, I. Dokal, *Clin. Genet.* **73**, 103 (2008).
8. D. Fu, K. Collins, *Mol. Cell* **28**, 773 (2007).
9. V. Pogacic, F. Dragon, W. Filipowicz, *Mol. Cell. Biol.* **20**, 9028 (2000).
10. F. Dragon, V. Pogacic, W. Filipowicz, *Mol. Cell. Biol.* **20**, 3037 (2000).
11. B. E. Snow *et al.*, *Curr. Biol.* **13**, 698 (2003).
12. P. Reichenbach *et al.*, *Curr. Biol.* **13**, 568 (2003).
13. G. Schnapp, H. P. Rodi, W. J. Rettig, A. Schnapp, K. Damm, *Nucleic Acids Res.* **26**, 3311 (1998).
14. A. S. Venteicher, Z. Meng, P. J. Mason, T. D. Veenstra, S. E. Artandi, *Cell* **132**, 945 (2008).
15. C. Hoareau-Aveilla, M. Bonoli, M. Caizergues-Ferrer, Y. Henry, *RNA* **12**, 832 (2006).
16. U. T. Meier, G. Blobel, *J. Cell Biol.* **127**, 1505 (1994).
17. B. E. Jady, E. Bertrand, T. Kiss, *J. Cell Biol.* **164**, 647 (2004).
18. Y. Zhu, R. L. Tomlinson, A. A. Lukowiak, R. M. Terns, M. P. Terns, *Mol. Biol. Cell* **15**, 81 (2004).
19. G. Cristofari *et al.*, *Mol. Cell* **27**, 882 (2007).
20. B. E. Jady, P. Richard, E. Bertrand, T. Kiss, *Mol. Biol. Cell* **17**, 944 (2006).
21. R. L. Tomlinson, T. D. Ziegler, T. Supakorndej, R. M. Terns, M. P. Terns, *Mol. Biol. Cell* **17**, 955 (2006).
22. F. Wang *et al.*, *Nature* **445**, 506 (2007).
23. H. Xin *et al.*, *Nature* **445**, 559 (2007).

24. This work was supported by Medical Scientist Training Program grant GM07365 (A.S.V.) and NCI grant CA104676 (M.P.T. and R.M.T.), with a Supplement to Promote Diversity in Health-Related Research (E.B.A.). This project has been funded in part with federal funds from the NCI under contract NO1-CO-12400 (T.D.V.). This work was supported by NCI grants CA111691 and CA125453 (S.E.A.) and by Leukemia and Lymphoma Society Specialized Centers of Research grant 7007-09 (S.E.A.).

Supporting Online Material

www.sciencemag.org/cgi/content/full/323/5914/644/DC1
Materials and Methods
Figs. S1 to S7
References

2 September 2008; accepted 3 December 2008
10.1126/science.1165357

PAN1: A Receptor-Like Protein That Promotes Polarization of an Asymmetric Cell Division in Maize

Heather N. Cartwright,*† John A. Humphries,* Laurie G. Smith‡

Polarization of cell division is essential for eukaryotic development, but little is known about how this is accomplished in plants. The formation of stomatal complexes in maize involves the polarization of asymmetric subsidiary mother cell (SMC) divisions toward the adjacent guard mother cell (GMC), apparently under the influence of a GMC-derived signal. We found that the maize *pan1* gene promotes the premitotic polarization of SMCs and encodes a leucine-rich repeat receptor-like protein that becomes localized in SMCs at sites of GMC contact. PAN1 has an inactive kinase domain but is required for the accumulation of a membrane-associated phosphoprotein, suggesting a function for PAN1 in signal transduction. Our findings implicate PAN1 in the transmission of an extrinsic signal that polarizes asymmetric SMC divisions toward GMCs.

In plants, as in other eukaryotes, asymmetric cell divisions are associated with developmental patterning events, formation of new cell lineages and cell types, and maintenance of stem cell populations (*1*, *2*). In all of these processes, developmental asymmetry is closely tied to division polarity, which is thought to be oriented by either intrinsic or extrinsic cues. However, very little is known about such cues in plants or how cells perceive and respond to them.

Extrinsic cues appear to orient asymmetric cell divisions in maize during the development of epidermal stomatal complexes, each consisting of a pair of guard cells flanked by a pair of subsidiary cells that function in guard cell regulation (Fig. 1A). Stomatal complexes in grasses such as maize develop through an invariant sequence of coordinated asymmetric cell divisions (fig. S1) (*3*). After an asymmetric division that forms a guard mother cell (GMC), its lateral neighbors, called subsidiary mother cells (SMCs), polarize toward the GMC, positioning their nuclei and forming dense patches of cortical F-actin at the GMC contact site (Fig. 1E) (*4*–*6*). SMCs subsequently divide asymmetrically to form subsidiary cells flanking the GMC (Fig. 1E), and the GMC then divides longitudinally to form a guard cell pair. Analysis of stomatal complex formation in grasses led almost 50 years ago to the proposal that SMC divisions are polarized by a signal emanating from GMCs (*3*), but the mechanism of interaction between the GMC and SMC has remained unknown.

A recessive mutation in maize, *pan1*, causes defects in the premitotic polarization of SMCs and the formation of abnormal subsidiary cells (*5*). An ethylmethane sulfonate (EMS)–induced, non-allelic *pan2* mutation caused a similar phenotype (Fig. 1, B to D). In wild-type (WT) leaves, 92% of 317 SMCs analyzed in files of developing stomata containing at least one divided SMC had polarized nuclei, and 80% of those had well-focused actin patches (Fig. 1, E and H). In contrast, only 60% of 325 *pan1* SMCs and 62% of 392 *pan2* SMCs had polarized nuclei, and most of these SMCs either lacked an actin patch or had a delocalized patch (Fig. 1, F to H). The majority of mutant SMCs with unpolarized nuclei lacked actin patches, but many of them had delocalized or normal actin patches (Fig. 1, F to H). Thus, *pan* mutant SMCs exhibit defects in both nuclear polarization and actin-patch formation, but these defects are not closely correlated, suggesting that they are largely independent effects of the *pan* mutations on SMC polarity.

We used a mutant allele containing a *Mutator1 (Mu1)* transposon insertion to clone the *pan1* gene (*7*). In this allele, *Mu1* is inserted into the codon encoding amino acid 135 of a 662–amino acid leucine-rich repeat receptor-like kinase (LRR-RLK) belonging to the LRRIII subfamily (*8*). This protein consists of a predicted extracellular domain containing five LRR motifs, a transmembrane domain, and an intracellular serine/threonine kinase domain. In plants carrying an EMS-induced *pan1* mutation (*pan1-EMS*), a premature stop codon in the first exon truncates this protein at amino acid 47, confirming the identity of this gene as *pan1*. Other LRR-RLKs function as receptors or co-receptors in diverse aspects of plant development and defense (*9*, *10*). Extracellular LRR motifs are implicated in ligand binding; intracellular kinase domains are implicated in signal transduction via autophosphorylation and phosphorylation of target proteins.

To further investigate PAN1 function, we raised a polyclonal antibody that recognized a protein of around 75 kD by immunoblotting, which is close to the predicted molecular mass of PAN1 (68.4 kD). This protein was depleted in extracts of both *pan1-Mu* and *pan1-EMS* mutants, confirming its iden-

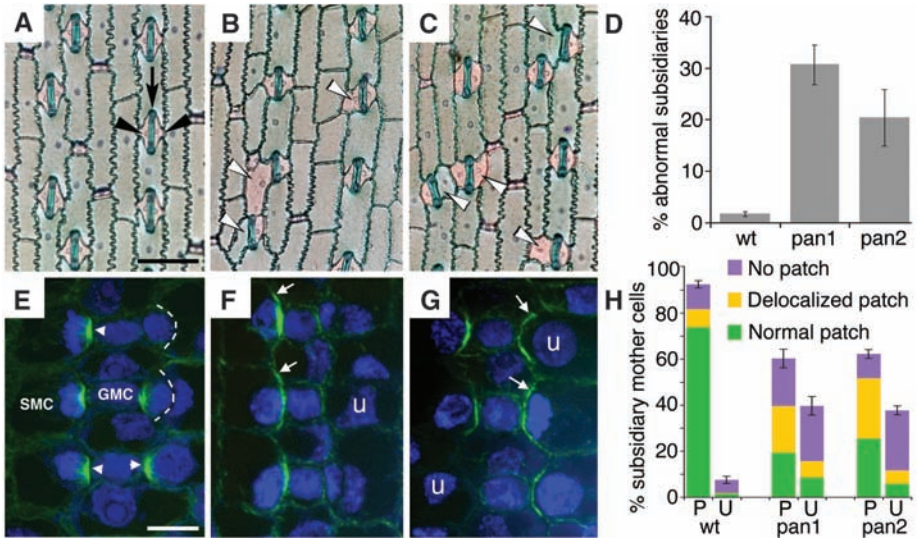

Fig. 1. Stomatal complex formation in WT and *pan* mutant maize leaves. (**A** to **C**) Toluidine blue O–stained epidermal peels from adult leaves of WT (A), *pan1* (B), and *pan2* mutant (C). Guard cells stain blue [black arrow in (A)]; subsidiary cells stain pink [black arrowheads in (A)]. White arrowheads in (B) and (C) indicate abnormal subsidiary cells in *pan* mutant leaves. Scale bar, 100 μm. (**D**) Quantitative analysis of abnormal subsidiary cells in mature leaf tissue. Error bars represent SEM (n = 5 plants per genotype; >600 subsidiary cells were analyzed for each genotype). (**E** to **G**) F-actin (green) in developing stomata of WT (E), *pan1* (F), and *pan2* (G) with propidium iodide-stained nuclei in blue (single confocal planes). In (E), arrowheads on GMCs point to normal actin patches in adjacent SMCs, and dashed lines indicate division planes in two divided SMCs. In (F) and (G), arrows indicate delocalized actin patches, and u indicates unpolarized nuclei. Scale bar, 10 μm. (**H**) Quantitative analysis of SMC polarity defects (P, polarized nucleus; U, unpolarized nucleus). Error bars represent SEM [n = 5 plants per genotype, the same plants analyzed for the graph in (D); >300 SMCs were analyzed for each genotype].

Section of Cell and Developmental Biology, University of California San Diego, 9500 Gilman Drive, San Diego, CA 92093–0116, USA.

*These authors contributed equally to this work.
†Present address: Stowers Institute for Medical Research, 1000 East 50th Street, Kansas City, MO 64110, USA.
‡To whom correspondence should be addressed. E-mail: lgsmith@ucsd.edu

tity as PAN1 (Fig. 2). This protein was found in the microsomal fraction of extracts from the division zone of WT maize leaves (Fig. 2), consistent with the expected membrane localization for PAN1. Immunoblot analysis indicated that in developing leaves, PAN1 was most abundant in the division zone, but the protein was also found in dividing regions of other tissues that lack stomata (fig. S2), suggesting that PAN1 may function in other processes besides stomatal development. However, *pan1* mutants do not have obvious developmental defects affecting other tissues or cell types.

In WT leaves, whole mount immunofluorescence revealed PAN1 only in SMCs and newly formed subsidiary cells at sites of contact with GMCs (Fig. 3A). These "PAN1 patches" were absent in *pan1* mutants (Fig. 3B), confirming the specificity of immunolabeling for PAN1. Specific labeling with the PAN1-specific antibody to (anti-PAN1) was observed only at the cell periphery, consistent with localization to the plasma membrane. Alternatively, although the cortical endoplasmic reticulum (ER) itself was not specifically enriched in SMCs at GMC contact sites (fig. S3), some or all of the PAN1 protein may be ER-localized. PAN1 protein was present in *pan2* mutants at reduced levels and remained associated with the microsomal fraction (Fig. 2), but no specific PAN1 staining was observed in *pan2* mutants (Fig. 3C).

Double labeling of PAN1 and actin was employed to investigate the timing of PAN1 patch formation relative to nuclear polarization and actin-patch formation in WT cells. 92% of 168 SMCs with fully polarized nuclei had both PAN1 and actin patches (Fig. 3, D to I). Among 119 SMCs with unpolarized or partially polarized nuclei (presumably in the process of becoming polarized), 27% had neither PAN1 nor actin patches, 33% had only PAN1 patches, and 40% had both PAN1 and actin patches (Fig. 3, D to I). None of these SMCs had actin patches only. GMC length provides a measure of developmental age, increasing from inception, when flanking SMCs have unpolarized nuclei, through nuclear polarization and SMC division (Fig. 3M). The average lengths of adjacent GMCs were lowest for the SMC class lacking both PAN1 and actin patches, intermediate for the PAN1$^+$ actin$^-$ class, and highest for the PAN1$^+$ actin$^+$ class (Fig. 3N). Thus, PAN1 and actin patches both appeared after GMC formation and before nuclear polarization, but PAN1 patches were detectable before actin patches. The presence of PAN1 and actin patches exclusively at sites of contact with GMCs supports the conclusion that these patches are induced by GMCs rather than by intrinsic cues. Further supporting this conclusion, in unusual cases where a single SMC flanks two GMCs, PAN1 and actin patches were observed adjacent to both GMCs (n = 14) (Fig. 3, J to L).

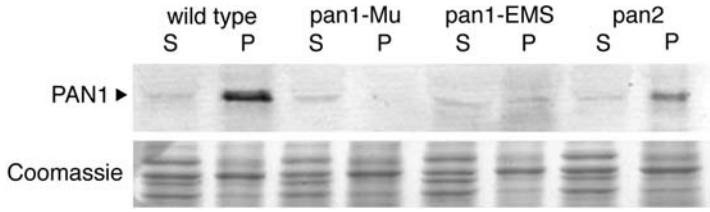

Fig. 2. Immunoblot of proteins extracted from the division zone of leaves of the indicated genotypes probed with anti-PAN1 antibody. Extracts were separated into 110,000*g* supernatants (S) and pellets representing the microsomal fraction (P). Coomassie staining of the equivalent region of a duplicate gel demonstrates equal loading.

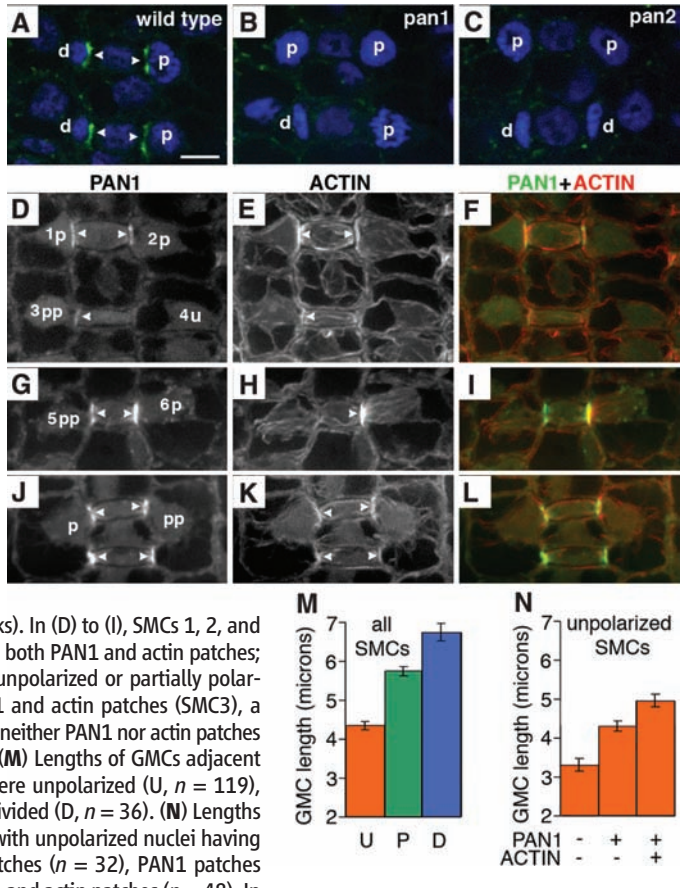

Fig. 3. PAN1 and actin localization in developing stomata. White arrowheads on GMCs indicate PAN1 and actin patches in adjacent SMCs. SMC nuclei are identified as unpolarized (u), partially polarized (pp), polarized (p), or divided (d) and are numbered in (D) and (G) for reference. (**A** to **C**) PAN1 staining in green and propidium iodide-stained nuclei in blue (single confocal planes). (**D** to **L**) Double staining of PAN1 [monochrome in (D), (G), and (J); green in (F), (I), and (L)] and actin [monochrome in (E), (H), and (K); red in (F), (I), and (L)] in WT leaves (Z projections of confocal stacks). In (D) to (I), SMCs 1, 2, and 6 have polarized nuclei and both PAN1 and actin patches; the remaining SMCs have unpolarized or partially polarized nuclei with both PAN1 and actin patches (SMC3), a PAN1 patch only (SMC5), or neither PAN1 nor actin patches (SMC4). Scale bar, 10 μm. (**M**) Lengths of GMCs adjacent to SMCs with nuclei that were unpolarized (U, n = 119), polarized (P, n = 168), or divided (D, n = 36). (**N**) Lengths of GMCs adjacent to SMCs with unpolarized nuclei having neither PAN1 nor actin patches (n = 32), PAN1 patches only (n = 39), or both PAN1 and actin patches (n = 48). In M and N, error bars indicate SEM; all differences shown are significant ($P < 0.01$) by Student's t test.

Although the PAN1 kinase domain is well conserved with enzymatically active serine/threonine kinases, it lacks several amino acid residues conserved in active kinases, including a lysine residue in subdomain II that is critical for kinase activity (*11*) (fig. S4), suggesting that it is not an active kinase. Consistent with this prediction, the kinase domain of PAN1 did not detectably phosphorylate itself or the artificial substrate myelin basic protein (MBP) in vitro under conditions where the kinase domain of the LRR-RLK BRI1 phosphorylated both substrates robustly (Fig. 4A). Some LRR-containing transmembrane proteins lack intracellular kinase domains altogether and are thought to function in signal transduction processes by associating with an active kinase (*9*). To investigate whether PAN1 might function similarly, microsomal fractions of extracts from WT, *pan1*, and *pan2* mutants were probed on immunoblots with anti-phosphoamino acid antibodies. No differences between wild type and mutant were observed with anti-phosphoserine or anti-phosphotyrosine, but a 52-kD protein (smaller than PAN1) identified by anti-phosphothreonine was almost undetectable in both *pan1-Mu* and *pan1-EMS* mutants (Fig. 4B). This protein was depleted in *pan2* mutants and in WT extracts treated with lambda phosphatase (Fig. 4B and fig. S5). Thus, it appears that phosphorylation of a 52-kD membrane protein of unknown identity depends on PAN1, suggesting a role for PAN1 in signal transduction. Alternatively, the 52-kD phosphoprotein may depend on PAN1 and PAN2 for its synthesis or stability rather than its phosphorylation. As demonstrated or proposed for other LRR-RLKs with conserved but enzy-

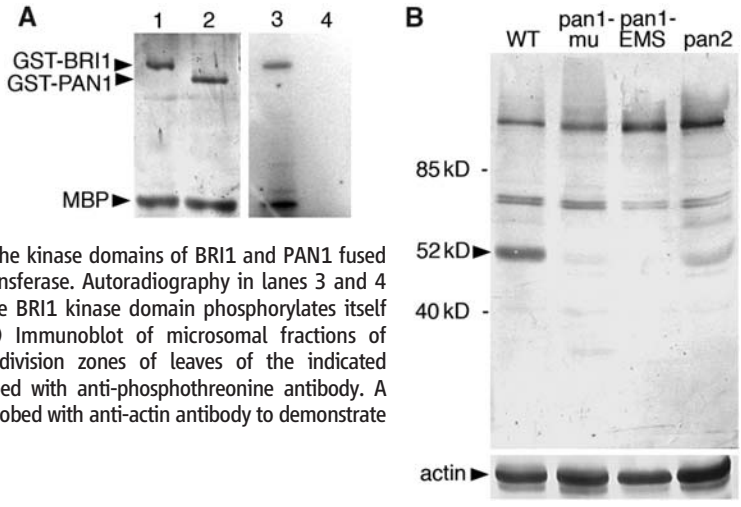

Fig. 4. Analysis of PAN1-dependent protein phosphorylation. (**A**) In vitro kinase assays. Lanes 1 and 2 show Coomassie staining of the proteins used in each reaction: MBP and the kinase domains of BRI1 and PAN1 fused to glutathione *S*-transferase. Autoradiography in lanes 3 and 4 reveals that only the BRI1 kinase domain phosphorylates itself (*19*) and MBP. (**B**) Immunoblot of microsomal fractions of extracts from the division zones of leaves of the indicated genotypes was probed with anti-phosphothreonine antibody. A duplicate blot was probed with anti-actin antibody to demonstrate equal loading.

matically inactive kinase domains (*12*, *13*), the PAN1 kinase domain may mediate interaction(s) with other proteins that function in concert with or downstream of PAN1.

Our results implicate PAN1 as a receptor or co-receptor of GMC-derived signals that promote the polarization of SMCs in preparation for their asymmetric division. Because SMC polarization is not completely abolished in *pan1* null mutants, it is clear that PAN1 is not solely responsible for the reception of polarizing cues from GMCs. Thus, parallel or cooperating pathways may work together with the PAN1 pathway to promote SMC polarization. The reduction in PAN1 protein levels and lack of detectable PAN1 patches in *pan2* mutants suggest that PAN2 functions in the PAN1 pathway, but the identity of PAN2 and its functional relationship to PAN1 remains to be determined. If PAN1 relays polarity cues from GMCs, why is it already localized at sites of GMC contact at its earliest appearance? PAN1 may be initially distributed uniformly at the SMC surface but detectable by immunolocalization only after becoming locally concentrated as a result of binding to a GMC-derived ligand. Alternatively, PAN1 may be recruited directly to GMC contact sites in response to an upstream sensor of GMC position, functioning there as a secondary sensor. The localization of PAN1 at a specific site on the cell surface, its enzymatically inactive kinase domain, and its cellular function differentiate it from two other receptor-like proteins previously shown to play a role in polarized cell division or growth in plants. The *Arabidopsis* TMM protein, which contains LRR and transmembrane domains but lacks a kinase domain, functions in a well-characterized signal transduction pathway that controls the entry of epidermal cells into the stomatal lineage and the orientation of asymmetric, stomate-forming divisions (*14*). However TMM does not promote the polarization of these divisions, nor is it asymmetrically localized (*15*). Tomato LRR-RLK proteins LePRK1 and LePRK2 promote the polarized growth of pollen tubes (*16*). They have active kinase domains and are localized uniformly at the pollen tube surface but appear to interact with rho of plants (ROP) guanine nucleotide exchange factors only at the tube tip to stimulate localized actin assembly and polarized growth (*17*, *18*).

References and Notes

1. B. Scheres, P. N. Benfey, *Annu. Rev. Plant Physiol. Plant Mol. Biol.* **50**, 505 (1999).
2. C. A. ten Hove, R. Heidstra, *Curr. Opin. Plant Biol.* **11**, 34 (2008).
3. G. L. Stebbins, S. S. Shah, *Dev. Biol.* **2**, 477 (1960).
4. S. Cho, S. M. Wick, *Protoplasma* **157**, 154 (1990).
5. K. Gallagher, L. G. Smith, *Curr. Biol.* **10**, 1229 (2000).
6. E. Panteris, P. Apostolakos, B. Galatis, *Cell Motil. Cytoskeleton* **63**, 696 (2006).
7. Materials and methods are available as supporting material on *Science* Online.
8. S. H. Shiu, A. B. Bleecker, *Proc. Natl. Acad. Sci. U.S.A.* **98**, 10763 (2001).
9. K. U. Torii, *Int. Rev. Cytol.* **234**, 1 (2004).
10. A. Dievart, S. E. Clark, *Development* **131**, 251 (2004).
11. S. K. Hanks, T. Hunter, *FASEB J.* **9**, 576 (1995).
12. B. Llompart *et al.*, *J. Biol. Chem.* **278**, 48105 (2003).
13. D. Chevalier *et al.*, *Proc. Natl. Acad. Sci. U.S.A.* **102**, 9074 (2005).
14. D. C. Bergmann, F. D. Sack, *Annu. Rev. Plant Biol.* **58**, 163 (2007).
15. J. A. Nadeau, F. D. Sack, *Science* **296**, 1697 (2002).
16. J. Muschietti, Y. Eyal, S. McCormick, *Plant Cell* **10**, 319 (1998).
17. P. Kaothien *et al.*, *Plant J.* **42**, 492 (2005).
18. Y. Zhang, S. McCormick, *Proc. Natl. Acad. Sci. U.S.A.* **104**, 18830 (2007).
19. D. M. Friedrichsen, C. A. Joazeiro, J. Li, T. Hunter, J. Chory, *Plant Physiol.* **123**, 1247 (2000).

20. We thank A. Wright and F. Delgado for help with experiments and J. Bolado, J. Chory, and R. Boston for reagents. This work was supported by NSF grant IOB-0544226. *pan1* gene and PAN1 protein sequences are available at GenBank (accession number FJ231525).

Supporting Online Material

www.sciencemag.org/cgi/content/full/323/5914/649/DC1
Materials and Methods
Figs. S1 to S5
References

11 June 2008; accepted 21 November 2008
10.1126/science.1161686

Calcineurin/NFAT Signaling Is Required for Neuregulin-Regulated Schwann Cell Differentiation

Shih-Chu Kao,[1,2] Hai Wu,[1,2] Jianming Xie,[1] Ching-Pin Chang,[1,2] Jeffrey A. Ranish,[3] Isabella A. Graef,[2]* Gerald R. Crabtree[1,2]*

Schwann cells develop from multipotent neural crest cells and form myelin sheaths around axons that allow rapid transmission of action potentials. Neuregulin signaling through the ErbB receptor regulates Schwann cell development; however, the downstream pathways are not fully defined. We find that mice lacking *calcineurin B1* in the neural crest have defects in Schwann cell differentiation and myelination. Neuregulin addition to Schwann cell precursors initiates an increase in cytoplasmic Ca^{2+}, which activates calcineurin and the downstream transcription factors NFATc3 and c4. Purification of NFAT protein complexes shows that Sox10 is an NFAT nuclear partner and synergizes with NFATc4 to activate *Krox20*, which regulates genes necessary for myelination. Our studies demonstrate that calcineurin and NFAT are essential for neuregulin and ErbB signaling, neural crest diversification, and differentiation of Schwann cells.

Rapid transmission of action potentials in the vertebrate nervous system is achieved by insulating axons with myelin sheaths, the membrane outgrowth from Schwann cells in the peripheral nervous system (PNS) and oligodendrocytes in the central nervous system (*1*). Defects in myelination occur in many human diseases; however, the mechanisms regulating myelin formation are still not fully understood. Neuregulin-1 (NRG1) and its receptor tyrosine kinase, ErbB2/3 are required for Schwann cell development (*2*–*7*). Genetic studies implicate Sox10, Oct6 (SCIP or Tst1), Ets, Brn1 and 2, Krox20 (Egr2) and Nab1 and 2 in PNS myelination (*8*–*12*). The expression of Sox10 is maintained throughout Schwann cell development,

whereas Oct6, Brn1/2, and Krox20 are induced later in immature and promyelinating Schwann cells after axonal contact (*13*–*16*). Krox20 is of particular interest because it coordinates the expression of several myelin structural proteins.

In many cell types, Ca^{2+} influx activates the phosphatase calcineurin, which dephosphorylates NFATc proteins, which in turn leads to their nuclear entry and assembly into NFAT transcription complexes (*17*–*20*). We observed that NFAT was active in migrating mouse neural crest cells at embryonic (E) day 9.0 (Fig. 1A) (*21*); therefore, we deleted *CnB1*, the essential regulatory subunit of calcineurin in neural crest, using *Wnt1*^{cre} (*22*, *23*) (Fig. 1B). By E11.5, CnB1 protein was almost undetectable in dorsal root ganglia (DRG) and sympathetic ganglia (SG) (fig. S1A). The loss of CnB1 expression in DRG, SG, and Schwann cells persisted until death (within 20 hours after birth) (Fig. 1C and fig. S1, B and C). However, *CnB1* was not deleted in axons of ventral roots derived from motor neurons where *Wnt1*^{cre} is inactive (Fig. 1C). *CnB1* was deleted in vitro in sensory neurons and Sox10-positive Schwann cell precursors (SCPs) (Fig. 1D and fig. S1D). NFATc3 and c4 were hyperphosphorylated, which indicated loss of calcineurin phosphatase activity (Fig. 1E). DRG architecture, cell proliferation, and cell death were not changed in the *CnB1* mutant embryos (fig. S2A), and peripheral nerve projections were comparable to those of controls (fig. S2B). However, myelination of mutant sciatic nerves was defective, and fewer axons were sorted into a 1:1 ratio with Schwann cells (Fig. 2, A and B, and fig. S3, A and B). Mutant nerves also had a higher *g* ratio (axon diameter to total myelinated fiber diameter) (fig. S3C). They expressed less of the promyelinating protein Krox20, the early myelin protein MAG, and major compacted myelin components such as MBP and P_0 (myelin basic protein and myelin protein zero, respectively) (Fig. 2, C and D). Furthermore, NFATc3 and c4 were hyperphosphorylated in mutant Schwann cells (Fig. 2C). These observations indicate that mice lacking *CnB1* have defective myelination.

Investigation of the Schwann cell lineage revealed that SCPs were found in both control and mutant peripheral nerves at E11.5 (fig. S4A). At E13.5, control and mutant DRG contained similar numbers of sensory neurons and SCPs (fig. S4B). Unlike *neuregulin* or *erbB* mutant mice (*2*, *5*), SCPs from *CnB1* mutant embryos showed no differences in proliferation or apoptosis in vitro in response to NRG1 stimulation (fig. S4, C and D). We observed comparable numbers of proliferating Schwann cells in control and mutant newborn sciatic nerves (fig. S5A).

Survival of SCPs has been shown to be dependent on trophic support from sensory neurons (*24*). To rule out the possibility that hypomyelination was due to dysfunction of mutant sensory neurons, we cocultured mutant SCPs with control sensory neurons under conditions that supported sensory neuron survival. Fewer MBP-positive Schwann cells were found in mutant SCP cocultures, although comparable numbers of sensory neurons were present in both control and mutant cocultures (fig. S5, B to D). ErbB2 and 3 expression and phosphorylation levels were normal in mutant SCPs, and sensory neurons expressed comparable amounts of pro-NRG1 and the cleaved form of NRG1 (NTF), which suggested that BACE1, an enzyme involved in NRG1 processing, functioned normally in mutant sensory neurons (fig. S5E).

To investigate cell autonomy of the myelination defects, we took advantage of selective deletion of *CnB1* in Schwann cells, but not in motor neurons of *CnB1*$^{\Delta/f}$*; Wnt1*^{cre} mice and found that axonal sorting was reduced in mutant ventral roots and phrenic nerves (Fig. 2, E and F, and fig. S6A). This was similar to the defect seen in dorsal roots from *CnB1*$^{\Delta/f}$*; Wnt1*^{cre} mutants, where *CnB1* is deleted in both sensory neurons and Schwann cells (fig. S6B). In a second approach, we examined *CnB1*$^{f/f}$*; Nestin*^{cre} mice, where *CnB1* is deleted in sensory neurons, but not in Schwann cells (fig. S7, A and B). *CnB1* deletion did not affect the numbers of MBP-positive Schwann cells or axonal sorting (fig. S7, C to F). These two lines of evidence indicate that the myelination defects in *CnB1* mutant mice are due to a Schwann cell–autonomous mechanism.

In our analysis of signaling pathways that activated calcineurin/NFAT in DRG cocultures, we found that NRG1 induced phospholipase C–γ (PLC-γ)–dependent Ca^{2+} influx in SCPs (Fig. 3A) and CnB1-dependent dephosphorylation of NFATc3 and c4 (Fig. 3B). NRG1 also stimulated Ca^{2+} influx in sensory neurons (fig. S8A). *CnB1* deletion had no effect on NRG1-induced phosphorylation of the ErbB3 receptor, which indicated that calcineurin functions downstream of ErbB (Fig. 3C). ErbB kinase inhibitors specifically blocked NRG1-stimulated NFATc3 and c4 dephosphorylation, whereas neither phosphatidylinositol 3-kinase nor mitogen-activated protein kinase kinase inhibitors had an inhibitory effect (fig. S8, B and C).

NRG1 not only induced changes in NFATc phosphorylation, but also activated NFAT-dependent transcription, measured with two NFAT reporters (*25*, *26*) (Fig. 3D). NRG1-stimulated reporter activity was not detected in mutant cocultures, which indicated that calcineurin functions downstream of ErbB and upstream of NFAT. The observation that Krox20 expression was reduced in *CnB1* mutant Schwann cells led us to examine the role of NFAT in *Krox20* regulation. We found that both the promoter and the myelin-specific enhancer (MSE, +35 kilobases) (*27*) required calcineurin for their activity (Fig. 3D). Three NFATc consensus sites were present in the MSE that bound NFAT complexes (fig. S9, A and B). Because Krox20 is expressed selectively in Schwann cells, but not in DRG neurons (*16*), these results provide a third line of evidence that calcineurin/NFAT functions in Schwann cells to directly promote myelination.

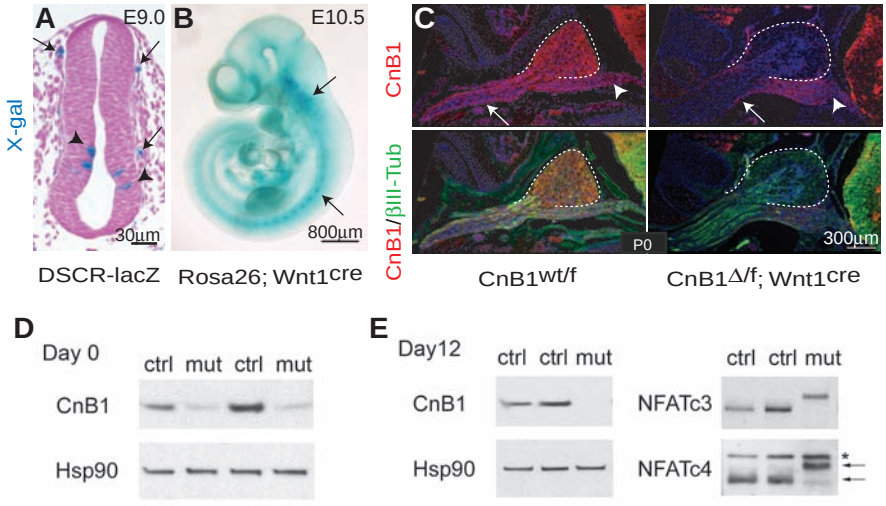

Fig. 1. *CnB1* is deleted in the PNS by *Wnt1*^{cre}. (**A**) X-gal staining of E9.0 neural tube from a NFAT-reporter mouse line harboring *LacZ* under control of the *DSCR1* enhancer region counterstained with nuclear fast red. Arrows, migrating neural crest cells; arrowheads, interneuron progenitors. (**B**) Whole-mount X-gal staining of E10.5 *Rosa26; Wnt1*^{cre} mouse embryo. Arrows, sensory ganglia. (**C**) Immunostaining of newborn DRG and peripheral nerves at thoracic limb region by using CnB1-specific antibody. Arrows, CnB1-positive motor axons of peripheral nerves; arrowheads, ventral roots. (**D** and **E**) Immunoblots of CnB1 and NFATc3 and c4 from E13.5 DRG cocultures at day 0 (D) and day 12 (E). Heat shock protein 90 (Hsp90) is a loading control. Arrows, NFATc4 proteins. *Cross-reactive protein.

[1]Howard Hughes Medical Institute, Stanford University, Stanford, CA 94305, USA. [2]Department of Pathology and Department of Developmental Biology, Stanford University, Stanford, CA 94305, USA. [3]Institute for Systems Biology, Seattle, WA 98103, USA.

*To whom correspondence should be addressed. E-mail: crabtree@stanford.edu or igraef@stanford.edu

The specificity of NFAT complexes on target genes arises from assembly of NFATc family members with nuclear partner proteins (*18*–*20*). To identify nuclear partners, we purified NFAT complexes from E11.5 mouse neural tubes (as sufficient quantities of SCPs were not available) using oligonucleotide affinity columns. Mass spectrometry analysis identified the B group of the Sox family proteins (Sox1, 2, 3, 14, and 21) (fig. S10, A and B). Because Sox10 has a similar binding sequence and is expressed throughout Schwann cell development (*10*), we tested whether Sox10 interacts with NFATc using a Schwann cell line expressing NFATc4 and Sox10. Sox10 copurified with NFATc4 using control but not mutant oligonucleotides containing the NFATc-binding sites of the *DSCR1* (Down syndrome critical region 1) enhancer or *Krox20* MSE (NRE4-s) (figs. S10C and S13). Because these oligonucleotides do not contain Sox10-binding sites, the isolation of Sox10 by control, but not mutant, oligonucleotides supports the direct interaction of NFATc4 and Sox10. Protein domain deletion studies indicated that Sox10

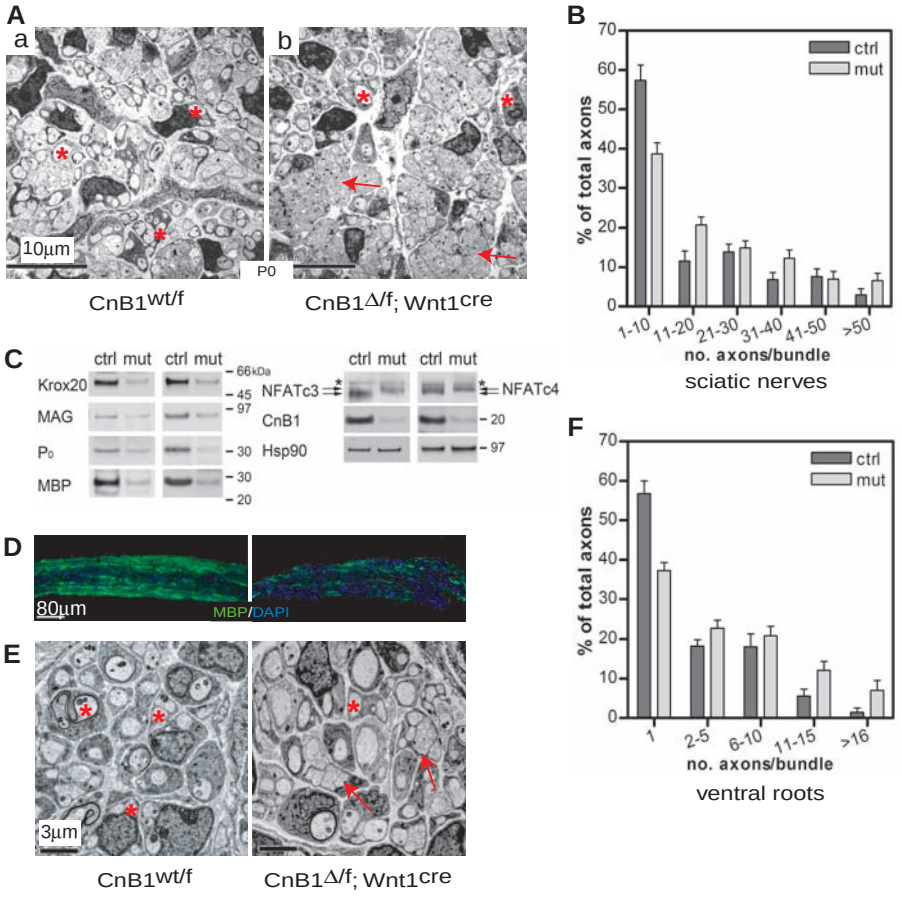

Fig. 2. Schwann cell differentiation is defective in *CnB1* mutant mice. (**A**) Schwann cells in newborn mutant sciatic nerves fail to establish one-to-one relations with axons. Low-power electron microscopic images showing overall structure of sciatic nerves. Asterisks, sorted axons; arrows, unsorted axon bundles. (**B** and **F**) Quantification of axonal sorting (number of axons in bundles) of sciatic nerves and ventral motor roots of spinal cord ($n = 4$ per group; error bars, +SEM; $P < 0.001$; two-tailed t test). (**C**) Immunoblots of newborn sciatic nerves showing expression levels of myelin-specific proteins. Results from two different litters of animals are shown. Arrows, NFATc3 and c4 proteins. *Cross-reactive protein. Hsp90 is a loading control. (**D**) Immunostaining of cryosections of newborn sciatic nerves using MBP-specific antibody (green). (**E**) Electron microscopic images of ventral motor roots. Asterisks, sorted axons; arrows, unsorted axon bundles. All experiments were performed with at least four littermate pairs of mice.

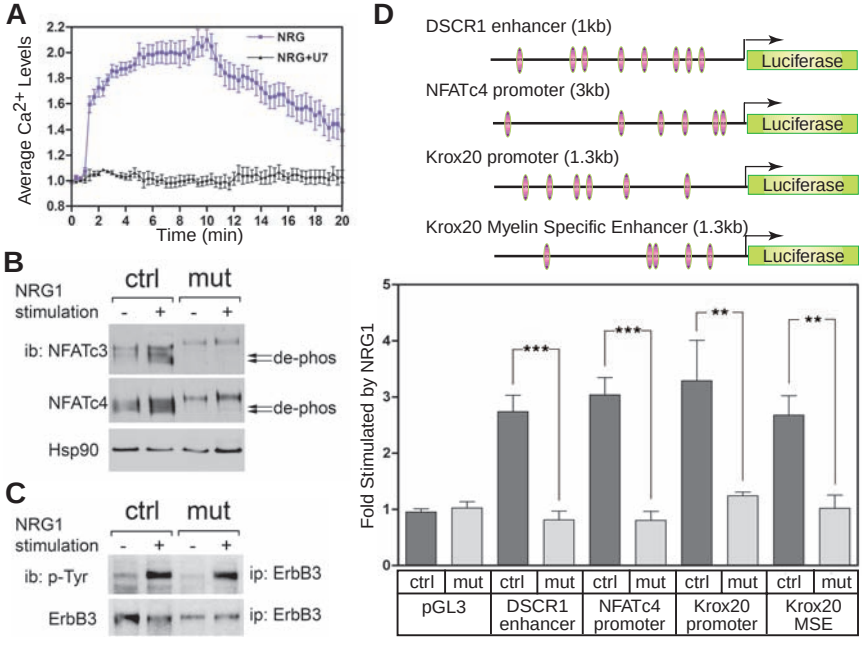

Fig. 3. Calcineurin/NFAT is required for NRG1 and ErbB signaling. (**A**) Ca^{2+} influx stimulated by NRG1. DRG cocultures were preloaded with the Ca^{2+} sensor Fura-2AM in the presence or absence of PLC-γ inhibitor U73122, 30 min before stimulation. Ca^{2+} influx was detected, and average Ca^{2+} levels were measured. (**B**) Dephosphorylation of NFATc3 and c4 is not induced in mutant cocultures after NRG1 stimulation, as examined by immunoblotting (ib). Arrows, dephosphorylated (active) NFATc3 and c4. (**C**) Tyrosine phosphorylation levels of ErbB3 following the activation by NRG1. ErbB3 were isolated by immunoprecipitation (ip). Tyrosine phosphorylation was detected by immunoblotting using phosphotyrosine-specific antibody. The blot was reprobed with ErbB3-specific antibody to verify protein expression levels. (**D**) Calcineurin/NFAT-dependent transcription is stimulated by NRG1. E13.5 DRG cocultures were transfected with luciferase reporter constructs containing the *DSCR1* enhancer, *NFATc4* promoter, *Krox20* promoter, or *Krox20* MSE. Luciferase activities were measured after 20 hours of NRG1 stimulation. Fold activation is relative to unstimulated cells ($n = 6$; error bars, +SEM; $^{**}P < 0.01$; $^{***}P < 0.001$; t test).

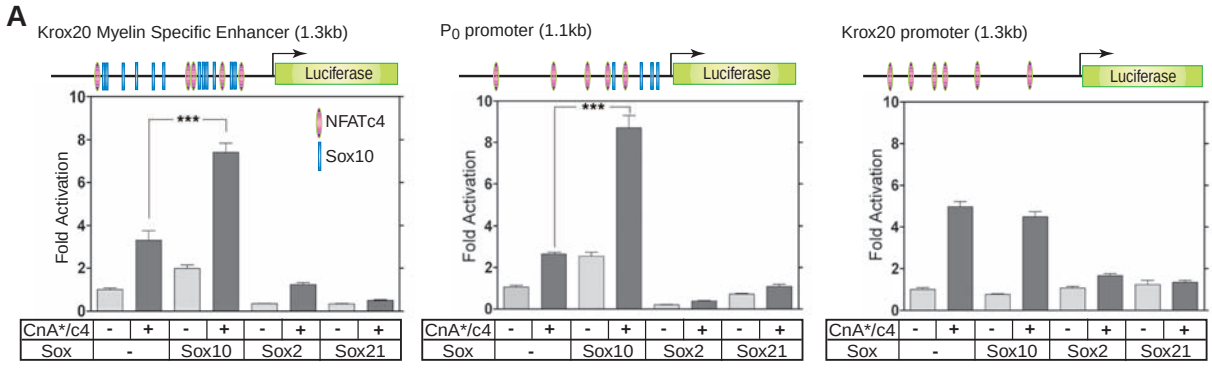

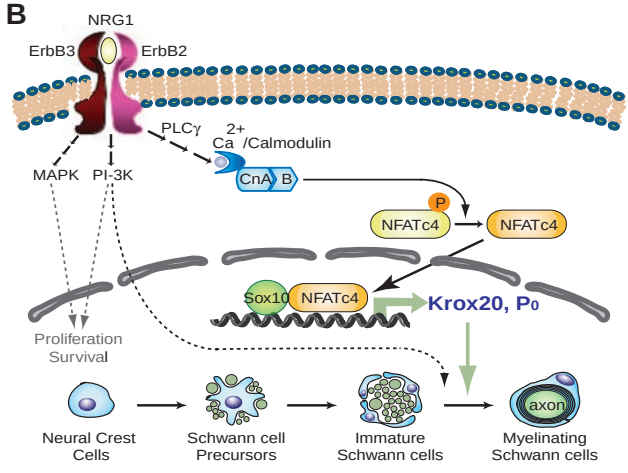

Fig. 4. Synergistic effects of NFATc4 and Sox10 on myelin gene expression. (**A**) NFATc4 and Sox10 synergistically activate the *Krox20* MSE and P_0 promoter. DRG cocultures were transfected with luciferase reporter constructs containing the *Krox20* MSE, P_0 promoter or *Krox20* promoter. Expression constructs encoding constitutively active calcineurin A (CnA*), NFATc4, and Sox family members were co-transfected. Luciferase activities were measured. Fold activation is relative to reporter baseline activities ($n = 6$, error bars, +SEM, ***$P < 0.001$; t test). (**B**) Model of myelination process regulated by calcineurin/NFAT signaling pathway. Solid arrows, calcineurin/NFAT signaling pathway; dotted arrows, pathways defined by previous literature.

bound to the Rel homology domain of NFATc4 (fig. S10D).

Because several conserved NFATc-binding sites lie next to putative Sox10-binding sites in the *Krox20* MSE (fig. S9A), we tested coactivation of the *Krox20* MSE by NFATc4 and Sox10 (Fig. 4A). NFATc4 and Sox10 synergistically activated *Krox20* MSE-driven luciferase expression in DRG cocultures. Brn2 and Oct6 are also important regulators of *Krox20* transcription (*28*). The functional interaction between calcineurin/NFAT and Sox10 might provide NRG1 responsiveness to the *Krox20* MSE and might assist Brn2 and Oct6 in its regulation.

Synergy between NFATc4 and Sox10 was also observed with the P_0 promoter (Fig. 4A and fig. S11) but not with the *Krox20* or *NFATc4* promoters (Fig. 4A and fig. S12B). Sox10 and Krox20 have been shown to regulate the P_0 intron1 (*29*). We found that calcineurin/NFAT also stimulated the P_0 intron1 (fig. S12). Thus, calcineurin/NFAT signaling likely regulates P_0 expression directly through the P_0 promoter by cooperating with Sox10 and indirectly through stimulating intron1 activity by inducing Krox20 expression. Sox2 blocked transcriptional activation (Fig. 4A), consistent with the observation that it is an inhibitor of Schwann cell differentiation (*30*). Using oligonucleotide affinity purification, we found that NFATc4 facilitated Sox10 binding to the NRE4 region of *Krox20* MSE (NRE4-L), because mutation of the NFATc-binding sequence led to reduced cobinding of Sox10 (fig. S13). Together, these data indicate cooperation between NFATc4 and Sox10 in myelin gene expression.

Our data indicate that calcineurin/NFAT signaling regulates the development of Schwann cells at two steps (Fig. 4B). One is by acting downstream of neuregulin and ErbB to directly activate *Krox20* at the promyelination stage, which in turn activates later myelin genes. Another is by activating genes encoding myelin structural proteins, such as P_0, at the myelination stage. NFATc4 interacts with Sox10 and provides specificity to the calcineurin/NFAT pathway for the Schwann cell lineage.

References and Notes

1. K. R. Jessen, R. Mirsky, *Nat. Rev. Neurosci.* **6**, 671 (2005).
2. D. Meyer, C. Birchmeier, *Nature* **378**, 386 (1995).
3. Z. Dong *et al.*, *Neuron* **15**, 585 (1995).
4. K. A. Nave, J. L. Salzer, *Curr. Opin. Neurobiol.* **16**, 492 (2006).
5. M. T. Woldeyesus *et al.*, *Genes Dev.* **13**, 2538 (1999).
6. P. Maurel, J. L. Salzer, *J. Neurosci.* **20**, 4635 (2000).
7. M. Rahmatullah *et al.*, *Mol. Cell. Biol.* **18**, 6245 (1998).
8. S. Britsch *et al.*, *Genes Dev.* **15**, 66 (2001).
9. C. Paratore, D. E. Goerich, U. Suter, M. Wegner, L. Sommer, *Development* **128**, 3949 (2001).
10. D. W. McCauley, M. Bronner-Fraser, *Nature* **441**, 750 (2006).
11. D. B. Parkinson, K. Langner, S. S. Namini, K. R. Jessen, R. Mirsky, *Mol. Cell. Neurosci.* **20**, 154 (2002).
12. R. Srinivasan *et al.*, *BMC Mol. Biol.* **8**, 117 (2007).
13. R. P. Friedrich, B. Schlierf, E. R. Tamm, M. R. Bosl, M. Wegner, *Mol. Cell. Biol.* **25**, 1821 (2005).
14. M. Jaegle *et al.*, *Genes Dev.* **17**, 1380 (2003).
15. M. Jaegle *et al.*, *Science* **273**, 507 (1996).
16. P. Topilko *et al.*, *Nature* **371**, 796 (1994).
17. J. P. Shaw *et al.*, *Science* **241**, 202 (1988).
18. W. M. Flanagan, B. Corthesy, R. J. Bram, G. R. Crabtree, *Nature* **352**, 803 (1991).
19. H. Wu, A. Peisley, I. A. Graef, G. R. Crabtree, *Trends Cell Biol.* **17**, 251 (2007).
20. J. Jain, P. G. McCaffrey, V. E. Valge-Archer, A. Rao, *Nature* **356**, 801 (1992).
21. Materials and methods are available as supporting material on *Science* Online.
22. J. R. Neilson, M. M. Winslow, E. M. Hur, G. R. Crabtree, *Immunity* **20**, 255 (2004).
23. P. S. Danielian, D. Muccino, D. H. Rowitch, S. K. Michael, A. P. McMahon, *Curr. Biol.* **8**, 1323 (1998).
24. K. R. Jessen *et al.*, *Neuron* **12**, 509 (1994).
25. J. R. Arron *et al.*, *Nature* **441**, 595 (2006).
26. H. Wu *et al.*, *J. Biol. Chem.* **282**, 30673 (2007).
27. J. Ghislain *et al.*, *Development* **129**, 155 (2002).
28. J. Ghislain, P. Charnay, *EMBO Rep.* **7**, 52 (2006).
29. S. E. LeBlanc, S. W. Jang, R. M. Ward, L. Wrabetz, J. Svaren, *J. Biol. Chem.* **281**, 5453 (2006).
30. N. Le *et al.*, *Proc. Natl. Acad. Sci. U.S.A.* **102**, 2596 (2005).

31. We thank B. A. Borres for insightful comments; K. J. Liu, Q. Lin, and J. Perrino for technical assistance; and J. I. Wu for critically reading this manuscript. G.R.C is an Investigator of HHMI. These studies were supported by grants from NIH (NS046789, HD55391, and AI60037) to G.R.C.

Supporting Online Material

www.sciencemag.org/cgi/content/full/323/5914/651/DC1
Materials and Methods
Figs. S1 to S13
References

29 September 2008; accepted 10 December 2008
10.1126/science.1166562

Robotic Platform

AutoMAP is a robotic platform for high throughput microplate, tube, and vial processing in a self-contained environment for a variety of drug discovery applications. The platform can be operated as a stand-alone system or integrated with additional platforms, including the MiniStore (an automated sample management system) or MACCS (an automated cell culture system). Temperature, humidity, carbon dioxide, nitrogen, or other gases or gas mixtures can be regulated internally, ensuring optimized experimental conditions. It offers a biological safety cabinet level 1 classification, minimizing potential hazards to laboratory personnel and the environment by isolating dangerous biological agents in an enclosed facility. Its list of applications is almost limitless, including chemical and biological sample management, polymerase chain reaction purification and preparation, cycle sequencing preparation, sample normalization, chemical assays, plate replication, cell-based assays, and more.

MatriCal
For information 509-343-6244
www.matrical.com

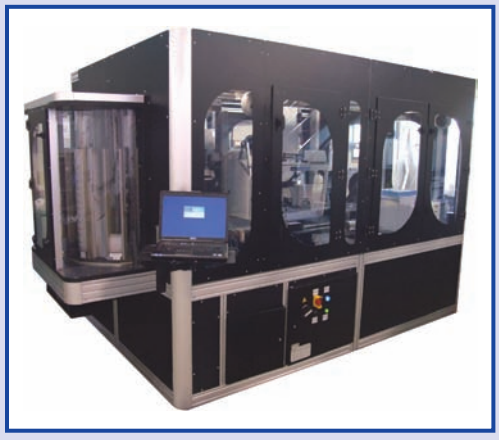

Portable Light Box

The ViewOne is a portable light box designed to fit into limited laboratory space. Measuring 20.5 cm by 14 cm by 0.6 cm and weighing 160 g, it is slightly larger than a passport. The ViewOne LED provides a consistent white light source for hours of dependable operation. It has three selectable light intensities and fixed retainers molded in to hold petri dishes and enzyme-linked immunosorbent assay plates in place. Its smooth, water-resistant surface makes it easy to wipe down and clean.

Embi Tec
For information 858-684-3190
www.embitec.com

Pipetting System

An integrated pipetting system with epT.I.P.S. LoRetention features "Pearl Effect" technology to ensure maximum sample recovery when dispensing detergent solutions. The low-retention tips are designed for users engaged in polymerase chain reaction (PCR), real-time PCR, proteomics, and molecular biology applications. When liquids that contain detergents wet polypropylene, they leave a film on a standard tip's surface that can lead to loss of precious sample, increased consumption of reagents, and poor precision and reproducibility. The "Pearl Effect" technology involves no coating or additive that might affect or bleed into the sample, but instead renders the tip surface ultrahydrophobic through a modification at the molecular level so detergent solutions roll off completely.

Eppendorf
For information +49-40-53801-0
wwww.eppendorf.com

Electronic Laboratory Notebook

The Symyx Notebook is an electronic laboratory notebook (ELN) that is configurable to meet the needs of biologists and analytical chemists. It can simplify operations and lower costs by enabling research and development organizations to replace multiple discipline-specific ELNs with a single, multidiscipline application that is deployable across the enterprise. Built on an enterprise-scale informatics platform, Symyx Notebook consolidates experimental data from multiple domains into shareable and searchable documents controlled by customizable document workflows with secure document versioning, electronic signature, and audit trails.

Symyx Technologies
For information +41-22-884-1331
www.symyx.com

Protein Assay

CB-X Protein Assay is designed to be compatible with all commonly used buffers and reagents. For samples in simple aqueous buffers, CB-X is a sensitive, single-reagent assay that can be performed in five minutes. For complicated protein samples, CB-X is supplied with reagents to clean up the samples and remove all reagents and chemicals that interfere with accurate protein estimation. These reagents include detergents, chaotropes, reducing agents, alkylating agents, sugars, high salt concentrations, buffering agents, and chelating agents. The cleanup stage and subsequent protein assay is performed in a single tube to ensure no protein loss and to maintain the accuracy of the assay.

G-Biosciences
For information 314-991-6034
www.GBiosciences.com

Antigen Standards

Verify Antigen Standard is a collection of tagged overexpression cell lysates for use as protein immunoblot standards. The line covers 5,000 overexpressed human proteins, each with a built-in C-terminal Myc/DDK tag for easy expression verification and antibody validation. These initial 5,000 Verify Antigen Standards will not only provide scientists with easy access to a validated antigen of interest, they can also be easily quantified with an Myc/DDK tag standard to provide definitive detection sensitivity of a particular antibody.

OriGene Technologies
For information 240-620-0270
www.origene.com

Electronically submit your new product description or product literature information! Go to **www.sciencemag.org/products/newproducts.dtl** for more information.

Newly offered instrumentation, apparatus, and laboratory materials of interest to researchers in all disciplines in academic, industrial, and governmental organizations are featured in this space. Emphasis is given to purpose, chief characteristics, and availabilty of products and materials. Endorsement by *Science* or AAAS of any products or materials mentioned is not implied. Additional information may be obtained from the manufacturer or supplier.